Technische Universität München
Physik-Department
Lehrstuhl für Molekulare Nanowissenschaften & Chemische Physik von Grenzflächen

Assembly and Characterization of Hybrid Nanomaterials on Noble Metal Surfaces

Martin Schwarz

Vollständiger Abdruck der von der Fakultät für Physik der Technischen Universität München zur Erlangung des akademischen Grades eines

Doktors der Naturwissenschaften

genehmigten Dissertation.

Vorsitzender: Prof. Dr. Martin Zacharias

Prüfer der Dissertation:
1. Prof. Dr. Wilhelm Auwärter
2. Priv.-Doz. Dr. Anna Cattani-Scholz

Die Dissertation wurde am 23.03.2018 bei der Technischen Universität München eingereicht und durch die Fakultät für Physik am 12.06.2018 angenommen.

Abstract

Novel hybrid materials are an emerging research field, holding great promise for applications in next-generation nanoscale devices. In this thesis, we investigate the structural, electronic and magnetic properties of two-dimensional (2D) epitaxial layers, tetrapyrrolic molecules and single atoms on surfaces in an ultra-high vacuum environment by means of various surface science techniques, such as scanning tunneling microscopy (STM), atomic force microscopy (AFM), low-energy electron diffraction (LEED), X-ray photoelectron spectroscopy (XPS) and X-ray standing waves (XSW).

Specifically, we investigate atomically thin hexagonal boron nitride (*h*-BN) layers on the noble metal surfaces of Cu(111) and Ag(111) single crystals. In a combined AFM and XSW analysis we determine the adsorption height of the *h*-BN layer on Cu(111) and find a — hitherto — unrecognized geometric corrugation in the system. Furthermore, we demonstrate that the growth of *h*-BN is possible on the relatively inert Ag(111) substrate, and we exploit intercalation of silver in *h*-BN/Cu(111) to tune the electronic properties of the resulting system between those of *h*-BN on Cu(111) and *h*-BN on Ag(111).

Moreover, the structure and the functionality of tetrapyrroles on copper and *h*-BN supports are characterized and compared. First, the adsorption geometry of prototypic cobalt porphine on Cu(111) is identified and its exact lateral registry is determined. Next, we analyze the adsorption and the molecular conformation of cobalt porphine on monolayer *h*-BN, highlighting the modifications through the *h*-BN layer that electronically decouples the molecule from the substrate. Finally, we introduce a surface-confined coordination architecture on an sp^2-hybridized *h*-BN sheet based on deliberately functionalized porphyrins and promoted by cobalt adatoms.

Eventually, two approaches to obtain planar *h*-BNC heterostructures are discussed. Besides the direct growth of *h*-BN and graphene on Cu(111) leading to *h*-BN–G interfaces stitched together in-plane, borazine derivatives are utilized. In this particular class of molecules doping BN-units are embedded in a carbon-based scaffold. We show that the symmetry and porosity of the network, its density and the degree of interdigitation between molecules can be controlled by the selection of specific metal substrates.

Zusammenfassung

Neuartige Hybrid-Materialien sind Gegenstand aktueller Forschung und haben großes Potential für Anwendungen in elektronischen Bauteilen der nächsten Generation. In dieser Arbeit werden die strukturellen, elektronischen und magnetischen Eigenschaften von zweidimensionalen epitaktischen Schichten, Tetrapyrrolen und einzelnen Atomen in einer Ultra-Hochvakuum-Umgebung untersucht. Dabei kommen verschiedene Techniken der Oberflächenwissenschaften zum Einsatz, wie beispielsweise Rastertunnelmikroskopie, Rasterkraftmikroskopie, niederenergetische Elektronenbeugung, Röntgenphotoelektronenspektroskopie, sowie stehende Röntgenwellenfelder.

Im Speziellen untersuchen wir atomar dünne hexagonale Bornitrid(h-BN)-Schichten auf den Edelmetalloberflächen von Cu(111) und Ag(111) Einkristallen. In einer multi-methodalen Analyse bestimmen wir die Adsorptionshöhe der h-BN-Schicht auf Cu und finden eine bislang unerkannte geometrische Korrugation im System. Darüber hinaus zeigen wir, dass das Wachstum von h-BN auf der relativ innerten Ag(111)-Oberfläche möglich ist. Schließlich nutzen wir die Interkalation von Silber unter h-BN/Cu(111), um die elektronischen Eigenschaften des resultierenden Systems zwischen denen von h-BN auf Cu(111) und h-BN auf Ag(111) einzustellen.

Darüberhinaus werden die Struktur und die Funktionalität von Tetrapyrrolen auf Kupfer und auf h-BN-Trägern charakterisiert und verglichen. Zuerst wird die Adsorptionsgeometrie und die exakte laterale Anordnung vom prototypischen Kobalt-Porphin auf Cu(111) bestimmt. Danach wird die Adsorption und die Molekül-Konformation von Kobalt-Porphin auf h-BN-Monolagen analysiert und die Auswirkungen der h-BN Schicht dargestellt, welche das Molekül elektronisch vom Substrat entkoppelt. Schließlich stellen wir ein oberflächenbeschränktes Koordinationsnetzwerk auf einer h-BN-Schicht vor, das auf ganz bewusst funktionalisierten Porphyrinen und Kobalt-Adatomen basiert.

Abschließend werden zwei Ansätze zum Erstellung von planaren h-BNC-Heterostrukturen diskutiert. Neben dem direkten Wachstum von planaren h-BN-Graphen-Schnittstellen auf Cu(111), werden Borazin-Derivate verwendet. In dieser speziellen Klasse von Molekülen werden dotierende BN-Einheiten in ein kohlenstoffbasiertes Gerüst eingebettet. Wir zeigen, dass Symmetrie, Porosität und Dichte des Netzwerks, sowie der Grad der Vernetzung zwischen den Molekülen durch die Wahl spezifischer Metall-Substrate kontrolliert werden kann.

Contents

List of Figures

List of Abbreviations

2H–P	Free-Base Porphine
AFM	Atomic Force Microscopy
Co–P	Cobalt Porphine
DFT	Density Functional Theory
DLS	Diamond Light Source
DOS	Density of States
FCC	Face Centered Cubic
FER	Field Emission Resonance
FFT	Fast Fourier Transform
h-BN	Hexagonal Boron Nitride
HOMO	Highest Occupied Molecular Orbital
LDOS	Local Density of States
LEED	Low-Energy Electron Diffraction
LT-STM	Low Temperature Scanning Tunneling Microscopy
LUMO	Lowest Unoccupied Molecular Orbital
NIXSW	Normal Incidence X-ray Standing Wave
OMBE	Organic Molecular Beam Epitaxy
SPM	Scanning Probe Microscopy
STM	Scanning Tunneling Microscopy
STS	Scanning Tunneling Spectroscopy
TPCN	(free-base) Tetra[(4-Cyanophenyl)Phen-4-yl]Porphyrin
UHV	Ultra High Vacuum
vdW	van der Waals
XPS	X-ray Photoelectron Spectroscopy
XSW	X-ray Standing Waves

Chapter 1

Introduction

Numerous key challenges facing mankind in the 21^{st} century such as data storage and processing, sustainable energy harvesting or climate change are closely linked with the endeavor to achieve progress in scientific material research.[Liu03, Gie16] It is well known, that the discovery and utilization of novel materials often coincide with technological advancement. In particular nanoscience and nanotechnology play a decisive role ever since the dawn of the digital and information age in order to provide solutions to the quest of miniaturization in the electronic industry.[Moo65, Moo75] Nanotechnology, a term coined independently by Taniguchi and Drexler in the mid 70s and early 80s,[Tan74, Dre86] subsumes research that aims to create, manipulate and utilize structures in the size range of about 0.1 to 100 nm, thus covering the length scale of atomic, molecular and supramolecular systems.[Bar05]

Although the genesis of nanotechnology is frequently dated back to Richard Feynman's classic and visionary talk "There's plenty of room at the bottom" held at the meeting of the American Physical Society at Caltech in 1959, in which he anticipated the possibility of synthesis *via* "manipulating and controlling things on a small scale",[Fey60] it was not until the development of the scanning probe microscopes in the 80s that seminal experimental advances were achieved in this field.[Bin82b, Bin86, Tou09] Boosted by the emergence of these and other surface science techniques, research has accomplished various important breakthroughs in the following decades, including the manipulation of single atoms,[Eig90] the discovery of fullerenes,[Kro85] and carbon nanotubes,[Iij91] as well as the utilization of molecular self-assembly and supramolecular chemistry to fabricate nanoscale devices from the bottom-up.[Ert08, Bar05, Bar07, Auw15, Boe94, Got15, Kum17, Ruf16]

Especially molecular nanotechnology holds great prospects for applications in diverse fields such as energy harvesting,[Was92, Mat14] light emission,[Li04, End09] gas sensing[Pur99], spintronics[Wäc10] or catalysis.[Meu92, Yos03] The controlled, autonomous and deterministic organization of individual molecular building blocks into functional complex nanoarchitectures on surfaces is highly appealing.[Bar07] In particular tetrapyrrole porphyrin molecules, an interesting class of π-conjugated organic molecules with relevance in natural and artificial

systems,[Bat00] attracted a great deal of interest in the last decades.[Auw15, Got15] The versatile functionality of porphyrins can be tailored *via* metalation of the central macrocycle and by addition of lateral substituents.

Moreover, the mechanical exfoliation of graphene, an atomically thin two-dimensional (2D) sheet of carbon, in 2004[Nov04] has generated unprecedented interest in a new field of nanotechnology and has since fuelled intense research in the area of 2D materials.[Nov05, Gei07, Nov12, Nov16] Many 2D layered materials possess new and distinctive properties compared with their bulk counterparts and can be directly synthesized by chemical vapor deposition (CVD) or other van der Waals epitaxy techniques.[Avo17, Man17, Kim14] Besides the materials outstanding properties on their own, various intriguing fundamental phenomena of condensed matter physics have been rendered accessible in experiments for the first time, in particular in high-quality crystalline graphene: *e.g.* massless Dirac fermions,[Nov05] an anomalous electric field effect,[Nov04] and the room temperature quantum hall effect.[Nov07] As the research on graphene itself has probably passed its zenith,[Gei13] applications utilizing combinations of 2D materials in vertically stacked van der Waals heterostructures or in hybridized atomically flat layers are more and more in the focus of the scientific community.[Nov16]

Especially the combination of 2D materials with functional molecular units or nanostructures is envisaged to provide a vast playground for further exploration.[Weh08, Avo17, Kum17] Different approaches are conceivable: Functionality might be introduced to a layered system, either by molecular overlayers adsorbed on top of 2D sheets effectively gating the structure or by integration of molecular units into planar hybrid materials as has been reported very recently.[He17b] Moreover, atomically thin layers can be utilized to decouple the adsorbates from the predominantly metallic supports required for electrical contacting.[Kum17] Furthermore, intercalation of atomic or molecular species is actively studied for the purpose of *e.g.* gating,[Fed15, Sch17a] and decoupling (Ag, Au)[Uih15] in the first case, as well as protecting a system from detrimental environments in the latter case.[Duc18, Al 16, Mon15, Var10]

Implicated by the nature of atomically thin layers, the peculiar interfaces between the individual components of the systems are of fundamental relevance. Surface science provides an ample toolbox of techniques to investigate those interfaces on the atomic level in a well-defined environment. Functionalities of materials and in particular of molecules are closely associated with their structure. The phrase “If you want to understand function, study structure”, supposedly said by Francis Crick,[Ame16] the co-discoverer of the structure of DNA molecules, can, therefore, be interpreted as one of the motivations of the experiments conducted within the framework of this PhD project.

This thesis presents research at the interface of surface science, material engineering and supramolecular chemistry contributing to the field of molecular nano science. We study the structural, electronic and magnetic properties of 2D epitaxial layers, functional molecules and single atoms in surface-confined model systems. Specifically, we explored atomically thin sp^2-bonded hexagonal boron nitride (h-BN), graphene (G) and in-plane h-BN–G heterostructures. Moreover, we investigated tetrapyrrole porphyrin molecules, cobalt atoms and borazine derivatives on noble metal substrates and h-BN supports. The thesis is structured as follows:

Chap. 2 delineates the basic concepts of the surface science techniques that were utilized in the experiments in the course of this PhD project. We employed various complementary techniques, such as scanning tunneling microscopy (STM), atomic force microscopy (AFM), low-energy electron diffraction (LEED), X-ray photoelectron spectroscopy (XPS) and X-ray standing waves (XSW) to obtain a comprehensive understanding of the systems under investigation. First-principle density functional theory (DFT) calculations, conducted by collaborators, were employed in several cases to complement and rationalize the experimental findings.

In Chap. 3, the instrumentation and the applied technologies are described in detail. Specifically, the ultra-high vacuum system combining an STM and an XPS setup that was designed and assembled as part of this PhD project, is outlined. Furthermore, the sample geometry is illustrated, and the tip and sample preparation procedures are presented. In addition, the Diamond Light Source synchrotron and the endstation of its beamline I09 are depicted, where integral parts of the experiments have been conducted.

Chap. 4 elucidates the growth and the characterization of monolayer h-BN on the surfaces of single crystal Ag(111) and Cu(111). In the case of h-BN on Cu(111), the adsorption height above the copper surface and the geometric corrugation of the layer were determined, both key structural parameters. Subsequently, the growth of h-BN on the relatively inert Ag(111) surface will be depicted, and intercalation of silver in h-BN/Cu(111) will be presented as an alternative strategy to obtain h-BN layers on silver. With the performed measurements, the adsorption energy, the surface potential, the chemical environment of the atomic species in h-BN, and the band structure of the obtained h-BN layers on silver were characterized.

Chap. 5 presents a characterization of tetrapyrrolic porphyrin molecules on copper and h-BN supports. First, the local adsorption geometry and the exact atomic registry of cobalt porphine (Co–P) on Cu(111) is determined. Next, the adsorption structure of Co–P on a monolayer h-BN/Cu(111) is analyzed quantitatively. The adsorption height above the h-BN sheet is determined, and the significant modifications of the adsorption conformation of the molecule through the decoupling h-BN layer are highlighted. Moreover, an exemplary surface-confined coordination architecture on a h-BN sheet, based on carbonitrile-

functionalized porphyrins and promoted by cobalt adatoms, is introduced. Finally, the magnetic properties of cobalt atoms in different environments are studied through their characteristic Kondo exchange interaction with the metallic substrate.

Chap. 6 discusses two different experimental strategies to obtain planar *h*-BNC heterostructures. The first approach is based on the direct growth of *h*-BN and graphene (G) on Cu(111) leading to in-plane *h*-BN–G junctions that were characterized on the atomic scale. The second approach utilizes borazine derivatives, custom-designed and synthesized molecules that consist of B, N and C atoms. We studied the self-assembly of two particular borazine derivative molecules on Cu(111) and Ag(111), and achieved distinct network architectures on the two metal surfaces. Our measurements indicate that the BN core is electronically decoupled from the conductive substrate.

To conclude, the detailed results presented in this thesis are summarized and some perspectives for future experiments are sketched in Chap. 7.

Chapter 2

Concepts

In the course of this thesis, several complementary techniques have been employed to study metallic surfaces, interfaces, molecules, and single atoms. The following chapter gives an overview of these surfaces science techniques. First, the basic concepts and the theory of scanning probe microscopy (SPM) are elucidated. Specifically, scanning tunneling microscopy (STM) was utilized in many experiments presented in this thesis, supported by atomic force microscopy (AFM) measurements. Next, X-ray photoelectron spectroscopy (XPS) and the X-ray standing wave technique (XSW) are introduced. Finally, a concise introduction to low-energy electron diffraction (LEED) is presented.

2.1 Scanning Probe Microscopy (SPM)

SPM subsumes a multitude of techniques that are based on the image formation by scanning the surface of a material with a physical probe. The image of the sample is generated by measuring the interaction between probe, usually referred to as tip, and sample at each point of a grid. The obtained information is visualized in real-time as an intensity map. Both, vertical and lateral resolution of scanning probe techniques can reach the angström (Å) regime and hence provide atomic resolution.[Che90, Che08] The most famous and powerful members of the SPM family are STM (see section 2.1.1) and AFM (see section 2.1.2), which are historically closely related.

The invention of the STM by Binning and Rohrer at IBM Zurich Research Laboratory in 1981 was a milestone in the history of nanotechnology.[Bin82b] STM was the first instrument capable of imaging surfaces in real-space with atomic precision.[Bin82a] Its first great success was the imaging of the 7×7 reconstruction of the Si(111) surface, solving a problem heavily debated in the surface science community at that time.[Bin83] In 1986, only a few years after its invention, Binnig and Rohrer were awarded the Nobel Prize in Physics "for their design of the scanning tunneling microscope".[Nob86]

STM is based on the concept of quantum mechanical tunneling. Therefore, a sharp, conductive tip is positioned in a few Å distance above a conductive surface. A bias voltage applied between tip and sample gives rise to an electric tunneling current, which depends on both the distance between tip and sample and their density of states. The information displayed in the obtained intensity map is a convolution of the topographic and electronic structure of the surface. Section 2.1.1 explains the basic concept of STM in detail.

Apart from the simplicity of the operational principle, STM suffers one major limitation. As the concept is based on an electrical current flowing between two conductive electrodes, the studied samples are restricted to be metals or semiconductors, and the obtained information is not solely topographic. Importantly, systems comprising an atomically thin layer (like *e.g.* *h*-BN or graphene) supported on a metal crystal are accessible by STM, which has been utilized in the course of this thesis as discussed later (see sections 4 and 5).

A second development - the atomic force microscope - introduced by Binnig, Quate, and Gerber in 1985 circumvents the necessity of conductivity.[Bin86] AFM measures the force acting between tip and sample, and thus enables to study any kind of surface. Over the last three decades, several operation modes comprising contact and non-contact AFM have been developed. In the following, only the frequency-modulation mode in non-contact AFM will be introduced. AFM was used as a complementary tool in the course of this thesis to obtain geometric information about a two-dimensional layer. Its basic principle is briefly introduced in section 2.1.2.

2.1.1 Scanning Tunneling Microscopy (STM)

In this chapter, the fundamental principles of STM are introduced. First, the working principle of STM is explained with a qualitative explanation for its impressive resolution. Next, a quantitative expression for the tunneling current is derived theoretically, followed by a discussion of scanning tunneling spectroscopy. Finally, the different operation modes of STM are discussed.

The STM is based on the quantum mechanical tunneling effect. Electrons with a certain energy have a finite probability to pass a potential barrier, which they could not surmount in classical mechanics. This phenomenon was observed for the first time by Giaever in 1960,[Gia60] when he measured the current between two metal electrodes separated by a thin insulating oxide layer. Instead of the oxide layer, the vacuum between tip and sample acts as a potential barrier in the STM. Binnig and Rohrer combined the principle of quantum mechanical tunneling with a feedback loop, realized by a precise motion control using piezoelectric actuators together with a proper vibration isolation to create the first STM.[Bin87]

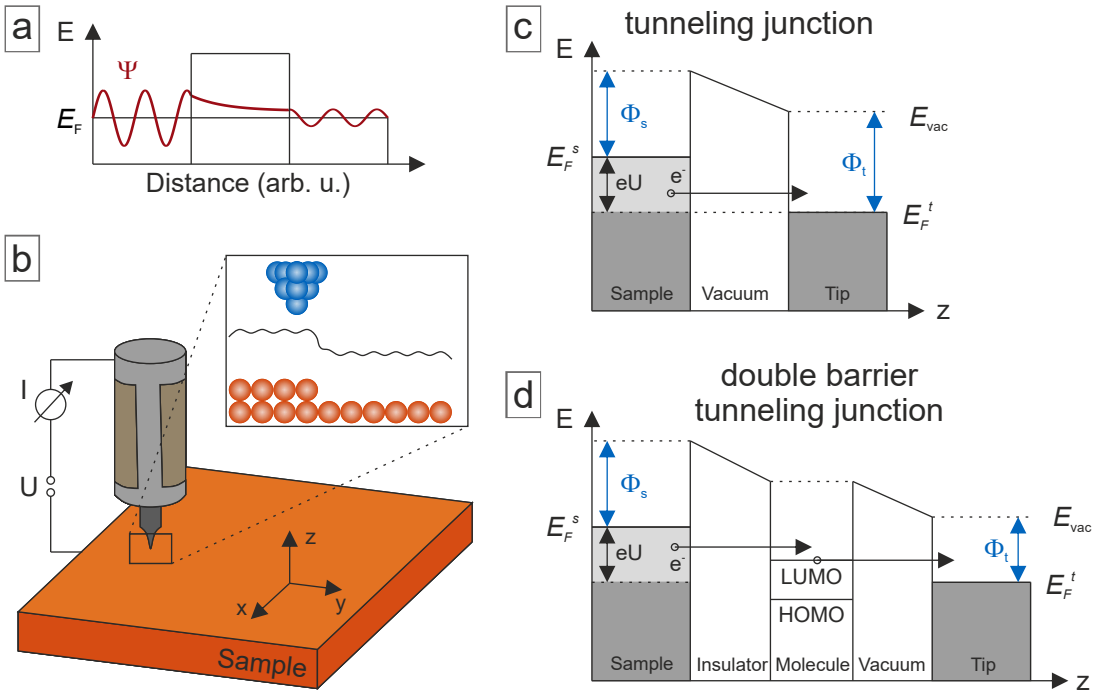

Figure 2.1: ***Working principle of STM.*** ***(a)*** *Sketch of an one-dimensional tunneling junction. The electron wavefunction* Ψ *decays exponentially in the tunneling barrier. Accordingly, the electron has a finite probability of presence on the right-hand side of the barrier.* ***(b)*** *Illustration of the basic components of an STM. A conductive tip is approached to a conductive substrate and scanned across the surface via a piezo scanner. Thereby, the tunneling current* I*, which is due to an applied bias voltage* U*, is recorded. The tunneling current depends on the tip-sample distance, the local density of states and the applied bias voltage. In constant-current mode, a feedback loop maintains a constant tunneling current* I *by adjusting the tip-sample distance* z *(see inset).* ***(c)*** *Energy diagram of the STM tunneling junction while a negative sample bias is applied. At zero temperature, the electronic states of tip and sample are occupied up to their respective Fermi levels* E_F^t *and* E_F^s*. Electrons tunnel from the sample into unoccupied states of the tip.* ***(d)*** *Energy diagram of a double barrier tunneling junction (DBTJ), which describes the case of molecules on insulating layers. At negative sample bias, electrons tunnel into unoccupied molecular states and subsequently into the tip.*

Figure 2.1b shows a schematic of an STM. A conductive tip is positioned some Å above a conductive sample surface. An applied bias between tip and sample of typically some V gives rise to a tunneling current in the range of pA to nA. The tip can be moved in all spatial directions *via* piezoelectric actuators with high precision of a few picometers. An image is acquired by scanning the tip over a grid of the surface line by line and recording either the tunneling current I or the tip height z for each data point.

In STM, two different operation modes are typically differentiated. In the most common operation mode, the so-called constant-current mode, a feedback loop controls the tip-sample distance z in order to maintain the tunneling current, which is an input variable for the feedback loop. The tunneling current is amplified by a current-voltage amplifier and converted

into a voltage, which is subsequently compared to a reference value. The difference between the two values is amplified again to drive the piezo actuator that adjusts the tip-sample distance z. The phase of the amplifier is chosen such that it provides negative feedback, *i.e.* if the tunneling current is larger than the setpoint value, the tip is withdrawn from the sample surface and *vice versa*.[Che08] The tip-sample distance z is recorded for each data point of the scanned grid and represents the imaging signal, including information about the topography and the local density of states (LDOS) of the surface. In constant-height mode, the tip is scanned laterally over the sample at a given, constant tip height z and the tunneling current is recorded for each data point. Although constant-height mode allows higher scan speeds, it is rarely used as it requires a perfectly flat surface, no thermal drift, and an exceptional vibrational damping.

Figure 2.1c displays an energy diagram of the tunneling junction between the tip and the sample surface. In a classical consideration, an electron with a total energy $E < E_F^s$ would not be able to pass the energy barrier (the vacuum) with a height $U = E_F^s + \Phi^s > E$. Here, Φ^s denotes the work function of the sample. However, in a quantum mechanical view, where the electron can be considered as a wave, the electron wavefunction decays exponentially in the vacuum region (see Figure 2.1a). This is a consequence of the Schrödinger equation, which solution indicates that the electron has a finite probability to be inside the potential barrier and also in the electrode on the other side of the potential barrier, *i.e.* the tip. The exponential decay of the electron wavefunction translates into an exponential decay of the tunneling current as a function of the tip-sample distance. It is this dependence that eventually makes the impressive atomic resolution of STM possible.

As briefly mentioned above, tunneling through an additional ultra-thin insulating layer, which is present between the tip and the sample, is possible. This was exploited in the course of this thesis when atomic and molecular adsorbates on h-BN supports were studied (see section 5). Upon adsorption on metal surfaces, the electronic states of the adsorbates are usually perturbed due to the strong interaction with the metal. In order to prevent this perturbation and solely probe the intrinsic energy levels of the adsorbate, atomically thin insulating layer have been utilized in recent years.[Qiu04, Hei04, Rep04b, Rep05b, Wu04, Jos14] Consequently, the energy diagram has to be adapted to the modified tip-sample geometry with an adsorbate and an insulator between tip and sample. The proposed double-barrier tunneling junction[Sch93, Rep05a] is depicted schematically in Figure 2.1d. Here, the electron tunnels sequentially from the substrate state into an adsorbate state and thereafter into a tip state.[But88] This enables to probe the electronic states of adsorbates near the Fermi energy.

2.1.1.1 Basic Theory of STM

In the last few decades, various methods to calculate the tunneling current in STM have been developed. Historically, the first quantitative expression of the tunneling current in a metal-insulator-metal junction was introduced by Bardeen in 1961.[Bar61] A comprehensive introduction to STM has been published by Chen,[Che08] which is the basis of the following section. In the following, a brief summary of the perturbation approach is presented, which is based on Bardeen's Hamiltonian and some additional approximations proposed by Tersoff and Hamann are briefly discussed.[Bar61, Ter83, Ter85]

In Bardeen's approach, the tip and the sample are treated as separate entities.[Bri99, Hof03] Both, the tip and the sample are described by separate wavefunctions ψ and χ, respectively, which can be treated as a perturbation potential for each other in the proximity of both electrodes.[Che88] The Schrödinger equation of the system with the Hamiltonian $\mathcal{H}$ is given by

$$i\hbar\frac{\partial\Psi}{\partial t} = \left(-\frac{\hbar^2}{2m}\nabla^2 + U_s + U_t\right)\Psi \tag{2.1}$$

where U_t (U_s) is the potential of the tip (sample). If the tip and the sample states are zero in the respective counter-electrode, the total wavefunction can be approximated by the eigenstates, *i.e.* the wavefunctions that solve the Schrödinger equation correctly in their respective systems,[Bri99]

$$\Psi(\boldsymbol{r}) = \begin{cases} \psi_\mu(\boldsymbol{r}) & \text{, for } \boldsymbol{r} \in \text{tip} \\ \chi_\nu(\boldsymbol{r}) & \text{, for } \boldsymbol{r} \in \text{sample} \\ \widetilde{\Psi}(\boldsymbol{r}) & \text{, otherwise} \end{cases} \tag{2.2}$$

with μ and ν denoting the different states. The electronic states ψ_μ and χ_ν can be obtained from the solution of the time-independent Schrödinger equations of the two individual subsystems. In the tunneling process, an electron, which is initially in the tip state ψ_μ is transferred to the sample state χ_ν. The transition probability w of this tunneling event can be calculated by applying time-dependent perturbation theory, *i.e.* Fermi's Golden rule. For an electron with energy E_μ in state ψ_μ it reads

$$w = \frac{2\pi}{\hbar}\left|M_{\mu\nu}\right|^2 \delta(E_\mu - E_\nu) \tag{2.3}$$

with the transition matrix element $M_{\mu\nu} = \langle\psi_\mu\left|\mathcal{H}\right|\chi_\nu\rangle$ between the electron tip state ψ_μ and the electron sample state χ_ν given by [Bar61]

$$M_{\mu\nu} = -\frac{\hbar^2}{2m} \int (\chi_\nu^* \boldsymbol{\nabla} \psi_\mu - \psi_\mu \boldsymbol{\nabla} \chi_\nu^*)\, d\boldsymbol{S}. \tag{2.4}$$

Note, that the integral is a summation over an arbitrary separation surface running through the vacuum between tip and sample. Taking into account energy conservation (*i.e.* elastic tunneling), only transitions from tip states to sample states with $E_\mu = E_\nu$ are allowed. Furthermore, electrons can only tunnel from an occupied state of the electrode into an unoccupied state of the counter-electrode. Besides, the transmission rate in the opposed direction needs to be subtracted as there is no preferred direction of electron tunneling. With these considerations the tunneling current I at a bias voltage V is, to first order, given by [Che08]

$$I = \frac{4\pi e}{\hbar} \int_{-\infty}^{\infty} [f(E_F - eV + \epsilon) - f(E_F + \epsilon)] \cdot \rho_t(E_F - eV + \epsilon) \rho_s(E_F + \epsilon) \left|M(\epsilon, V)\right|^2 d\epsilon. \tag{2.5}$$

Here, $f(E)$ is the Fermi–Dirac distribution that describes the mean occupation probability of the state at energy E. A factor of 2 is included to account for the spin degeneracy. ρ_t and ρ_s are the density of states of tip and sample, respectively, which are given by

$$\rho_t(E) = \frac{1}{V} \int_V \left(\sum_\mu \left|\psi_\mu(\boldsymbol{r})\right|^2 \delta(E_\mu - E) \right) d\boldsymbol{r}, \tag{2.6}$$

and

$$\rho_s(E) = \frac{1}{V} \int_V \left(\sum_\nu \left|\chi_\nu(\boldsymbol{r})\right|^2 \delta(E_\nu - E) \right) d\boldsymbol{r}. \tag{2.7}$$

For low temperatures (*i.e.* room temperature or below), where the Fermi-Dirac distribution can be approximated by a step function, and in the case of small bias voltages ($eV \ll \Phi_t$, with Φ_t the tip work function) Eq. (2.5) simplifies to

$$I = \frac{4\pi e}{\hbar} \int_{E_F}^{E_F + eV} \rho_t(\epsilon - eV) \rho_s(\epsilon) \left|M(\epsilon, V)\right|^2 d\epsilon. \tag{2.8}$$

The essential difficulty to obtain the tunneling current from Eq. (2.8) is the unknown transition matrix element $M_{\mu\nu}$. Therefore, Tersoff and Hamann introduced an approximation based on the assumption that the tip is locally spherical symmetric with radius R and centered at $\boldsymbol{r_0}$.[Ter83, Ter85] Hence, the tip wavefunction ψ_μ is represented by a spherical symmetric s-wave. With this assumption, Eq. (2.8) can be recast to

$$I = \frac{32\pi^3 e^2 V \Phi_s^2 \rho_t(E_F) R^2}{\hbar \kappa^4} e^{2\kappa R} \sum_\nu \left|\chi_\nu(\boldsymbol{r_0})\right|^2 \delta(E_\nu - E_F), \tag{2.9}$$

where $\kappa = \sqrt{2m\Phi_s/\hbar^2}$ is the minimum inverse decay length of the wavefunctions in vacuum, Φ_s is the work function of the sample, $\rho_t(E_F)$ is the local density of states (LDOS) of the tip at the Fermi level, R is the radius and $\boldsymbol{r_0}$ the center of the tip. Remarkably, the tunneling current is proportional to the LDOS of the sample at the Fermi level $\rho_s(\boldsymbol{r_0}, E_F)$ (see the sum in Eq. (2.9)) defined by

$$\rho_s(\boldsymbol{r_0}, E_F) = \sum_\nu |\chi_\nu(\boldsymbol{r_0})|^2 \delta(E_\nu - E_F), \tag{2.10}$$

the LDOS of the tip, and the position of the tip $\boldsymbol{r_0}$. Importantly, with the assumption of an s-wave tip state, an STM image acquired in constant-current mode represents a topographic map of constant sample density of states. The imaged contour is thus a convolution of topographic and electronic information. The tunneling current

$$I \propto V\rho_s(\boldsymbol{r_0}, E_F) \propto e^{-2\kappa z} \tag{2.11}$$

decays exponentially in the vacuum between tip and sample. This predicted behavior agrees well the exponential dependence observed by Binnig and Rohrer in their first STM measurements.[Bin82a, Bin82b] With a typical work function of metals $\Phi_s \approx 5\,\text{eV}$, a distance change of 1 Å results in a change of the tunneling current by one order of magnitude. In order to simulate STM images, the Tersoff-Hamann approximation is nowadays incorporated into nearly every state-of-the-art DFT code.[Dra01]

2.1.1.2 Scanning Tunneling Spectroscopy

Scanning tunneling spectroscopy (STS) is an extension to the imaging capability of STM. STS can be utilized to probe the density of electrons in a sample as a function of their energy. The concept was initially proposed by Selloni in 1985 [Sel85] and realized first by Binnig *et al.* on a Ni(100) surface.[Bin85] STS allows measuring occupied and unoccupied electronic states (LDOS) near the Fermi level with a spatial resolution on the atomic scale.

In the last decades, STS was employed to study *e.g.* metal surface and interface states [Cro93b, Cro93a, Bie96, Gar16], the energy level of adsorbed molecules,[Rep05b, Jos14] as well as vibrational modes of molecules.[Sti98, Qiu04, Gar14c] In addition, spin-polarized STS developed by Wiesendanger *et al.* allows assessing the magnetic properties of surfaces, molecules, and atoms.[Bod01, Pie01, Wie01, Gar13a]

STS exploits the fact that the tunneling current in STM depends on the sample density of states. The number of states available for tunneling can be adjusted by the applied bias voltage: tunneling is suppressed when no occupied and unoccupied are aligned in tip and sample, respectively, while it is strongly enhanced when numerous states are accessible (*i.e.*

resonant tunneling). Resonant tunneling is visualized as peaks in the differential conductance $\mathrm{d}I/\mathrm{d}V$, the derivative of the experimentally accessible I-V curve.

A mathematical description of STS was given *e.g.* by Hamers.[Ham89, Ham01] He uses the Wentzel-Kramers-Brillouin (WKB) approximation, which takes into account that large bias voltages are applied during STS measurements and therefore all electronic states up to an energy eV contribute to the tunneling current.[Ham01] According to his work, the tunneling current in Eq. (2.8) can be rewritten as

$$I \propto \int_0^{eV} \rho_s(\boldsymbol{r_0}, E)\rho_t(\boldsymbol{r_0}, E - eV)T(\boldsymbol{r_0}, E, eV)\, dE, \tag{2.12}$$

if the transition matrix is approximated by an average transmission probability, $M_{\mu\nu} = T(\boldsymbol{r_0}, E, eV)$. Here, ρ_t and ρ_s are the LDOS of the tip and the sample, respectively. Differentiating Eq. (2.12) with respect to the voltage yields

$$\frac{dI}{dV} \propto \rho_s(\boldsymbol{r_0}, eV)\rho_t(\boldsymbol{r_0}, 0)T(\boldsymbol{r_0}, eV) + \int_0^{eV} \rho_s(\boldsymbol{r_0}, E)\rho_t(\boldsymbol{r_0}, E - eV)\frac{dT(\boldsymbol{r_0}, E, eV)}{dU}\, dE. \tag{2.13}$$

The integral in Eq. (2.13) vanishes for a voltage-independent transmission probability as assumed by Hamers in the WKB approximation.[Ham01] Furthermore, the tip LDOS is assumed to be constant, resulting in

$$\frac{dI}{dV} \propto \rho_s(\boldsymbol{r_0}, eV). \tag{2.14}$$

Thus, Eq. (2.14) reveals, that STS indeed probes the LDOS, the local electronic structure of the sample by measuring the differential conductance $\mathrm{d}I/\mathrm{d}V$. Due to the high precision in positioning the STM tip, sub-molecular lateral resolution is achievable.[Ham01]

Experimentally, STS is commonly realized *via* the lock-in technique. This technique is based on a small modulation voltage superimposed onto the applied DC bias voltage. The sinusoidal modulation voltage has a frequency ω that is larger than the lowpass cut-off of the feedback loop. Thereby, the tunneling current I is modulated with this sinusoidal voltage whereas the feedback loop does not take it into account for the adjustment of the tip-sample distance. The $\mathrm{d}I/\mathrm{d}V$ is calculated with the modulated AC signal component that is in phase with the initial modulation frequency ω.[Bin85, Bai00] STS can be acquired for a single position on the sample or on a grid together with a regular STM image. The latter is referred to as $\mathrm{d}I/\mathrm{d}V$ map.

2.1.1.3 Manipulation Modes

Besides the imaging operation modes (constant-current and constant-height mode), and the scanning tunneling spectroscopy mode, described above, there are two additional STM operation modes: the manipulation modes, which shall be introduced here. In 1990, Eigler and Schweizer demonstrated at the IBM Almaden research center, that STM can not only be used as a tool to observe sample surfaces but that it can also be utilized to manipulate the position of individual atoms in a controlled way. Therefore, they moved 35 xenon atoms on a Ni(110) crystal to spell the name of their company "IBM",[Eig90] convincing the scientific community that nanotechnology and Feynman's vision of controlling atoms and molecules was real.[Fey60, Tou10] Later, in 1993, the technique was used by Crommie, Lutz, and Eigler to confine surface state electrons of a copper substrate within a ring of 48 iron atoms, resulting in one of the most iconic STM images.[Cro93a]

In the lateral manipulation (LM) mode, the STM tip is positioned over an area of interest and utilized to manipulate a single atom or a molecule.[Str91] First, the STM tip is approached to the atom or molecule. Depending on the tip-atom (molecule) interaction, different kinds of forces can be distinguished, which drive the movement. If the interaction is attractive the atom or molecule adheres to the tip and is pulled across the surface. With a repulsive interaction between tip and atom/molecule, it is pushed along the direction of the tip movement. At the final location, the tip is retracted to the regular imaging height.

The vertical manipulation (VM) mode works similar to the LM mode. It can be employed to pick up single atoms or molecules by the STM tip. Therefore, the tip height and the electric field, controlled by the current and the bias are utilized. Additionally, molecules and atoms can be moved on the surface *via* small voltage pulses.

2.1.2 Non-Contact Atomic Force Microscopy (nc-AFM)

In the course of this PhD project, complementary nc-AFM measurements were conducted to corroborate the results obtained by XSW (see section 4.1). A concise overview of the frequency-modulation nc-AFM technique will be presented in this section while a comprehensive review and an in-depth introduction to the AFM can be found elsewhere.[Gie03, Mor15, Bis17]

The imaging mechanism of nc-AFM is based on the force interaction between the probe and the sample. In state-of-the-art nc-AFM, the tip is located on a cantilever, which is driven by a very stiff quartz crystal resonator (*e.g.* qPlus sensor[Gie98]). The AFM cantilever can be characterized by its spring constant k and its eigenfrequency f_0. In frequency-modulation (FM-)AFM, the resonator oscillation is maintained by two feedback loops. The phase-locked feedback loop ensures that the cantilever is on resonance with the external excitation by

adjusting the phase. An additional feedback loop maintains the resonance amplitude by adjusting the drive amplitude. The force interactions are directly tracked by changes in the resonance frequency, *i.e.* the frequency shift Δf that is one of the measurement signals in AFM measurements. In analogy to STM (*cf.* section 2.1.1), an AFM image is generated by raster scanning the tip across the sample surface and measuring Δf at every data point of the grid.

As pointed out by Giessibl,[Mor15] the oscillation amplitude should be chosen such that it is on the order of the characteristic length scale of the force components that are studied. The drive amplitude, reflected in the excitation channel, provides information on the dissipated energy due to non-conservative tip-sample interactions.[Oya06, Kan04, La 16] The utilized qPlus sensor is capable of stable operation with sub-angström oscillation amplitudes,[Sch15a] which is the range of the forces that are responsible for the atomic contrast and of particular interest in the course of this thesis.

A relationship between the frequency shift Δf and the total force F_{TS} acting between tip and sample can be derived by treating the AFM cantilever motion as an externally driven, damped harmonic oscillator, as discussed *e.g.* in references [Gie97, Gie03, Mor15]. It can be shown, that the frequency shift Δf is a measure of the force gradient

$$\Delta f = -\frac{f_0}{2k_0}\frac{\partial F_{TS}}{\partial z}. \tag{2.15}$$

Here, f_0 is the eigenfrequency of the harmonic oscillator, k_0 is its spring constant, and z is the direction of the oscillation. The net force F_{TS}, which acts between tip and sample, is a sum of different force components. In the following, the most important components and their effect on Δf are briefly discussed.

Electrostatic force: The electrostatic force originates from the potential difference between the tip and the sample. On a macroscopic scale, tip and sample form a capacitor with capacitance C. The long-range and always attractive electrostatic force is given by [Mor15]

$$F_{el} = -\frac{1}{2}\frac{\partial C}{\partial z}(U - U^*), \tag{2.16}$$

with the contact potential difference U^*. With Kelvin probe force microscopy (KPFM), the local contact potential difference (LCPD) can be mapped.[Non91, Moh12, Mor15] In the particular case of a supported h-BN layer (see section 4.1), the electrostatic force is relevant due to significant lateral differences induced by the electronic superstructure of the surface.

van der Waals force: van der Waals (vdW) forces represent interactions between (fluctuating) polarizations of particles and are usually attractive, but can also be repulsive.[van80] The vdW force between a spherical tip with radius R and a flat sample surface in distance z can be calculated by the Hamaker approach and reads [Ham37, Isr11]

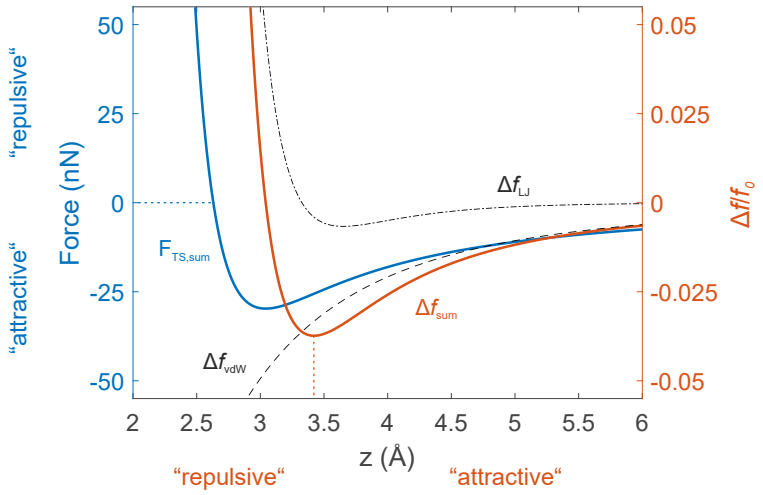

Figure 2.2: *Distance dependance of the force and the frequency shift derived from a Lennard-Jones (LJ) and a van der Waals (vdW) potential. The LJ (black dotted line) and vdW contributions (black dashed line) to the total frequency shift Δf (red line) are indicated. The blue curve corresponds to the total force F. The attractive and the repulsive regime is based on the minimum in $\Delta f(z)$. Used parameters: $E_{min} = 2\,\mathrm{eV}$, $z_0 = 3\,\text{Å}$, $A_H = 1\,\mathrm{eV}$, and $R = 100\,\mathrm{nm}$.*

$$F_{vdW} = -\frac{A_H R}{6z^2}. \tag{2.17}$$

A_H denotes the material-dependent Hamaker constant. As vdW forces act between the microscopic tip apex and a large surface area, they can be considered long-ranged. Eq. (2.17) indicates that a sharp tip is desirable in AFM experiments as it reduces the vdW forces.

Chemical force: Chemical forces are present when two particles are in close proximity to each other where their wavefunctions begin to overlap. The interaction between the outermost tip atom and the closest surface atom is composed of a short-range repulsive term and an attractive term that arises from vdW forces. The repulsive interaction term describes the Pauli repulsion, which originates from overlapping orbitals. The total chemical interactions in AFM are usually well described by the empirical Lennard-Jones (LJ) potential.[Gie97] The respective tip-sample force reads

$$F_{LJ} = -\frac{12E_{min}}{z_0}\left(\left(\frac{z_0}{z}\right)^{13} - \left(\frac{z_0}{z}\right)^{7}\right), \tag{2.18}$$

with the energy potential depth E_{min} (binding energy), and the equilibrium distance z_0.

The total tip-sample force can be calculated as a sum of the vdW (Eq. (2.17)) and the LJ (Eq. (2.18)) force taking into account the short-range and the long-range force contributions. Figure 2.2 schematically displays the total force and the individual contributions to Δf, modeled with typical parameters.

2.2 X-ray Photoelectron Spectroscopy (XPS)

XPS is a spectroscopic technique that allows to measure, in a quantitative fashion, the elemental composition of solid surfaces. It is based on the photoelectric effect, a phenomenon first observed by Hertz in 1887,[Her87] and later, in 1905, explained theoretically by Einstein in one of his seminal *Annus Mirabilis* papers,[Ein05, Aro65] for which he was awarded the Nobel Prize in 1921.[Nob21] The photoelectric effect describes the emission of electrons from a solid upon absorption of photons. In the 1950s and 60s, Siegbahn *et al.* finally demonstrated the potential of the controlled utilization of core-level photoemission for chemical analysis, thus modern XPS.[Sie56, Nor57, Sie67, Nor72] Siegbahn also received the Nobel Prize in Physics in 1981 "for his contribution to the development of high-resolution electron spectroscopy".[Nob81]

On occasion, the acronym ESCA (Electron Spectroscopy for Chemical Analysis) is used, a synonym for XPS, which was initiated by Siegbahn to emphasize its ability to probe also the chemical environment of an atomic species on the surface.[Vic09] XPS is nowadays a widespread analytical tool in surface science, yielding element specific information that allows to determine the composition of surfaces and even enables to study adsorbates on solid surfaces. Thereby, the technique is only sensitive to the outermost layers,[Hüf10] due to the limited inelastic mean free path of the photo-emitted electrons in solids.

2.2.1 Basic Theory of XPS

XPS is based on the emission of core-level electrons upon absorption of X-ray radiation. Core-level electrons in a solid have a certain binding energy E_b, defined relative to a reference zero level (*e.g.* the vacuum level). Thus, if one considers the isolated sample, the kinetic energy E^s_{kin} of an emitted core-level electron after being excited into the continuum of unbound states above the vacuum level is given by

$$E^s_{kin} = \hbar\omega - E^V_b\,, \tag{2.19}$$

where $\hbar\omega$ is the photon energy, and E^V_b is the binding energy of the electron relative to the vacuum level. Figure 2.3a shows a schematic of the photoemission process. For the generation of X-ray radiation with a fixed photon energy either laboratory X-ray tubes (typically with Al and Mg anodes, see section 3.2.1) or synchrotrons (see section 3.7.1) are utilized. Photons with energies from 100 to 2000 eV, the so-called soft X-ray regime, are required to probe atomic core levels. Within this energy range, electrons have an inelastic mean free path of $\lambda_{mfp} \approx 0.5$ to 3 nm.[Alf07, Wat03] Consequently, only the topmost surface layers of the

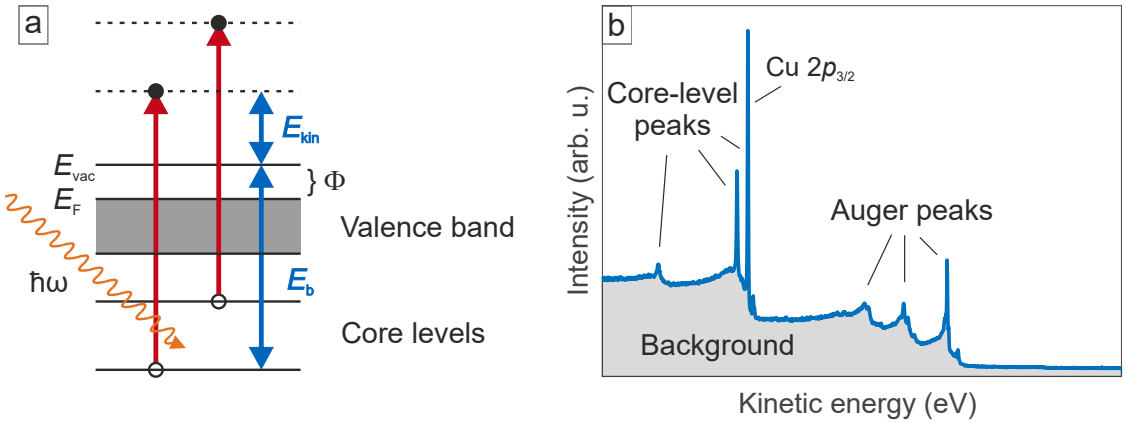

Figure 2.3: ***(a)*** *Schematic of the photoemission process in XPS. Core-level electrons are excited and escape the solid upon absorption of photons of energy ħω. The measured kinetic electron energy distribution can be related to the actual binding energy distribution via Eq. (2.19). The binding energy E_b^V is defined relative to the vacuum level E_{vac}.* ***(b)*** *Exemplary XP spectrum of a bare Cu(111) crystal consisting of characteristic core-level features, which are superimposed on a continuous background of inelastically scattered electrons. Additional features, such as Auger peaks, can also show up in XP spectra.*

sample contribute to the photoemission signal. The kinetic energy of the emitted electrons is analyzed by means of an electron energy analyzer (see sections 3.2.2 and 3.7.2).

As the energy of the X-ray radiation is fixed in XPS experiments and the kinetic energies are measured by the spectrometer, the electron binding energy can be determined. A typical XP spectrum of a bare Cu(111) crystal is shown in Figure 2.3b. The kinetic energy distribution $I(E_{kin})$ of the photoelectrons largely reflects the distribution of binding energies present within the sample, and the binding energy of an electron unambiguously identifies its specific parent element and the atomic energy level.[Hüf10]

In solid-state physics, binding energies are usually defined relative to the Fermi level rather than to the vacuum level.[Alf07] With the sample in electrical contact with the detector, thus in thermodynamic equilibrium, both Fermi levels are aligned. However, in order to obtain the binding energy, one needs to consider that, in general, the spectrometer work function Φ_{spec} and the sample work function Φ_s are different. The work function Φ_s is the energy barrier, which electrons at the Fermi level have to overcome to leave the sample surface. An electron ejected from the sample and passing through the spectrometer feels a potential equal to the difference between Φ_{spec} and Φ_s.[Alf07] The electron kinetic energy measured in the spectrometer is hence given by

$$E_{kin} = E_{kin}^s - (\Phi_{spec} - \Phi_s). \tag{2.20}$$

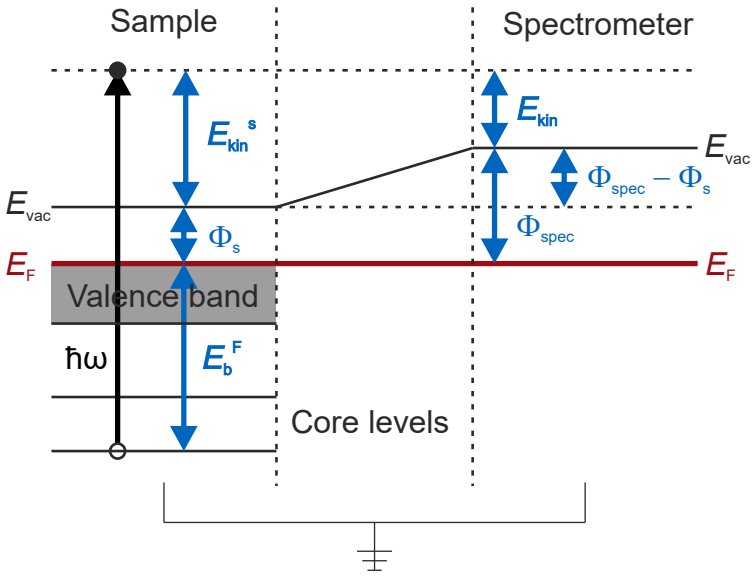

Figure 2.4: *Schematic of the energy level diagram in XPS measurements. The sample and the detector are in electrical contact, and thus their Fermi levels are aligned. Absorbed photons with energy $\hbar\omega$ cause ejection of electrons of kinetic energy E^s_{kin}, defined relative to the vacuum level of the sample. The kinetic energy of the photoelectron measured by the spectrometer is $E_{kin} = E^s_{kin} - (\Phi_{spec} - \Phi_s)$. Reproduced from [Alf07].*

Figure 2.4 schematically shows the energy diagram of the XPS system. Combining Eq. (2.19) and (2.20), and utilizing that $E^V_b = E^F_b + \Phi_s$, the binding energy E_b relative to the Fermi level is given by

$$E_b = \hbar\omega - E_{kin} - \Phi_{spec}. \tag{2.21}$$

The spectrometer work function Φ_{spec} needs to be determined, usually *via* characteristic (substrate) binding energy peaks or the Fermi edge.

In summary, XPS allows to identify atomic species by means of the characteristic sequence of core-level peaks in the XP spectrum, which reflect the unique set of electronic states in the elemental species under investigation. However, in order to describe all subtle features and extract quantitative information of an XP spectrum, one needs to consider initial- and final-state effects of the photoemission process.[Wat03, Alf07, van12, Bri03] These effects induce, *e.g.* satellite features or lead to peak shifts in the measured spectrum and cannot be explained by the simplistic approach that leads to Eq. (2.21). The origin and consequences of distinct initial- and final-state effects are briefly discussed in the following section.

2.2.2 Initial and Final State Effects

In photoemission, the binding energy E_b of an electron is defined as the energy difference between the final $(n-1)$-electron state and the initial n-electron state [Vic09, Hüf10]

$$E_b = E_f(n-1) - E_i(n). \tag{2.22}$$

However, the measured E_b in XPS is not exactly equal to the expected ground-state value of the free atom.[van12] The binding energy varies compared to the free atom as the atom is usually bound within different solids or molecules. Additionally, the creation of a core hole upon photoemission effectively alters the measured binding energy of the electron due to a response of the environment to the excitation and relaxation of the system. Thus, various contributions affect the binding energy values measured in XPS, which can be categorized as [van12]

- **Initial-state effects**: *i.e.* the effects induced by ground-state polarization and bonding with other atoms. Note that although only valence electrons take part in bonding, all electrons (valence and core electrons) experience the change in electron density, leading to the capability of XPS to probe the chemical environment of atoms.
- **Final-state effects**: *i.e.* the effects induced by the perturbation of the electronic structure upon photoemission. They comprise spin-orbit splitting, photo-induced polarization effects, and rearrangement effects, which lead to *e.g.* shake-up satellites or plasmons.

The initial state, denoted $E_i(n)$ in Eq. (2.22), is the ground state of the atom prior to photoemission. The energy of this state can be altered by the formation of a chemical bond with other atoms, which will change the binding energies of all electrons in that atom. This change is called the chemical shift.[Vic09]

The change of E_b can be explained by a change of the formal oxidation state of the atom. A net positive charge on the atom, established *e.g.* by binding to a more electronegative atom, leads to an increased E_b of photoelectrons. This can be understood by less valence electrons being able to screen the positive nuclear charge leading to a stronger Coulomb interaction with the core-level electrons and thus an increased E_b. This approximation assumes that final-state effects such as relaxation have similar magnitudes for different oxidation states, which is valid in most cases.[Vic09] The chemical shift due to different oxidation states can result in binding energy shifts up to 8 eV in case of C 1*s* and S 1s for example, as shown in the literature.[Sie67, Wil11] An example of a chemical shift is discussed in this thesis in section 5.1, where two chemically distinct C 1*s* species (C–C and C–N) are observed for cobalt porphine on Cu(111).

It should be noted that, in a more careful approach, it is rather the distribution and density of electrons that contribute to the chemical shift than only its formal oxidation state. This becomes clear if one considers that the formal oxidation state is only attained when the chemical bonding is not covalent but completely ionic. This leads to the description of the binding energy shift correlated to the charge transfer Δq_i to the atom by a formation of bonds with i neighboring atoms,

$$\Delta E_b = k\Delta q_i + V_i. \tag{2.23}$$

Here, k is a constant and V_i denotes the potential change in the surrounding atoms due to charge transfer as discussed in detail in Ref. [Vic09]. Besides the chemical shift, also charging induced by the incident X-ray radiation can lead to binding energy changes of core levels. This is, in particular, the case for insulating or multilayer systems with a poor electrical contact to the metallic support. Upon creation of photoelectrons, a positive net charge builds up and leads to increased apparent binding energies for subsequently removed electrons.

Additionally, in some cases final-state effects like relaxation effects can contribute significantly to the binding energy shift. For example, the sequence of the Co $2p_{3/2}$ E_b values is Co^0 (778.2 eV) < Co^{+3} (779.6 eV) < Co^{+2} (780.5 eV).[Bru76] Relaxation effects occur, if the remaining $(n-1)$ electrons of the atom respond to the creation of the core hole upon photoemission more rapidly than the photoelectron is ejected from the sample. Eq. (2.22) is thus modified with an additional relaxation energy term E_r:[Vic09]

$$E_b = E_f(n-1) - E_i(n) - E_r. \tag{2.24}$$

The relaxation energy E_r accounts for both inter- and intra-atomic relaxation effects.[van12, Bri03] Intra-atomic relaxation describes the response of the $(n-1)$ electrons of the atom itself, *i.e.* the screening of the generated core hole to minimize the total energy of the atomic system. On the other hand, inter-atomic relaxation, especially prevailing in metals, describes the screening of the core hole by delocalized valence electrons from surrounding atoms. Both relaxation effects are due to electron rearrangements and as a result of energy conservation increase the kinetic energy of the photoelectron in Eq. (2.22), thus increasing the apparent binding energy of the latter.[Vic09]

Another type of finale-state effect contributing to E_b is the so-called shake-up satellite, which arises when part of the energy of the absorbed photon is used to excite valence electrons into an unoccupied state, resulting in a lower kinetic energy of the emitted photoelectrons. Shake-up peaks have discrete energies corresponding to a specific quantized energy transition (*e.g.* a $\pi \rightarrow \pi^*$-transition) and appear on the higher binding energy side of the respective

core-level peak.[Vic09] In the case of metals, which have a continuous band of unoccupied electron states (*i.e.* the conduction band) above the Fermi level, an asymmetric tail is observed on the low kinetic energy side of the photoemission peak. This feature stems from multi-electron excitations, where part of the photon energy has been used to excite valence band electrons into the conduction band.[Bri03] Furthermore, collective electron oscillations (surface plasmons) can be excited in metal samples. Consequently, plasmon loss peaks are also observed on the low kinetic energy side of the photoemission peak. Plasmon peaks appear as equally spaced peaks, separated by the characteristic plasmon energy of the metal.[Vic09]

Moreover, multiplet splitting can contribute with additional final-state features to XP spectra. Multiplet splitting's arise from the interaction of the core hole with unpaired electrons in the outer shell orbitals. They are predominantly observed for transition metals, which have unpaired electrons in the *d*-shells.[Gro05]

Finally, another important final-state effect is the spin-orbit splitting. It occurs for core levels with orbital quantum number $l > 0$, *i.e.* *p*, *d* or *f* orbitals. Here, the spin-orbit coupling between the unpaired electron spin left behind upon photoemission and its orbital angular momentum leads to a splitting of the degenerate state into two distinct components.[Vic09] The resulting intensity ratio is determined by the respective degeneracy ratio $2j + 1$.

It should also be noted that additional satellite peaks are observed for non-monochromatic X-ray radiation produced by laboratory X-ray sources. These satellite peaks stem from additional excitation lines present along with the principle K_α line, albeit with lower intensity. In the case of an Al anode, an additional satellite peak can be observed at a binding energy 9.6 eV lower than the main peak.[Bri03, Dil13a]

2.2.3 Background Signal

All core-level photoemission peaks discussed above are superimposed onto a continuous background signal, as can be seen in Figure 2.3b. The origin of this background lies in the inelastic scattering of photoelectrons.[Vic09] The background increases abruptly at the photoemission peak and subsequently decreases slowly with increasing binding energy (*i.e.* decreasing kinetic energy). This can be explained by photoelectrons that lost part of their kinetic energy after the excitation process due to inelastic scattering but still have enough energy to surmount the work function of the sample.[van12] Therefore, the inelastic scattering process takes place before the electron can reach the vacuum and leave the sample. In the XP spectrum, each peak is accompanied by a continuous inelastic loss tail toward lower kinetic energy.

2.2.4 Curve Fitting

XP spectra are usually acquired relatively fast within few minutes. However, in order to extract detailed information from a measured XP spectrum, it is crucial to analyze it properly. Therefore, the intensity distribution within the desired binding energy range needs to be fitted. This data reduction is not trivial as one can, in principle, fit any spectrum with an infinite number of combinations of peaks of different widths and shapes.[Art17] To illustrate this, it has been shown, that even rather complex structures like an elephant can be drawn (and thus, in turn, fitted) by a Fourier expansion of a set of only four complex numbers.[May10] Consequently, one needs to think about the physical reasons behind the utilized peak shapes, the number of distinct peak components and fundamental limits contributing to the full width at half maximum (FWHM), in order to accurately describe and interpret measured XPS data.

In general, one desires to use as little components as possible to model the XP spectrum, while the relevant contributions are resolved and reasonable constraints are applied. In a first step, the binding energy needs to be calibrated. To this end, either a reference spectrum of a characteristic substrate peak (*e.g.* Cu $2p_{3/2}$ or Ag $3d_{5/2}$) or the Fermi edge is recorded for each experiment with the same set of parameters (photon energy, pass energy, lens and iris settings) as used for data acquisition and compared to reference values, which are given *e.g.* in Refs. [Sea90, Sea98]. Next, one needs to deal with the background signal, which needs to be subtracted by either a constant offset, a linear background, a Shirley-type background [Shi72] or a combination of all of them. A Shirley background is, in essence, a step function convoluted with a Gaussian. The Shirley background routine is proportional to the intensity of the total peak area above the background in the lower binding energy range.[van12] Although it is not exact, its relative simplicity and acceptable accuracy have made the Shirley background the most popular routine nowadays.[van12] With its S-shaped background, it is a good approximation to account for inelastically scattered electrons contributing to the background signal at lower (higher) kinetic (binding) energy.[Vég06]

Furthermore, an appropriate line shape needs to be chosen to model the spectrum. For a symmetric peak, a Gaussian, a Lorentzian or a Voigt function, which is a convolution of a Gaussian and a Lorentzian, are commonly used. Asymmetric peaks can be treated with *e.g.* a Doniach-Šunjić profile.[Don70] XPS data acquired at synchrotrons have in general superior energy resolution, and therefore, a Voigt function can tap its full potential and accurately describe this data with the Lorentzian width accounting for the atomic properties like the core-hole lifetime, and the Gaussian width reflecting the instrumental energy resolution of the experiment.[Hes07]

The width of the peak used for curve fitting depends on various fundamental processes, *e.g.* the natural line width of the incident X-ray radiation, thermal broadening, the pass energy of the analyzer, and the lifetime of the core hole in the atom. All those contributions need to be considered and rationalized. Especially, in the case of several peaks arising from one particular element, all peaks need to be described with exactly the same Lorentzian width, and the Gaussian FWHM should be similar unless one peak does not include more unresolved components than another peak.

Finally, when analyzing a set of data obtained through modification of the sample (*e.g.* annealing, gas adsorption, *etc.*), the relevant components need to be identified in the reference sample. Thereupon, the binding energy and the FWHM of all components of the pristine sample have to be constrained in order to monitor the changes provoked by sample treatment. The curve fit can thus be applied to all the data in the series.

2.3 X-ray Standing Waves (XSW)

The XSW technique combines traditional spectroscopic techniques (*cf.* XPS, section 2.2) with spatial resolution.[Zeg09] It can be utilized for a quantitative determination of the surface structure, which is crucial for a comprehensive understanding of the chemical and electronic properties of a system.[Woo94a] In contrast to diffraction methods such as low-energy electron diffraction (*cf.* section 2.4) or surface X-ray diffraction,[Fei89, Rob92] XSW does not rely on a long-range lateral order of the adsorbate system to study adsorption heights above the surface, as it is solely based on diffraction in the supporting bulk crystal. However, if a well-defined long-range order is present, XSW can even provide quantitative insight into the lateral adsorption geometry of atoms and molecules on single crystal surfaces. The primary benefit of the XSW technique is that the analysis is direct (through Fourier inversion), in contrast to any other surface structural technique such as *e.g.* LEED-$I(V)$, photoelectron diffraction (PhD) or surface X-ray diffraction (SXRD) that all utilize trail-and-error modelling to determine the surface structure.[Woo05] It should be noted that there has been progress in devising inversion algorithms for those techniques that provide at least approximations of the real-space structure.[Woo05]

XSW exploits the diffraction of X-rays by single crystals, which was discovered by von Laue in 1912.[Fri13, Eck12] This ground-breaking discovery at the beginning of the 20^{th} century, which confirmed the nature of crystals, is considered as the birth of modern solid-state physics and yielded von Laue the Nobel Prize in Physics only two years later, in 1914.[Nob14] Within a year after the discovery of X-ray diffraction, the Braggs (father and son) utilized the phenomenon to resolve the first crystal structure and proposed a simple formula to de-

scribe the diffraction pattern. This discovery was honored with the Nobel Prize in Physics in 1915.[Nob15] It was then Batterman who conceived the XSW method,[Bat64a] and pioneered this technique for application in surface science,[Bat69, Zeg93, Zeg09] promoted by the emergence of synchrotron light in the mid-1980s.

An XSW is generated by the superposition of an incident and a reflected plane wave upon diffraction of X-rays by a single crystal. Quantitative information is obtained by monitoring the relative X-ray absorption of specific atoms *via* photoemission. Hence, the technique provides element specific and, beyond that, even chemical-state specific structural information.[Woo05] In essence, the XSW technique yields the average adsorption height of atoms above the projected substrate crystallographic planes. If those planes are parallel to the surface plane, XSW yields the height above the surface.

In the last decade, a multitude of molecular systems have been examined by means of XSW, including organic molecules like phthalocyanines and porphyrins, which are also in the focus of this thesis.[Sta06, Bob11, Krö11, Bür14, Dun15] Further, 2D-layers like *h*-BN on metal supports became subject of studies in recent years.[Zum16, Sch17b] In the following, an introduction to XSW with a particular emphasis on one variant of the technique, the so-called normal incidence XSW (NIXSW) is presented. NIXSW has proved to be particularly effective in studying systems comprising metal crystals.[Woo98, Woo05] A comprehensive description of XSW is given *e.g.* by Zegenhagen.[Zeg93, Zeg09]

2.3.1 Basic Theory of XSW

The underlying principles of the XSW method are simple. An X-ray standing wave field is created above a crystal upon interference of an incident and a reflected plane wave at the Bragg condition, which is given by

$$n\lambda = 2d_H sin\Theta. \tag{2.25}$$

Here, n is the order of the Bragg reflection, d_H is the spacing between the scatterer planes, and Θ is the angle between the incident wave and the scatter plane. The spatial intensity modulation of the resulting X-ray interference field (XIF) equals the periodicity of the scatterer planes, which correspond to the crystal lattice planes. Accordingly, the positions of maximum field intensity are given by planes parallel to the scatterer planes and are also separated by d_H.

To exploit the established XIF, a result derived from dynamical theory of X-ray diffraction is utilized.[Jam62, Bat64b] The intensity distribution of a Bragg reflection peak is not given by a delta function at the nominal Bragg condition. Instead of a single discrete set of values (photon energy or incidence angle), it occurs over a finite range of incident conditions,[Woo05]

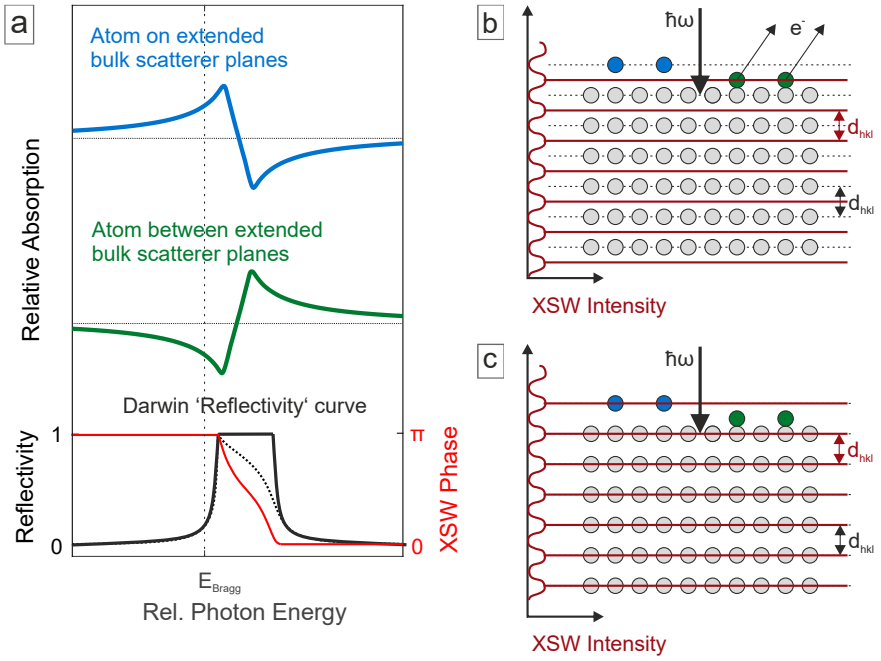

Figure 2.5: *Basic principle of the X-ray standing waves technique.* ***(a)*** *Upon Bragg reflection, a standing wave field is created above a crystal, with a periodicity equal to the crystal scatterer planes. At the leading edge of the Darwin reflectivity curve (solid black line), the anti-nodes of the standing wave field are located midway between the scatterer planes, as depicted in* ***(b)****. When the photon energy increases and one reaches the trailing edge of the reflectivity curve, the anti-nodes have traveled and now lay exactly on the scatterer planes, as displayed in* ***(c)****. Thus, the phase of the standing wave field shift by* π*, when scanning across the reflectivity curve. Consequently, the absorption profiles of atoms vary depending on both, their vertical location above the surface and the phase of the XSW. Two absorption profiles are shown exemplarily in (a) for atoms depicted in blue and green in (b) and (c), respectively.*

and can be described by the so-called Darwin reflectivity curve. Figure 2.5a schematically shows the reflectivity curve with its flat-topped shape (solid black line). Importantly, the phase of the X-ray standing waves (red line) shifts by π when scanning across this range of unity in the reflectivity curve. In general, scanning over the reflectivity curve can be realized by varying either the photon energy or the incidence angle. For NIXSW (see section 2.3.2) as used for all experiments presented in this thesis, the photon energy is varied.

The phase of the XIF equals π at the leading edge of the reflectivity curve, implying that the anti-nodes (maximum intensity) are located exactly between the scatterer planes (see Figure 2.5b). With increasing photon energy, the phase shifts to 0 at the right onset of the reflectivity curve, implying that the anti-nodes are now located exactly on the scatterer planes (see Figure 2.5c). The standing waves thus shifts by $d_H/2$, when scanning through the reflectivity curve. Note, that in reality, *i.e.* for a (partially) absorbing crystal, the intensity at the trailing edge of the Darwin reflectivity curve is reduced (see Figure 2.5a, dashed black line) and its shape is slightly modified.[Woo05]

Any adsorbate (atom, molecule, epitaxial 2D layer) will consequently face a maximum or a minimum of the XIF, depending on both, its vertical position above the scattering planes (*i.e.* its adsorption height if the scattering plane is parallel to the surface), and the phase of the standing wave. Figure 2.5b and c illustrate two different configurations of adsorbate atoms with different adsorption heights: the atomic species depicted in blue are located exactly on an extended bulk scatterer plane, while the atomic species depicted in green are located midway between the scatterer planes. The lineshape of the X-ray absorption, the so-called absorption profile or absorption yield, as a function of photon energy is characteristic of the location of the atom relative to the scatterer planes and expresses the basis of the XSW technique. The respective absorption profiles are illustrated schematically in Figure 2.5a.

It is important to note, that due to the absorption of the crystal resulting in a modified reflectivity curve, the modulation amplitude of the absorption profile at the trailing edge of the reflectivity curve is also reduced. Further, as the XIF extends far above the surface and exhibits a periodicity of d_H, the atom vertical position is always referred to the nearest extended bulk scatterer plane and is therefore not unambiguous.

To assess the X-ray absorption experimentally, the photoemission yield acquired by XPS (see section 2.2) as a function of photon energy is utilized. Note that, besides photoemission, also Auger and fluorescence emission can be utilized as absorption signal in a different variant of the XSW method. It is, of course, beneficial to monitor the element- and chemical-state specific photoemission signal for XSW, as these specificities are preserved and thus enhance the obtained results. To satisfy the Bragg condition for metal crystals, tunable energies in the hard X-ray regime (2 to 3 eV) are required, which can be realized easily at synchrotron beamlines (see section 3.7). Additionally, the exact atomic position of an atom can be determined *via* experiments performed for several different Bragg scatterer planes and subsequent triangulation as discussed later in section 2.3.5.

In essence, XSW allows to determine the vertical position of adsorbate atoms, relative to the nearest extended bulk scatterer plane, by monitoring the absorption *via* photoemission while scanning through the Darwin reflectivity curve.

2.3.2 Normal Incidence X-ray Standing Waves (NIXSW)

In the experiments presented in this thesis, a particular variant of XSW, the normal-incidence X-ray standing waves (NIXSW) was used. The reason for this is the width w_D of the Darwin reflectivity curve, which is determined by the incidence angle Θ that is defined with respect to the scattering plane:[Wil11]

$$w_D \sim \tan\Theta. \tag{2.26}$$

Obviously, for incident angles far from normal incidence (small angles), the width of the Darwin curve is very small [$\tan(\Theta \to 0°) \to 0$]. This imposes high experimental demands. For instance, the X-ray beam angular spread is required to be very narrow, while the crystal needs to be highly perfect. This implication is not easily achievable, especially for metal crystals, where some degree of mosaicity is present even in single crystals, compared to semiconductor crystals like *e.g.* silicon.

To circumvent these issues, XSW experiments are conducted at normal X-ray incidence. Although the formally diverging w_D for $\Theta \to 90°$ is just a theoretical artifact (the approximation is not valid anymore in this limit), and the w_D is significantly broadened, which facilitates the experiment. In fact, a Darwin curve width of $\sim 1\,\text{eV}$ is typically achieved in NIXSW.[Woo98] Consequently, the NIXSW technique is suitable to study in particular adsorbates on metal crystals. In the experiments, a small angular deviation ($\sim 2.5°$) of the normal incidence was used due to practical reasons (see section 3.7).

2.3.3 The Structural Parameters of XSW

To interpret XSW measurements quantitatively, one needs to consider the mathematical description of the standing wave field. The intensity of the standing wave field above the crystal is given by [Woo05]

$$I(R, \Phi, z) = 1 + R + 2\sqrt{R}\cos\left(\Phi - \frac{2\pi z}{d_H}\right). \tag{2.27}$$

Here, R is the reflectivity given by the square modulus of reflected over incident X-ray amplitudes $R = |\frac{E_r}{E_0}|^2$, Φ is the phase difference between reflected and incident wave and z is the vertical distance from the nearest extended scatterer plane. Eq. (2.27) describes the above statements mathematically: The cosine function reflects the spatial modulation with periodicity d_H. The phase difference can be understood as follows: For an absorbing atom at position $z = d_H$ (*i.e.* exactly on an extended scatterer plane), a XSW phase $\Phi = 0$ ($\Phi = \pi$) implies that the anti-nodes (nodes) of the standing wave are located on the scatterer planes and that the absorption of this atom is maximal (minimal), as the cosine term takes its maximum (minimum) value.[Wil11]

To determine the vertical position z of an adsorbed atom, the Darwin reflectivity curve R needs to be recorded and the phase Φ as a function of the photon energy needs to be deduced. The vertical position z is then used as a fitting parameter to the experimental absorption profile.[Wil11]

However, in realistic experimental settings, atoms do not solely occupy a single discrete vertical position. This can be due to static (*e.g.* several discrete adsorption sites) and

dynamic (*e.g.* thermal vibrations) disorder. Consequently, one needs to take into account the spatial distribution $f(z)$ of several adsorption sites, which is normalized by

$$\int_0^{d_H} f(z)dz = 1. \tag{2.28}$$

Accordingly, the absorption intensity can be recast to

$$I = 1 + R + 2\sqrt{R}\int_0^{d_H} f(z)\cos\left(\Phi - \frac{2\pi z}{d_H}\right)dz. \tag{2.29}$$

This equation can be written as [Woo05]

$$I = 1 + R + 2f^H\sqrt{R}\cos\left(\Phi - \frac{2\pi p^H}{d_H}\right), \tag{2.30}$$

with two structural parameters: the coherent position p^H and the coherent fraction f^H. In simplistic terms, the former can be interpreted as the average position of a chemical species relative to the extended bulk Bragg planes in units of d_H and the latter is related to the distribution of these positions, either through a static variation (*e.g.* multiple adsorption sites), or a dynamic one (*e.g.* thermal vibrations). In particular, f^H can only take values between 0 and 1, low values arising from dynamic or static local disorder. For a single site occupation, the coherent fraction is expected to be less, but close to unity (typically around 0.9). The dynamic disorder can be expressed by a product of two Debye-Waller factors. One is accounting for the vibrations of the crystal lattice, which render the standing wave slightly incoherent, and the second one describes the disorder of the absorber atoms.[Woo94a, Woo05]

Figure 2.6 displays exemplarily calculated XSW absorption profiles. In Figure 2.6a, a set of absorption profiles with an identical coherent fraction f^H are plotted for different values of p^H. Absorber atoms with a different vertical spacing relative to the extended bulk scatterer planes give rise to clearly distinct absorption profiles. Hence, one can determine the vertical position with high precision *via* fitting the experimental data to a theoretically expected absorption profile. Moreover, Figure 2.6b illustrates the influence of f^H on the shape of an absorption profile. Pronounced modulations are visible for a high coherent fraction, while they are clearly eased in case of a reduced f^H, where the shape resembles that of a typical reflectivity curve. Using the equivalence of Eq. (2.29) and (2.30), it is obvious that

$$f^H\cos\left(\Phi - \frac{2\pi p^H}{d_H}\right) = \int_0^{d_H} f(z)\cos\left(\Phi - \frac{2\pi z}{d_H}\right)dz. \tag{2.31}$$

Expressing the cosine function with its complex notation, the equation reads

$$f^H\exp\left(\frac{2\pi i p^H}{d_H}\right) = \int_0^{d_H} f(z)\exp\left(\frac{2\pi i z}{d_H}\right)dz. \tag{2.32}$$

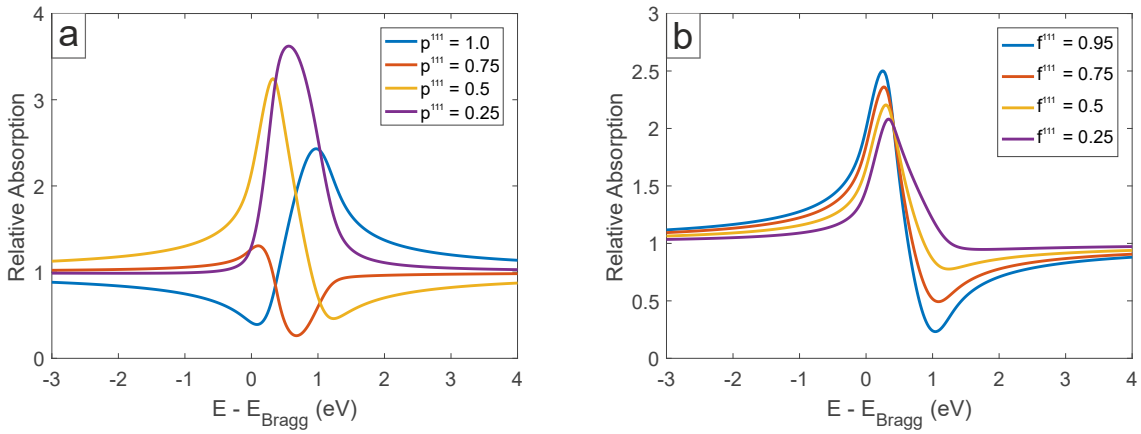

Figure 2.6: *Calculated XSW absorption profiles resulting from a normal-incident* (111) *Bragg reflection as a function of the photon energy relative to the Bragg energy.* ***(a)*** *The four curves illustrate absorption profiles of an atom with a coherent fraction* $f^{111} = 0.9$ *and different coherent positions* p^{111} *relative to the extended bulk scatterer planes.* ***(b)*** *The four curves illustrate absorption profiles of an atomic species adsorbed at* $p^{111} = 0.6$ *and exhibiting different coherent fractions* f^{111}*. A typical instrumental energy broadening of* 0.1 eV *is included.*

The formulation in Eq. (2.32) allows a simple graphical representation of XSW data for multiple site adsorption in a so-called Argand diagram. Therefore, each discrete adsorption component of the spatial distribution function $f(z)$ is represented as a vector with the direction given by the phase angle $2\pi z/d_H$ and the length by the probability of this component, *i.e.* $f(z)$. Summation over all of these components results in a vector of length f^H and phase angle $2\pi p^H/d_H$.

2.3.4 Angular Effects in Photoemission

As discussed above, the absorption in NIXSW measurements is monitored *via* photoemission. The photoemission process is, however, not isotropic but has an angular dependence due to the intrinsic emission process as well as elastic electron scattering.[Woo05] Photoelectrons are excited by both the incident and the reflected X-rays, which, in combination, generate the standing wave field. The unequal angular dependence of these two excitations together with the limited acceptance angle of the electron detector leads to the measured intensities being no longer proportional to the total absorption. To account for the angular effects, Eq. (2.30) that describes the intensity of the standing wave, needs to be adapted.

The probability of the photoemission process can be described by the matrix element

$$\mathbf{M}_{fi} = \langle f | \exp(2\pi i \mathbf{k} \cdot \mathbf{r}) \mathbf{A} \cdot \mathbf{p} | i \rangle, \tag{2.33}$$

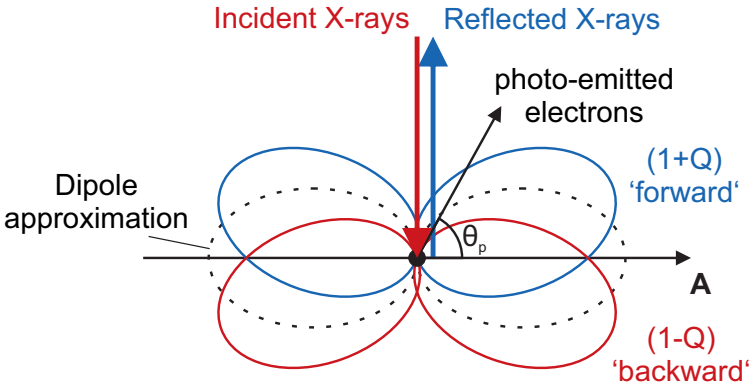

Figure 2.7: *Schematic diagram illustrating the angular dependence of the photoemission signal. In a NIXSW experiment, non-dipole contributions are responsible for a forward-backward asymmetry of the photoemission signal. The incident and reflected X-ray beams posses different photoemission distributions (red and blue lobes, respectively, for photoelectrons from an s-orbital). Therefore, the photoelectron yield detected at an angle θ_p is not proportional to the relative absorption. This issue is circumvented with the forward-backward asymmetry parameter Q. The incident X-ray beam polarization **A** is parallel to the crystal scatterer planes.*

where i and f are the initial and final states of the emitted electron, respectively, $\mathbf{k}$ is the photon wave vector, $\mathbf{r}$ is the electron position vector, $\mathbf{A}$ is the photon polarization vector, and $\mathbf{p}$ is the electron momentum operator.[Woo05]

For high X-ray energies (*i.e.* small wavelengths) as utilized for XSW, the spatial variation of the electromagnetic wave over the electron wavefunction is no longer negligible. Consequently, the electric dipole approximation (*i.e.* the zero order approximation of the exponential function in Eq. (2.33)) is not sufficient any more.

Taking into account the first-order approximation ($\exp(2\pi i\mathbf{k}\cdot\mathbf{r}) = 1 + 2\pi i\mathbf{k}\cdot\mathbf{r}$) leads to two additional terms in the matrix element, the electric quadrupole and the magnetic dipole term. The angular dependence of the photoemission probability is then calculated by the square modulus of the matrix element $\boldsymbol{M}$ and given by [Coo69, Coo93, Woo05]

$$\frac{d\sigma}{d\Omega} = \left(\frac{\sigma}{4\pi}\right)\left[1 + \left(\frac{\beta}{2}\right)\left(3\cos^2(\theta_p) - 1\right) + \left(\delta + \gamma\cos^2(\theta_p)\right)\sin(\theta_p)\cos(\phi)\right]. \tag{2.34}$$

Here, $d\sigma/d\Omega$ and σ are the differential and the total photo-ionization cross-sections, β, γ and δ are the electric dipolar, electric quadrupolar and magnetic dipolar asymmetry factors, respectively, θ_p is the angle between the photon polarization vector $\mathbf{A}$ and the photoemission direction and ϕ is the angle between the direction of the photon and the projection of the photoelectron wave vector onto the plane perpendicular to the photon polarization $\mathbf{A}$.[Woo05] Both, θ_p and ϕ are determined by the experimental setup, while β, γ and δ depend on the core level to be studied.

Depending on whether the photoelectron emission is detected in forward or backward direction, relative to the direction of the X-ray photons, the $\cos\phi$ term is either $+1$ or -1. This forward/backward asymmetry due to non-dipolar effects has an important implication on the XSW absorption monitored *via* photoemission.[Woo05] Figure 2.7 shows schematically the angular dependence of the photoemission from an *s*-orbital depending on the propagation direction of the photon: the photoemission is skewed into the photon direction. As the detected photoemission intensity in XSW measurements is a superposition of two distinct photoemission distributions, resulting from two waves that propagate in opposite directions, the measured photoemission at a given detection angle does not measure directly the total absorption. To circumvent this issue, a forward/backward asymmetry parameter Q is introduced,[Lee01, Woo05] which is defined as

$$\frac{1+Q}{1-Q} = \frac{1+\frac{1}{2}\beta\left(3\cos^2\left(\theta_p\right)-1\right)+\left(\delta+\gamma\cos^2\left(\theta_p\right)\right)\sin\left(\theta_p\right)\cos\left(\phi\right)}{1+\frac{1}{2}\beta\left(3\cos^2\left(\theta_p\right)-1\right)-\left(\delta+\gamma\cos^2\left(\theta_p\right)\right)\sin\left(\theta_p\right)\cos\left(\phi\right)}, \tag{2.35}$$

and relates the photoemission intensities due to incident $(1-Q)$ and reflected $(1+Q)$ X-ray beams to each other. For the fitting procedure, Q is calculated from tabulated values of β, γ, δ,[Trz01, Trz02] and the angle θ_p is defined by the experimental geometry. Taking these non-dipolar corrections Q into account, the absorption profile in NIXSW experiments resulting from photoemission of an *s*-orbital reads [Var99, Lee01]

$$\frac{d\sigma}{d\Omega} \propto \left[1 + R\frac{1+Q}{1-Q} + 2f^H\sqrt{R}\frac{\sqrt{\left(1+Q^2\tan^2\left(\Delta\right)\right)}}{1-Q}\cos\left(\Phi+\psi-\frac{2\pi p^H}{d_H}\right)\right]. \tag{2.36}$$

In this equation, two terms are added besides the asymmetry parameter Q, compared to Eq. (2.30). Both, Δ and $\psi = \tan^{-1}\left(Q\tan\left(\Delta\right)\right)$ describe dipole-quadrupole interference effects as discussed in.[Lee01, Woo05] However, since Lee *et al.* showed that neglecting the Δ term results only in a minor systematic error of 0.04 Å in p^H and 5% in f^H,[Lee01] the following simplified final equation as proposed in literature[Lee01, Woo05] is applied to model all NIXSW absorption profiles discussed in this thesis:

$$\frac{d\sigma}{d\Omega} \propto \left[1 + R\frac{1+Q}{1-Q} + 2f^H\sqrt{R}\frac{\sqrt{\left(1+Q\right)}}{\sqrt{\left(1-Q\right)}}\cos\left(\Phi-\frac{2\pi p^H}{d_H}\right)\right]. \tag{2.37}$$

It is worth to note, that the theoretical model behind this equation is formally only valid for photoemission from 1*s* states. Since there is no appropriate model for higher states, Eq. (2.37) is usually also applied to higher states, resulting in an additional systematic error in the order of the one made by neglecting Δ.[Woo05]

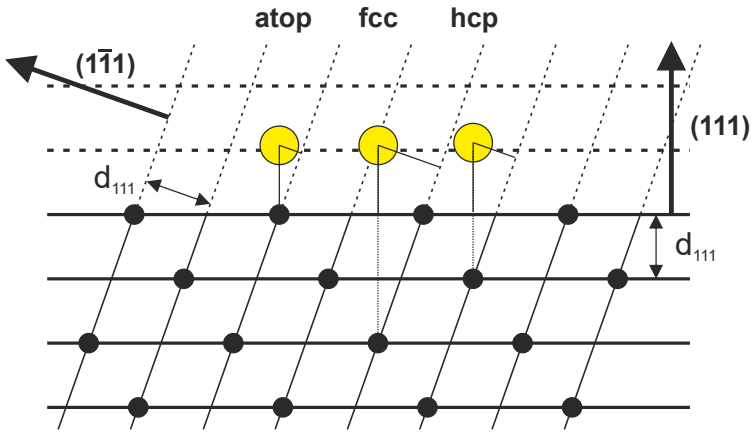

Figure 2.8: *Schematic of XSW triangulation. In the specific case of an fcc (111) crystal, the absolute adsorption position can be identified by real-space triangulation of NIXSW results obtained from experiments utilizing two different sets of Bragg scatterer planes that are not parallel [e.g. (111) and (1$\bar{1}$1)]. The cross section of an fcc (111) crystal surface shows the relationship of (111) and (1$\bar{1}$1) layer spacings for the three high symmetry adsorption sites.*

2.3.5 Triangulation

Besides the determination of the layer spacing perpendicular to the surface, XSW is also capable to identify the exact atomic coordinates in all three spatial dimensions *via* triangulation. This kind of application of the XSW method has been conceived by Golovchenko *et al.* in 1982.[Gol82] In addition to the atom position normal to the surface, determined using a Bragg scatterer plane that is parallel to the crystal surface, its position relative to a plane inclined to the surface is also measured. The combined information of two independent layer spacings is sufficient to reveal the registry of the surface atoms relative to the underlying crystal surface.[Gol82, Woo94a] Studies conducted on fcc (111) metal crystals usually utilize the (111) and the (1$\bar{1}$1) Bragg reflection,[Ker92d, Ker92c, Ker92b, Ker92a, Scr94] which is tilted by 70.5° as the energies of both Bragg reflections are identical.[Woo05] Note that only in the specific case of an fcc (111) crystal, two sets of Bragg scatterer planes are sufficient to discriminate the exact adsorption site (due to symmetry reasons), while in general, at least three different sets of scatterer planes are required.

The three high-symmetry sites retaining the $3m$ symmetry of the fcc (111) surface are adsorption sites atop an outermost layer atom, in the *hcp* hollow site that is atop a second layer substrate atom, and in the *fcc* hollow site that is atop a third layer substrate atom.[Woo05] Figure 2.8 illustrates the relationships of the (111) and the (1$\bar{1}$1) layer spacings of the respective adsorption sites. By measuring both, the layer spacing z^{111} obtained from the (111) Bragg reflection, and the layer spacing $z^{1\bar{1}1}$ obtained from the (1$\bar{1}$1) Bragg reflection, the adsorption sites can be determined as follows, utilizing that $\cos 70.5° = \frac{1}{3}$: An atom sitting

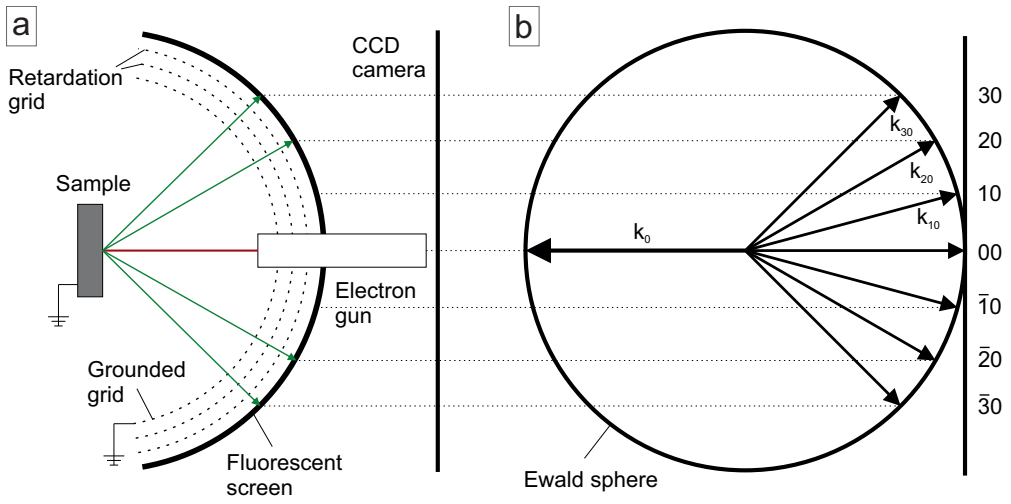

Figure 2.9: ***(a)*** *Schematic of a LEED apparatus. Electrons generated by an electron gun are elastically backscattered on the sample. The electron beam passes several hemispherical grids with the purpose of retarding electrons with kinetic energies lower than those incident onto the sample in order to suppress inelastically scattered electrons. Finally, the electrons are accelerated toward a phosphor screen causing fluorescence.* ***(b)*** *Schematic of the Ewald sphere construction.*

on the atop site obeys the relation $z^{1\bar{1}1} = z^{111}/3$, while for the hcp hollow site one obtains $z^{1\bar{1}1} = (z^{111} + d_{111})/3$ and for the fcc hollow site $z^{1\bar{1}1} = (z^{111} + 2 \cdot d_{111})/3$.

Besides the occupation of a single adsorption site, also a partial or equal occupation, *e.g.* of both hcp and fcc hollow sites is possible. In this case, the obtained layer spacing $z^{1\bar{1}1}$ is given by the average of both individual layer spacings, $z^{1\bar{1}1} = (d_{111} + 3/2 \cdot z^{111})/3$, and the coherent fraction $f^{1\bar{1}1}$ is reduced to half of its original value f^{111}.

2.4 Low-Energy Electron Diffraction (LEED)

Low-energy electron diffraction (LEED) is another standard technique in surface science for the determination of the surface structure of single crystals. It was discovered at almost the same time by Davisson and Germer as well as Thomson and Reid in 1927.[Dav27b, Dav27a, Tho27] Davisson and Thomson were awarded the Nobel Prize in Physics for their pioneering work in electron diffraction in 1937.[Nob37] LEED exploits the effect that low-energy electrons (20 to 200 eV)[Our03] are scattered elastically by a crystal. The spatial distribution of the diffracted electrons is observed on a fluorescent screen and contains information about the ordering of the surface and/or the adsorbate layer.[Our03] LEED was utilized as a complementary technique during this PhD project and is therefore only introduced succinctly. A more in-depth description of LEED and its applications can be found in the literature.[van86, Pen90, Hen94, Woo94b, Our03]

Figure 2.9a depicts a schematic LEED apparatus. A collimated electron beam is focused onto a single crystalline surface in a UHV environment. The low energy electrons are elastically back-scattered on the surface within the topmost layers as they interact strongly with matter and hence their mean free path in matter is only in the order of some Å.[van86, Pen90] The de Broglie wavelength of the electrons is given by

$$\lambda = \sqrt{\frac{h}{2mE}} \tag{2.38}$$

where h is the Planck constant, m is the mass and E the electron energy. With the approximation

$$\lambda[\text{Å}] \approx \sqrt{\frac{150\,\text{eV}}{E_{kin}(eV)}} \tag{2.39}$$

the wavelength of low-energy electrons can be calculated to be in the order of 0.5 to 3 Å. Since this wavelength is in the order of inter atomic distances, diffraction at the crystal lattice is possible.

Diffraction of electron waves give rise to constructive interference if the von Laue condition

$$\boldsymbol{k} - \boldsymbol{k_0} = \boldsymbol{G_{hk}}, \tag{2.40}$$

$$|\boldsymbol{k}| = |\boldsymbol{k_0}| \tag{2.41}$$

is satisfied. Here, $\boldsymbol{k_0}$ and $\boldsymbol{k}$ are the incident and scattered wave vectors and $\boldsymbol{G_{hk}}$ is the scattering vector. The set of discrete numbers that satisfy this condition is given by

$$\boldsymbol{G_{hk}} = h\boldsymbol{a^*} + k\boldsymbol{b^*}, \tag{2.42}$$

where h and k are integers (Miller indices) and a^* and b^* are the primitive reciprocal space net vectors defined by

$$\boldsymbol{a^*} = 2\pi\frac{\boldsymbol{b}\times\boldsymbol{n}}{\boldsymbol{a}\cdot\boldsymbol{b}\times\boldsymbol{n}}, \tag{2.43}$$

$$\boldsymbol{b^*} = 2\pi\frac{\boldsymbol{a}\times\boldsymbol{n}}{\boldsymbol{a}\cdot\boldsymbol{b}\times\boldsymbol{n}}. \tag{2.44}$$

Here, $\mathbf{a}$ and $\mathbf{b}$ denote the primitive real space net vectors and $\mathbf{n}$ is the normal unit vector of the surface. Since electrons scatter predominantly at the topmost surface layer as discussed above, there are only two lattice vectors in this formulae representing the lateral periodicity of the surface. Diffraction that satisfies Eq. (2.40) and (2.41) can be represented graphically in an Ewald sphere (Figure 2.9b) and displays the observed LEED pattern.

Chapter 3

Instrumentation and Technology

Experiments in surface science are facilitated by a controlled and clean environment. Consequently, ultra-high vacuum (UHV) chambers were utilized, housing all preparation and analysis tools applied in experiments in the course of this thesis. The major part of the work presented here was carried out at the Technical University of Munich, where three different setups were employed. First, an XPS-STM system that was designed and assembled in this PhD project. The powerful *in-vacuo* combination of two surface analysis techniques, scanning tunneling microscopy (STM) and X-ray photoelectron spectroscopy (XPS) allows to characterize surfaces and interfaces. The setup comprises a custom-designed UHV chamber equipped with an STM from CreaTec Fischer & Co GmbH operated at room temperature and a SPECS XPS system consisting of a twin-anode X-Ray gun and an electron analyzer. All components are described in detail in the following sections and listed in appendix A.2. Second, a low temperature (LT-)STM was utilized. Its components are very similar to the ones employed in the XPS-STM setup, except that in the LT-STM setup the CreaTec STM is based on a Besocke-beetle type scanner [Bes87, Fro89, Mey96a, Zöp00] and operated at liquid helium temperature ($\sim$6 K). The components of this setup are described in detail in older publications,[Seu11a, Wie15, Urg15a] and listed in appendix A.1. Third, an LT-STM/AFM setup that combines an atomic force microscope (AFM) and an STM, was utilized for data acquisition in a short, complementary experiment. This setup is technically similar to the one introduced here, and is described in detail in earlier theses.[Bis17, He17a] Subsequently, the experimental procedures to prepare samples and tips are outlined in section 3.5 and 3.6. All experiments utilizing X-ray standing waves (XSW) were carried out at the synchrotron facility of Diamond Light Source (beamline I09) located on the Harwell Science and Innovation Campus in Oxfordshire, United Kingdom, in collaboration with Dr. David Duncan. A brief introduction to synchrotron light generation and the properties of the employed electron energy analyzer is presented in section 3.7. The main components of the beamline are summarized in appendix A.3.

3.1 UHV System

The XPS-STM setup was designed using computer-aided design (CAD) software including 3D STEP models made available by several companies.[Cre17, SPE17, VAC17, FOC17, Ley17, VAT17, ite17] Figure 3.1 shows the isometric drawing of the complete UHV system supported on an aluminum frame, which is planned to be positioned on four pneumatic vibration isolators and additionally equipped with four rigid supports. The UHV system comprises two independent chambers, the STM chamber (colored in purple) and the preparation and XPS chamber (colored in green). Both chambers are custom-designed stainless steel cylinders manufactured by Vacom,[VAC17] connected by a VAT gate valve.[VAT17]

UHV with a base pressure in the medium 10^{-10} mbar range is maintained by a combination of pumps with different working principles. First, a diaphragm pump generates a fore-vacuum with a pressure in the order of 1×10^{-1} mbar by oscillating a diaphragm up and down. Thereby, the diaphragm sucks in the gas particles to be pumped *via* the inlet valve on the downward stroke. On the upward stroke, the gas particles are forced out *via* the outlet valve. The second pumping stage is a series of two turbo molecular pumps (TMPs), an Oerlikon Leybold TURBOVAC SL 80 operating at 72 000 rpm and a MAG W 400 iP operating at 58 800 rpm.[Ley17] A TMP consists of a multitude of rapidly rotating rotor and stationary stator pairs. In each stage, gas particles receive a momentum through collision with the rapidly moving rotor blades. With this newly gained momentum, the gas particles enter into the stator where they are pushed toward the next stage. Thereby the medium is successively compressed and led to the backing fore vacuum pump. Both TMPs work with magnetic bearings for vibrational noise reduction. The main TMP is separated from the preparation chamber by a pneumatic VAT gate valve. This valve allows to switch off all mechanically vibrating pumps to reduce noise in the STM while the vacuum in the UHV chamber is maintained by the ion pump. Furthermore, the gate valve closes upon power failure preventing the uncontrolled venting of the chamber.

Additionally, a GammaVacuum 600TV [Gam17] ion (getter) pump is installed at the STM chamber. In an ion pump, an assembly of cylindrical anodes is arranged between two parallel cathodes.[Oer07] The entire electrode system is surrounded by strong permanent magnets creating a homogeneous magnetic field. A potential of 6.5 kV is applied between the electrodes whereby field-emitted electrons ionize gas particles in the anode cylinder. Long spiral tracks of the electrons make for sufficient ion yield to maintain a self-sustaining gas discharge. Due to higher masses, the ionized gas particles are almost unaffected by the magnetic field and can leave the anode cylinder in a straight track. The ions impinge on the negatively charged titanium cathode where they are implanted deeply into the cathode. Additional titanium is released upon impact acting as getter film for reactive gas particles (*e.g.* hydrogen,

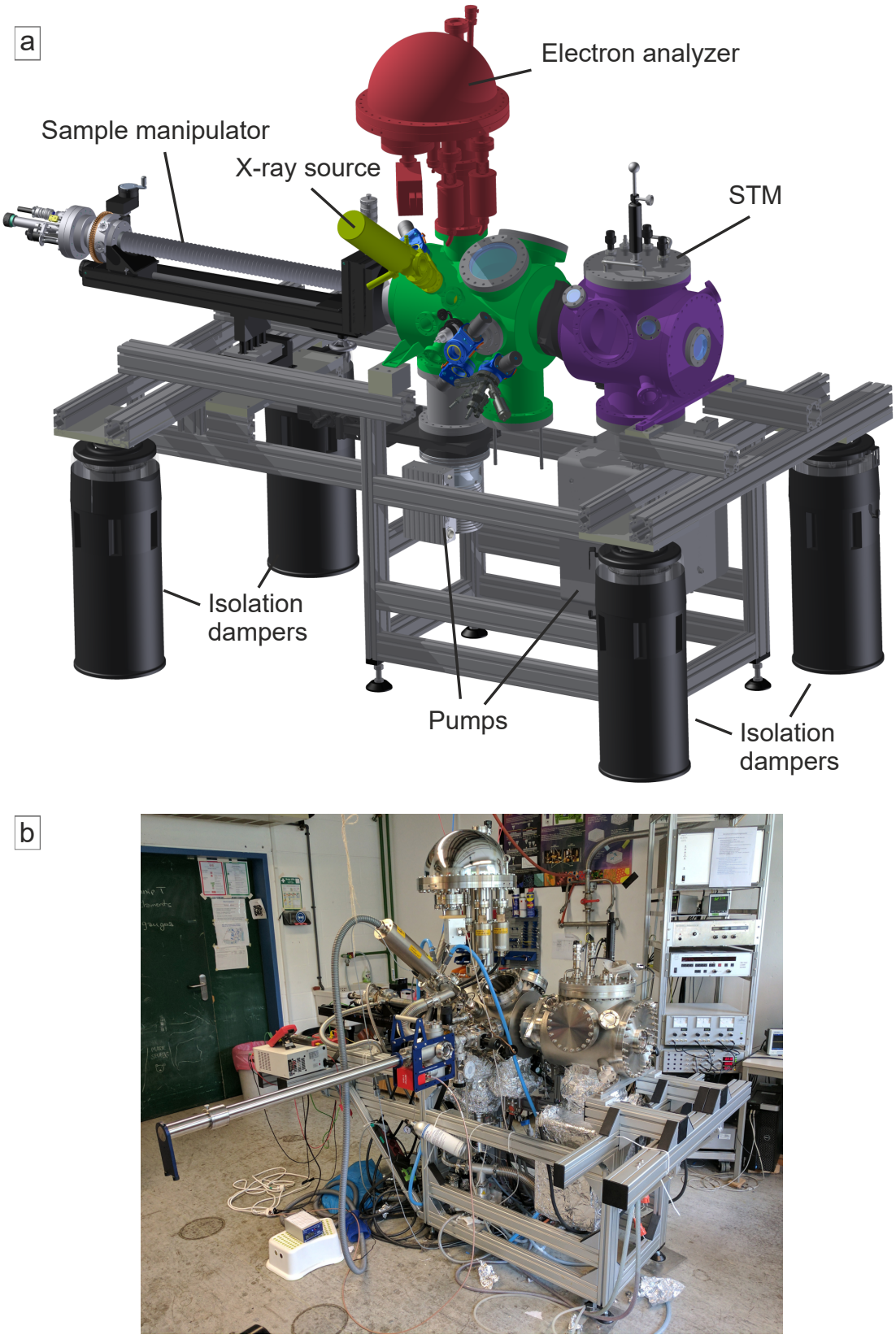

Figure 3.1: ***(a)*** *Isometric drawing and* ***(b)*** *photograph (Aug. 2017) of the XPS-STM setup.*

nitrogen, oxygen) on the inner ion pump surfaces. Note that the ion implantation works for all types of ionized particles including noble gas particles which do not chemically react with the sputtered titanium film.

Furthermore, a titanium sublimation pump (TSP) is installed at the preparation/XPS chamber together with a cold trap. In a TSP, titanium is resistively evaporated from a filament and deposited onto the liquid nitrogen cooled walls of the cold trap. Especially active gases are pumped effectively by this technique forming stable compounds with the getter film.

The STM chamber (purple in Figure 3.1a) houses the STM apparatus (described in detail in section 3.3) and provides several CF flanges of different size for modifications. At its current state (March 2018) flanges are occupied with a pressure gauge (Vacom Barion [VAC17], Bayard-Alpert type), a home-built sample parking (4 slots) mounted on a linear drive as well as several viewports. Free flanges provide optical access to the sample that is placed in the STM, allowing for *in-situ* evaporation or photo-catalytic experiments. The STM chamber is designed in a way that a future upgrade to a low-temperature STM with a cryostat is possible.

The second chamber (green in Figure 3.1a) is used for both sample preparation and XPS measurements. It contains an ion source (sputter gun) as well as high precision leak valves for gas dosing (*e.g.* Ar, CO, O_2). Moreover, one leak valve is equipped with a glass tube where the borazine precursor (liquid with a considerable amount in gas phase due to its vapor pressure of $\sim 350\,\mathrm{mbar}$ at room temperature[Che18a]) is stored. Several flanges are equipped with VAT mini gate valves [VAT17] to access the chamber with, *e.g.* molecule and metal evaporators, without breaking the vacuum inside the chamber. Molecules are deposited onto the samples from a commercially available Dodecon 4-cell OMBE [Dod17] as well as from a home-built 2-cell OMBE source. In both cases, the molecular powder is evaporated from a quartz crucible that is heated resistively. Moreover, a Focus EFM 3s electron beam evaporator [FOC17] was utilized for the deposition of silver and cobalt, and a home-build resistive evaporator was used for deposition of copper and cobalt atoms. A Stanford Research Systems RGA-100 [Sta17] quadrupole mass spectrometer allows for leak testing, the spectroscopic detection of the residual gas composition, and monitoring the gas purity. Up to 5 sample holders and 4 STM tips can be stored *in-vacuo* on the sample parking in the preparation chamber. A load lock chamber can be employed to transfer sample holders in and out of the UHV chambers. Transfer of samples *in-vacuo* to the LT-STM or LT-AFM chamber is realized with a vacuum suitcase. Samples are mounted on CreaTec sample holders (described in detail in section 3.4) and can be transferred between the two chambers and different preparation positions *via* a linear manipulator (manufactured by VAb [VAb17]), which allows for movement along three spatial directions plus azimuthal

rotation. Rotation is realized by a differentially pumped and viton-sealed rotary double-stage feed-through. Its first stage is connected to the roughing pump while the second stage is connected to the TMP pumping line. Sample holders are attached to the manipulator by mechanical clamping. A built-in flow cryostat can be used to cool the samples with liquid nitrogen or liquid helium down to ∼90 K. The temperature of the manipulator head can be monitored by a Pt100 resistance. Additionally, the manipulator provides electrical contacts for sample heating and (sample) temperature read-out. Furthermore, the chamber is equipped with a Vacom Barion [VAC17] pressure gauge and the XPS system comprising a SPECS XR50 X-ray gun and a SPECS PHOIBOS 100 electron analyzer,[SPE17] which is described in detail in the following section 3.2.

3.2 XPS System

There are two basic requirements for XPS as described in section 2.2: a fixed energy radiation source (X-ray source) for the excitation of the core electrons and an electron kinetic energy analyzer to measure the flux of the emitted electrons at a certain energy. In the XPS-STM setup a SPECS XR 50 X-ray source is installed together with a SPECS PHOIBOS 100 electron analyzer [SPE17]. Both are described in the following sections 3.2.1 and 3.2.2. The X-ray source is mounted with an angle of 54.7° (“magic angle“) with respect to the inlet axis of the electron analyzer. The sample is usually positioned with its surface normal along the inlet axis of the electron analyzer (normal emission) and in a working distance of 40 mm. XP spectra are recorded with the SpecsLab2 Prodigy data acquisition software and processed with either CasaXPS [Cas16] or the Matlab software.

3.2.1 Lab-based X-ray Source

Lab-based X-ray sources are standard tools for generating X-rays in laboratories due to their compact size and comparatively low costs. A photograph of the twin anode SPECS XR 50 X-ray source is displayed in Figure 3.2a. It comprises a body with water inlets for the source head cooling, a filament feed through, and the source head. The acceleration high voltage is applied through the cooling water. A closed circuit cooling unit (Van der Heijden KÜHLMOBIL [Van17]) is utilized to ensure a constant supply of cooling water. A close-up view of the source head with a schematic working diagram is illustrated in Figure 3.2b. Electrons are emitted from a tungsten filament and accelerated toward the metal anode by the high voltage that is applied between filament and anode. The X-ray source is equipped with two different anode materials: aluminum (Al) and magnesium (Mg). Depending on the anode material, a high voltage of 10 to 12 kV and an emission current of 20 mA are employed.

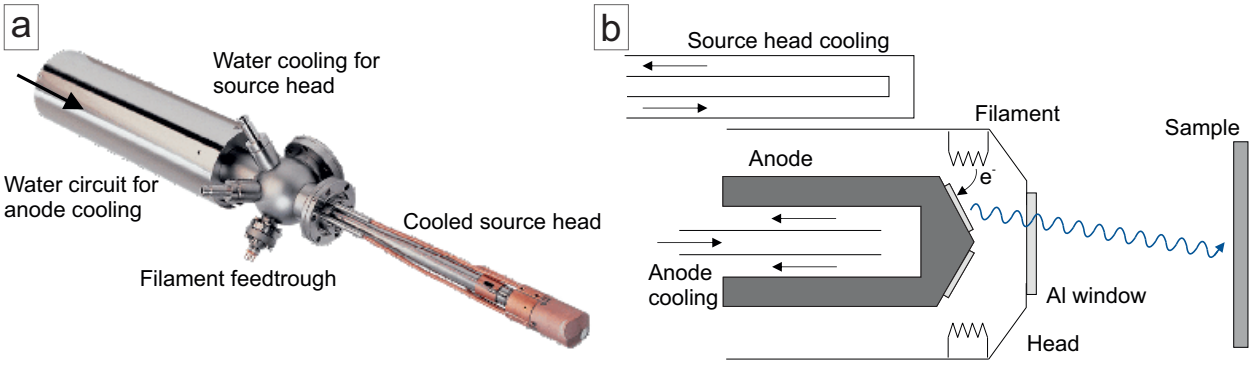

Figure 3.2: ***(a)*** *Photograph of the SPECS XR 50 X-ray Source (adapted from [SPE13]).* ***(b)*** *Schematic drawing of the source head. Electrons from a filament are accelerated toward the anode by an applied high voltage generating X-rays that radiate to the sample surface. Two independent cooling circuits are employed to account for heat dissipation in anode and source head.*

Upon impact of electrons on the metal anode, X-ray fluorescence emission with two distinct components is generated.[Des11] Electrons that are decelerated or partially stopped inside the metal make for Bremsstrahlung radiation. This continuous spectrum has a maximum energy, which corresponds to the applied high voltage between filament and anode. Superimposed onto this broad background are sharp emission lines: The impinging electrons are able to knock out electrons from core atomic orbitals (predominantly from the K shell) creating vacancies, *i.e.* core holes. These core holes are filled by electrons descending from outer orbitals (*e.g.* from the L or M shells) giving rise to characteristic, *i.e.* element-, and therefore material-specific X-ray emission reflecting the energy difference between the two shells. A detailed explanation of the physics behind XPS is presented in section 2.2. The aluminum window suppresses Bremsstrahlung radiation and prevents stray electrons from the filament to enter the electron analyzer.

In case of the Al anode, photons with an energy of 1486.6 eV and a natural line width (FWHM) of ∼0.85 eV are predominantly emitted, originating from L to K shell transitions and denoted as Al-K_α X-rays.[Col15] In fact, the Al-K_α line consists of two distinct and overlapping emission lines $K_{\alpha,1}$ and $K_{\alpha,2}$ with energies of 1486.27 eV and 1486.70 eV, respectively, due to the spin-orbit interaction of the L shell.[Bea67, Kra79, Fel86] Photons originating from the Mg anode have an energy of 1253.60 eV and a natural line width of 0.70 eV.[van12]

The energy resolution of XPS is in general defined by several contributions including the intrinsic width of the photoemission line of the atom to be analyzed, as well as the energy resolution of the electron energy analyzer. However, it is mostly governed by the X-ray source line width. The intensity of the X-ray source, defining the signal-to-noise ratio of the experiment, is also limited, as most of the kinetic energy of the incident electrons is dissipated into heat. The maximum flux is therefore determined by how effectively the source head

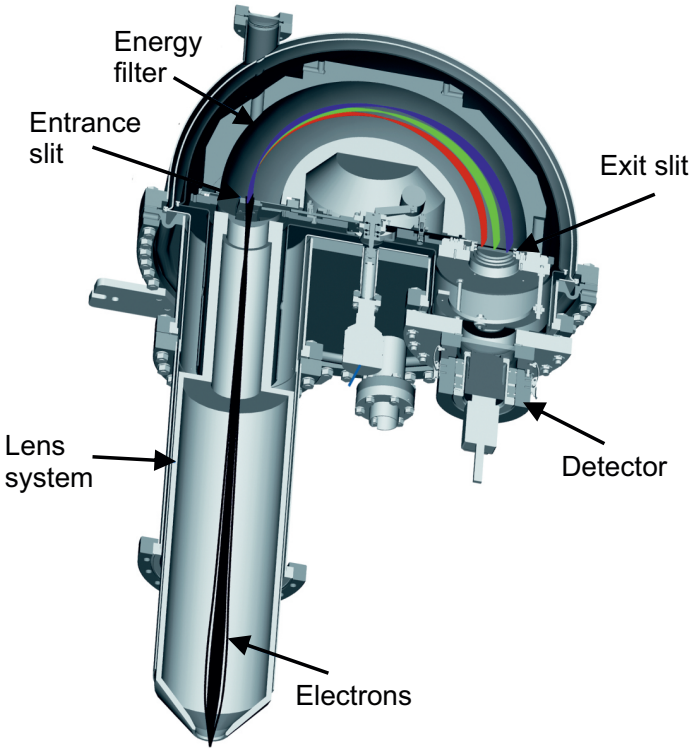

Figure 3.3: *Schematic working principle of the SPECS PHOIBOS 100, a concentric hemispherical analyzer (CHA). Electrons are accelerated/decelerated within a lens system and enter the analyzer via the entrance slit. Due to a potential difference applied between the two concentric hemispheres only electrons with a specific kinetic energy E_{kin} are able to pass through the exit slit and reach the detector. Adapted from [SPE12].*

can be cooled. In addition, X-ray emission occurs over a large solid angle and is not focused on the sample. All these drawbacks are overcome by synchrotron radiation, which offers extremely a high photon flux with a narrow bandwidth, brilliant beam collimation, and a tunable photon energy by means of monochromators (see section 3.7.1).

3.2.2 Electron Kinetic Energy Analyzer

In order to obtain information by means of XPS, the kinetic energy of the photo-generated electrons needs to be analyzed with high energy resolution and high transmission. Therefore, a SPECS PHOIBOS 100 electron analyzer together with a MCD-5 detector is installed in the XPS-STM setup. The PHOIBOS 100 is a concentric hemispherical analyzer (CHA), the type by far most commonly used in modern XPS instrumentations.

Figure 3.3 displays the schematic working principle of the CHA. The CHA consists of two concentric hemispheres of radius R_{in} and R_{out} where specific potentials U_{in} and U_{out} are

applied, respectively. Thus only electrons with a certain kinetic energy E_{pass} are able to travel through the analyzer following a tangential trajectory along $R_0 = (R_{out}/R_{in})/2$ and eventually reach the detector through the exit slit.[van12] The pass energy, a parameter set by the user that influences the energy resolution of the measurement, is defined as [Wil11]

$$E_{pass} = e(U_{in} - U_{out}) \left(\frac{R_{in} R_{out}}{R_{out}^2 - R_{in}^2} \right). \tag{3.1}$$

XP spectra are usually acquired in fixed analyzer transmission (FAT) mode: prior to entering the analyzer through the entrance slit, the electrons are decelerated (or accelerated) in a retardation stage. This lens system (referred to as electron optics) changes the kinetic energy of the electrons without changing their absolute energy spread, and thus enhances the effective resolution by a factor E_{kin}/E_{pass}.[Hüf10] The relative energy resolution of a CHA is given by [Wil11]

$$\frac{\delta E}{E_{pass}} = \frac{2 \cdot W}{R_{out} + R_{in}} + (\delta\alpha)^2, \tag{3.2}$$

where W is the width of both entrance and exit slit and $\delta\alpha$ is the angular divergence of incoming electrons in the plane of the electron trajectory. Note that the relative energy resolution $\delta E/E_{pass}$ is independent of the kinetic energy of the electron and can be increased by choosing a smaller entrance slit. In order to keep the instrumental energy resolution constant over the course of one XP spectrum, E_{pass} needs to be kept constant by varying the retardation lens voltage. The energy resolution that is achievable with a CHA is in principle better than 0.01 eV, which is much better than the energy spread of X-ray sources. Hence, the total energy resolution in XPS is mainly governed by the X-ray source and not by the electron analyzer.[van12]

To measure the flux of electrons, a MCD-5 multi-channel plate detection unit is employed, which consists of a five channel electron multiplier (CEM). Electron multiplication by a factor of $\sim 1 \times 10^8$ is achieved through an emissive layer along the inner surface of the CEM.[SPE12]

Since charged particles are influenced by external stray electromagnetic fields (*e.g.* the magnetic field of the earth) the analyzer needs to be shielded. Therefore μ-metal (∼76 % Ni, ∼17 % Fe, ∼5 % Cu, and ∼2 % Cr) is employed within the enclosed volume of the analyzer and detector to screen these fields down to an uncritical level.[van12]

3.3 STM Apparatus

The STM apparatus installed in the XPS-STM setup is based on a design by G. Meyer and S. Zoephel developed at the Freie Universität Berlin,[Mey96b] and now commercially available from CreaTec Fischer & Co. GmbH.[Cre17] An isometric drawing of the STM stage

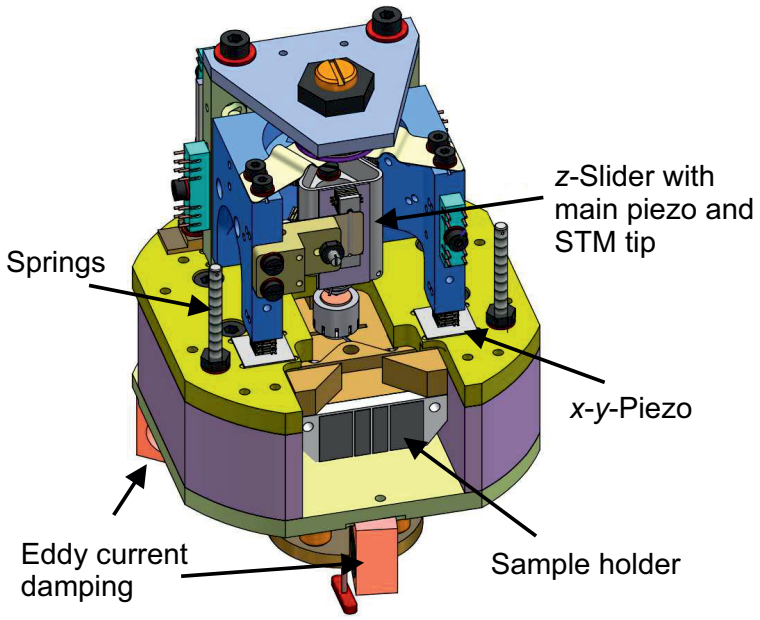

Figure 3.4: *Isometric drawing of the CreaTec scanning tunneling microscope head. The scanner (depicted in blue) is positioned on top of the metal baseplate (yellow and purple) an can move via x-y piezoelectric actuators on ceramic pads (white). The scanner head encompasses the z-slider and the main piezo where the STM tip is attached. Adapted from [Cre13].*

is displayed in Figure 3.4. The stage consists of two main parts, a baseplate (colored yellow and purple) and the scanner (blue and gray) sitting on top of it.

The base plate is a solid U-shaped metal part with a clearance for the sample holder (see section 3.4). It includes a retainer with spring-loaded pins through which the electric contact with the sample is realized. The retainer can be pulled down forcing the sample holder and the entire STM stage into a fixed position for sample transfer. For vibration isolation, the STM stage is hanging freely on three springs during scans and is additionally equipped with an eddy current damping system to damp oscillations.

The scanner consists of a tripod metal frame (colored blue in Figure 3.4) that is fixed between three ceramic pads and a metal rack (colored light blue). The legs of the scanner tripod are equipped with stacked piezoelectric actuators (piezos), which are utilized for coarse motion on the length scale of several millimeters on the ceramic pads. The Pan-type slider,[Pan93] a triangular prism inside the tripod frame is actuated *via* two triples of piezo stacks responsible for the coarse movement in z-direction. Inside the prism, a separate main piezo is located, which is utilized for scanning and fine positioning of the tip in the sub-Å to micrometer range. The STM tip is magnetically attached to the main piezo.

The piezo actuators exploit the piezoelectric effect of certain ceramic materials. When an electric field is applied the ceramic material, it generates strain resulting in a controlled deformation. This deformation translates into a displacement by means of a stick-slip motion.

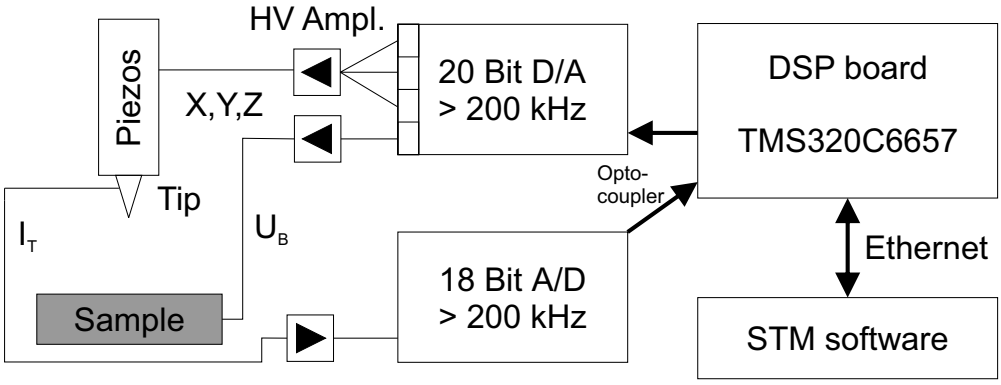

Figure 3.5: *Working diagram of the CreaTec STM electronics. Piezo voltages are generated in the HV amplifier and the tunneling current is read out by the digital signal processor (DSP) board. The communication with the CreaTec STMAFM* 3.0 *software is established via ethernet. Adapted from [Cre15].*

When the piezos are driven fast, the piezo stack slips over the supporting ceramic pads whereas slow relaxation in the opposite direction results in a displacement of the piezo stack. To move the scanner laterally all three piezo stacks are addressed simultaneously with the same signal. A combination of piezos rotated by 90° within each piezo stack makes for movement in x- an y-direction. For movement in z-direction two piezo stack triples are employed in a way that one triple is moving while the other triple is fixed thus preventing the slider to fall due to gravity. The main piezo used for scanning is a tube piezo, which is fixed on the upper end. It consists of two electrode pairs for deformations in x- and y-direction, which are placed on the piezos outside walls, as well as a ring electrode for deformation in z-direction. When an electric field is applied to one electrode, the piezo wall expands while the opposite wall contracts, resulting in a lateral deformation of the piezo tube.

Note that the Pan-type scanner in the XPS-STM (and the LT-AFM setup) offers a significantly larger travel distance in z-direction compared to the Besocke-type scanner in the LT-STM (∼20 mm vs. ∼2 mm). The larger travel distance allows for better access from the sides, *e.g.* for optical experiments as well as *in-situ* evaporation. Nevertheless, caution is advised when sample holders are mounted, as the exchangeability of sample holders between all systems requires the samples to be mounted with a well-adjusted height.

The electronics necessary for STM operation comprise the digital signal processor (DSP) board, the high voltage (HV) amplifier, and a Femto DLPCA-200 current voltage amplifier. The CreaTec DSP board is based on the TMS320C6657 DSP by Texas Instruments and is controlled *via* the CreaTec STMAFM 3.0 software. Figure 3.5 shows a working diagram of the electronics for scanning the tip over the sample surface. The DSP receives the amplified tunneling current fed in through an analog–digital (A/D) converter. In the most commonly used constant-current mode (see Section 2.1.1) the feedback loop calculates the piezo volt-

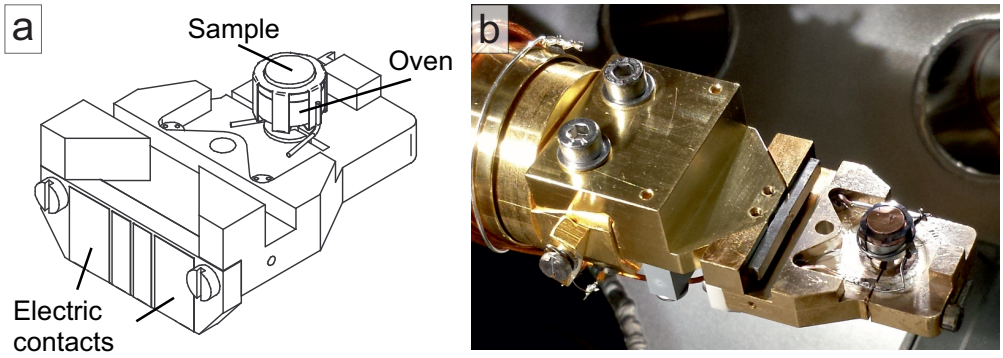

Figure 3.6: ***(a)*** *Technical drawing of a CreaTec sample holder with a single crystal sample mounted on an electrically isolated oven (adapted from [Cre02]).* ***(b)*** *Photograph of a sample holder with a Cu(*111*) single crystal clamped on the manipulator in UHV.*

ages that are subsequently output by an HV amplifier to adjust the tip–sample distance, maintaining a constant tunneling current. Both the x-, y- and z-piezo voltages and the sample bias is output by the DSP board through a D/A converter. For real-time readout, a VOLTCRAFT DSO-1062D oscilloscope is used.

Note that an Ethernet adapter is installed in the host PC, which is dedicated solely to communication with the electronics.[Cre15] During the start-up process of the DSP board, a running TFTP server (*e.g.* TFTPD64 [Tft17]) on the PC is necessary to flash load the configuration file.

3.4 Sample Geometry

The experiments presented in this thesis have been carried out utilizing metal single crystals, specifically, Ag(111) and Cu(111), purchased from Surface Preparation Laboratory.[Sur17] The single crystals have a cylindrical hat shape with a diameter of 6 mm, and are mounted on a CreaTec sample holder as depicted in Figure 3.6. The sample holder consists of a gold-coated copper framework, a button heater oven and a ceramic plate coated with metal contacts. The metal crystal is fixed on the oven by a star-shaped molybdenum clamp. The oven is isolated from the metal sample holder by sapphire half-shells. Heating wires are soldered to the back side of the ceramic plate and fed through a pair of ceramic inlays in the sample holder. One of the heating wires is coiled up inside the ceramic oven to make for direct Joule heating of the sample. The second heating wire contacts the molybdenum clamp. The temperature can be read out *via* K-type thermocouples that are spot-welded onto the Molybdenum clamp and also attached to the metal contacts of the ceramic plate. When the sample holder is placed in the STM, the sample bias is applied *via* one of the six metal contacts.

3.5 Sample Preparation

Cleaning metal crystals is a standard procedure in surface science and usually consists of cycles of ion bombardment (referred to as sputtering) and thermal annealing. For sputtering, a beam of Ar^+ ions is focused perpendicularly onto the sample. Therefore, the preparation chamber is backfilled with Ar to a partial pressure of 2.5×10^{-5} mbar and an ion gun is utilized to generate and accelerate the ions with a bias of typically 800 to 1000 V, which translates into an ion current of 4 to 5 µA hitting the sample. The ion bombardment removes atomic and molecular contaminants as well as surface atoms and thus roughens the substrate. Subsequent annealing to temperatures of ∼830 K and ∼770 K for copper and silver, respectively, heals the crystal and recovers an atomically flat and well-ordered surface.[Feu16]

While medium annealing temperatures are sufficient for the preparation of clean metal surfaces, a more sophisticated treatment is necessary for experiments that include the growth of boron nitride and graphene overlayers (see section 4). The synthesis of two dimensional (2D) hexagonal boron nitride (*h*-BN) and graphene layers require substrate temperatures up to 1110 K for copper and 900 K for silver, respectively. Therefore the sample needs to be repeatedly annealed to elevated temperatures to deplete the metal crystals of common contaminants like carbon and sulfur prevalent at high temperatures.[Poe92, Stu94]

h-BN monolayers are the key component in several projects of this thesis (see Chap. 4, 5 and 6). The growth of *h*-BN is achieved by chemical vapor deposition (CVD) of borazine ($B_3N_3H_6$), purchased from KatChem.[Kat17] In CVD, the catalytically active metallic substrate facilitates the decomposition of the precursor molecules. Borazine is the isoelectronic and isostructural inorganic analog of benzene.[Bon15] At ambient conditions, the borazine precursor is a meta-stable transparent liquid that decomposes in the presence of moisture and easily degenerates with temperature and light. Therefore it is necessary to store it cold (using a Peltier cooling unit), in vacuum and protected from light. Figure 3.7 shows borazine in a glass tube that is attached to a leak-valve for dosing into the UHV chamber. To avoid contaminations, borazine was transferred into the glass tube *via* vacuum distillation from a stainless steel container, in which it was delivered. The procedure is described in detail in appendix B. Chap. 4 describes the growth of *h*-BN on metallic surfaces in detail. Besides *h*-BN, graphene was grown utilizing a home-built e-beam evaporator and a solid graphite rod as carbon source (see section 6.1).

In addition, metals (*e.g.* copper, silver, and cobalt) and molecules have been deposited onto the clean sample surface using evaporators described in section 3.1. For molecule deposition, a home-built two-cell organic molecular beam epitaxy (OMBE) evaporator has been employed. Quartz crucibles filled with molecular powder are loaded into the evaporator and

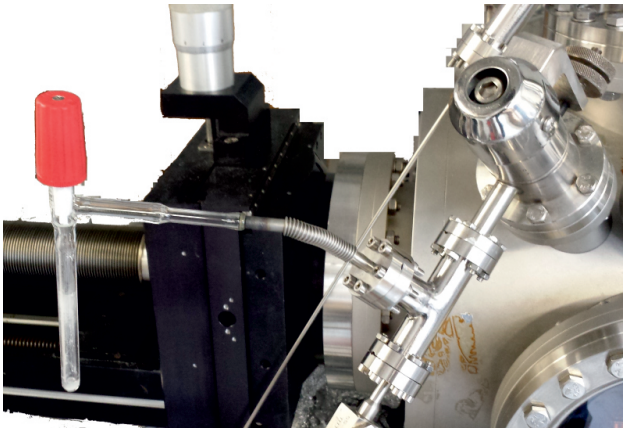

Figure 3.7: *Borazine in the glass tube attached to the leak valve. The peltier cooler is removed while borazine is dosed into the UHV chamber.*

heated resistively to sublime the molecules. Typical deposition times are in the range of 5 to 60 min. Cobalt porphine (Co–P) molecules (see section 5.1 and 5.2) were purchased from Frontier Scientific.[Fro17] The borazine derivatives BNPPy and BNAPy, which are characterized in section 6.2 as well as the functionalized porphyrin (2H–TPCN) molecules (see section 5.3) were synthesized by the group of Davide Bonifazi.[Bon17]

3.6 Tip Preparation

A crucial requirement for STM measurements is the preparation of a well-defined, clean and sharp STM tip. Although only the tip atoms closest to the sample surface, *i.e.* the tip apex dominates the tunneling process, a macroscopic sharp and clean tip is desirable to enhance the stability during the measurement. In the course of this thesis two commonly used tip materials were employed, namely platinum-iridium (Pt–Ir) and tungsten (W). Pt–Ir tips are relatively inert not only to oxidation but also to contaminations making it suitable for measurements with insulating layers. The straightforward preparation of Pt–Ir tips is realized by mechanical cutting of 0.25 mm diameter platinum-iridium wire with pliers resulting in sufficiently sharp tips. Tungsten tips are widely used in STM due to their mechanical stability and comparatively smooth DOS around the Fermi energy.[Nes95] W tips were fabricated from polycrystalline tungsten wire (diameter 0.25 mm) by electrochemical etching. The procedure is depicted in Figure 3.8. The W wire is placed inside a ring-shaped copper wire. The ring contains a lamina of NaOH solution (2 mol/l) created by dipping it into a bath placed underneath. By applying a voltage of 3 to 4.5 V between W wire and copper loop, the tungsten is oxidized into soluble WO_4^{2-}. The reaction reads

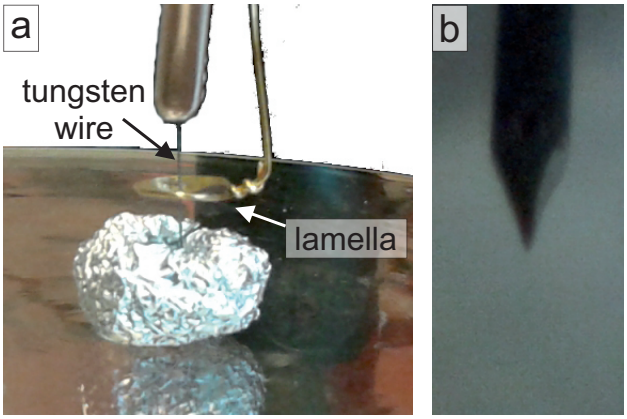

Figure 3.8: ***(a)*** *Photo of the tip preparation procedure. A thin tungsten wire is placed in a lamella and etched electro-chemically in a NaOH solution.* ***(b)*** *Magnified picture of the extraordinarily sharp STM tip.*

$$W(s) + 2OH^- + 2H_2O \rightarrow WO_4^{2-} + 3H_2(g).$$

Within some minutes, the W wire becomes thinner and eventually breaks resulting in a very sharp wire that can be used as an STM tip. The as-prepared tip is rinsed with distilled water and isopropyl alcohol to remove solvents and then fixed rigidly on the tip holder. Once introduced into the UHV chamber, the W tips are sputtered *via* Ar^+ ion bombardment in order to remove the oxide layer and transferred to the STM with a special tip holder fork.

During STM measurements the tip frequently changes its shape and composition of the apex because of interactions with the substrate or adsorbed molecules. To recover a sharp tip and to remove contaminants, which might perturb tunneling, *in-situ* tip conditioning methods can be applied. First, voltage pulses can be applied. To this end, the bias voltage is quickly sweept to voltages up to 10 V, while the tip is approached several Å to the crystal surface. Second, the tip apex can be changed drastically by bringing it into physical contact with the metal substrate *via* the ramp controller, which will cover the tip with substrate atoms. Another applicable method is field emission, where a high voltage of up to 80 V is applied between tip and sample, while the current is limited to some tens of µA.[Alb94, WB07] After the tip was in contact with the substrate, the tip is slowly retracted. Thereby, the STM tip usually gets longer and changes its shape significantly.

The quality of the tip can be tested by recording $\mathrm{d}I/\mathrm{d}V$ spectra around the Fermi energy (see section 2.1.1.2). On (111)-terminated silver and copper surfaces, characteristic (Shockley) surface states are present,[Kev87] which are preserved as interface states upon *h*-BN and graphene growth.[Jos12, Gar16] If this state is observed without significant other contributions to the spectrum, the tip is assumed to be metallic and suitable for spectroscopy. In

the LT-AFM, an additional indicator to judge the sharpness of the tip is available, namely the frequency shift Δf. Usually, a $\Delta f \approx -2\,\mathrm{Hz}$ indicates a very sharp and stable tip.

3.7 I09 Beamline at Diamond Light Source

All XSW and some XPS measurements presented in this thesis were conducted at the I09 beamline at Diamond Light Source (DLS), United Kingdom.[I0917] In the following, the general characteristics of the synchrotron and the I09 beamline endstation are elucidated with a particular emphasis on synchrotron X-ray light generation (see section 3.7.1). The UHV chambers of the beamline endstation comprise two preparation chambers and one analysis chamber. The preparation chambers contain standard equipment for Ar^+ ion sputtering and sample annealing (*via* electron bombardment). Metal and OMBE evaporators, as described in section 3.1, can be mounted at gate valves of the preparation chambers. The base pressure of all UHV chambers is $\sim 4 \times 10^{-10}$ mbar. The sample is mounted on Omicron sample plates and can be transferred between the different chambers *via* a 4-axis and a 5-axis manipulator, respectively. The latter allows for movement along three spatial coordinates plus polar and azimuthal rotation in the analysis chamber. In contrast to the CreaTec sample holders described in section 3.4, the Omicron sample plate has no thermocouple attached to the sample. The sample temperature is set by referring to a calibrated power *vs.* temperature curve and can be measured above 600° *via* a pyrometer. Sample cooling down to ∼50 K can be realized by liquid helium.

3.7.1 Synchrotron Light

DLS is a third-generation synchrotron (technically 3.5^{th} generation). A schematic of its most important components is displayed in Figure 3.9. Contrary to laboratory X-ray sources (*cf.* section 3.2.1) the synchrotron produces highly collimated and narrow beams of X-ray light with high intensity. To this end, electrons are accelerated in a linear accelerator and a booster synchrotron and thereupon fed into a storage ring where they are circulating in a closed path at nearly the speed of light. Bending magnets at the arced sections of the storage ring are utilized to steer the highly relativistic electrons around the ring. Synchrotron light is generated in insertion devices, so-called undulators situated at straight sections of the storage ring.[Wil11] Beamlines are positioned tangentially to the undulator segments of the storage ring, and consist of an optics hutch where certain wavelengths of the synchrotron light are selected and focused, and an experimental hutch (endstation) housing the experimental equipment. The stored electron beam in the ring is continuously topped-up by injections of electrons and maintained at a level of ∼300 mA, enabling continuous user operation. Energy

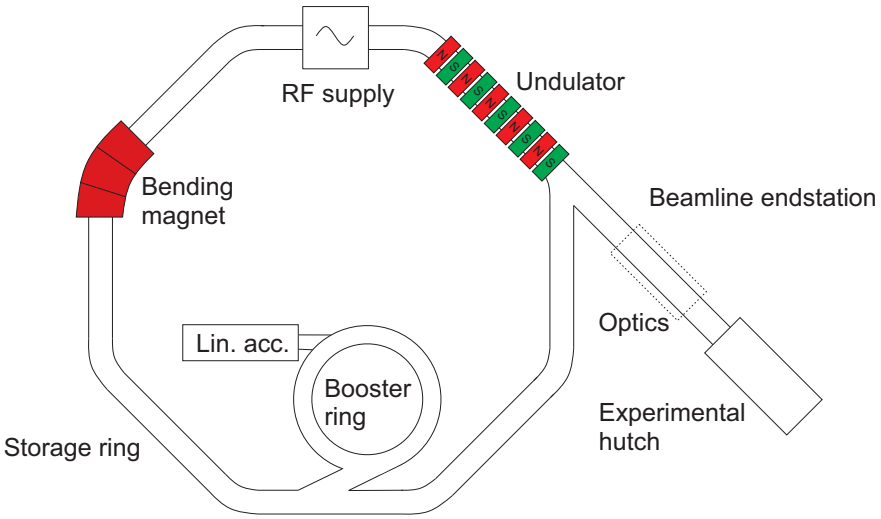

Figure 3.9: *Schematic of the most important components of a third-generation synchrotron. Electrons are accelerated in a linear accelerator and a booster ring prior to insertion into the storage ring. Bending magnets are utilized to steer the electrons on a closed path around the storage ring. Synchrotron light is created in insertion devices, so-called undulators and shaped with several optics and gratings before it arrives at the experimental hutch of the beamline endstation. The radiative energy loss of the electrons is replenished by a radio frequency (RF) supply. Adapted from [Wil11].*

lost by the electrons due to the radiative emission of synchrotron light is replenished by radio frequency supply. Coulomb repulsion between the electrons is compensated by quadrupole magnets.

Whenever the electrons are deflected (*i.e.* accelerated) at the curved sections of the storage ring they will emit electromagnetic radiation tangentially to their trajectory (see Figure 3.10), known as synchrotron radiation.[Mob15] The high flux of light is emitted in an extremely narrow cone with an opening angle $\theta \sim \gamma^{-1}$ where γ is the Lorentz factor

$$\gamma = \frac{E}{m_0 c^2}, \tag{3.3}$$

with the electron energy E and $m_0 c^2$ the rest mass energy of the electron.[Wil11] The opening angle is typically within some tenth of milliradian and has a broad energy spectrum ranging from 10 eV to 20 keV dependent on the electron velocity. However, the flux of light emitted from bending magnets is limited since their primary purpose is to steer the electrons around the storage ring. Even higher X-ray flux can be achieved in insertion devices like undulators.

A schematic drawing of an undulator is shown in Figure 3.10. An undulator consists of small magnets with alternating polarity arranged in two parallel arrays. Electrons passing through the undulator are subject to an alternating centripetal acceleration in the magnetic field and oscillate (undulate) in the plane of the storage ring. The arrangement of the

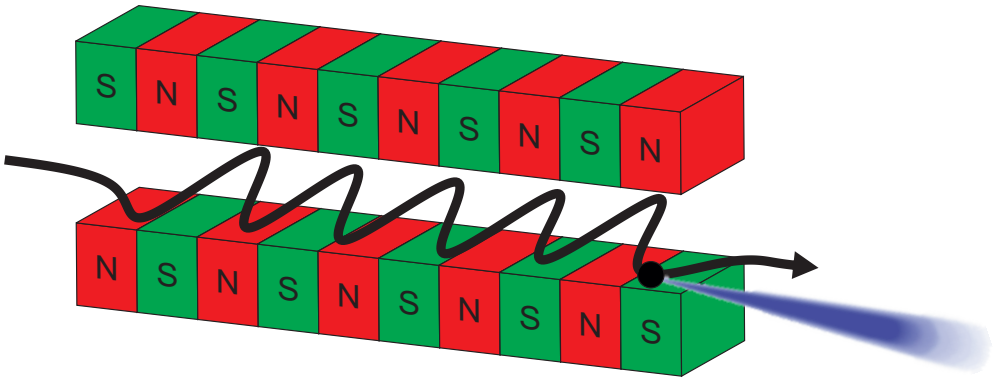

Figure 3.10: *Schematic drawing of an insertion device (undulator). Magnets with alternating polarity are arranged in two parallel arrays. Electrons travelling through this magnetic array are forced on oscillating trajectories, generating synchrotron radiation.*

magnets is designed in such a way that the electrons are forced to have small oscillation amplitudes. This causes interference, coherently adding up the individual amplitudes of the fields radiated at each point of their sinusoidal trajectory in the undulator.[Mob15] The wavelength λ of the emitted radiation with maximum intensity is given by

$$\lambda = \frac{L}{2\gamma^2}\left(1 + \frac{1}{2}\left(\frac{eBL}{2\pi m_0 c}\right)^2 + \gamma^2\theta^2\right), \tag{3.4}$$

and accompanied by higher harmonics with shorter wavelengths $\lambda_n = \lambda/n$ and weaker intensity. Here, L is the length of the undulator, e is the electron charge, B is the applied magnetic field, m_0 is the electron rest mass, γ is the Lorentz factor and θ is the opening angle. Eq. (3.4) highlights that the wavelength of the synchrotron light that has maximum intensity can be varied by means of the applied magnetic field B. This can be realized by varying the gap distance between the two magnetic arrays and allows for a continuous selection of the X-ray energy.

In practice, soft and hard X-rays with energies of 110 to 1100 eV and 2.15 to 18 keV, respectively, are available.[I0917] During our beamtime at DLS, the adjustment mechanism of the monochromator of the soft X-ray line was broken, and thus only a fixed (soft X-ray) energy of 641 eV was usable. The installed hemispherical electron analyzer, a VG Scienta EW4000 HAXPES with an acceptance angle of ±28°, was mounted with an angle of 90° with respect to the incident synchrotron light and the center of its angular acceptance in the plane of the photon polarization.

The beams originating from two separate undulators are focused on the same sample spot. Figure 3.11 depicts the different sample orientations for XPS and NIXSW experiments. In

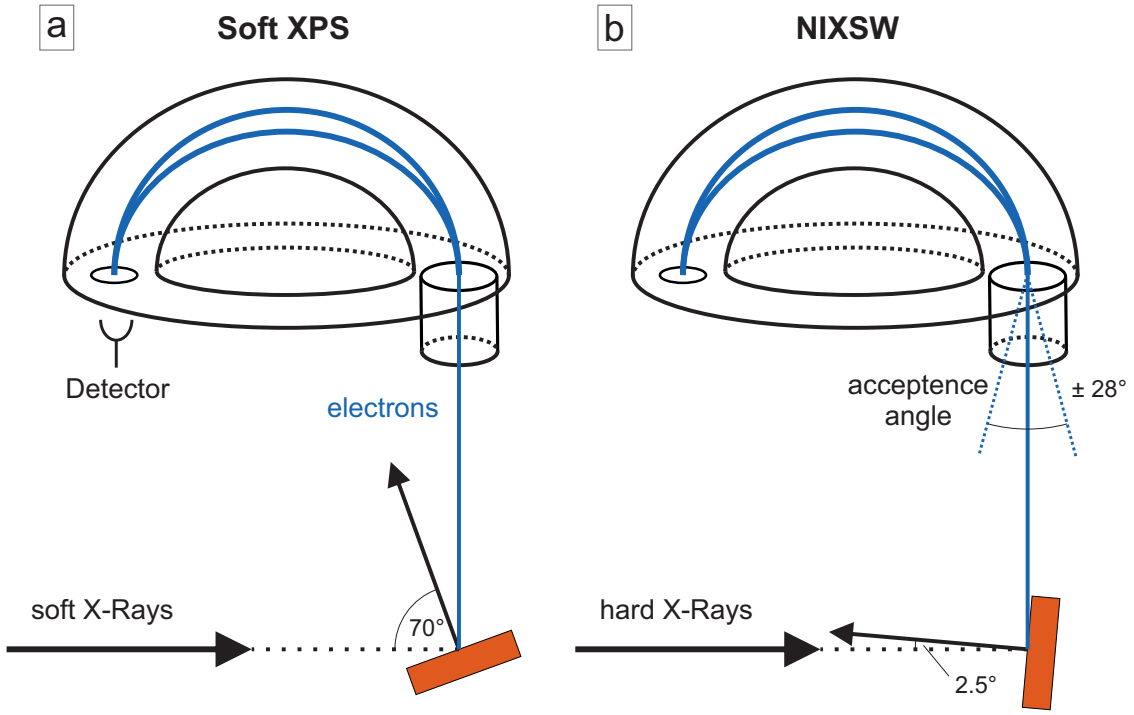

Figure 3.11: *Schematic of the sample orientations for* ***(a)*** *(soft) XPS and* ***(b)*** *NIXSW experiments at DLS. The electron analyzer is mounted with an angle of* 90° *with respect to the incident synchrotron light and the center of its angular acceptance in the plane of the photon polarization. The sample normal has an angle of* 70° *(*2.5°*) with respect to the incident X-rays for XPS (NIXSW) measurements.*

the first case, the sample normal has an angle of 70° with respect to the incident X-ray beam. The spot size of the soft X-ray beam for the utilized soft XPS photon energy (641 eV) is about $60 \times 60\,\mu m^2$.

In the latter case, for the (111) NIXSW measurements, the polar angle is only 2.5° such that the photon incidence direction was almost normal to the Bragg scattering plane utilized to generate the standing waves (see section 2.3). For the XSW measurements, the X-ray beam was defocused to approximately $400 \times 400\,\mu m^2$ and stepped over the sample such that each XSW curve was acquired at a different sample position. To further avoid beam damage to adsorbed molecules, the beam intensity was reduced to 20% by detuning the undulator. Possible beam damage was monitored by comparing the relevant core-level spectra before and after each XSW measurement. The XSW scans were obtained from the (111) and $(1\bar{1}1)$ Bragg reflection of Cu (E_{Bragg} ≈2972 eV at 300 K and ≈2981 eV at 50 K). Note that we used a polar angle of 70.5° for the $(1\bar{1}1)$ NIXSW measurements in order to be normal to the $(1\bar{1}1)$ planes.[Woo05] The intensity of the crystal Bragg reflection was recorded simultaneously with the absorption profiles. The former was acquired *via* a fluorescent screen mounted on the port of the incident X-ray beam by means of a CCD camera, and the latter was acquired

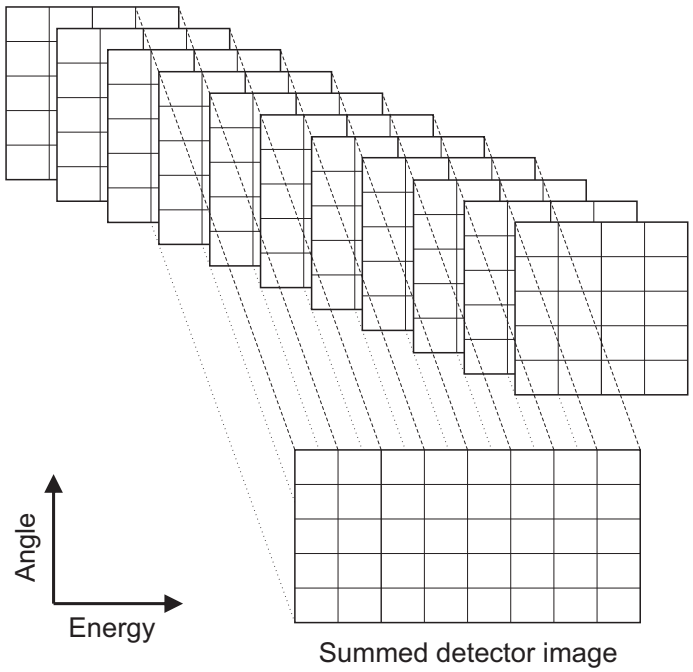

Figure 3.12: *Schematic of the swept scan detector mode of the DLS electron analyzer. The summed detector image consists of m pixels in the energy direction. Each pixel itself is the sum of n properly aligned slices of 2D images.*

from core-level photoemission yields. Prior to each XSW measurement, a reflectivity curve was recorded to determine the Bragg energy at a given position on the sample, and the subsequent XSW measurement was restricted to a window of ±5 eV around that energy.

3.7.2 Electron Kinetic Energy Analyzer

The working principle of the electron analyzer is similar to the on-campus analyzer in Munich described in section 3.2.2. The total energy resolution of the detector is ∼0.4 eV for hard and ∼0.1 eV for soft X-rays. However, the DLS electron analyzer allows for both angular and transmission (*i.e.* angle-integrated) operation modes. The detected 2D image of the electron signal is resolved in energy along the x-axis and in angle along the y-axis. The electron analyzer can operate in two acquisition modes for a selected kinetic energy range: in fixed mode and in swept mode.[Lee17a]

In a fixed mode scan, an image, which maps the angular and the energy distribution of the photoelectrons is recorded at a fixed retarding voltage on the lens. The energy width of the scan is determined by the pass energy, and the angular width is determined by the selected lens mode. In a swept mode scan (Figure 3.12), a series of 2D images are acquired while the retarding voltage is stepped through the selected energy range. All images are subsequently properly aligned in the energy direction and then summed. The summed detector image has

m pixels in the energy direction with each pixel being the sum of n images. Consequently, each image has n slices and the total number of acquired 2D images is $m + n - 1$.

The acquisition time of a fixed mode scan is shorter than that of swept mode scans. However, due to the inhomogeneity of the multi-channel plate detector, the acquired spectra in fixed mode need to be normalized with a calibration curve.

Chapter 4

Hexagonal Boron Nitride (*h*-BN) on Metallic Substrates

This chapter includes content that has been published in

M. Garnica, M. Schwarz, J. Ducke, Y. He, F. Bischoff, J. V. Barth, W. Auwärter, D. Stradi, **Comparative study of the interfaces of graphene and hexagonal boron nitride with silver**, *Phys. Rev. B* **94**, 155431 (2016); Copyright (2016) by the American Physical Society.

and

M. Schwarz, A. Riss, M. Garnica, J. Ducke, P. S. Deimel, D. A. Duncan, P. K. Thakur, T.-L. Lee, A. P. Seitsonen , J. V. Barth, F. Allegretti, W. Auwärter, **Corrugation in the Weakly Interacting Hexagonal-BN/Cu(111) System: Structure Determination by Combining Noncontact Atomic Force Microscopy and X-ray Standing Waves**, *ACS Nano* **11**, 9151-9161 (2017); Copyright (2017) by the American Chemical Society.

Two-dimensional hexagonal boron nitride (*h*-BN) grown on various transition-metal substrates has attracted tremendous interest in the scientific community due to its fascinating properties like, *e.g.* inertness, high mechanical strength, and a large electronic bandgap, which are complementary to those of graphene and other two-dimensional materials.[Wat04, Shi10, Kim12] In particular, the structural similarity of *h*-BN monolayers to graphene, reflected in a small lattice mismatch of 1.6 %,[Pas02] makes these materials compatible for applications in vertically stacked van der Waals heterostructures and in hybridized atomically flat layers.[Osh97, Ci10, Dec11, Gei13, Hwa16] Moreover, single-layer *h*-BN has shown its potential as a template to steer the adsorption of atoms, molecules, and nanostructures

with control of their spin and energy level alignment.[Jos14, Urg15a, Sch15b, Jac15, Lee17b, Kum17] In addition, it has been predicted that metal-supported *h*-BN layers might serve as catalysts, *e.g.* for oxygen reduction reactions.[Lya14, Uos14, Lin15, Mah17]

Depending on the interaction with the metal substrate, one can categorize the *h*-BN layer adhesion as strong [such as on the Rh(111), Ni(111) and Ir(111) surfaces] or weak [on the Pt(111), Cu(111) and Ag(111) surfaces].[Cor04, Pre07a, Jos12, Zum16, Gar16, Sch14b, Auw99] The strength of the interaction, together with the lattice mismatch between *h*-BN and support determines the corrugation of the system, which forms a nanomesh in the case of *h*-BN/Rh(111) and a flat overlayer with a minute height difference between boron and nitrogen in the case of *h*-BN/Ni(111).[Auw99, Cor04, Mun17]

This chapter introduces atomically thin *h*-BN layers grown on metal substrates by chemical vapor deposition (CVD). Specifically, the two noble metal substrates, copper and silver, have been utilized in the course of this thesis. Although both *h*-BN/Cu(111) and *h*-BN/Ag(111) are considered as weakly interacting systems, they present remarkable differences regarding the structural and electronic properties of the resulting *h*-BN layer. We find a hitherto unrecognized geometric corrugation in the case of *h*-BN/Cu(111), which is intimately related to the electronic moiré pattern (see section 4.1). Section 4.2 outlines the ion-gun assisted growth of *h*-BN/Ag(111) and discusses the electronic structure of the resulting *h*-BN layer. In section 4.3 we show that intercalation is a route to obtain high-quality *h*-BN on silver where the electronic properties of the layered system can be tuned by the thickness of the intercalated silver.

4.1 *h*-BN on Cu(111)

Cu(111) is a particularly interesting substrate as it features both a small lattice mismatch and a weak interaction with *h*-BN. Furthermore, the use of Cu foils as a support can be an economic route to large-scale *h*-BN synthesis *via* CVD.[Kim12, Jos12, Mah15] However, to realize the myriad of applications for this layer, and to integrate it into real devices *via* the bottom-up approach, a proper knowledge of the precise structure of the *h*-BN–metal interface is crucial. Density functional theory (DFT) calculations have, to date, struggled to describe the experimentally realized *h*-BN/Cu system in detail. Specifically the adsorption height of the *h*-BN layer, the key structural parameter in such a layered system, has been predicted to take a gamut of values, from 2.65 to 3.34 Å.[Lya14, Lin15, Fei15, Koi13, Gom13, Las08] Therefore, determining this parameter experimentally to serve as an unambiguous benchmark is a necessary step toward predictive-level DFT calculations in this field.

Previous quantitative studies of the geometric structure of *h*-BN/Ir(111) and *h*-BN/Ni(111) have been pursued by XSW and X-ray photoelectron diffraction (PhD), respectively.[Zum16, Mun17] In case of the former system, a significant modulation of the *h*-BN layer was observed and modeled by two distinct *h*-BN species located at 2.20 ± 0.02 Å and 3.72 ± 0.02 Å, respectively, above the surface, a marked difference in adsorption height of ∼1.5 Å.[Zum16] The latter study, addressing *h*-BN/Ni(111), instead reported a uniform adsorption height of the entire *h*-BN layer of 2.11 ± 0.02 Å, *i.e.* 0.1 Å closer to the substrate than even the lower adsorption height of the *h*-BN on Ir.[Mun17] Although the corrugation of the *h*-BN/Ni(111) was a fitting parameter, no values were quoted. Now, by contrast to Ni(111) and Ir(111), Cu(111) is a comparatively noble substrate and, although a strong moiré pattern has been observed by STM, it was concluded that this reflects purely electronic modulations.[Jos12, Jos17]

While the lateral structure of two-dimensional layers is usually analyzed by means of STM, AFM, standard LEED, and PhD, a determination of the adsorption height, as well as the corrugation of two-dimensional layers is notoriously difficult to obtain, even by high-resolution nc-AFM. Only elaborate LEED-$I(V)$ and surface X-ray diffraction studies gave access to these parameters, *e.g.* for graphene on Ru(0001).[Mor10, Mar10c] In the following, we present an in-depth structure determination of the *h*-BN/Cu(111) system with the lateral structure analyzed by means of STM and LEED and the vertical structure *via* a combination of nc-AFM, XPS, and XSW. The interpretation of the data is assisted by first-principle calculations carried out by Ari P. Seitsonen. Ultimately, we introduce an approach to extract the detailed nature of an exemplary 2D sheet system *via* nc-AFM, which can also be applied to quantify the corrugation of other two-dimensional materials.

4.1.1 Growth

Single layer *h*-BN was grown on Cu(111) in both the LT-STM and LT-AFM chamber, as well as the preparation chamber of the I09 end station at Diamond Light Source (DLS) following the established procedure described in section 3.5 and Ref. [Jos12]. In the LT-STM/LT-AFM chambers the sample was held at 1080 K and positioned in close vicinity of a needle doser through which the borazine was introduced, resulting in a chamber pressure of 7×10^{-7} mbar for 5 min. At I09, the sample was exposed to borazine (also held at 1080 K – monitored by pyrometer) by backfilling of the chamber to 7×10^{-6} mbar for 25 min resulting in a total exposure of 7900 L. The higher pressure compared to the home lab was chosen to compensate for the lack of directional dosing at the I09 end station. Subsequently, the sample was cooled at a rate of 0.7 K/s. Both preparation conditions result in a single layer of *h*-BN and show the same characteristic LEED patterns. XP survey spectra showed no significant components other than the expected B, N and Cu. A detailed description of the

experimental and computational methods applied during the measurements presented in the following section is summarized in appendix C.0.1.

4.1.2 Lateral Structure

The lateral structure of *h*-BN/Cu(111) is investigated by means of STM and LEED. Here, we highlight our present findings on the basis of the results presented in earlier studies,[Jos12, Jos17] which are consistent with reports from other groups.[Rot13, Li15] Figure 4.1a displays the STM topography image of an extended *h*-BN domain on Cu(111) at 4 V bias voltage, where the electronic corrugation is visualized as a moiré superstructure.[Jos12, Jos17] Previously, the high symmetry registries, giving rise to different regions of the moiré, were labeled "hills" (corresponding to a $N_{top}B_{fcc}$ registry) and "valleys" (corresponding to a $N_{fcc}B_{hcp}$ registry). Following the notation of studies on *h*-BN/Rh(111) and *h*-BN/Ir(111)[Cor04, Zum16] the respective regions will be labeled "pore" (P) and "wire" (W) from now on (see Figure 4.2a) as justified by the observed geometric corrugation discussed below. The most abundant moiré periodicities observed are in the range from 4 to 15 nm and originate from different rotation angles of the *h*-BN lattice with respect to the copper substrate. All rotational domains were originally understood by a small spread (<3°) in the angle between a slightly stretched *h*-BN lattice and the Cu(111) substrate lattice and show the same electronic behavior in terms of their templating effect.[Jos12, Jos14]

The LEED pattern of a single layer of *h*-BN/Cu(111) is displayed in Figure 4.1b. The first-order Cu(111) substrate spots are surrounded by one concentric ringlike structure with a slightly larger *k* vector,[Rot13, Uch17] indicative of various rotational *h*-BN domains.[Mül10] Maximum intensity of the *h*-BN ring is found in directions varying up to ±4° from the main crystallographic directions of the copper substrate (inset of Figure 4.1b). Local maxima are also observed at rotation angles of $(30 \pm 4)°$ with respect to the close-packed directions of the substrate. Atomically resolved *h*-BN lattices observed in STM (Figure 4.1c, d) corroborate this finding. Analysis of the lattice parameters obtained from LEED measurements conducted at room temperature yields a lattice mismatch of (1.5 ± 0.5) %, slightly reduced compared to the 1.9 % mismatch reported by Roth *et al.*,[Rot13] and the nominal 2.0 % lattice mismatch between an isolated *h*-BN layer and the Cu(111) plane.[Str69, Pas02] To accurately model experimentally observed moiré superstructures in graphene on metal systems, the consideration of multiple beatings per moiré unit cell appeared essential.[Art16, Zel14] Indeed, such a modeling approach applied to *h*-BN/Cu(111) reveals the existence of large moiré periodicities even for *h*-BN domains rotated up to 30° (see Figure C.1). Scanning tunneling spectroscopy (STS) measurements probing the field emission resonances reveal a local work function difference of ∼250 mV between high-symmetry positions within the moiré supercell

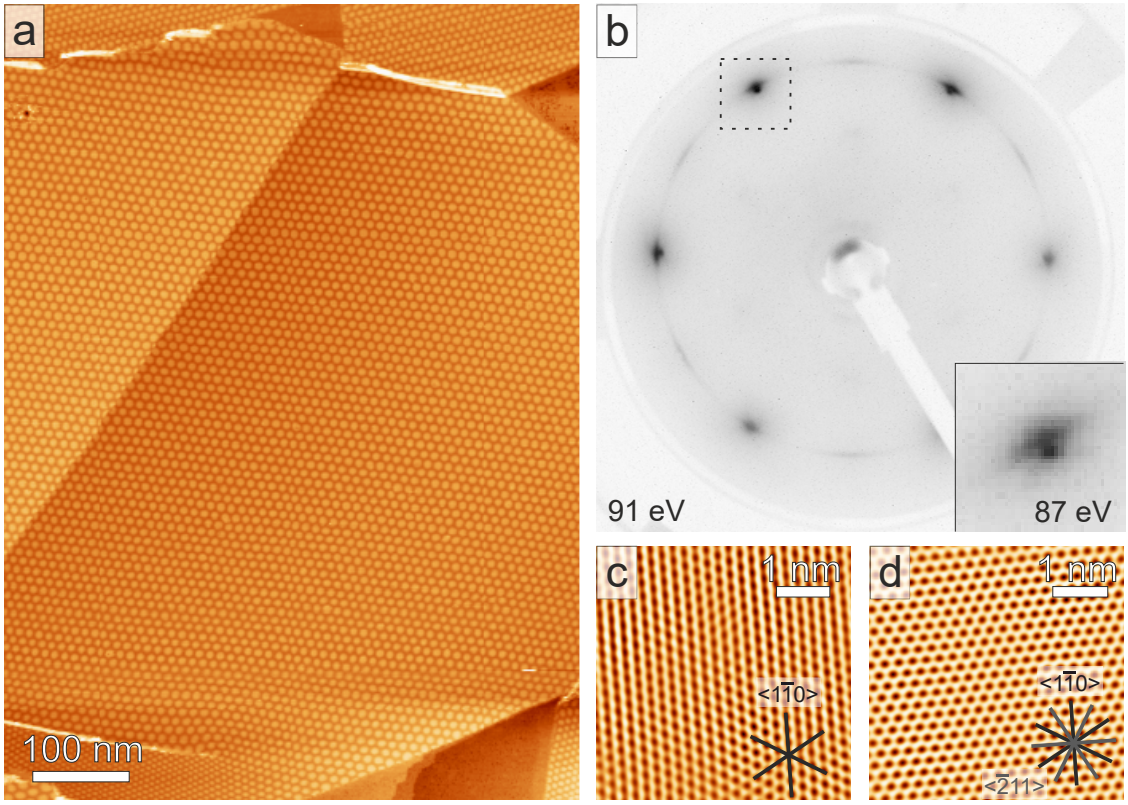

Figure 4.1: *Single layer of h-BN on Cu(111). **(a)** Large scale STM topography image showing extended and regular h-BN domains with sizes up to a micrometer. Scan parameters: $U_b = 4.0\,\mathrm{V}$, $I_t = 0.4\,\mathrm{nA}$ **(b)** Contrast-inverted LEED pattern of a single layer h-BN/Cu(111) recorded at room temperature with an electron energy $E = 91\,\mathrm{eV}$. The Cu spots are surrounded by a ring originating from the h-BN lattice with highest intensity at a small azimuthal rotation relative to the (111) directions. At rotation angles of $(30 \pm 4)°$ local intensity maxima are observed. Inset (recorded with $E = 87\,\mathrm{eV}$) shows a zoom into the first order spot indicated by the dotted square. **(c, d)** Atomically resolved STM images of h-BN lattices (FFT-filtered). Black lines indicate the high-symmetry copper directions. The h-BN lattice in (c) is aligned along the Cu(111) directions, while in (d) it is rotated by almost 30° with respect to the copper. Scan parameters: (c) $U_b = 0.11\,\mathrm{V}$, $I_t = 2.5\,\mathrm{nA}$, (d) $U_b = 0.23\,\mathrm{V}$, $I_t = 0.8\,\mathrm{nA}$.*

(see Figure C.2). Regions of bright contrast at a sample bias of 4 V in STM (pores) possess a lower local work function compared to the darker regions (wires), in agreement with our refined DFT calculations. A work function difference of 340 to 390 meV is calculated for high-symmetry registries of *h*-BN/Cu(111) with the Quantum ESPRESSO code including vdW-DF2-rB86[Lee10, Ham14] and vdW-DF-optB86[Kli11] exchange-correlation functionals (see Table C.1). The discrepancy to the previously reported values[Jos12] highlights the sensitive role of the exchange-correlation functional for a precise description of *h*-BN on metal systems.

4.1.3 Vertical Structure

The local corrugation of *h*-BN on Cu(111) (see section 4.1.3.1) as well as the mean adsorption height (see section 4.1.3.2) are quantified by a combined nc-AFM and XSW approach. The XSW method has been widely applied to structural studies of adsorbates, to accurately determine the mean adsorption height. Quantifying the corrugation amplitude of the *h*-BN layer is, however, much less straightforward. Although XSW measures the spatially averaged distribution center of the overlayer with high precision, the extracted distribution width from a single Bragg reflection can be strongly model-dependent. Laterally resolved measurements by nc-AFM are possible, however, the interaction forces between tip and sample can still be different, even for chemically equivalent species when different areas of the moiré superlattice are probed. Most notably, the different electronic structure across the moiré unit cell (see Figure C.2) is expected to lead to different electrostatic interactions.[Sie17] Recent studies have estimated the molecular adsorption geometries utilizing force-distance maps obtained from nc-AFM.[Moh11, Sch13a, Pat17] Importantly, also the force-distance relationship can be significantly altered by the variation of electrostatic forces across the moiré supercell, thus making the applicability of this method more challenging.[Ono17, van16]

4.1.3.1 Geometric Corrugation

To estimate the influence of electrostatic forces, bias-dependent constant frequency shift (Δf) measurements with sample biases both, smaller and larger than the measured contact potential difference $U_b^* \approx 0.13 - 0.16\,\mathrm{V}$ were carried out.[Sch17b] The absence of contrast inversion in these measurements suggests that the observed corrugation of the *h*-BN in the nc-AFM measurements is not purely based on work function differences for the high-symmetry registries of the moiré unit cell. However, as the tip-sample distance is rather large in these measurements, which is necessary to maintain stable imaging conditions,[Wey11] spatial averaging can play an important role and thus impedes a quantitative determination of the corrugation.

We recorded atomically resolved constant-height AFM images (Figure 4.2a), where pore and wire regions are clearly discernible. Interestingly, this contrast can be inverted depending on the tip termination. In some cases the pores are imaged darker, *i.e.* more attractive than the wires (Figure 4.2a), in other cases this contrast is inverted.[Sch17b] Such an inversion of contrast can originate from different work functions of the tip, which give rise to different electrostatic interactions with the sample. Strikingly, independent of the moiré contrast, the images show that the atomic contrast is significantly higher on the wire regions compared to the pore regions in the constant height images. This finding suggests a difference between the tip-sample distances of the wire and pore regions. To quantify the corrugation of the

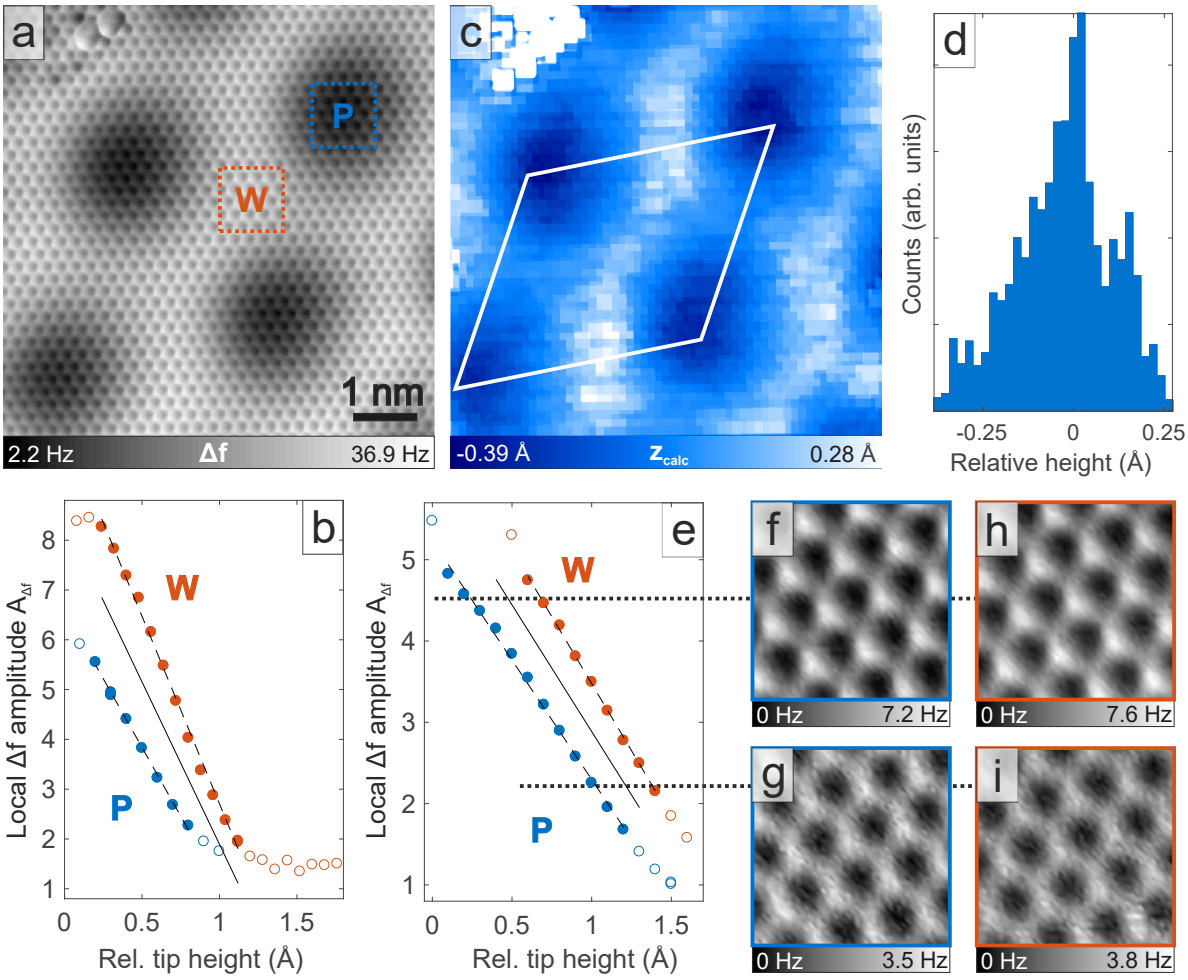

Figure 4.2: *Geometric corrugation of h-BN/Cu(111) determined from nc-AFM.* ***(a)*** *Constant-height AFM image of a single layer h-BN/Cu(111) showing the h-BN lattice together with the moiré unit cell. Orange (blue) square indicates the wire (pore) region of the moiré pattern.* ***(b)*** *Calibration curve $A_{\Delta f}(z)$ (solid line), obtained from the atomic h-BN contrast in pore (P) and wire (W) regions. Dashed lines represent linear fits of filled data points. The relative tip height is defined with respect to a reference point, which corresponds to the lowest tip height that was probed within the experiment.* ***(c)*** *Calculated height map z_{calc} $(A_{\Delta f})$ obtained by converting the atomic contrast in (a) into relative heights via the calibration shown in (b). The color scale represents the values within the unit cell, which is marked by a white rhombus.* ***(d)*** *Height distribution histogram for the indicated moiré unit cell.* ***(e)*** *Calibration curve $A_{\Delta f}$ (solid line) for a second measurement that is displayed in the appendix, Figure C.7, conducted with a different tip apex on a different sample spot. Again a similar characteristics is seen for pore and wire regions.* ***(f)-(i)*** *AFM scans associated with two different $A_{\Delta f}$ values, marked by dotted lines in (e), showing the atomic contrast of the h-BN lattice on pore [(f) and (g)] and wire regions [(h) and (i)]. Scan areas in (f)-(i) are $1\,\mathrm{nm} \times 1\,\mathrm{nm}$. For better comparability across images we use relative Δf scales, Δf^{rel} , where the lowest Δf value in each image amounts to $0\,\mathrm{Hz}$. All images were acquired with $0\,\mathrm{V}$ bias and at $5\,\mathrm{K}$.*

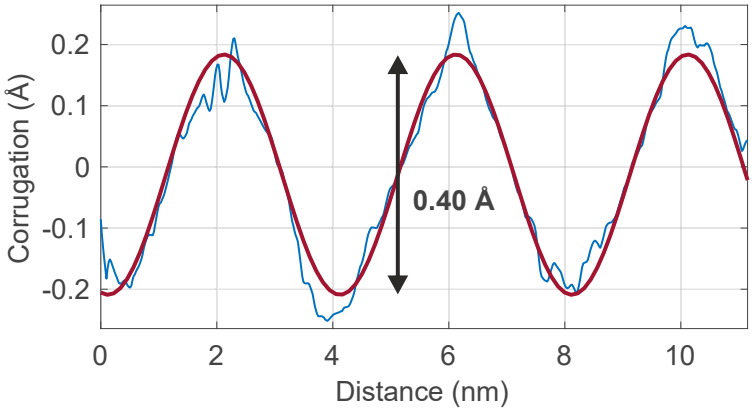

Figure 4.3: *Line profile (blue curve) extracted from a trace in the calculated height map of h-BN/Cu(111) shown in Figure 4.2. The sinusoidal fit (red curve) indicates a peak-to-peak amplitude of* 0.40 Å.

h-BN layer we employed a method in which we calibrate the variation of the atomic contrast as a function of the tip height z (see section 4.1.1). We define the atomic contrast by the Δf difference between the darkest and the brightest regions at the length scale of a *h*-BN unit cell, expressed as Δf amplitude $A_{\Delta f}(z)$. Figure 4.2b and e show $A_{\Delta f}$ derived from constant-height scans for a series of tip heights on wire and pore regions. Selected slices are shown in Figure 4.2f,g (pore) and Figure 4.2h,i (wire) as well as in Figure C.3. The obtained calibrations, $A_{\Delta f,W}$ and $A_{\Delta f,P}$, appear linear over a range of about 1 Å for both, wire and pore regions exhibiting similar slopes.

An averaged calibration curve (solid line in Figure 4.2b and e) correlates the Δf amplitude $A_{\Delta f}$ to a tip-sample distance $\Delta d_{tip-sample}$, *i.e.* $A_{\Delta f} \propto d_{tip-sample}$, allowing us to convert the atomic contrast in the large-scale constant-height image (Figure 4.2a) into a relative height map, $z_{calc}(A_{\Delta f})$, representing the geometric corrugation shown in Figure 4.2c. A clear corrugation is observed, closely resembling the *h*-BN moiré pattern, where the pores are lower than the wire regions. A height distribution histogram of the marked moiré unit cell is plotted in Figure 4.2d and reveals a total width of 0.64 Å. In analogy to the $\mu \pm 2\sigma$ ($\pm 1\sigma$) intervals used for Gaussian distributions, we calculated the height range encompassing 95 % (68 %) of the values to be 0.50 Å (0.26 Å). A sinusoidal fit to representative height profiles yields a peak-to-peak amplitude of 0.40 Å (Figure 4.3). Our DFT calculations (see Table C.1) indicate a height difference of 0.24 to 0.27 Å between high-symmetry sites of the *h*-BN unit cell, which show the same trend as our experimental results but underestimate the magnitude.

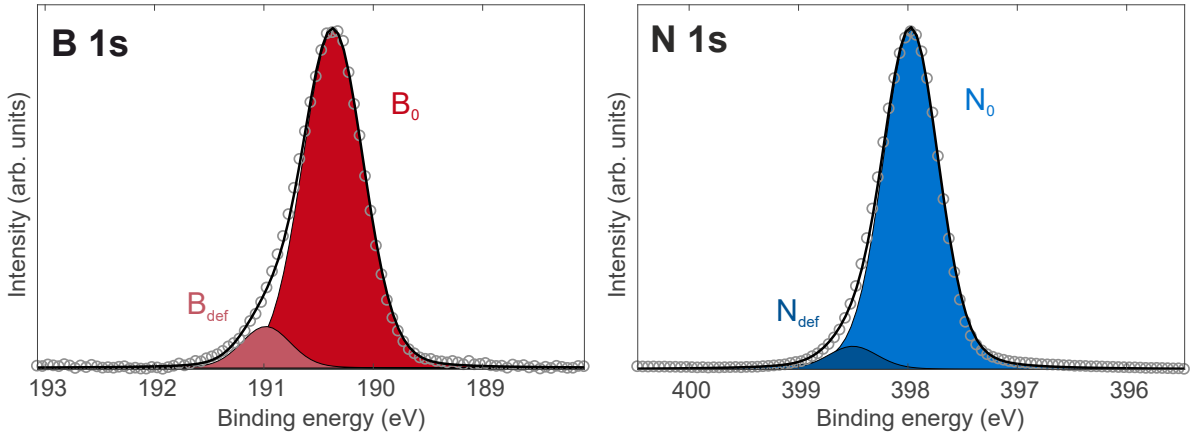

Figure 4.4: *High-resolution soft XPS N 1s and B 1s spectra for a single layer of h-BN/Cu(111). A Shirley background was subtracted from the data. The colored areas are fits of the indicated components. Solid black line is the sum of the fits. A photon energy of* 641 eV *was used for all spectra.*

4.1.3.2 Mean Adsorption Height

High-resolution soft X-ray core-level spectra of *h*-BN/Cu(111) are displayed in Figure 4.4. Both B 1*s* and N 1*s* spectra are asymmetric with a characteristic shoulder at high binding energies.[Sie17, Orl14, Pre05, Pre07b] This shoulder results from a clearly separate chemical species, and cannot be explained as a loss feature, as a distinct absorption profile was observed in the XSW measurements described below, which indicates significantly different adsorption heights for the two species. Therefore, we model the B 1*s* and N 1*s* spectra with two distinct components [B_0 (N_0) and B_{def} (N_{def}), see section C.0.1 for details], whose parameters are summarized in Table 4.1. The primary B 1*s*/N 1*s* species (B_0/N_0, respectively) is assigned to the *h*-BN layer and the B 1*s*/ N 1*s* shoulder (B_{def}/N_{def}, respectively) is assigned to defective, polymeric components[Koe16] where the local B:N stoichiometry is no longer 1:1. This assignment is justified below. The binding energy difference between B_0 (N_0) and B_{def} (N_{def}) was found to be 0.6 eV (0.5 eV) (respectively).

	E_{b0} (eV)	Γ (eV)	σ (eV)
B_0	190.4	0.08	0.52
B_{def}	191.0	0.08	0.42
N_0	398.0	0.11	0.46
N_{def}	398.5	0.11	0.40

Table 4.1: *Soft XPS parameters: Peak position E_{b0}, Lorentzian width Γ and Gaussian width σ obtained from the fits for the indicated components. Voigt line shapes are used for the curve-fitting of the B 1s and N 1s core-level spectra.*

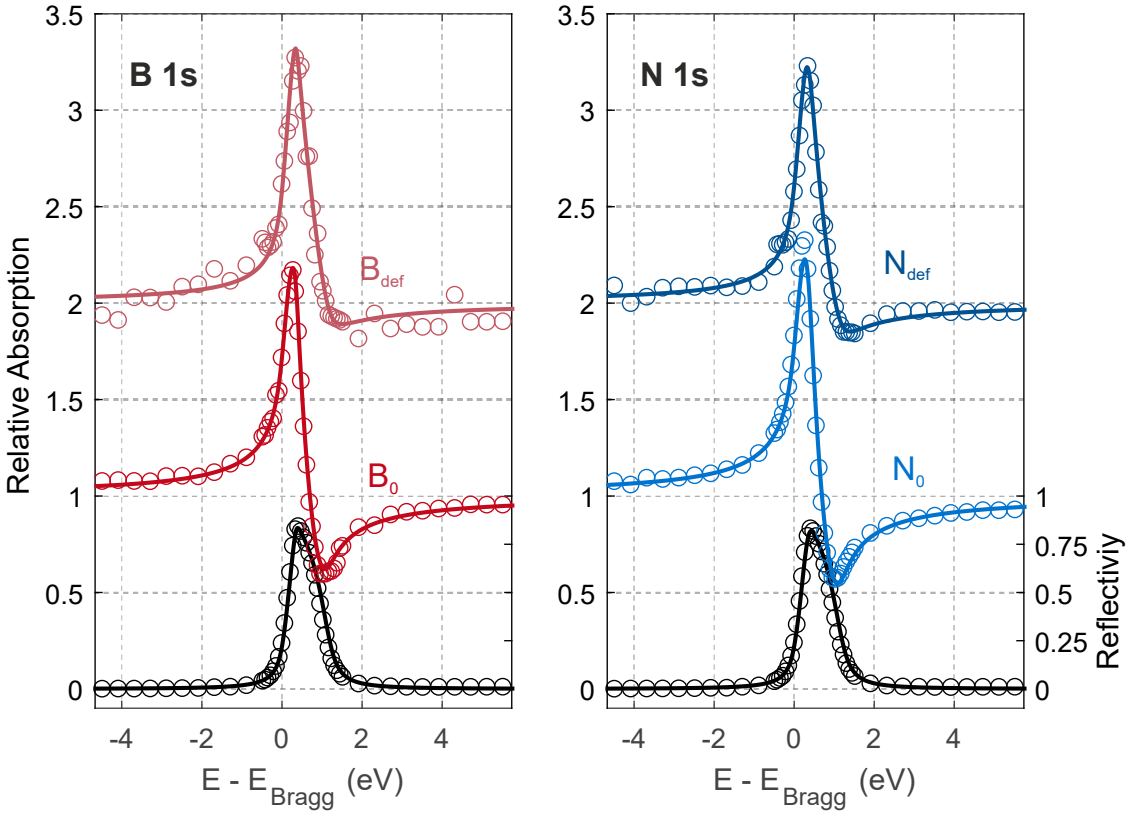

Figure 4.5: *X-ray standing wave absorption profiles of B1s (red) and N1s (blue) for a single layer of h-BN/Cu(111). Solid lines are fits to the data. Black data points correspond to the Cu(111) reflectivity curve. The XSW profiles of the defective h-BN components B_{def} and N_{def} are offset vertically +1 for clarity.*

The mean adsorption height of *h*-BN on Cu(111) is obtained unambiguously through XSW analysis (see section 2.3 for details) yielding two fitting parameters: the coherent position (p^H) and the coherent fraction (f^H). In simplistic terms, the former can be interpreted as the average position of a chemical species relative to the extended bulk Bragg planes in units of d_H and the latter is related to the distribution of these positions, through disorder (*e.g.* amorphous regions), a static variation (*e.g.* multiple adsorption sites), or a dynamic one (*e.g.* thermal vibrations). In particular, f^H can only take values between 0 and 1, and has contributions from the ordered fraction (C), a geometric factor (a_H) and the Debye-Waller factor (D_H) such that:

$$f^H = C \cdot a_H \cdot D_H, \tag{4.1}$$

which model, respectively, the level of order, the static geometric distribution, and the dynamic geometric distribution. For adsorbates with low atomic numbers, the Debye-Waller factor alone is typically around 0.9 at room temperature.

	Main components			Defective components		
	p^{111}	Adsorption height $\overline{h}_0$(Å)	f^{111}	p^{111}	Adsorption height $\overline{h}_{def}$(Å)	f^{111}
B 1s	0.63 ± 0.02	3.39 ± 0.04	0.65 ± 0.03	0.56 ± 0.04	3.26 ± 0.09	0.34 ± 0.07
N 1s	0.62 ± 0.02	3.37 ± 0.04	0.71 ± 0.02	0.58 ± 0.03	3.30 ± 0.06	0.40 ± 0.03

Table 4.2: *Structural parameters obtained from XSW measurements. Summary of the structural parameters obtained from the XSW measurement shown in Figure 4.5: coherent position p^{111}, the corresponding adsorption height of the h-BN layer on Cu(111), and coherent fraction f^{111} for both chemical species B_0/N_0 and B_{def}/N_{def}.*

The result of our Cu(111) XSW analysis, utilizing the B 1s and N 1s core levels, is displayed in Figure 4.5 for B_0, B_{def}, N_0, and N_{def}. The absorption profiles of N_0 and B_0 show pronounced standing wave modulations with nearly identical shapes, indicating that the mean height is the same for both species; N_{def} and B_{def} exhibit a small but noticeable shift of their maxima and minima, with respect to N_0 and B_0, toward a higher photon energy and a slight reduction of the modulation amplitudes, indicating a lower adsorption height and a greater spread in positions for these minority species. The coherent positions and fractions deduced from the XSW analysis for all four chemical species are summarized in Table 4.2.

Assuming a bulk terminated Cu(111) surface the average adsorption height, $\overline{h}$, is related to p^{111} as $\overline{h} = (p^{111} + n) \cdot d_{111}$, where the integer n accounts for the periodic nature of the standing wave field. As the d_{111} spacing for Cu(111) is 2.087 Å[Pat89] and with the measured values for p^{111} (shown in Table 4.2), it can be easily verified that only $n = 1$ renders physically reasonable values for $\overline{h}$. Thus, the average adsorption heights are determined to be $\overline{h}_0 = 3.37 \pm 0.04$ Å (3.39 ± 0.04 Å) for the main component N_0 (B_0) and $\overline{h}_{def} = 3.30 \pm 0.06$ Å (3.26 ± 0.09 Å) for the defective component N_{def} (B_{def}). Furthermore, our analysis reveals a f^{111} of 0.71 ± 0.02 (0.65 ± 0.03) for N_0 (B_0), which is significantly lower than the value expected for a perfectly flat h-BN layer ($f^H \sim 0.9$), and a further reduced f^{111} of 0.34 ± 0.07 (0.40 ± 0.03) for N_{def} (B_{def}).

4.1.4 Discussion

The XPS binding energies of the main B 1s and N 1s components (B_0: 190.4 eV, N_0: 398.0 eV) are in very good agreement with previous studies of h-BN/Cu(111).[Pre05] These values are characteristic for physisorbed systems, midway between the ones of h-BN/Au (189.8 eV and 397.6 eV) and the ones of h-BN/Ag(111) (190.8 eV and 398.3 eV).[Mül10, Usa10] The XP core-level spectra of B 1s and N 1s are asymmetric with a shoulder at high binding energies and both 1s levels are best described by two Voigt functions, rather than an asymmetrical

line shape (*e.g.* Doniach-Šunjić). This assignment is in contrast to previous publications on the *h*-BN/Cu(111) system,[Pre05] where an asymmetrical peak shape has also been observed but the peaks were modeled with a single component. In the *h*-BN/Ir(111) system[Zum16] the asymmetrical line shape was assigned to the presence of "strongly" and "weakly" bound regions of the *h*-BN layer. This was justified by the XSW measurements indicating that the minority component was adsorbed 1.5 Å closer to the substrate than the majority component. However, the difference in adsorption height of the two components in *h*-BN/Cu(111) is only ∼0.1 Å (15 times smaller than on Ir), but yet the binding energy shifts observed, ∼0.5 eV / 0.6 eV, are comparable in magnitude to those observed for *h*-BN on Ir(111) (0.8 eV / 0.9 eV). It is highly improbable that such a large binding energy difference could originate from such a minor difference in adsorption height. In fact, the XPS binding energies of the N 1*s* and B 1*s* core-levels, in *h*-BN/Cu(111) and *h*-BN/Ir(111) are remarkably similar, despite the difference in substrate, interaction strength, corrugation and adsorption height. Finally, DFT calculations (see Table C.1) reveal only a modest N 1*s* binding energy variation between the weakly bound wire regions and the more strongly bound pore regions, that is too small to explain the difference observed in our combined XPS-XSW analysis. Therefore, it is inferred that the two components are inherently chemically different, and do not arise from a geometric corrugation in the layer. Effects of wrinkles within the layer and from step edges, domain boundaries and edge terminations as the possible origin are also excluded due to their low abundance. Potentially, there could be a chemical difference between the *h*-BN domains mostly aligned azimuthally along the $\langle 1\bar{1}0 \rangle$ symmetry directions of the substrate surface and the domains mostly aligned along the $\langle 11\bar{2} \rangle$ directions. It is clear from the recorded LEED pattern (Figure 4.1b) that the *h*-BN domains that align mostly along the $\langle 11\bar{2} \rangle$ results in smaller or fewer islands, however, there is no indication, from the STM images (Figure 4.1c and d), of the $\langle 11\bar{2} \rangle$ aligned islands being rougher than the $\langle 1\bar{1}0 \rangle$ aligned islands, as the lower coherent fraction observed for N_{def}/B_{def} would suggest. Further, our DFT calculations suggest that no significant change in the mean adsorption height of the rotated *h*-BN domains would be expected. The significant difference between B_0:B_{def} and N_0:N_{def} ratios (10:1 and 16:1, respectively) would further rule out the possibility that the minor components represent a different crystalline *h*-BN layer. Occasionally, in the STM images, inhomogeneous *h*-BN moiré patches formed by strain, were observed, which could potentially result in chemically different atomic species.[Nee13] They were, however, not observed frequently enough to solely account for the observed B_0:B_{def} and N_0:N_{def} ratios. Instead, the more likely origin of these components are molecular polymeric fragments,[Koe16] constrained inside triangular shaped holes that are found occasionally on the substrate (Figure 4.1a). As atomic nitrogen desorbs from Cu(111) at around 750 K,[Ber92] whereas atomic B melts into the Cu(111) substrate,[Pre05, Sch17b] a stoichiometric B:N deficiency in these fragments might exist,

however, this deficiency results in a lowered binding energy for boron.[Pre05] Conversely, assuming these polymeric fragments to be stoichiometrically abundant, presumably leading to the formation of sp^3 bonds, a significant shift toward a higher binding energy can be rationalized.[Koe16] In agreement with recently published calculations on defective *h*-BN nanosheets,[Gao16] we find that the defective components are closer to the copper substrate. Finally, as there is likely a continuum of such polymeric fragments (*e.g.* polyaminoborane, polyiminoborane, polyaminoborazine *etc.*), as can be observed in the mixture of species present in the triangular shaped holes in the STM images, the origin of the dramatically lower coherent fractions also becomes clear.

Based on these considerations, we focus on the majority *h*-BN species on Cu(111) and we show that combined AFM and XSW measurements yield a consistent picture regarding the geometric structure of the *h*-BN layer. Our AFM analysis displays measurable differences in the adsorption heights of the wire and pore regions. Regarding the validity of the experimentally determined corrugation of the *h*-BN layer *via* AFM analysis of the atomic contrast, two questions need to be investigated: (i) how is the atomic contrast influenced by tip-sample interactions that can be different for the wire and pore regions, and (ii) what is the influence of the AFM tip on the *h*-BN layer? To shed light on the first question, let us consider a hypothetical layer that exhibits a geometric corrugation and is composed of entities that show exactly the same tip-sample interaction across the whole layer. Here, the measurement of the Δf amplitude versus tip height would yield calibration curves that exhibit exactly the same z-dependence, but are offset along the z-axis, reflecting the geometric corrugation. This is the behavior that is observed in our experiments. In particular, it can be seen that the z-dependence of the local Δf amplitude is almost the same for the respective wire and pore regions in the two measurement series shown in Figure 4.2. These series were performed on different areas of the surface with different tip configurations. Thus, the calibration curves may vary from experiment to experiment, but, importantly the wire and pore regions exhibit similar characteristics. However, we want to point out that, particularly in the experiment corresponding to the data shown in Figures 4.2a-d, small differences can be seen in the z-dependence of the local Δf amplitude for wire and pore. Apart from a slight difference in the slope of the calibration curves, the deviation from the near-linear regime at close tip sample-distances sets in earlier on the pore areas, *i.e.* at lower local Δf amplitudes (Figure 4.2b). These differences are much less pronounced in the second measurement series (Figures 4.2e-i). Here, the z-dependence of the local Δf amplitude is almost identical for wire and pore areas. The height distributions derived from both measurement series are comparable, suggesting that the slight differences between the wire and pore regions do not substantially affect the results. Further evidence supporting that the local Δf amplitude is a useful measure for the tip-sample distance comes from the atomic features in the calibration

scans: AFM scans corresponding to local Δf amplitudes of $A_{\Delta f} \approx 6\,\mathrm{Hz}$ (Figures 4.2f, h) and $A_{\Delta f} \approx 3\,\mathrm{Hz}$ (Figures 4.2g, i) are shown for both wire and pore regions. Note, that in order to obtain the same $A_{\Delta f}$ for the respective regions, the tip height has to be lowered by $\sim$0.4 Å on the pore regions. The images in Figures 4.2g and i ($A_{\Delta f} \approx 3\,\mathrm{Hz}$) show a hexagonal lattice with a honeycomb-like appearance which develops into a rather triangular appearance at higher $A_{\Delta f}$ in Figures 4.2f and h ($A_{\Delta f} \approx 6\,\mathrm{Hz}$). The measurements reveal that the Δf amplitude is correlated with the (asymmetric) features in the atomic contrast, which can be assumed to reflect the tip-sample distance. To estimate the influence of the tip on the measurements, we analyzed the dissipation in the AFM experiments. Upon decrease of the tip-sample distance, the dissipation increases by up to 10% in the linear regime in the calibration curves. For the closest tip-sample distances the dissipation channel shows a pronounced contrast that correlates with the *h*-BN lattice (see Figure C.4). A noticeable change in dissipation hints at the tip exhibiting an influence on the *h*-BN layer, presumably a geometric distortion as discussed in literature.[Vol13, La 16, Her14, Oya06, Kan04, Tre07, Pis15] However, the similarity of the *z*-dependence of the local Δf amplitude, as well as of the atomic features in the AFM images, suggest that the influence of the tip on wire and pore regions is comparable. Based on these considerations, it is justified to assume that in our experiments, the local Δf amplitude can be directly correlated with relative height differences.

The XSW measurement yields an average adsorption height of the *h*-BN layer of $\overline{h}_0 = 3.38 \pm 0.06$ Å with boron and nitrogen sitting effectively at the same height as expected for a weakly interacting, physisorbed two-dimensional network. Within the uncertainties, the adsorption height is comparable to the bulk *h*-BN interlayer spacing (3.33 Å) at room temperature.[Pea52] The coherent fractions of 0.71 for N 1*s* and 0.65 for B 1*s* suggest a variation in the adsorption height arising from a combination of the effects of an imperfect crystallinity of the *h*-BN layer and the geometric corrugation of the crystalline *h*-BN layer in addition to thermal vibrations of the B and N atoms. Vibrational amplitudes can be estimated using the Debye temperature of Cu ($\sim$320 K at room temperature)[Fli61] and bulk *h*-BN ($\sim$410 K at room temperature),[Pea52] which results in a root mean square (rms) vibrational amplitude of $\sim$0.08 Å and $\sim$0.15 Å, respectively. If these two vibrations are uncoupled, then the net rms vibrational amplitude of the *h*-BN layer will be $\sim$0.17 Å. These values result in a Debye-Waller factor of 0.88 and thus, cannot be used to solely explain the significantly lower coherent fractions observed here. Indeed, in addition to this dynamic distribution of positions, in order to model a coherent fraction of $\sim$0.7, a static distribution is also required. Based on the experimentally observed high quality of the sample, it is unlikely that the noncrystalline areas of the *h*-BN layer (*e.g.* at step edges on the Cu(111) surface, at domain boundaries between different rotations of the *h*-BN layer, *etc.*) are sufficient enough in size to result in an ordered fraction that differs significantly from 1. If the ordered

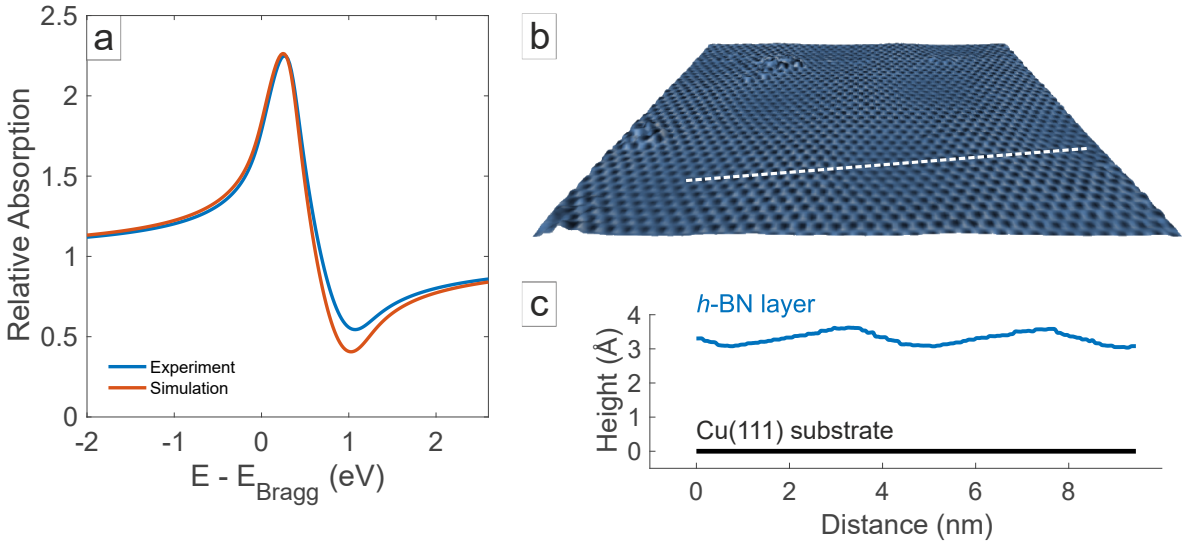

Figure 4.6: ***(a)*** *Comparison between the experimental (blue line) and a simulated (orange line) XSW absorption profile. For the simulation, the height distribution obtained from our AFM measurements was utilized.* ***(b)*** *3D representation of the calculated height map z_{calc} overlaid with the corresponding high-pass filtered Δf image showing the corrugation of the h-BN layer on Cu(111) relative to its lateral dimension. Size:* $10\,\text{nm} \times 10\,\text{nm}$. ***(c)*** *Illustration of the h-BN/Cu(111) corrugation relative to its adsorption height. The h-BN layer is displayed as line profile extracted from the calculated height map z_{calc} as indicated in the 3D plot in (c) (white dashed line).*

fraction is effectively unity, and the Debye-Waller factor is 0.88, then, by Eq. (4.1), the geometric factor must be in the order of 0.8. As the various orientations of the *h*-BN layer are predicted (by DFT) to adsorb at effectively the same height, the most likely explanation for such a geometric factor is a corrugation in the *h*-BN layer. If either a Gaussian or an uniform height distribution is used to model such a geometric factor of the *h*-BN layer, then a corrugation with a 2σ of 0.45 Å or a total width of 0.75 Å, respectively, is required (see Figure C.5). The height distribution, obtained *via* AFM measurements of the atomic contrast (Figure 4.2d), indicates a total width of 0.64 Å and a geometric factor of 0.92. Using this geometric factor, combined with the above Debye-Waller factor, a coherent fraction of 0.81 is obtained (compared to 0.71 ± 0.02 and 0.65 ± 0.03, for B and N atoms, respectively). The resulting profile, shown in Figure 4.6a (orange curve), is in remarkably good agreement with the experiment (blue curve), and the remaining difference can now likely be explained by the various effects discounted above: *e.g.* noncrystalline areas of the *h*-BN layer, step edges, *etc.* Therefore, we can conclude that the coherent fraction, extracted for the majority species of the *h*-BN on Cu(111), results from a highly crystalline *h*-BN layer with a peak-to-peak geometric corrugation in the order of ∼0.6 Å. To illustrate this corrugation and its scale, Figure 4.6b shows a 3D plot of the calculated height map $z_{calc}(A_{\Delta f})$ and Figure 4.6c

a cross-section of the same height map in comparison to the adsorption height of the *h*-BN layer above the Cu(111) substrate. The geometric corrugation in the *h*-BN layer, which is already smaller than the atomic radii of either element, is spread over a length scale of nanometers, such that neighboring atoms are effectively coplanar. Nevertheless, in this weakly interacting system, the corrugation amounts to a significant fraction, about 10-20%, of the mean adsorption height. Based on our DFT calculations in the (1×1) cell at different lateral registries, we expect the corrugation of the terminal Cu layer under the *h*-BN to be below 0.002 Å, *i.e.* the Cu substrate is considered to be planar (Figure 4.6c).

It should be noted, that another structural analysis of *h*-BN on Cu(111) has been published recently by the Sokolowski group.[Brü17] They investigated the interface by means of high-resolution LEED and XSW, and report an adsorption height of 3.25 ± 0.02 Å and 3.22 ± 0.03 Å for B and N atoms, respectively, slightly reduced compared to our results. However, in contrast to our study, they claim that a vertical buckling of the *h*-BN layer can be excluded based on their diffraction data, although the obtained coherent fractions in the XSW measurements indicate a quite significant corrugation (peak-to-peak amplitude of 0.7 Å[Brü17]), which would agree very well with our results. Moreover, the dramatic difference in coherent fraction between boron ($f^{111} = 0.57$) and nitrogen ($f^{111} = 0.80$) in their measurements should be considered critically, as this indicates a minor (or at least a different) *h*-BN layer quality compared to our experiments. It should be mentioned that both evaluations of the respective XSW data are solid, as they could be reproduced by the other group.

Before concluding, we briefly discuss our findings in relation to the previous report on *h*-BN/Cu(111).[Jos12, Jos17] As the electronic interface state was observed in any region below the *h*-BN, we ruled out strong spatially localized *h*-BN–Cu interactions and thus a major geometric corrugation.[Jos12, Jos17] This interpretation is consistent with our present findings, where the *h*-BN–Cu separation exceeds 2.9 Å in any region (Figure 4.6c). Our previous DFT results yielded a corrugation of 0.16 Å and 0.04 Å for a moiré supercell and a 1×1 structure, respectively. We thus considered the *h*-BN overlayer to be topographically smooth.[Jos12, Jos17] In view of our present experiments and the refined DFT modeling, this assignment was not precise. Even though moderate corrugations with amplitudes much smaller than the nanometer-scale moiré periodicity in sp^2 layers are often considered negligible,[Sac11] we now recognize – and emphasize – the nonplanar nature of *h*-BN on Cu(111). At first sight, the combination of a large mean adsorption height reminiscent of the bulk *h*-BN layer separation with a relevant electronic and geometric modulation seems puzzling. However, we would like to point out that even surfaces of single-crystal *h*-BN flakes are not imaged as perfectly planar by AFM[Dea10] and considerable stacking-induced electronic modifications are described in bilayer *h*-BN or sp^2 heterostructures.[Lin13, Mar10a]

It is intriguing to envision *h*-BN morphologies in surface-supported sheets reminiscent of nonplanar distortions anticipated for free-standing sp^2 sheets.

4.2 *h*-BN on Ag(111)

In recent years, silver has come up as a promising platform for the synthesis of atomically thin materials after the growth of silicene has been proposed,[Vog12] which presents potential advantages for future device applications.[Tao15] The synthesis and investigation of other 2D materials on Ag(111) at the atomic scale opens up new possibilities to design 2D heterostructures that can provide new fundamental physics and an improved flexibility to realize devices.[Gei13] As an initial step for these potential applications, a reliable synthesis of single- and few-layer 2D materials becomes crucial. In particular, the CVD technique has been used to fabricate ultra-thin *h*-BN sheets on highly reactive metals like Ru, Rh, Ir, Co, Ni, Pt and Pd.[Auw99, Gam97, Pre08, Var09, Mur10] However, the low catalytic activity of noble metals impairs the growth of *h*-BN [Mül10, Cam14] by standard CVD procedures.

The pertaining interfaces are of great interest and importance. One can classify them depending on the interaction strength between the 2D layer and the metal.[Pre08] Silver is considered a weakly interacting system where the electronic properties of both, the 2D layer and the silver substrate would remain practically unperturbed. In particular, a unique feature of the close-packed surfaces of noble metals is the presence of a surface state with nearly free electron-like properties. STM (see section 2.1) proved to be a perfect probe of these states, which are confined in perpendicular direction to the surfaces. Relevant and quantitative information can be extracted from the study of the evolution and modification of these states by the adsorption of gases,[Par00, For03, Höv01] molecules,[Zir09, Pen07, Tem06, Kan15, Roj12] ionic films,[Rep04b], and 2D honeycomb layers.[Hol15, Jol15, Lei14] On the other hand, STS has been exploited to investigate the unoccupied states of ultra-thin layers on metals, in particular, the image potential states.[Bor10, Hol15, Jos12, Sch14b] They are bound to a solid by the response of the substrate to the presence of the electron and kept outside the surface by the reflective properties of the substrate. Experimentally, one can access these states in the field-emission regime by STS and they are thus known as field emission resonances (FERs).[Bin85] The evolution of the FERs can provide quantitative information on changes in the local electrostatic surface potential, which manifests as local work function variation. In this section, we present an investigation of the modification of the surface state on the (111) face of a silver crystal after the growth of *h*-BN yielding information about the interface. We track back the modification of the Shockley-type surface state to local work function modifications (“push-back“ effect) upon the formation of the 2D layer.

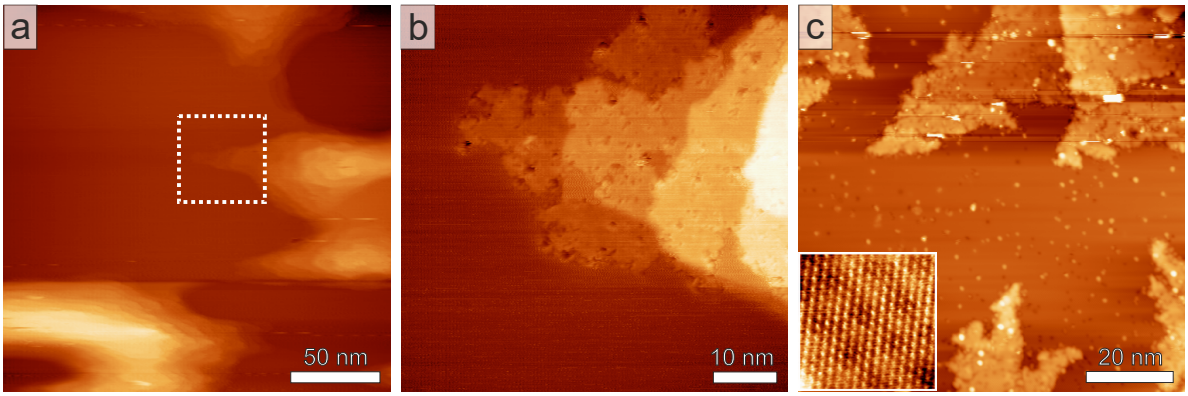

Figure 4.7: *STM images of h-BN/Ag(111). **(a)** Large-scale STM image acquired at 300 K reveals an array of substrate step edges ($U_b = 1.5\,\mathrm{V}$, $I_t = 0.45\,\mathrm{nA}$). A close-up view of the marked region is shown in panel **(b)**: The h-BN islands growth proceeds across the step edges protecting the underlying silver layers. $U_b = -1.0\,\mathrm{V}$, $I_t = 1.4\,\mathrm{nA}$. **(c)** STM image acquired at 5 K showing the tree-shaped h-BN islands ($U_b = 1.0\,\mathrm{V}$, $I_t = 2\,\mathrm{nA}$). The inset shows an atomically resolved STM image of the h-BN. The periodic electronic modulation of the moiré superstructure is faintly visible.*

Experimental Methods

The experiments were performed in both the LT-STM and the XPS-STM setup (see section 3). The base pressure was below $<5 \times 10^{-10}$ mbar. All STM images were taken in constant-current mode and the differential conductance ($\mathrm{d}I/\mathrm{d}V$) spectra were recorded at 5 K using a lock-in amplifier ($f = 969\,\mathrm{Hz}$, $\Delta V_{rms} = 18\,\mathrm{mV}$). We measured the FERs with the feedback loop connected at a current setpoint of 0.8 nA.

4.2.1 Growth

Sub-monolayer coverages of *h*-BN were prepared by thermal decomposition of borazine ($B_3N_3H_6$) assisted by an ion gun. The ion gun used in the classic surface preparation in UHV is utilized to create a beam of ionized precursors, which is accelerated toward the hot sample.[Mar11] This procedure enhances the thermal decomposition of the precursor compared to a normal CVD procedure and allows us to grow patches of *h*-BN even at moderate substrate temperatures. Figure 4.7 shows STM images recorded after exposing the Ag substrate at 900 K to 2700 L of borazine using an acceleration voltage of 300 eV. The STM image displayed in Figure 4.7a reveals several arrays of substrate steps. A close-up view (Figure 4.7b) displays that the *h*-BN islands growth proceeds across the step edges and presumably protects the underlaying Ag substrate layers from evaporation during the growth at the utilized elevated substrate temperature. The structural quality of the *h*-BN islands is highlighted by the inset of Figure 4.7c. At this particular set point, the atomic corrugation

of the 2D layer is superimposed by a periodic superstructure (moiré pattern). The lateral periodicity of the moiré is 1 nm with a small apparent corrugation of less than 10 pm, independent of the bias voltage. Even if this is the most common moiré superstructure for our samples, the presence of several rotational domains due to the weak interaction between *h*-BN and silver has previously been reported.[Mül10] We infer that the *h*-BN island growth is rather slow compared to the evaporation rate of the silver impairing the formation of large-scale *h*-BN layers on Ag(111).

The as-grown *h*-BN/Ag(111) was further characterized by different surface science techniques. Through STS (see section 4.2.2), the surface state was probed yielding information about the adsorption energy of the *h*-BN layer, whereas the analysis of the field emission resonances (FERs) shed light on the work function and thus on the interface charge transfer. Moreover, XPS measurements (see section 4.2.2) gave an indication of the chemical state of the B and N atoms. The experimental characterization is complemented by DFT calculations providing information about the band structure of *h*-BN/Ag(111) (see section 4.2.3).

4.2.2 Spectroscopic Characterization

To get further insight into the interaction between the 2D layers and the metallic substrate, we performed STS measurements. Figure 4.8a shows an STM image of the interface between *h*-BN and Ag(111). The spectrum displayed in Figure 4.8c measured around the Fermi level on Ag(111) (green line) shows the classic step-like feature in agreement with earlier findings.[Li98, Kli00] This step corresponds to an increased local density of states (LDOS) due to the presence of the two-dimensional surface state of silver. For the *h*-BN areas (blue line) the onset of the surface state is up-shifted by 119 mV compared to the bare Ag(111). It also presents some structure due to the scattering at the boundaries of the *h*-BN island. Instead of a smooth shift of the surface resonance going from the bare Ag(111) to the 2D layer, the transition is abrupt and the surface state vanishes in the vicinity of the step edge (see Figure C.9).

Further, a change in the local work function upon adsorption of the *h*-BN is observed. Figure 4.8e shows the evolution of the FERs on the *h*-BN/Ag(111) system where a clear shift between Ag(111) and *h*-BN areas is discernible. A very similar behavior has already been observed for *h*-BN on other metals,[Jos12, Sch14b] however, in these cases, the moiré provides a corrugated potential. The local work function of the surface was determined by fitting the energy positions of the FERs (see Figure 4.9) following the Gundlach expression.[Gun66, Coo88] Figure 4.9c shows a 2D color plot of $\mathrm{d}I/\mathrm{d}V$ spectra taken along the line in Figure 4.9a. Each vertical line in this plot corresponds to one spectrum taken at one point of the line in the topographical image. The FERs appear as bright features in these plots. Clearly, a

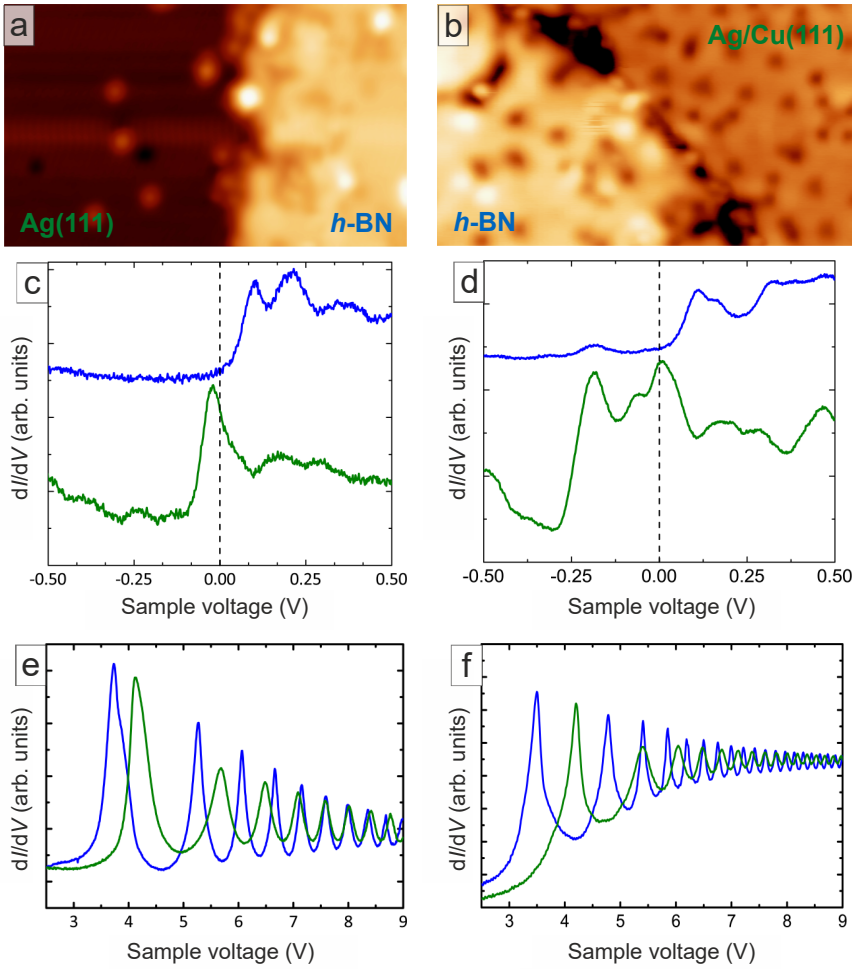

Figure 4.8: *STM images of* ***(a)*** *h-BN/Ag(111) ($U_b = 1.0\,\mathrm{V}$, $I_t = 0.8\,\mathrm{nA}$) and* ***(b)*** *h-BN/Ag/Cu(111) ($U_b = 0.5\,\mathrm{V}$, $I_t = 0.1\,\mathrm{nA}$). Individual dI/dV curves* ***(c)*** *around the Fermi level and* ***(e)*** *in the field emission regime measured on bare Ag(111) (green) and h-BN/Ag (blue) areas. Individual dI/dV curves* ***(d)*** *around the Fermi level and* ***(f)*** *in the field emission regime measured on Ag/Cu(111) (green) and h-BN/Ag/Cu(111) (blue) areas.*

shift toward lower energies and a variation of peak positions is observed on the *h*-BN island. Figure 4.9g shows the work functions extracted from the fits of all individual $\mathrm{d}I/\mathrm{d}V$ spectra (Figure 4.9e) using the Gundlach equation:

$$E_n = \Phi + \alpha\,(n - 1/4)^{2/3}\,F^{2/3} \tag{4.2}$$

Note that the energy of the low order FER peak(s) typically deviate from the linear fit due to the additional image potential, which changes the shape of the tunneling barrier and thus both, the tunneling current and the energy position of $\mathrm{d}I/\mathrm{d}V$ oscillations[Kol00] for the first resonance(s).[Coo88, Pau10] Therefore, the gray data points in Figures 4.9e,f are excluded from the fits. This fit works well on the metal and on the *h*-BN sheet but fails in

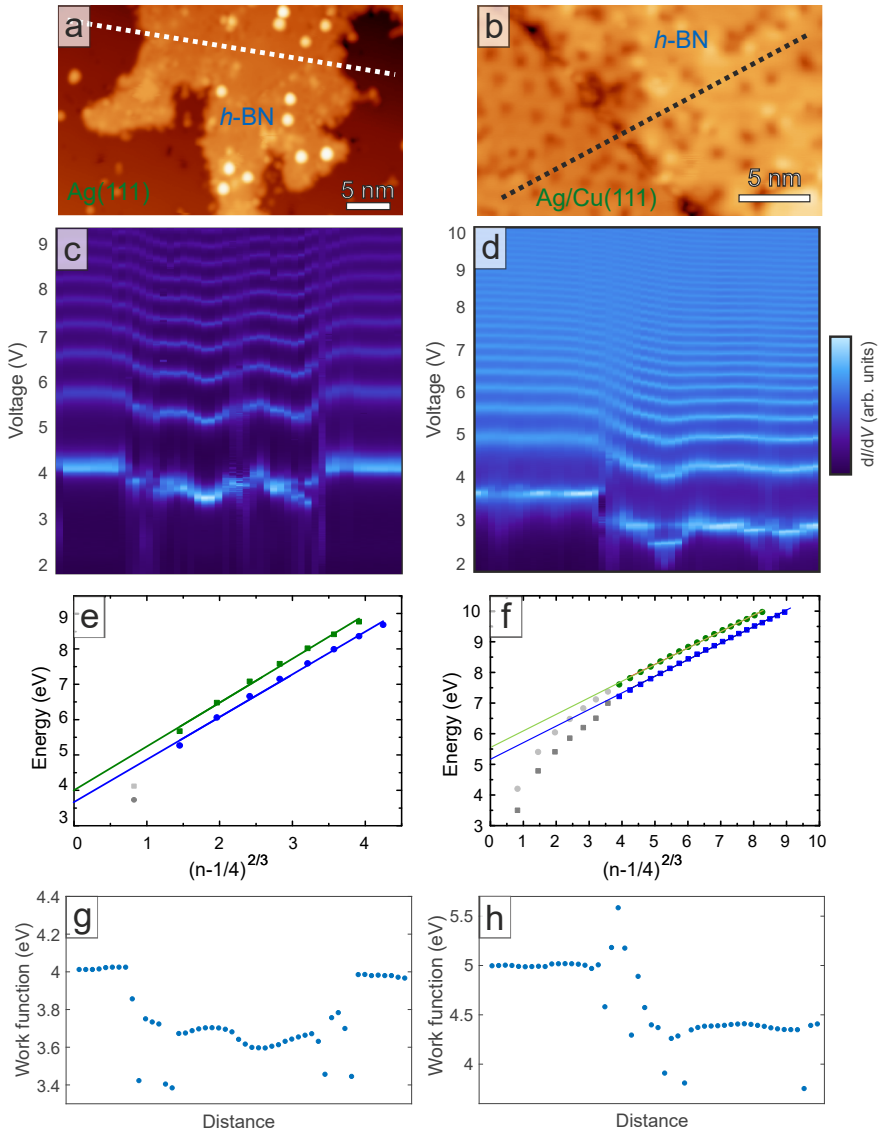

Figure 4.9: *Field emission resonances. STM images of* ***(a)*** *h-BN on Ag(111) ($U_b = 1.0\,\mathrm{V}$, $I_t = 0.8\,\mathrm{nA}$) and* ***(b)*** *3 ML of Ag intercalated on h-BN on Cu(111) ($U_b = 0.5\,\mathrm{V}$, $I_t = 0.1\,\mathrm{nA}$).* ***(c)*** *and* ***(d)*** *Corresponding color-coded dI/dV maps measured along the line marked in (a) and (b).* ***(e)*** *and* ***(f)*** *Exemplary fits of individual dI/dV spectra on h-BN (blue line) and silver (green line). Gray data points are excluded from the fit.* ***(g)*** *and* ***(h)*** *Plot of the resulting work function for the spectra along the line in (a) and (b).*

the transition regime because of inhomogeneities. Figure 4.9e shows an exemplary fit for one spectrum on the metal (green) and one spectrum on the *h*-BN (blue). The work function, reflected by the energy where the fit intersects with the energy axis, is decreased by ∼0.35 eV upon formation of the *h*-BN layer on Ag(111) (Figure 4.9g).

Figure 4.10 displays XP spectra of *h*-BN/Ag(111). The binding energy of the B 1*s* (N 1*s*) core level is found to be $E_b = 191.0\,\mathrm{eV}$ ($E_b = 398.5\,\mathrm{eV}$). Both energies are in good agreement with the values reported by Müller *et al.* ($E_b = 190.8\,\mathrm{eV}$ and $E_b = 398.3\,\mathrm{eV}$,

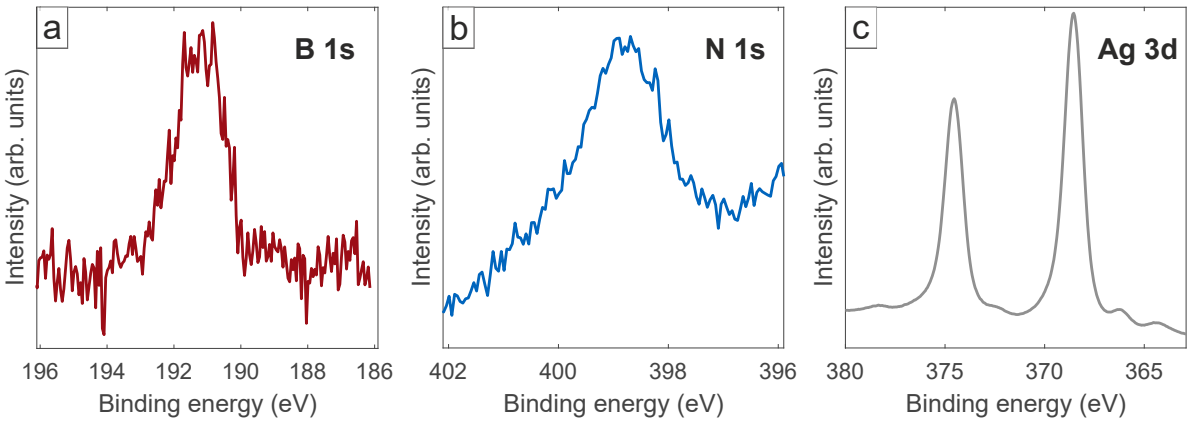

Figure 4.10: *The XP spectra of h-BN/Ag(111) comprising the* ***(a)*** *B 1s core level (E_b = 191.0 eV), the* ***(b)*** *N 1s core level (E_b = 398.5 eV), and the* ***(c)*** *Ag $3d_{5/2}$ core level. All spectra were excited with photons from the Mg anode and are calibrated against the Ag $3d_{5/2}$ binding energy of* 368.26 eV. *[Sea98]*

respectively).[Mül10] The peak ratio deduced from the cross-section corrected B:N peak areas is found to be 1:1.08, close to the nominal 1:1 stoichiometry of *h*-BN. We want to mention that a small carbon contamination is observed on the sample, which can presumably be attributed to impurities originating from the ion gun.

4.2.3 Theoretical Characterization

To achieve a comprehensive understanding of the experimental data and to fully characterize the electronic structure, Daniele Stradi from the Technical University of Denmark carried out DFT calculations. Figure 4.11a shows the structure of *h*-BN/Ag(111) used in the calculations where the supercell is highlighted in yellow. The calculated band structure (Figure 4.11b) reproduces the silver surface state shift observed in the experiment. Specifically, we obtain a shift of 115 mV for *h*-BN at a distance of 3.3 Å from the Ag(111) surface, which is close to the exact binding distance reported for the similar graphene/Ag system.[Ols13] At this distance, the calculated adsorption energy per two atoms (BN) is $E_{ads} = -112.5\,\mathrm{meV}/BN$.

The surface state shift strongly depends on the equilibrium distance.[Gar16] The present large interlayer distance is a consequence of the weak interaction between the *h*-BN and the Ag(111) and seems to allow for the confinement of the silver surface state at the interface. This finding is in contrast to strongly interacting systems, *e.g.* nanomesh structures such as *h*-BN/Rh(111) (d_{N-Rh} = 2.1 Å),[Las08] graphene/Ni(111) (d_{Ni-Gr} = 2.1 Å),[Gar14a] and graphene/Ru(0001) (d_{Ru-Gr} = 2.4 Å).[Bor10] In particular in the latter two cases, the surface state of the metal evolves into an interface state as a result of a considerable interaction between C and metal atoms. Figures 4.11c and d show the distance dependence of the

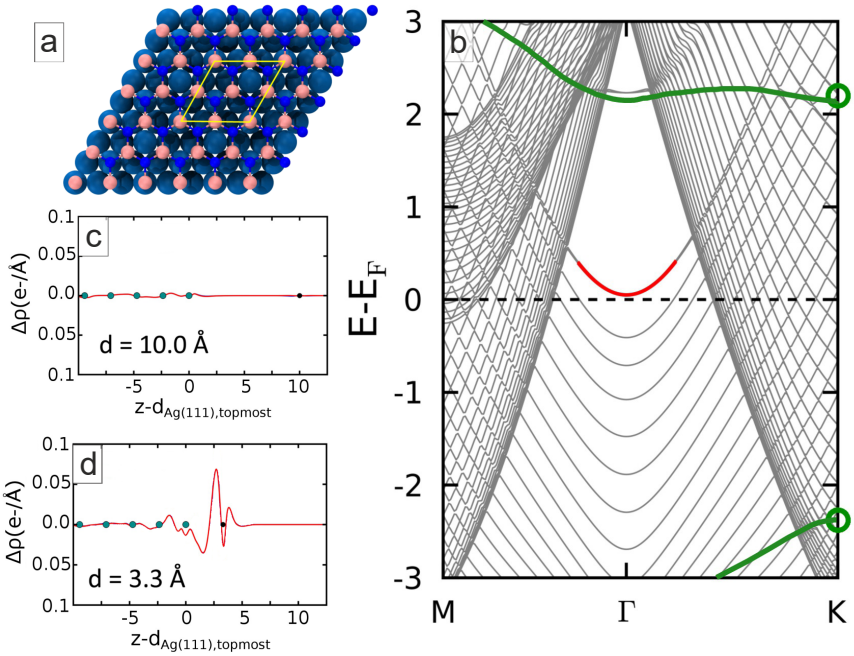

Figure 4.11: ***(a)*** *Top view of the h-BN/Ag(111) structure used in the calculations (the supercell is highlighted in yellow).* ***(b)*** *Electronic band structure of h-BN/Ag(111) with the Shockley surface state highlighted in red. The green circles mark the position of h-BN bands (green lines) and the Dirac point at K. Distance dependence of the charge redistribution $\Delta\rho$ upon adsorption of h-BN on Ag(111) for* ***(c)*** *$d = 10\,\text{Å}$, and* ***(d)*** *$d = 3.3\,\text{Å}$. $\Delta\rho$ has been integrated in the x-y plane. The black and dark cyan dots indicate the positions of the h-BN and Ag(111) layers, respectively.*

charge redistribution $\Delta\rho$ upon adsorption of *h*-BN on Ag(111). Note that at the equilibrium distance (3.3 Å) the charge redistribution mainly affects the interface.

4.2.4 Discussion

Here, only a concise review of the results obtained from the *h*-BN/Ag(111) system will be presented and the discussion will be resumed below in section 4.3.4 where a comparison to the related *h*-BN/Ag/Cu(111) system is made.

This STM study sheds light on the local *h*-BN/Ag(111) structure and reassesses the earlier reports on *h*-BN/Ag(111),[Mül10, Mül13] which have been conducted with space averaging techniques. The refined growth protocol presented in the above section allows for the growth of *h*-BN on the inert Ag(111) substrate below the critical temperature for melting the crystal. However, the *h*-BN islands are still rather small in size. They presumably have different orientations with respect to the substrate lattice, giving rise to the ring surrounding the Ag substrate spots that is observed in LEED, which is consistent with an earlier report.[Mül10] The overall *h*-BN/Ag(111) quality is clearly inferior to the one observed for *h*-BN/Cu(111),

which might hamper the use of *h*-BN/Ag(111) as a substrate to study molecular adsorbates. Notably, the adsorption distance of *h*-BN on Ag(111) predicted by DFT (3.3 Å) is close to the adsorption height of *h*-BN/Ag/Cu(111) determined by means of XSW (see discussion below).

4.3 Intercalation of Silver on *h*-BN/Cu(111)

The previous section 4.2 has shown that the direct growth of *h*-BN on Ag(111) is hampered due to the low catalytic activity of the silver substrate and does not yield large coverages of *h*-BN, independent of the borazine dose and the substrate temperature. To circumvent this issue and obtain *h*-BN monolayers on silver, we successfully investigated an alternative strategy, *i.e.* intercalation. Intercalation is the insertion of guest atoms into a layered host structure,[O'B17] which is in our case the interface between the *h*-BN layer and the Cu(111) substrate. In the following, the method will be introduced and the electronic properties of the resulting *h*-BN/Ag/Cu(111) system will be analyzed and compared to the ones of *h*-BN directly grown on Ag(111). We show that the electronic properties of the *h*-BN/silver system can be tuned *via* the thickness of the intercalated silver layer.

Experimental Methods

The measurements presented in the following sections were conducted at the LT-STM setup and at DLS (see section 3).

4.3.1 Growth

Since a well-controlled growth of *h*-BN has been achieved on Cu(111), we first grow the desired coverage of *h*-BN on a Cu(111) crystal by CVD following the established recipe described in section 4.1. Subsequently, we intercalate silver by e-beam evaporation while keeping the sample at 573 K. This temperature has been shown to be suitable for a homogeneous intercalation of Ag on graphene on Ir(111),[Jol15] and for Co intercalation on *h*-BN on different metals.[Auw02, Pre09] Figure 4.12 shows STM images of a Ag/Cu(111) surface partially covered by *h*-BN. Previous studies of the growth of silver on Cu(111) showed a Stranski-Krastanov growth mode for temperatures higher than 300 K.[McM92, Ben02] A 9×9 superstructure is formed due to the mismatch between Ag and Cu lattices and is clearly observable by STM and LEED (see Figure C.8). The superstructure has a periodicity of 2.4 nm as can be seen in the high resolution STM image of Figure C.8a.

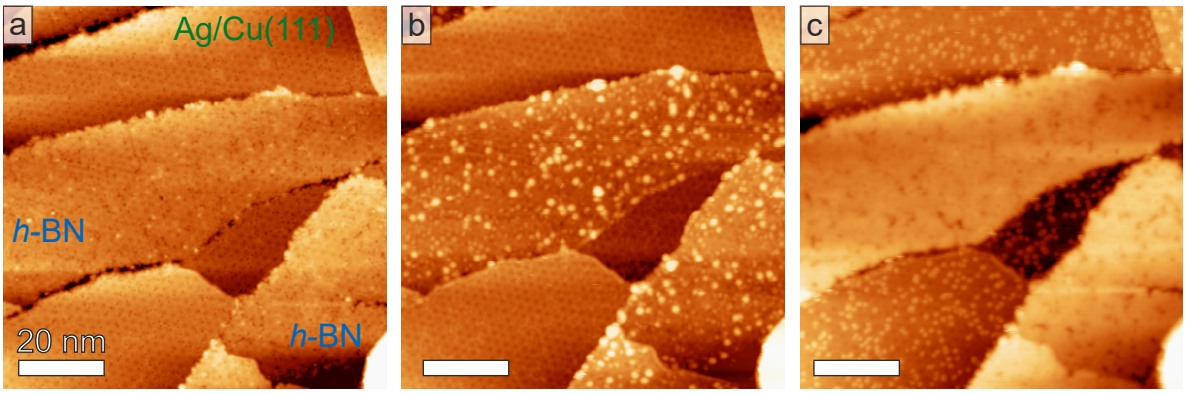

Figure 4.12: *Voltage dependent contrast in STM images of h-BN/Ag/Cu(111) acquired with* ***(a)*** $U_b = 1.0\,\mathrm{V}$, ***(b)*** $U_b = 3.0\,\mathrm{V}$ *and* ***(c)*** $U_b = 4.0\,\mathrm{V}$. *Set point* $I_t = 0.1\,\mathrm{nA}$.

4.3.2 STM Characterization

The STM voltage series displayed in Figure 4.12a-c reveals that the *h*-BN layer does not present a periodic superstructure at any probed bias voltage. Interestingly, the layer seems to be partly transparent at 1 V showing the Ag reconstruction underneath the *h*-BN layer. For higher bias voltages, randomly distributed bright protrusions appear in the STM images (Figure 4.12b). These protrusions have presumably an electronic origin as they appear at certain bias voltages. However, it remained unclear if a geometric contribution is also present. At a bias voltage of 4 V (Figure 4.12c) the *h*-BN islands are clearly distinguishable from the metal substrate and display a large apparent height without indication of a moiré pattern.

4.3.3 Spectroscopic Characterization

Following the experiments of *h*-BN on Ag(111), similar STS investigations have been carried out for *h*-BN/Ag/Cu(111). The right panels of Figure 4.8 show an STM image of the interface (Figure 4.8b) as well as the characteristic $\mathrm{d}I/\mathrm{d}V$ spectra around the Fermi level (Figure 4.8d) and in the field emission regime (Figure 4.8f), respectively. The same effect as discussed above for *h*-BN/Ag(111) is observed in the case of *h*-BN on Ag/Cu(111). Here, the surface state onset appears at −235 mV on the Ag/Cu(111) areas and at 79 mV on the *h*-BN areas resulting in a total shift of 314 mV. Even if the energy position of the spectral feature in the *h*-BN islands is similar in both systems, there is a significant difference in the onset on the Ag/Cu(111) areas with respect to the bare silver. Previous work has shown that the Ag film thickness on Cu(111) determines the energy shift of the Shockley-type surface state.[Wes04] Accordingly, we conclude that the copper surface is covered by 3 ML of silver (see Figure C.8). Analysis of the FERs reveals that the Ag/Cu(111) work function is decreased by ∼0.65 eV

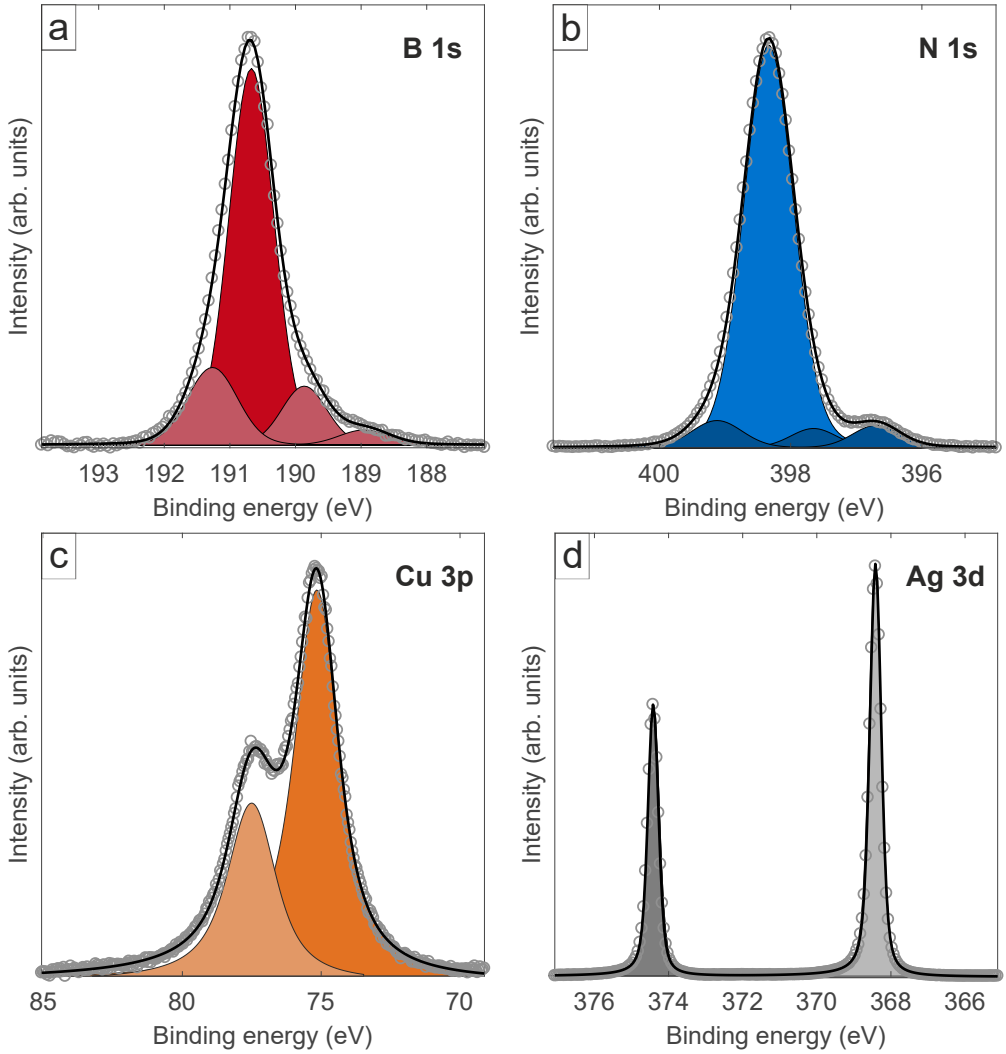

Figure 4.13: *High-resolution soft XPS N 1s, B 1s, Cu 3p and Ag 3d spectra of h-BN/1 ML Ag/Cu(111). A Shirley background was subtracted from the data. The colored areas are fits of the indicated components. Solid black line is the sum of the fits. Photon energy of* 641 eV *was used for all spectra.*

upon formation of the *h*-BN layer. In addition, also a splitting of the first two peaks of the FERs is observed for some spectra taken close to impurities (see Figure 4.9d).

High-resolution soft XP spectra of *h*-BN/Ag/Cu(111) are displayed in Figure 4.13. These spectra have been acquired at the DLS synchrotron following the growth protocols detailed above. The thickness of the Ag layer was ∼1 ML in the experiments carried out at DLS. The binding energy of the Cu $3p$ level has been used for calibration and the Ag $3d_{5/2}$ binding energy has been determined to be $E_b = 368.4$ eV, in good agreement with the reference value of the Ag $3d_{5/2}$ level ($E_b = 368.26$ eV [Sea98]) for a bulk crystal. The B $1s$ and N $1s$ levels of the *h*-BN layer are modeled with four components each, where the main components have a binding energy of $E_b = 190.7$ eV and $E_b = 398.3$ eV, respectively. Both values are slightly re-

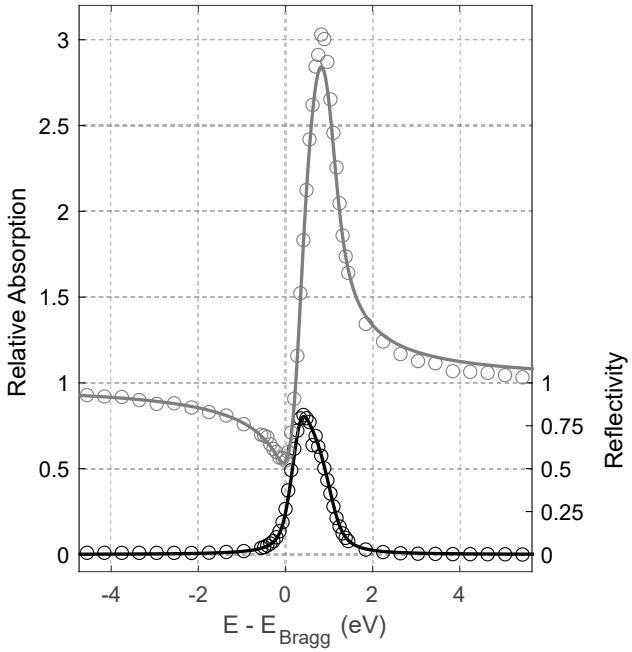

Figure 4.14: *X-ray standing wave absorption profile of Ag 3d. Solid line is a fit to the data. Black data points correspond to the Cu(111) reflectivity curve.*

duced compared to the ones observed for *h*-BN directly grown on Ag(111) (see section 4.2.2). The assignment of the different B 1*s* and N 1*s* components is based on XSW experiments, where all components show a clearly distinct modulation with photon energy implying that they adsorb at different heights. A comprehensive model will be presented in an upcoming publication and is not further discussed here. Analysis of the XSW absorption profile of the Ag 3*d* level, displayed in Figure 4.14, yields a coherent fraction of $f^{111} = 0.92 \pm 0.05$ and a coherent position of $p^{111} = 0.077 \pm 0.020$, which translates into a mean adsorption height of $\overline{h} = 2.25 \pm 0.04$ Å for the Ag layer. The very high coherent fraction suggests a homogeneous and planar Ag layer. The adsorption height of the Ag layer is slightly increased compared to the Cu interlayer spacing of 2.087 Å, as expected for the Ag that has an interlayer spacing of 2.358 Å[Li09] in the case of the Ag(111) single crystal. The coherent position obtained for the main boron and nitrogen components of the *h*-BN layer is $p^{111} = \sim 0.7$, which suggests an adsorption height of $\overline{h} = \sim 5.63$ Å above the topmost copper layer and hence a height of ∼3.38 Å above the Ag layer. The reduced coherent fractions of the main B ($f^{111} \approx 0.5$) and the N ($f^{111} \approx 0.5$) components compared to the *h*-BN/Cu(111) system (see section 4.1.3) can be rationalized by recent AFM measurements conducted by P. Leone,[Leo17] where indications of a (Volmer-Weber) island growth mode for *h*-BN/Ag/Cu(111) were found. Contrary to the layer-by-layer growth (Frank-van der Merwe), the island growth of intercalated Ag would lead to an uneven Ag substrate layer effectively increasing the corrugation of the *h*-BN layer.

	h-BN/Ag(111)	*h*-BN/Ag(3ML)/Cu(111)
ΔE_{SS}^{exp}(mV)	119	314
ΔE_{SS}^{theo}(mV)	115	-
$\Delta\Phi$(eV)	-0.35	-0.65
E_{ads}^{theo}(meV)	-112.5	-

Table 4.3: *Comparison of the observed surface state shifts and work function changes.* ΔE_{SS}^{exp} *and* ΔE_{SS}^{theo} *are the experimental and calculated surface state shift of the silver.* $\Delta\Phi$ *is the 2D layer induced change of work function with respect to the pristine surface.* E_{ads}^{theo} *corresponds to the adsorption energy per unit cell.*

4.3.4 Discussion

In the following, we discuss the results obtained for *h*-BN grown on Ag/Cu(111) and compare them to the ones obtained from the direct growth of *h*-BN/Ag(111) presented above. Table 4.3 summarizes the experimental surface state shifts and the work function changes for the two systems. Both values are larger in the case of *h*-BN/Ag/Cu(111). Although the *h*-BN layers appear similar in the STM images (see Figures 4.7 and 4.12), they are distinct from the electronic point of view. Prior to the silver intercalation, the surface state band onset of the bare Cu(111) is at −440 mV and at −334 mV for the *h*-BN/Cu(111) regions (ΔE_{SS} = 106 mV). The work function is reduced and, contrary to *h*-BN/Ag(111), spatially modulated following the moiré superstructure (see Figure C.2 and Ref. [Jos12, Sch17b]).

Once the silver intercalates, the surface state band minimum is shifted smoothly to higher values in the Ag/Cu(111) areas (*e.g.* at −235 mV for 3 ML of Ag).[Wes04] On the *h*-BN regions, the surface state depopulates and the band onset appears at similar energies as for *h*-BN on Ag(111) (see Figure 4.8c and d). Thus, the shift of the surface state induced by the *h*-BN is considerably larger on Ag/Cu(111) (314 mV) than in the case of Ag(111) (119 mV). It is interesting to note that the Ag thickness allows us to tune the properties of the system in a controlled manner.

We attribute the shift of the Shockley surface state band to the charge redistribution at the interface (see Figure 4.11d). A similar effect has been observed for graphene/Ag(111),[Gar16] which will be discussed in detail elsewhere. Following the charge redistribution and the empirical rule postulated by Ziroff *et al.* for physisorbed overlayers on noble metal (111) surfaces,[Zir09] the up-shift of the surface state energy can be correlated to the adsorption energy per surface area. For *h*-BN/Ag(111) (surface state shift of 115 eV compared to clean Ag(111)), an adsorption energy of −112.5 meV is predicted by DFT, whereas it is expected to be larger in the case of *h*-BN on Ag(3ML)/Cu(111), where a surface state shift of up to 314 eV has been measured.

Due to the presence of a wide gap in the *h*-BN band structure, the electronic states of silver around the Fermi level are not perturbed in excess upon adsorption. In particular, DFT calculations on *h*-BN/Ag(111) predict a bandgap of 4.52 eV at the K point (see green circles in Figure 4.11b). Neither the calculations nor the experimental data provide evidence for BN-related states in the gap, as expected for a weakly interacting system.[Pre08] However, as can be seen in Table 4.3, our results show a work function decrease upon adsorption of *h*-BN. This can be understood by the "push-back" effect, *i.e.* the surface electron density spilling out of the metal surface is pushed back into the crystal by Coulomb (Pauli) repulsion between the electron density of the physisorbed *h*-BN layer and the surface electrons leading to a reduction of the work function.[Brö10, Cri02] A similar behavior has been observed *e.g.* for the adsorption of Xe on various transition metal surfaces.[Cri02]

It should be mentioned that a corrugation of ∼30 pm was estimated in a recent AFM study[Leo17] for *h*-BN/Ag/Cu(111) using the AFM calibration method introduced in section 4.1.3.1. Hence the corrugation seems to be slightly reduced upon intercalation of Ag in *h*-BN/Cu(111).

4.4 Conclusions

In conclusion, we presented a study on *h*-BN (sub-) monolayers grown on two different noble metal substrates, Cu(111) and Ag(111). Our results obtained for the two systems corroborate the assertion that both can be categorized as weakly interacting systems, although the resulting *h*-BN layer quality is strikingly different. While for Cu(111) high-quality large-scale *h*-BN layers could be grown and a significant geometric corrugation, as well as the adsorption height, were determined quantitatively, the low catalytic activity of the Ag(111) substrate impedes the direct growth of satisfactorily large *h*-BN domains. Intercalation of silver in *h*-BN/Cu(111) opens new paths to obtain *h*-BN layer supported on silver in order to compare the properties of molecular adsorbates to studies carried out on bare Ag surfaces.

To study the geometric corrugation and the adsorption height of *h*-BN/Cu(111) we presented a multi-method study that provides a complete, quantitative structure determination of the sp^2 bonded *h*-BN layer. The lateral structure is elucidated *via* complementary STM and LEED measurements giving insight into the azimuthal epitaxial relation of *h*-BN to Cu(111). The mean absolute spacing between *h*-BN layer and copper substrate was found to be $\overline{h}_0 = 3.38 \pm 0.06$ Å based on XSW measurements. We further introduce an experimental method that allows to determine the local *h*-BN corrugation *via* analysis of the atomic contrast in AFM measurements. The pore areas of the *h*-BN layer were observed to be 0.3 to 0.7 Å closer to the Cu(111) substrate than the wires, contrasting the hitherto assumed flat

h-BN geometry. The obtained value for the local corrugation is in good agreement with the spatially averaged XSW results, providing insights into the physical origin of the coherent fraction. This study further provides a clear benchmark for theoretical calculations in terms of the mean adsorption height as well as the corrugation of the layer. DFT calculations based on the latest exchange-correlation functionals can yield the values of the mean adsorption height and the corrugation with good agreement.

In the case of the silver surface, we have investigated the electronic structure of the interface between *h*-BN and Ag, and found that the surface state of the metal is still present and its onset is shifted toward higher energies above the Fermi energy. We found that the energy shift can be controlled *via* the silver thickness. Interestingly, the surface state shift upon *h*-BN adsorption is larger in the Ag intercalated structure compared to the adsorption on the Ag(111) single crystal surface. This observation implies that also the interaction between the *h*-BN layer and the Ag/Cu(111) substrate is stronger than in the case of *h*-BN/Ag(111) and even the *h*-BN/Cu(111) system. Moreover, a decrease of the work function upon *h*-BN adsorption is observed on both Ag(111) and Ag/Cu(111), and attributed to the modification of the surface dipole upon adsorption of the 2D layer. XSW measurements indicate an adsorption height of $\sim 3.38\,\text{Å}$ of the *h*-BN layer above the Ag/Cu(111) surface, very similar to the value determined for *h*-BN/Cu(111).

Chapter 5

Tetrapyrrolic Molecules on Copper and *h*-BN Supports

This chapter includes content that has been published in

J. I. Urgel, M. Schwarz, M. Garnica, D. Stassen, D. Bonifazi, D. Ecija, J. V. Barth, W. Auwärter, **Controlling Coordination Reactions and Assembly on a Cu(111) Supported Boron Nitride Monolayer**, *J. Am. Chem. Soc.* **137**, 2420-2423 (2015); Copyright (2015) by the American Chemical Society.

and

M. Schwarz, M. Garnica, D. A. Duncan, A. Pérez Paz, J. Ducke, P. S. Deimel, P. K. Thakur, T.-L. Lee, A. Rubio, J. V. Barth, F. Allegretti, W. Auwärter, **Adsorption Conformation and Lateral Registry of Cobalt Porphine on Cu(111)**, *J. Phys. Chem. C* **122**, 5452-5461 (2018); Copyright (2018) by the American Chemical Society.

Transition metal complexes hold great promise for technological and medical applications such as in photonic and optoelectronic devices,[Kal98] catalysts,[Har85] and metal-based pharmaceuticals.[Che10a, Kil13] For instance, the metal ions in these molecules can be tailored such that they bind to a desired biomolecular target acting as a potential therapeutic agent [Zha03] and as catalyst they offer control over the active site and its selectivity.[Rog17, Tho05] Frequently the applications require the organization of the metal complexes on a solid surface, whereby the interaction between the coordinated metal ion and the surface can drastically affect the functional properties of the complexes themselves. Consequently, a detailed understanding of the interfacial interactions between the complexes and the support is important for future integration of these molecular systems in functional

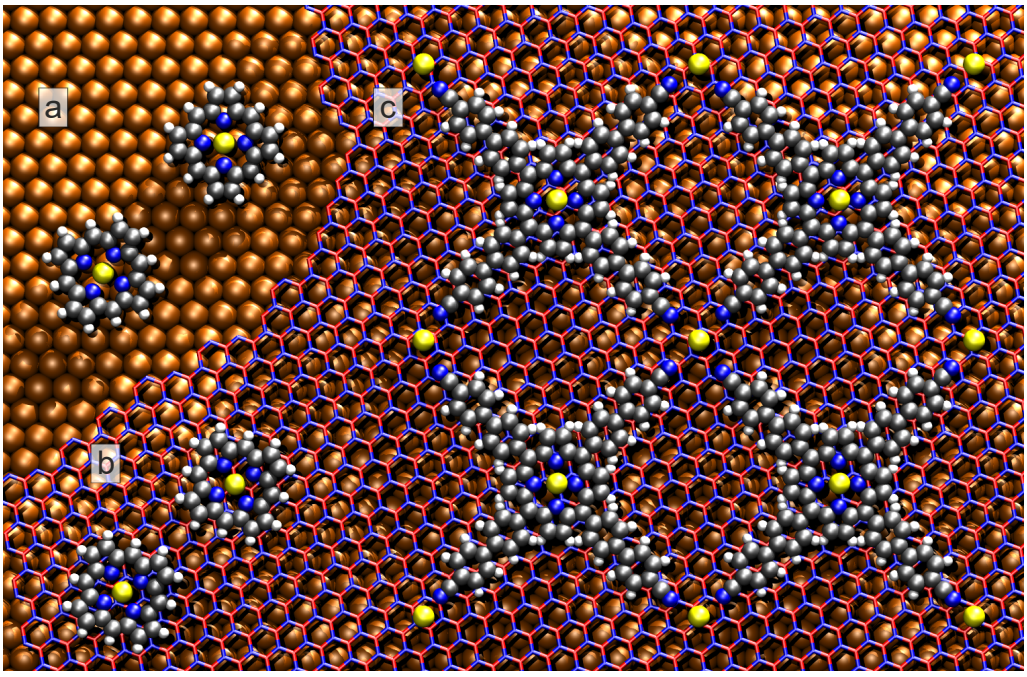

Figure 5.1: *Porphyrins in different environments.* ***(a)*** *Co–P on Cu(*111*),* ***(b)*** *Co–P on h-BN/Cu(*111*),* ***(c)*** *coordination network based on functionalized porphyrins on h-BN/Cu(*111*).*

nanodevices.[Bar07, Koc07] Tetrapyrroles, such as metalloporphyrins and metallophthalocyanines, are an important class of metal complexes because of their occurrence in biological systems,[Bat00] their high stability, structural versatility, promising electronic properties and tunable molecular functionality.[Got15, Kad03] The adsorption of these molecules on coinage metal surfaces has provided a rich playground for the engineering of complex nanoarchitectures by self-assembly and for understanding the reactivity and the electronic structure of metal-organic interfaces.[Auw15, Auw07b, Dil16] Moreover, the conformation of the molecule can be altered significantly by the interaction with the metal substrate resulting in changes of the intrinsic molecular properties.[Ros03]

This chapter presents the results on different porphyrin molecules that have been studied on Cu(111) and on Cu(111)-supported *h*-BN sheets (Figure 5.1). Specifically, cobalt porphine (Co–P) has been characterized quantitatively in different environments in complementary STM, XPS and XSW experiments. First, the adsorption geometry and the exact lateral registry of Co–P on the metallic Cu(111) surface (Figure 5.1a) will be described in section 5.1. Subsequently, we report on the adsorption height of Co–P on a *h*-BN monolayer on Cu(111) (Figure 5.1b), and highlight the significant modifications of the adsorption conformation of the molecule through the decoupling *h*-BN layer (see section 5.2). Moreover, carbonitrile-functionalized porphyrins have been used to create surface-confined coordination architectures on *h*-BN sheets (see Figure 5.1c and section 5.3) demonstrating the possibility

to achieve porous metal-organic frameworks on sp^2 layers, and offering a playground to probe the intrinsic properties of coordination nodes. Ultimately, we have studied single Co atoms, *i.e.* magnetic impurities in different environments (on Cu(111) and *h*-BN, see section 5.4), as Co centers constitute the active site of the Co-metallated porphyrin molecules studied in the prior sections. Due to the interaction between the unpaired valence electron of the Co atom and the bath of conduction electrons in the metal substrate, a characteristic spectroscopic feature near the Fermi energy — known as Kondo resonance — has been observed.

5.1 Lateral Registry and Adsorption Conformation of Cobalt Porphine on Cu(111)

In recent years, different combined experimental and theoretical studies were devoted to determine the adsorption geometry of organic molecules,[Sch13a, Wei17, Sne15, Bab17] and in particular porphyrins on various substrates.[Auw07a, Yok01, Dye11, Bür13, Mül16, Leu06, Mau16, Zha17b, Lep17, Alb16] Specifically, Bürker *et al.* have studied the vertical height variation of functionalized porphyrins on Cu(111) upon copper metalation by means of the XSW method.[Bür14] They observed that the two inequivalent N atoms in tetraphenyl porphyrin (TPP) adsorb at a height of 2.02 ± 0.08 Å and (2.23 ± 0.05) Å, prior to metalation, whereas after metalation only one N species at 2.25 ± 0.02 Å was found. However, no insight into the lateral registry was obtained. Furthermore, prior studies indicate that the lateral phenyl substituents of TPP can exert a significant influence on the final conformation of the molecule.[Dil13b, Dil12] Additionally, due to an overwhelming signal from the bulk, metalation with atoms of the substrate hampers the determination of the vertical position of the porphyrin metal centers, which, as it is the active site of the molecule, is of fundamental interest in, *e.g.* the ligation of adducts,[Wäc10] and the stacking behavior of multilayer systems.

The free-base porphine (2H–P), consists of four pyrrole rings connected by four methine (=C–) bridges forming an aromatic heterocyclic macrocycle and constitutes the base-unit of all porphyrinic nanosystems. Its central pocket can host a wide range of atoms including, but not limited to, lanthanides and transition metals, thus offering a vast playground to modify the functionality of the molecule.[Auw07b, Urg15c, Dil16] Along with changes of the physical, chemical and optoelectronic properties,[Sen07] the conformation can also be altered considerably.[Auw07a, Dil12] To understand the molecule–substrate interactions of the base-unit porphine, a proper knowledge of the exact adsorption geometry is of fundamental interest. Bischoff *et al.* suggested a bridge adsorption site for 2H–P on Ag(111) based on the molecular orientations and the intermolecular spacing observed in STM.[Bis13]

For 2H–P on Cu(111), DFT calculations predicted an average adsorption height of 2.40 Å at the bridge site, accompanied by a structural deformation of the molecule because of different interaction strengths of the nitrogen species with the substrate atoms.[Mül16]

Herein, we report the experimental determination of the adsorption site and the conformation of cobalt porphine (Co–P) on Cu(111). To this end, we conducted XSW experiments complemented by high-resolution XPS (HR-XPS) to measure the vertical height of Co–P on the Cu(111) surface, as well as to directly triangulate the lateral registry of the metal center. The capability of the XSW technique to resolve the substrate bonding of organic molecules has been reliably demonstrated in the last decade.[Bür13, Bür14, Krö11, Hau05, Krö16] STM measurements of sub-monolayer Co–P were utilized to rule out the presence of multiple lateral adsorption sites and the molecular registry of Co–P, coadsorbed with carbon monoxide (CO), was directly probed by this technique to confirm the XSW results on the single molecule level. The results of both experiments are interpreted and corroborated by DFT calculations with van der Waals corrections.

Experimental and Computational Methods

The XPS and XSW measurements were conducted at the Diamond Light Source at the end station of the I09 beamline. The Co–P molecules (purchased from Frontier Scientific, purity 95%) were degassed thoroughly and evaporated from a home-built evaporator at a temperature of 600 K while the sample was kept at room temperature. The final molecular coverage (∼20 % of a monolayer) was calculated using the intensity ratio of the cross-section corrected C 1*s* to Cu 3*p* core-level peaks measured at the same photon energy and the unit cell size of a Co–P molecule.[Bis13] The C 1*s* and N 1*s* core-level spectra were acquired using a photon energy of 641 eV and the Co 2*p* core-level spectra with a photon energy of 2400 eV. XP survey spectra, taken over a wide range of binding energies, showed no components other than the expected C, N, Co and Cu features. The binding energy scale of the C 1*s*, N 1*s* and Co 2*p* spectra were calibrated against the Cu 3*p* core level measured at the same photon energy and assumed to be at a binding energy of 75.14 eV.[Sea90]

In order to avoid beam damage during the XSW measurements, the beam intensity was reduced to 20% by detuning the undulator. Possible beam damage was monitored by comparing the C 1*s* and N 1*s* core-level spectra before and after each XSW measurement, where no changes were detected. The XSW scans were obtained from the (111) and ($1\bar{1}1$) Bragg reflection of Cu ($E_{Bragg} \approx 2972$ eV at 300 K with a Bragg angle of $\sim 90°$) as detailed in section 3.7. In total 16 distinct sample spots were used for the measurements, resulting in four individual XSW spectra for C 1*s*, N 1*s* and Co 2*p* at the (111) Bragg reflection and additional four Co 2*p* spectra at the ($1\bar{1}1$) Bragg reflection. The respective XP spectra were then averaged to improve the signal to noise ratio.

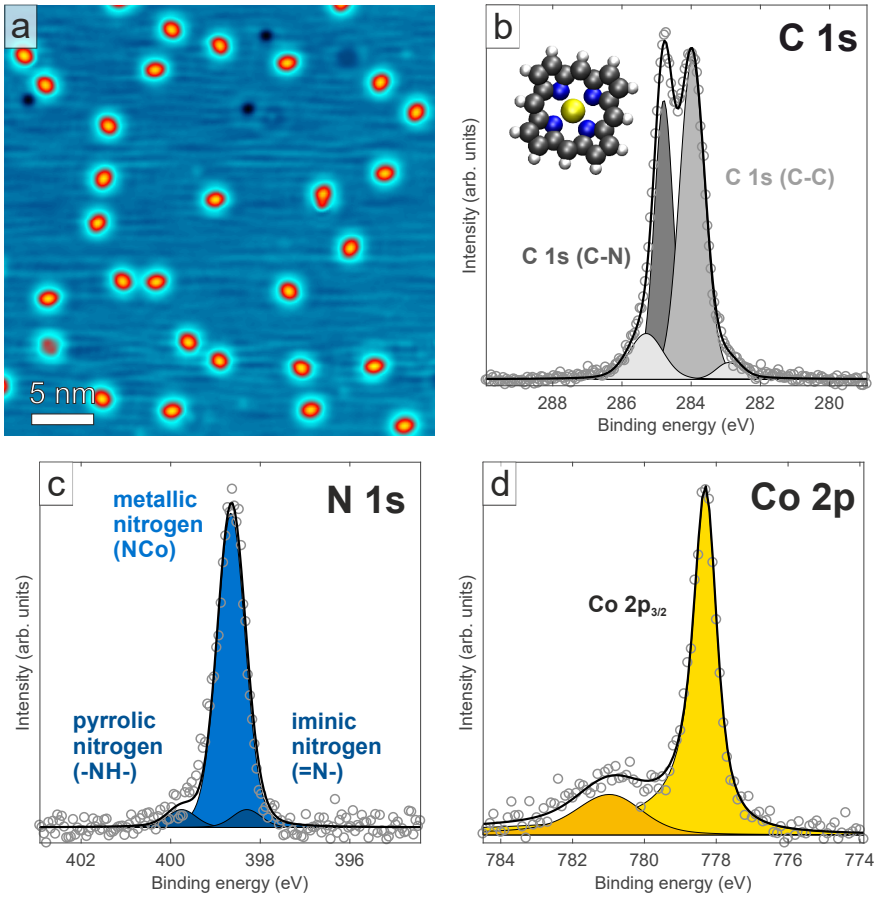

Figure 5.2: ***(a)*** *STM image showing a low coverage of Co–P/Cu(111). Scan parameters:* $U_b = -0.65\,\mathrm{V}$, $I_t = 0.23\,\mathrm{nA}$. *Corresponding high-resolution XP spectra of* ***(b)*** *C 1s,* ***(c)*** *N 1s, and* ***(d)*** *Co* $2p_{3/2}$ *core levels, respectively. Data points are background subtracted with a Shirley background. The colored areas are fits of the indicated components, and the solid black line is the global fit. The inset in (b) shows a ball model of the Co–P molecule (gray: carbon, blue: nitrogen, yellow: cobalt, white: hydrogen).*

The STM experiments were performed in the LT-STM setup and CO was deposited onto the surface at sample temperatures below 15 K. The DFT calculations were carried out by Alejandro Pérez Paz as explained in detail in Ref. [Sch18a].

5.1.1 Spectroscopic Characterization

The XPS experiments were conducted with a low molecular coverage ($\sim 20\,\%$ if a monolayer) comparable to the STM image shown in Figure 5.2a ($\sim 10\,\%$). Figure 5.2b-d displays high-resolution X-ray C 1*s*, N 1*s* and Co 2*p* core-level spectra of Co–P/Cu(111), whose fit parameters are summarized in Table 5.1. In the C 1*s* core-level spectrum (Figure 5.2b), two clearly distinct components with binding energies (E_b) of 284.8 eV and 284.0 eV, can be distinguished. The component at higher binding energy stems from the eight carbon atoms directly

Core level	E_b^0 (eV)	Γ (eV)	σ (eV)
C $1s$ (C–C)	284.0	0.12	0.69
C $1s$ (C–N)	284.8	0.12	0.53
N $1s$	398.6	0.11	0.58
Co $2p_{3/2}$	778.2	0.31	0.55

Table 5.1: *XPS fit parameters for the atomic species of Co–P/Cu(111): Peak position E_b^0, Lorentzian width Γ and Gaussian width σ obtained from the fits for the indicated components. Voigt line shapes are used for the curve-fitting of the C $1s$ and N $1s$ core level spectra, whereas a Doniach-Šunjić line shape was used to model the Co $2p_{3/2}$ line.*

bound to nitrogen atoms (C–N), whereas the lower binding energy component originates from the 12 carbon atoms that are bonded to only other carbon atoms (C–C).[Dil13b, Dei16] The intensity ratio of the two peaks, 0.76, is in good agreement with the expected value of 0.67 (= 8/12). An additional, comparatively weak component at $E_b = 285.6$ eV is tentatively assigned to a shake-up satellite, whereas the feature at $E_b = 282.9$ eV is most likely due to a minor amount of adventitious carbon on the surface of the crystal.

The N $1s$ photoemission spectrum (Figure 5.2c) shows a dominant peak at 398.6 eV with a small shoulder at higher binding energy (399.6 eV). An additional shoulder on the low binding energy side (398.3 eV) is identified by the curve-fitting analysis. The main peak is associated with nitrogen atoms bound to cobalt atoms (N–Co), whereas the shoulders are assigned to pyrrolic (–NH–) and iminic (=N–) nitrogen atoms of free-base porphine (2H–P) that are present as impurities from the Co–P powder. The area ratio of about 17:1 is in accordance the nominal purity. The binding energy of the main peak is in good agreement with values reported for metalloporphyrins on surfaces in the literature.[Dil13b, Scu00, Di 11, Got06, Niw74]

The Co $2p_{3/2}$ core level (Figure 5.2d) exhibits a more complex line shape associated with the multiplet structure resulting from the open-shell character of the Co ion and is consistent with the earlier reports on similar porphyrins.[Wäc10, Got06, Luk07, Fle07, Wec17] The main peak is found at a binding energy of 778.2 eV, in good agreement with these previous studies of cobalt porphyrins on surfaces,[Wäc10, Luk07, Fle07, Wec17] and the satellite feature at high binding energy is assigned to the unpaired electron in the $3d$ shell and its coupling to the core hole created in the $2p$ shell of the Co ion upon photoemission.[Luk07, Fle07, Wec17]

5.1.2 Mean Adsorption Height

The results of the XSW measurements performed in normal-incidence geometry with respect to the (111) Bragg reflection are displayed in Figure 5.3. A qualitative inspection shows that all absorption profiles exhibit a maximum around 1 eV above the Bragg energy, suggesting

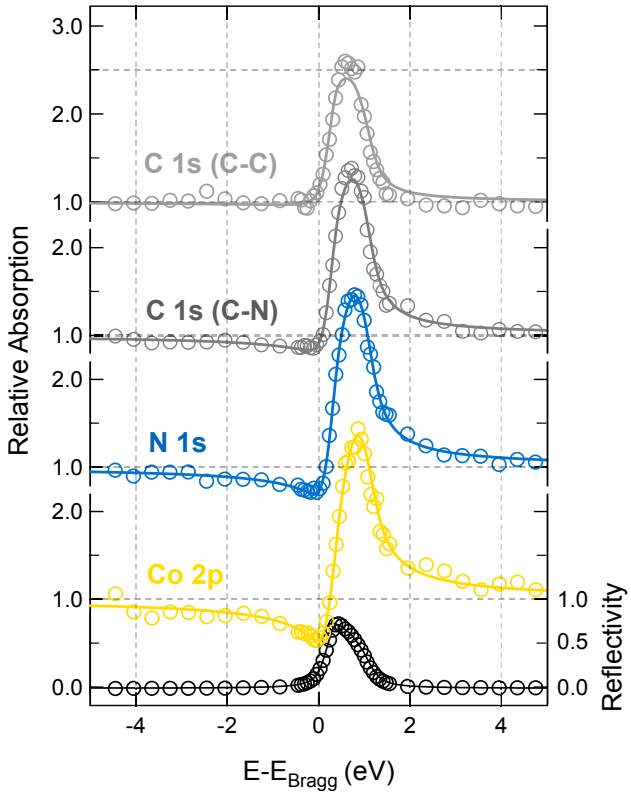

Figure 5.3: *Normal-incidence XSW absorption profiles of C1s, N1s and Co $2p_{3/2}$ of Co–P on Cu(111) at the (111) Bragg reflection. Solid lines are fits to the data and black data points are the reflectivity curve.*

that the mean height of each species is largely similar, however, the more distant the atom is from the center of the molecule, the lower the obtained coherent fraction is, as can be explained by the STM and DFT data discussed below. Quantitative analysis of the Co $2p_{3/2}$ absorption curve yields a very high coherent fraction, $f^{111} = 0.90 \pm 0.05$ and a coherent position of $p^{111} = 0.08 \pm 0.03$, which, assuming the adsorption height lies between the first and the second Cu(111) layer spacing projected above the surface, translates into an average adsorption height $\overline{h} = 2.25 \pm 0.04$ Å. The high coherent fraction indicates a well-defined adsorption height for all of the molecules and might also point to a well-defined adsorption site in terms of the lateral registry. For nitrogen, a coherent fraction of $f^{111} = 0.78 \pm 0.03$ and an average adsorption height $\overline{h} = 2.33 \pm 0.06$ Å are determined; for the carbon data, the C–N (C–C) species exhibits a coherent fraction $f^{111} = 0.61 \pm 0.04$ (0.30 ± 0.06) and an average adsorption height of $\overline{h} = 2.37 \pm 0.05$ Å $(2.44 \pm 0.09$ Å). The structural parameters are summarized in Table 5.2.

To determine the exact lateral adsorption site of the Co–P molecules, triangulation measurements [Woo98, Gol82] were conducted for the Co $2p_{3/2}$ core level utilizing the $(1\bar{1}1)$ Bragg reflection (Figure D.1). The best fit of the relative absorption of the Co $2p_{3/2}$ core level yields

	XSW – (111) Bragg reflection			DFT	DFT/XSW
	f^{111}	p^{111}	Adsorption height $\overline{h}_0$(Å)	Calculated adsorption height $\overline{h}_0$(Å)	Geometric factor a_{111}
C 1*s* (C–C)	0.30 ± 0.06	0.17 ± 0.05	2.44 ± 0.09	2.54	0.78
C 1*s* (C–N)	0.60 ± 0.04	0.14 ± 0.03	2.37 ± 0.05	2.46	0.91
N 1*s*	0.79 ± 0.03	0.12 ± 0.03	2.33 ± 0.06	2.38	0.96
Co $2p_{3/2}$	0.90 ± 0.05	0.08 ± 0.02	2.25 ± 0.04	2.22	
	XSW – (1$\overline{1}$1) Bragg reflection				
	$f^{1\overline{1}1}$	$p^{1\overline{1}1}$	Adsorption height $\overline{h}_0$(Å)		
Co $2p_{3/2}$	0.50 ± 0.06	0.91 ± 0.03	-		

Table 5.2: *Structural parameters obtained from the XSW analysis compared to the vertical distances calculated by DFT: The XSW data obtained from the (111) Bragg reflection comprises the coherent fraction f^{111}, the coherent position p^{111}, and the corresponding mean adsorption height on bulk-extrapolated Cu(111) Bragg plane for the different atomic species of Co–P. Calculated vertical distances from DFT and the resulting geometric factor a_{111} are given for comparison. The XSW data obtained from the Co $2p_{3/2}$ core level using the (1$\overline{1}$1) Bragg reflection (see Figure D.1) comprise the coherent fraction $f^{1\overline{1}1}$, and the coherent position $p^{1\overline{1}1}$.*

a coherent fraction of $f^{1\overline{1}1} = 0.50 \pm 0.06$ and a coherent position of $p^{1\overline{1}1} = 0.91 \pm 0.03$. Considering different lateral positions above the close-packed surface and assuming a single site adsorption model for cobalt, triangulation calculations by refinement, which take into account the coherent fractions and positions of both Bragg reflections, indicate that the measured data can only be reconciled with adsorption in a bridge site.[Sch18a] This site would be expected to have a $f^{1\overline{1}1} = 0.33$ (see Eq. (D.4) and Ref. [Woo05]), suggesting that the adsorption site might be slightly off the ideal bridge site. However, the higher coherent fraction is more likely the result of the previously observed positive non-linearity in the EW4000 analyzer.[Blo17] This latter interpretation is further reinforced by the quality of the fit being poor when the absorption rate is at its maximum (at around 1 eV in Figure D.1), suggesting that the experimental count rate is approaching the saturation rate of the detector and thus the fit curve overreaches the experimental data.

The experimentally determined adsorption heights are in good agreement with the ones theoretically obtained from DFT calculations using PBE exchange-correlation functional, supplemented with vdW corrections (see Table 5.2 and discussion below). Notably, the calculated heights are within 0.15 Å of the experimental values and lie within the experimental uncertainty for the Co species. Importantly, the DFT calculations predict that the Co atom is located closest to the surface at a vertical distance of 2.29 Å. Moreover, the DFT results

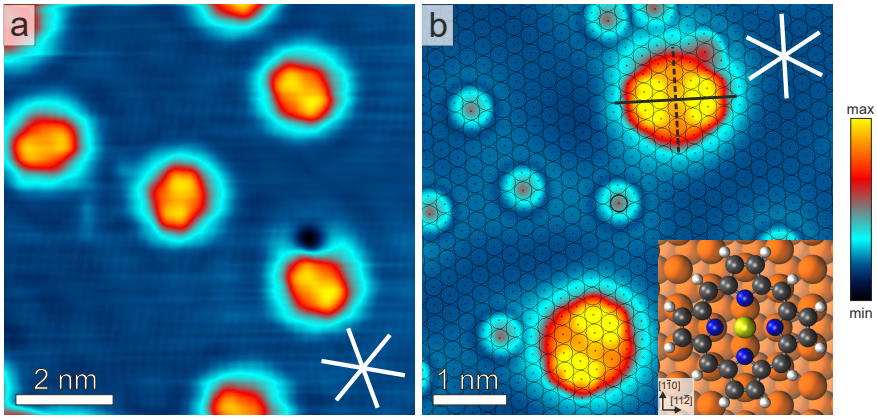

Figure 5.4: *STM images showing the adsorption geometry of Co–P/Cu(111). **(a)** The Co–P molecules adopt three different orientations where one molecular axis (see black dashed lines in (b)) is aligned with one of the principal directions of the crystal (close-packed rows, white lines). The bright features of the Co–P molecules are aligned with the long bridge direction of the Cu(111) substrate. **(b)** Close-up view of two Co–P molecules together with CO molecules, which appear bright and adsorb preferentially on atop sites. The atomic lattice is superimposed according to the CO adsorption sites. This clearly reveals that the Co atom in the center of the Co–P is located on bridge positions. The inset shows a top view of the relaxed adsorption geometry by DFT. Co, C, N, and H atoms are depicted by the yellow, gray, blue, and white spheres. Scan parameters: (a) $U_b = -0.5\,\mathrm{V}$, $I_t = 0.68\,\mathrm{nA}$; (b) $U_b = 0.5\,\mathrm{V}$, $I_t = 0.8\,\mathrm{nA}$.*

reveal adsorption centered over a bridge site and a distortion of the molecule (discussed later) that qualitatively matches the experimentally measured trend in coherent positions and is further corroborated by the STM measurements.

5.1.3 Lateral Registry and Conformation

At low coverage, dispersed Co–P are observed on the Cu(111) surface (see large-scale image in Figure 5.2a). Figure 5.4a displays the three orientations of Co–P/Cu(111) corresponding to the three-fold symmetry of the substrate: the two molecular axes (black dashed and solid lines in Figure 5.4b) are aligned along the $\langle 1\bar{1}0 \rangle$ and $\langle 11\bar{2} \rangle$ directions, respectively, of the underlying substrate. Specifically, the black dashed axis that corresponds to the weaker contrast of the molecule in the STM image, lies along one of the three equivalent densely packed $\langle 1\bar{1}0 \rangle$ directions of the substrate. Molecular rotation could be induced by the scanning STM tip, but only resulted in aligning the molecule along one of the other symmetrically equivalent directions. The bright contrast along one of the axes and the twofold symmetry of the molecule are observed for both positive and negative bias voltages and are largely independent of the shape and nature of the tip (see Figure D.2), as discussed in detail below.

To determine the adsorption site, CO molecules were deposited *in-situ* and used as markers, as CO is known to adsorb on atop sites on Cu(111) at low coverage at this particular

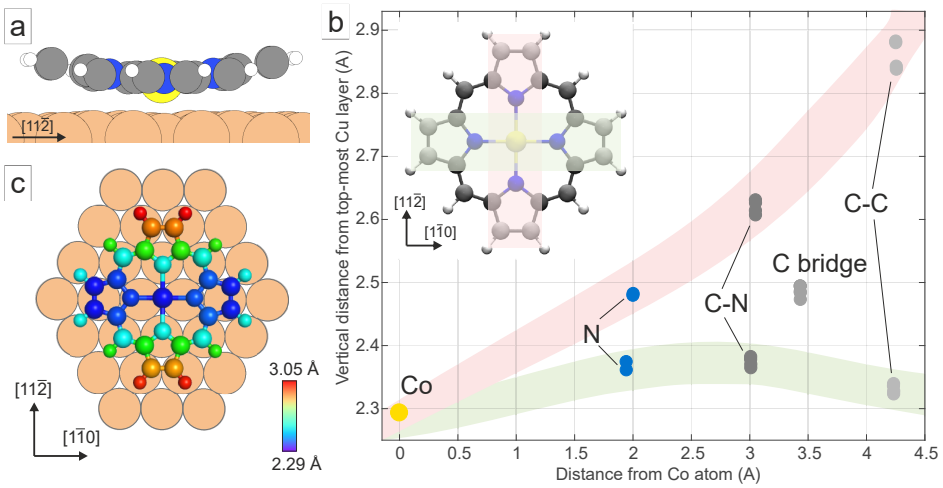

Figure 5.5: *Structural conformation predicted by the DFT calculations. In the most stable adsorption geometry of Co–P on Cu(111), the central Co atom (yellow) is located on a surface bridge site of the Cu substrate.* ***(a)*** *Side-view of the molecular model showing an asymmetric saddle-shape-like conformation (the porphine macrocycle is bent upwards along the* $\langle 11\bar{2} \rangle$ *direction).* ***(b)*** *The Co–P molecule has two molecular axes, marked red and green in the inset. The carbon and nitrogen atoms along the main axis (red-shaded) show an increased vertical position compared to the atoms along the second axis (shaded in green).* ***(c)*** *Color-coded plot indicating the adsorption height of each atom in the Co–P with respect to the mean top layer of Cu(111).*

temperature.[Bar98, Auw07a] The CO showed no discernible interaction with the Co–P molecules, suggesting that the molecules do not affect the other's adsorption site. We exploit the enhanced sub-molecular resolution obtained with CO-functionalized STM tips,[Jel17] together with the atomic substrate lattice defined by the CO molecules, imaged now as bright protrusions, to determine the exact registry of the Co–P on the surface (Figure 5.4b). The image clearly reveals that the center of the Co–P molecules and thus the Co atoms are exclusively located on bridge positions of the substrate, as predicted by the DFT calculations and determined by the XSW measurements.

The DFT calculations yield an adsorption energy of −4.80 eV for Co–P adsorption on bridge site (see Figure 5.4b). It should be noted that the adsorption energy obtained from DFT without vdW corrections is only −0.25 eV (*i.e.* the vdW stabilization contribution to the adsorption energy is large for Co–P/Cu(111): −4.55 eV). The Co–P macrocycle is bent upwards along the $\langle 11\bar{2} \rangle$ direction while nearly flat along the $\langle 1\bar{1}0 \rangle$ direction. Calculations starting with Co–P placed such that Co is on other high-symmetry sites (*e.g.* hcp hollow site) result in the molecule hopping back to the bridge site. Thus, we conclude that the bridge site is the global energy minimum. The Co atom, which lies above the bridge site, has a predicted adsorption height of 2.29 Å, corresponding to a Co–Cu bond length of 2.65 Å. The favored bridge adsorption geometry gives rise to two pairs of distinct nitrogen atoms (see inset of Figure 5.4b): The first pair are positioned along the short bridge direction,

which is one of the densely packed $\langle 1\bar{1}0\rangle$ directions of the crystal. This pair of N atoms are located off-atop, with an adsorption height, above the mean height of the outermost Cu layer, of 2.48 Å and a bond length of its nearest-neighbor (nn) Cu atom also of 2.48 Å (because of a subtle outward relaxation of the nn Cu atom). The N–Co bond length was predicted to be 1.95 Å (compared to 1.97 Å calculated for Co–P in gas phase). The second pair of N atoms are aligned along the long bridge direction (*i.e.* the $\langle 11\bar{2}\rangle$ directions of the crystal) in a near atop site, with a slightly decreased adsorption height (2.37 Å) above the outermost Cu layer, and a N–Cu bond length of 2.52 Å. The N–Co bond length was found to be slightly longer at 2.01 Å. A favored bridge adsorption position has also been reported for Co–Pc on Cu(111).[Cua10, Hei10c] Notably, an adsorption configuration with the Co–P molecule rotated by 90° was also found to be stable (adsorption energy: −4.73 eV), although energetically slightly less favorable by 0.07 eV.[Sch18a] This adsorption structure exhibits a saddle-shape conformation with the two pyrrole rings along the $\langle 1\bar{1}0\rangle$ directions of the crystal sitting significantly higher above the surface, in contrast to the global energy minimum configuration and the experimental STM data discussed next. Note that this local minimum more likely conforms to an asymmetric pyrrole stretch mode, similar to that observed for (NO)Fe–TPP,[Rai02] than an actual rotation of the molecule.

According to our Bader analysis, the Co–P molecule receives 0.66 e^- from the Cu(111) substrate. Upon adsorption, the N atoms keep almost the same Bader valence charge (a 0.03 e^- increase), whereas Co gets 0.24 e^-, C atoms get 0.72 e^-, and H atoms lose 0.33 e^- with respect to isolated gas-phase Co–P. Upon Co–P adsorption, the work function of the system is predicted to decrease by 0.59 eV.

Comparison of experimental and DFT results

Simulated and measured STM images of an isolated Co–P molecule are shown in Figure 5.6. The simulated images were obtained from a DFT-optimized Co–P on an $8 \times 8 \times 4$ slab of Cu(111). For tunneling into unoccupied states ($U_b = 0.5$ eV, Figure 5.6a–c), the experimental STM image, recorded with a CO-functionalized tip, features two bright lobes on the macrocycle that are mirrored across one axis of the molecule. The corresponding simulated STM image correctly reproduces these lobes, however, as pointed out by Gross *et al.*,[Gro11] a p-wave tip orbital (in our case the p_x) is required to mimic the CO-functionalized STM tip and to reproduce the fine sub-structure with all details. Both, experimental and simulated images show no significant signal at the position of the Co atom. For tunneling from occupied states ($U_b = -0.5$ eV, Figure 5.6d–f), the STM image maps the central Co atom as a bright protrusion, the global appearance being well reproduced by the simulated images. Similar findings have been reported for Co–Pc on Cu(111) [Cua10] and Cu–P/Cu(111).[Dil13b]

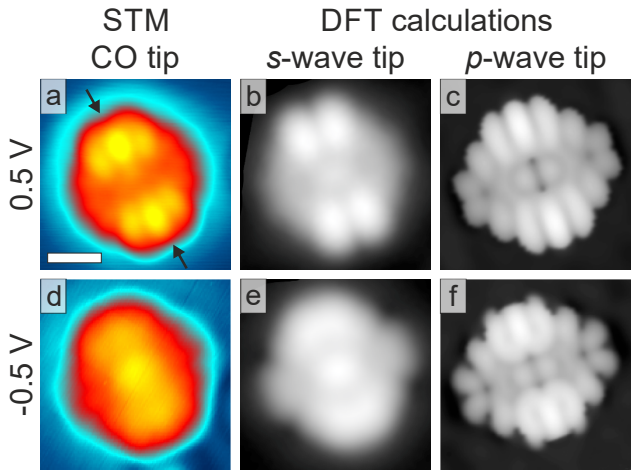

Figure 5.6: *Comparison between experimental and simulated STM images of Co–P/Cu(111). **(a,d)** Experimental STM images of an individual Co–P molecule imaged with a CO-terminated tip displaying the unoccupied and the occupied states, respectively. The black arrows in (a) indicate the $\langle 11\bar{2} \rangle$ direction of the crystal. The corresponding simulated images from DFT using an s-wave tip (displayed in **(b,e)**), as well as a p-wave tip (displayed in **(c,f)**) are in good agreement with the experimental STM images. Specifically, the saddle-shape conformation is reproduced, and the Co center becomes visible at negative bias voltage. Notably, p_x-wave tip orbitals are essential to mimic the three-lobe fine structure observed in the experiment. Scan parameters: (a) $U_b = 0.5\,\mathrm{V}$, $I_t = 0.8\,\mathrm{nA}$; (b) $U_b = -0.5\,\mathrm{V}$, $I_t = 0.68\,\mathrm{nA}$. Scale bar: 0.5 nm.*

A side-view of the structural Co–P model is displayed in Figure 5.5a, indicating that the twofold geometry results in an asymmetric saddle-shape-like conformation with the pyrrole rings along the densely packed $\langle 11\bar{2} \rangle$ directions sitting significantly higher above the surface than those along the $\langle 1\bar{1}0 \rangle$ directions, with the macrocycle being rather flat along the latter direction (see Figure 5.5b). The significant difference in height between the spectroscopically inseparable species (∼0.5 Å for the C–C species, see Figure 5.5c) aids to rationalize the significant decrease in coherent fraction observed in the XSW measurements. We want to point out, that the correlation between the strong contrast observed in STM images and the geometric structure predicted by DFT is in line with previous reports on the structure of functionalized porphyrins.[Auw10, Web08]

The vertical heights of the atomic species obtained by DFT were used to calculate geometric factors, a_{111} (one of three parameters that are used to model the coherent fraction, see appendix D.0 and Refs. [Woo05, Sch17b] for details), for the N, C–C and C–N species in the Co–P molecule (see Table 5.2). The geometric factors qualitatively model the experimentally measured trend in coherent fraction; however, for all species, the geometric factor is predicted to be too large to solely explain the observed coherent fractions (assuming an order factor of ∼0.90, the coherent fraction observed for Co 2*p*). Were these predicted geometric factors correct, and if the order factor is indeed ∼0.90, then, to explain the observed coher-

ent fractions for the C–C species, a Debye-Waller factor (D–WF) of 0.43 would be required. Such a D–WF would correspond to a very large root mean square vibrational amplitude of 0.53 Å, and thus a Debye temperature of only ∼100 K. It is unlikely that the C atoms would exhibit such an extreme vibrational amplitude, especially considering that the vibrational amplitude of the central Co atom must be significantly smaller. Another explanation for this quantitative disagreement may lie in the nature of the DFT calculations, which model the adsorption at 0 K, whereas the experiments were performed close to 300 K. Thus, finite temperature effects[Mer13] such as an adsorption potential of the pyrrole ring adsorbed along the $\langle 11\overline{2}\rangle$ directions that is strongly repulsive for small decreases in adsorption height, but weakly attractive for large increases, could well result in a significant change in the difference between in the mean adsorption of the two pairs of pyrrole rings.

5.1.4 Discussion

At low coverage, the adsorption of Co–P is driven by a dominating repulsive intermolecular interaction, together with a strong molecule-substrate interaction. This is evidenced by the tendency of molecules to remain far apart from each other (Figure 5.2a) and is fully in line with the previous studies that have shown sub-monolayer coverages of porphine molecules resulting in isolated molecules on the Ag(111) and the Cu(111) surface.[Bis13, Dil13b] Importantly, the determined adsorption geometry is therefore dominated by molecule–substrate interactions. Upon adsorption on the Cu(111) surface, the symmetry of the Co–P molecule is reduced from a fourfold D_{4h}-symmetry in gas phase to a two-fold symmetry on the surface. As demonstrated here, a moderate asymmetric saddle-shape conformation contributes to this symmetry reduction. Although geometric origins for the symmetry reduction on coinage metal surfaces could never be detected experimentally for porphines so far,[Dil13b, Bis13] deformations have been reported for larger tetrapyrrole derivatives. In the case of Co–Pc [Cua10] and Fe–Pc[Sne15] on Cu(111), the deformation results in one of the molecular axes getting closer to the surface, whereas in the case of 2H–TPP on Cu(111),[Dil12] or Co–TPP on Cu(110),[Don10] a more severe non-planar deformation is observed, revealing the conformational flexibility of these compounds. Interestingly, our own DFT calculations predict that copper-metalated porphine (Cu–P) is flat on Cu(111).

The only single-site interpretation of the XSW triangulation compatible with the experimental results involves adsorption in a bridge site, which would have an expected $p^{1\bar{1}1}_{theo} = 0.86$ (see appendix D.1) and $f^{1\bar{1}1}_{theo} = 0.33 \cdot f^{111}_{exp}$,[Woo05] compared to the experimental value of $p^{1\bar{1}1}_{exp} = 0.91 \pm 0.03$ and $f^{1\bar{1}1}_{exp} = 0.50 \pm 0.06$. As discussed above, although the measured coherent fraction is higher than would be expected, this effect is attributed to the detector non-linearity.[Blo17] However, if a two-site model is considered, then this coherent fraction

and position would correspond to coadsorption in hcp and fcc hollow sites. Such coadsorption is clearly refuted by the STM measurements, which only observe three distinct orientations of the Co–P molecules. A mixture of hcp and fcc sites would necessitate the presence of six possible orientations as the hcp site is a false mirror image of the fcc site. Furthermore, the analysis of the STM images, based on the well-known CO adsorption site on Cu(111) as well as the DFT prediction of the bridge site, corroborates the single-site interpretation. The same adsorption site has been proposed for 2H–P as well as for other metal derivatives[Auw07a] on Cu(111) indicating that the Co–Cu interaction does not dictate the bridge adsorption site.

The binding energy of the Co $2p_{3/2}$ core-level peak was found to be 778.2 eV, which is more compatible with a Co(0) oxidation state (778.1 eV for Co metal[Wag79]), than with the expected nominal oxidation state of +2 (780.0 eV for Co–TPP multilayer on silver[Luk07]). This results from the pronounced different electronic environment between these systems (metal, molecular multilayer and molecular monolayer on a metal). It can be mostly explained by the differing abilities of each system to screen the core hole left by the photoemission process and is thus a final state effect, as observed on numerous porphine-based species on various substrates.[Dil13b, Luk07, Wie14] Thus, such final states effects on the binding energy can dominate over the contribution from charge transfer. This is a strong reminder of the dangers of assigning oxidation state by simple inspection of binding energy. The significant overlap between the orbitals of the Co atom and the substrate, implied by the charge transfer, suggests that the primary local interaction between the substrate and the molecule is through the Co atom; thus its adsorption height markedly below the macrocycle. It is therefore likely that the Co–P would exhibit a significant surface trans-effect.[Dei16, Hie11] Note also that the determined adsorption heights are reduced compared to the 2.40 Å reported for 2H–P/Cu(111) in DFT calculations.[Mül16]

Furthermore, we were not able to resolve any signature of a Kondo resonance on the Co–P molecule by STS experiments conducted with a metallic tip. Observation of a Kondo signal is possible when the unpaired electron of the magnetic adsorbate is neither too weakly nor too strongly coupled to the substrate electron bath.[Kom14] It has been shown that switching of the Kondo effect in Co–tetrapyridyl porphyrin (Co–TPyP) on Cu(111) can be controlled *via* intermolecular interactions.[Zha15] In our case, the isolated gas-phase Co–P has a magnetic moment of 1.0 μ_B and a spin density clearly localized on the half-filled $3d_{z^2}$ orbital of the Co atom. However, upon adsorption, the $3d_{z^2}$ orbital of the Co atom interacts strongly with the Cu(111) substrate leading to a complete quenching of the magnetic moment of the Co–P. This assertion is in line with previous DFT calculations,[Cua10, Che10b] and experimental studies[Ann11] on Co–Pc/Cu(111) that also report a modification of the magnetic properties of the molecule upon adsorption. Although the quenching of magnetic properties, the sizable

charge transfer (0.66 e^-), and the large total adsorption energy (−4.80 eV) might suggest the Co–P molecules being strongly chemisorbed on the Cu(111) substrate, this interpretation has to be regarded with caution: In fact, vdW corrections dominate the total adsorption energy (−4.55 eV compared to −0.25 eV without vdW correction).

5.2 Adsorption Geometry of Cobalt Porphine on *h*-BN/Cu(111)

After the quantitative structure determination of Co–P on Cu(111) in the previous section, the impact of the decoupling *h*-BN layer on the adsorption height and the molecular conformation of Co–P will be discussed in this section. 2D epitaxial materials have increasingly been employed as decoupling layers in recent years, templating the adsorption and the self-assembly of molecules and atoms.[Kum17, Jos14] Research in this field is driven by both the ambition to tune the electronic properties of the 2D materials *via* a periodic potential modulation by molecular superstructures,[Cai15, Che07, Col10, Vog08, Das08, Mac14a, Tan11] as well as the interest in the characterization of fundamental intrinsic properties of adsorbates without the often appreciable perturbation provided by the underlying metal substrate.[Uih15] In particular the strong hybridization of molecular orbitals with metal states can be prevented by insulating spacer layers such as *e.g.* *h*-BN that electronically decouple the adsorbate.[Hir06, Rep05b, Cho12, Rep04a]

Molecule–substrate interactions are governed by the structural and electronic landscape of the *h*-BN/metal system and affect the self-assembly together with intermolecular interactions. In order to understand those intermolecular interactions, a precise knowledge of the adsorption structure of the molecule is crucial.[Tau07, Mer13] The adsorption geometry of organic molecules on metal substrates was subject to various experimental and theoretical studies in the last decade.[Bür13, Auw07a, Alb16] In particular atomic force microscopy and the X-ray standing wave (XSW) technique have proven their potential to enable a detailed and quantitative structure determination.[Sch13a, Sta06] Very recently, hydrogenated *h*-BN on Ni(111) has been studied by means of XSW,[Oht17] however, an experimental approach to obtain information on the modified molecular conformations of relatively large organic molecules on *h*-BN layers is still lacking, despite being highly relevant for benchmarking the various DFT calculations investigating adsorbates on *h*-BN sheets.[Tan11, Die14, Lee13, Al-15, Yu14, Che16, Zha16, Mat16, Kor15, Cac12] Additionally, the effect that molecules exert on the 2D layer has yet to be characterized experimentally.

Herein, we report the first quantitative experimental structure determination of an organic molecular adsorbate on an *h*-BN monolayer. We choose the tetrapyrrole compound cobalt

porphine (Co–P) on *h*-BN/Cu(111) as a model system to study the adsorption geometry and interaction of the molecule with the substrate in a combined approach based on XSW and STM. The geometric structure of both pristine *h*-BN and Co–P on Cu(111) have separately been determined quantitatively (see sections 4.1 and 5.1).[Sch17b, Sch18a] The *h*-BN layer was found to display an average adsorption height of 3.38 ± 0.04 Å and exhibits a moderate geometric corrugation of 0.3 to 0.7 Å.[Sch17b] Co–P molecules on Cu(111) were determined to adsorb in a single site, with the Co atom bridging surface Cu atoms at a height of 2.25 ± 0.04 Å.[Sch18a] The molecular backbone of the Co–P molecule presents an asymmetric saddle-shape-like conformation due to the strong interaction between the Co atom and the copper substrate. Our results presented here indicate that photoemission-based techniques are capable of characterizing adsorbates on insulating epitaxial layers quantitatively and shed light on the degree of interfacial interaction still present in those systems. Profound knowledge of the interfacial interaction in metal/insulator/semiconductor structures is essential for potential applications in future nanoscale hybrid devices. Further, we report the effect of coverage and temperature on the adsorption height of molecular structures on *h*-BN/Cu(111).

Experimental Methods

The STM experiments were performed in the LT-STM setup and the XPS and XSW measurements were carried out at the I09 beamline at Diamond Light Source (see section 3.7) as outlined in detail in the previous section 5.1. In total 17 distinct sample spots were used for the XSW measurements at 50 K, resulting in nine individual XSW spectra for Co 2*p*, three for C 1*s*, three for N 1*s* and two for B 1*s*. For the measurements at 300 K, in total 20 distinct sample spots were used, resulting in eight individual spectra for Co 2*p*, eight for C 1*s*, two for N 1*s* and two for B 1*s*.

For our XPS and XSW measurements we used a low Co–P coverage of ∼0.15 to 0.2 ML, comparable to the situation displayed in Figure 5.7a. The molecular coverage was calculated with the cross-section corrected peak areas of the Co–P core levels and the Cu substrate. We neglect the attenuation of the Cu peak by the *h*-BN layer and the adsorbates, which lowers the measured signal from the substrate and renders the calculated value an upper limit. Based on the strikingly different modulations of the individual N 1*s* components in XSW measurements (see Figures D.3, D.5 and D.6), we were able to differentiate in the XPS data between the nitrogen species of the *h*-BN layer and those assigned to nitrogen atoms in the Co–P. In accordance with the results of the previous section 4.1, two boron and nitrogen components were identified and assigned to the *h*-BN layer ($B_0 = 190.4$ eV and $N_0 = 398.1$ eV, respectively) and defective polymeric BN fragments ($B_{def} = 191.0$ eV and $N_{def} = 398.5$ eV), whereby the latter will be neglected in this section.

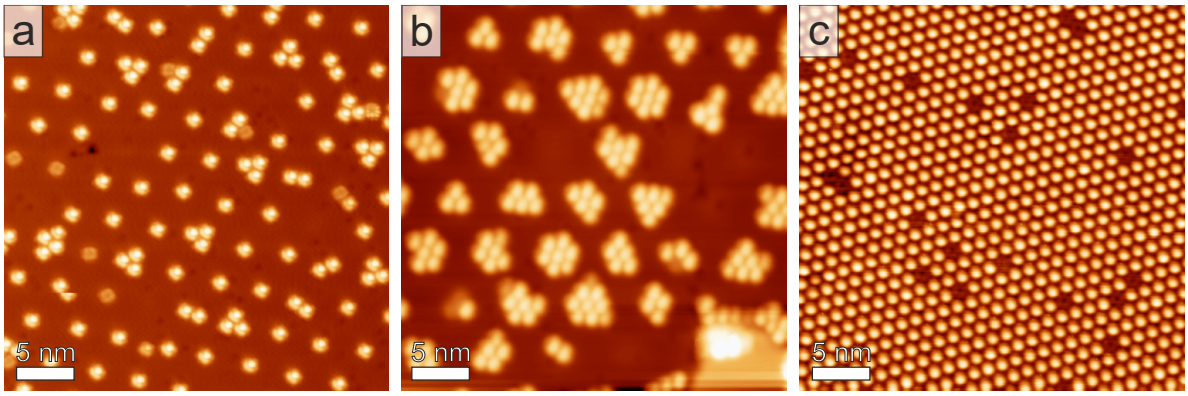

Figure 5.7: *STM images displaying the evolution of the Co–P adsorption on h-BN on Cu(*111*) with coverage.* ***(a)*** *The molecules adsorb in the pores of the h-BN layer at low coverage (*∼0.15 ML*).* ***(b)*** *Increasing deposition leads to larger islands in the pores (*∼0.3 ML*), before a full monolayer is formed* ***(c)****.*

5.2.1 Site-Specific Adsorption

The Co–P molecules show a site-specific adsorption on the *h*-BN monolayer on Cu(111). STM images taken at 6 K identify island formation starting from the pores of the *h*-BN layer (Figure 5.7a,b), which were determined to be closer to the metal substrate (see section 4.1.3) and present a lower local work function.[Sch17b, Jos12] Independent of the *h*-BN moiré size, these islands seem to grow from mainly individual molecules in the center of the pores, forming a nearly regular array of single molecules at very low coverage (Figure 5.7a). Increasing deposition of molecules leads to larger islands confined on the pores (Figure 5.7b) until a densely packed, uniform coverage across the whole *h*-BN layer is achieved (Figure 5.7c), which defines one monolayer (ML) of molecules according to the convention adopted here.

In the low Co–P coverage regime (∼0.15 ML, see STM image in Figure 5.7a, XPS in Figure 5.8 and XSW in Figures 5.9, D.3, D.5 and D.6) the Co $2p_{3/2}$ core-level line in XPS (Figure 5.8d) exhibits two clear peaks consisting of three features, labelled Co_1, Co_2, and Co_3. The former two features are assigned to two chemically distinct species (discussed below), the latter species is assigned to a satellite feature, presumably due to coupling of the core hole to unpaired electrons in the partially filled Co 3*d* shell (multiplet splitting).[Luk07, Mas14, Met16]

The binding energies of the Co_1 and Co_2 components are 780.3 eV and 781.1 eV, respectively, which are both clearly increased compared to the value of 778.2 eV recorded for the Co–P/Cu(111),[Sch18a] as well as the 778.0 eV reported for metallic Co.[McI02] Notably, the binding energy of the main Co $2p_{3/2}$ component of sub-monolayer Co-tetraphenyl-porphyrin (Co–TPP) on Ag(111) is also 778.2 eV,[Luk07, Auw10] and increases to 780.5 eV for multilayer coverages, due to the absence of the substrate-induced core-hole screening effects and,

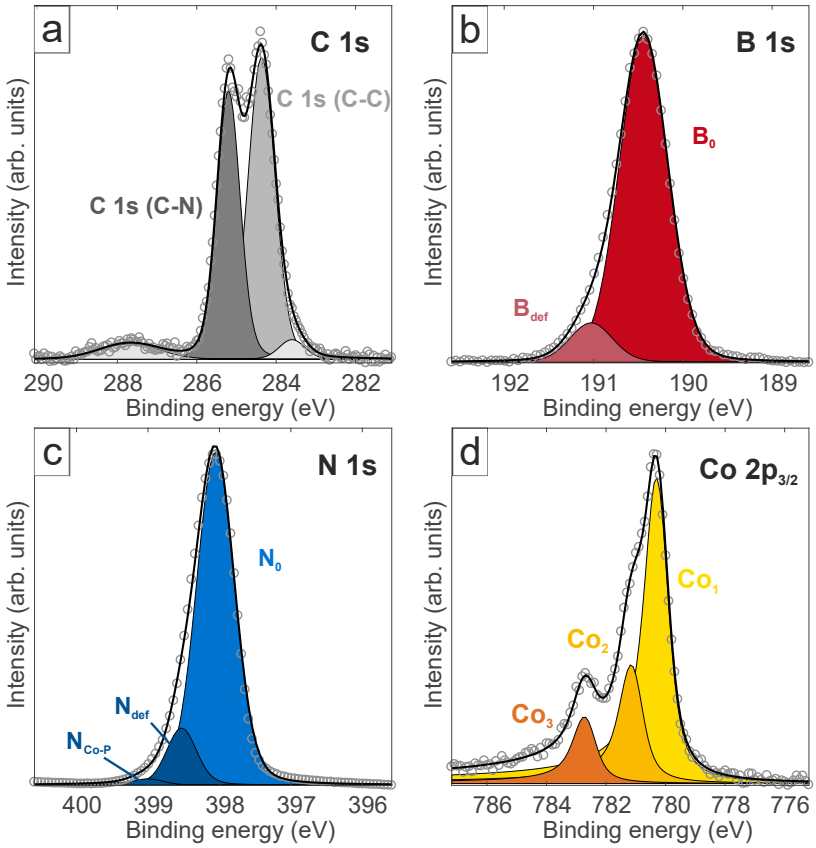

Figure 5.8: *XP spectra of the* ***(a)*** *C 1s,* ***(b)*** *B 1s,* ***(c)*** *N 1s and* ***(d)*** *Co 2p core levels of a low-coverage (∼0.15 ML) sample of Co–P on h-BN/Cu(111) recorded at* 50 K.

more noticeably, the change of the formal oxidation state at the organic-metal interface. The binding energy for Co–P/Cu(111) was ascribed to adsorption-related charge transfer from the copper substrate into the Co ion. Thus the significant increase in binding energy here is suggestive of, at least, a dramatic decrease in any such charge transfer. However, the significant binding energy shift (0.8 eV) between the Co_1 and Co_2 species could still be explained by a muted charge transfer to the former species or, more likely, a final state effect during the photoemission process (see discussion below).

In the high coverage regime (∼0.95 ML, see Co $2p_{3/2}$ XPS in Figure D.4, Co $2p_{3/2}$, B 1*s*, N 1*s*, C 1*s* XSW in Figure D.6), roughly the same line shape was observed for the Co $2p_{3/2}$ XPS data recorded at 300 K (Figure D.4), however the intensity ratio of Co_2 to Co_1 differed significantly. Specifically, at a coverage of ∼0.15 ML the Co_2:Co_1 ratio was ∼ 1 : 2.6, while at a coverage of ∼0.95 ML it increased to ∼ 1 : 1.5. Thus the Co_1 species (lower binding energy) is more dominant at low coverage, suggesting that the shift is related to the adsorption site in the pores. The C 1*s* and N 1*s* XP spectra (Figure 5.8, coverage ∼0.15 ML) of the Co–P both present a smaller upshift in binding energy of 0.4 eV, compared to Co–P/Cu(111).[Sch18a] The XPS data are summarized in Table 5.3.

Core level	E_b^0 (eV)	Γ (eV)	σ (eV)
C 1s (C–C)	284.4	0.12	0.63
C 1s (C–N)	285.2	0.12	0.54
B 1s (B_0)	190.4	0.08	0.50
B 1s (B_{def})	191.0	0.08	0.46
N 1s (N_0)	398.1	0.11	0.48
N 1s (N_{def})	398.5	0.11	0.37
N 1s (N_{CoP})	399.0	0.11	0.38

Table 5.3: *XPS fit parameters for the atomic species of Co–P/h-BN/Cu(111) comprising the peak position E_b^0, Lorentzian width Γ and Gaussian width σ obtained from the fits for the indicated components. Voigt line shapes are used for the curve-fitting of all core-level spectra.*

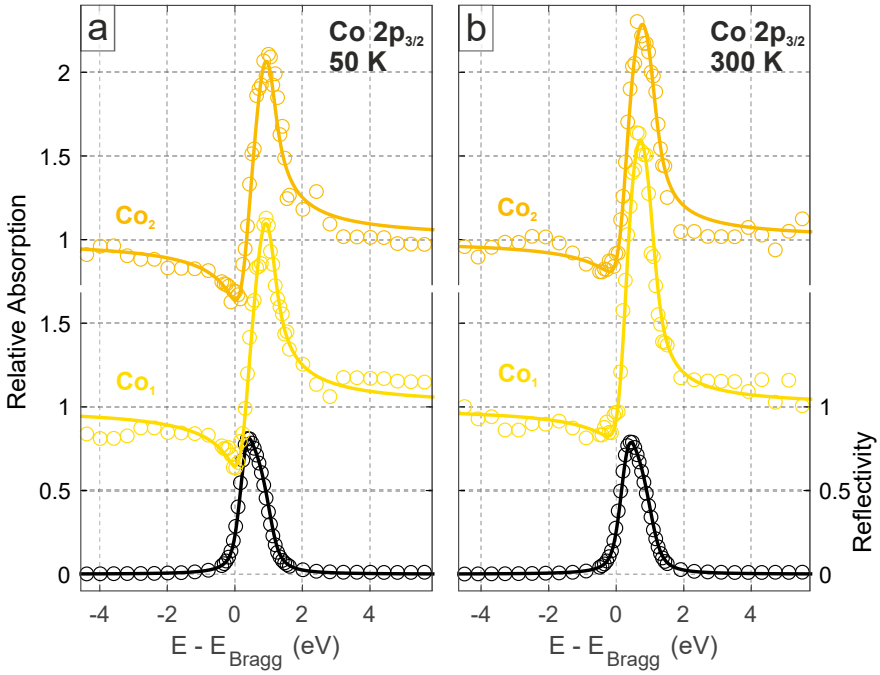

Figure 5.9: *Normal-incidence XSW Co $2p_{3/2}$ absorption profiles of Co–P on h-BN/Cu(111) in the low coverage regime (∼0.15 ML) at the (111) Bragg reflection acquired at* ***(a)*** 50 K *and* ***(b)*** 300 K*, respectively. Solid lines are fits to the data. Black data points are the reflectivity curve.*

5.2.2 Adsorption Height

The XSW data for Co_1 and Co_2 in the low coverage regime, obtained from the photoelectron yield of the Co $2p_{3/2}$ core level, are shown in Figure 5.9. In this regime the XSW data were acquired at two distinct temperatures: 300 K (room temperature) and 50 K. It is clear that the data for both Co species and both temperatures are largely similar, though subtle differences can be observed as both a function of species and temperature. The corresponding XSW profiles from the N 1s, C 1s and B 1s core levels are shown in Figures D.3 and D.5;

		Low coverage, 50 K			**Low coverage,** 300 K		
	Core level	f^{111}	p^{111}	Adsorption height $\overline{h}_0$ (Å)	f^{111}	p^{111}	Adsorption height $\overline{h}_0$ (Å)
Co–P	C 1*s* (C–C)	0.49 ± 0.04	0.06 ± 0.02	6.38 ± 0.04	0.32 ± 0.04	0.13 ± 0.02	6.53 ± 0.04
	C 1*s* (C–N)	0.53 ± 0.04	0.05 ± 0.02	6.37 ± 0.04	0.37 ± 0.04	0.10 ± 0.02	6.47 ± 0.04
	N 1*s* (N_{CoP})	0.47 ± 0.05	0.00 ± 0.04	6.26 ± 0.08	0.37 ± 0.08	0.12 ± 0.03	6.51 ± 0.06
	Co 2*p* (Co_1)	0.67 ± 0.04	0.98 ± 0.02	6.22 ± 0.04	0.59 ± 0.05	0.12 ± 0.02	6.51 ± 0.04
	Co 2*p* (Co_2)	0.68 ± 0.06	0.98 ± 0.03	6.22 ± 0.06	0.51 ± 0.05	0.06 ± 0.03	6.39 ± 0.06
	Co 2*p* (Co_3)	0.69 ± 0.09	0.98 ± 0.04	6.22 ± 0.08	0.60 ± 0.14	0.03 ± 0.07	6.32 ± 0.14
h-BN	B 1*s* (B_0)	0.58 ± 0.04	0.58 ± 0.02	3.30 ± 0.04	0.69 ± 0.04	0.63 ± 0.02	3.40 ± 0.04
	N 1*s* (N_0)	0.58 ± 0.02	0.58 ± 0.02	3.30 ± 0.04	0.69 ± 0.02	0.61 ± 0.01	3.36 ± 0.02

Table 5.4: *Comparison of the structural parameters of the XSW analysis of Co–P/h-BN/Cu(111) at* 50 K *and at* 300 K*. The table summarizes the coherent fraction* f^{111}*, the coherent position* p^{111} *and the mean adsorption height* $\overline{h}$ *for all atomic species in the Co–P molecule and the h-BN layer.*

table 5.4 summarizes the coherent fraction, coherent position, and absolute heights of all core levels. The adsorption height of Co–P above the *h*-BN layer at low coverage is 3.01 to 3.15 ± 0.06 Å at 300 K (Figure 5.10), slightly reduced compared to the predictions of DFT for other organic molecules such as benzene (3.29 Å) and borazine (3.24 Å),[Cac12] TCNQ (3.49 Å),[Tan11] or functionalized porphyrins (3.37 Å)[Kor15] on freestanding *h*-BN sheets as well as phthalocyanines (Pc) on *h*-BN/Rh(111) (∼3.25 Å).[Ian14] Notably, the Co_1 species have a greater adsorption height at room temperature compared to Co_2 (see Table 5.4).

Interestingly, for all elements in the Co–P molecule, the adsorption height at 300 K was significantly higher than at 50 K. The largest single increase is that of the Co_1 species, whose adsorption height, with respect to the underlying copper surface, increases by 0.29 ± 0.06 Å, ∼30 times greater than the thermal expansion of copper over the same temperature range. Even more remarkably, the difference in adsorption height was larger for the Co_1 species compared to the Co_2, where a more modest increase in height by a 0.17 ± 0.08 Å was recorded. Notably, even the *h*-BN layer exhibits an increase in mean adsorption height with temperature of 0.10 ± 0.06 Å (B 1*s*) and 0.06 ± 0.04 Å (N 1*s*), respectively. One should note that this is only slightly larger than the error bars, however the trend agrees well with the XSW data recorded at 300 K and the 0 K predictions by DFT (see section 4.1 and appendix C.0.2). It should be noted that the measurements for the two temperatures were performed on two different preparations of the *h*-BN layer and therefore have to be regarded with caution. Nevertheless, we will briefly discuss the observed indications of a pronounced temperature dependence below.

The XSW data of the high coverage regime (∼0.95 ML) recorded at 300 K are shown in Figure D.6 and summarized in Table D.1. The obtained mean adsorption height of the *h*-BN

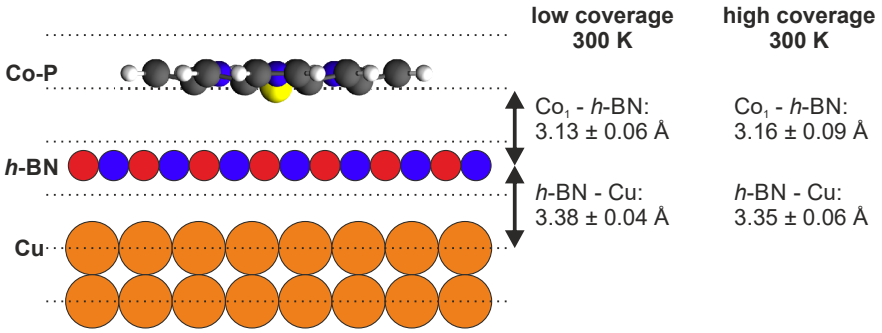

Figure 5.10: *Schematic model of Co–P on h-BN/Cu(111) with the indicated adsorption heights of the h-BN layer and the Co–P at* 300 K *for low (*∼0.15 ML*) and high (*∼0.95 ML*) coverage.*

layer (B: 3.36 ± 0.06 Å, N: 3.34 ± 0.03 Å) is slightly reduced compared to the low coverage regime, however within the error bars. Regarding the Co–P, a significant reduction of the coherent fractions is observed for all elements, accompanied by an appreciable increase of the main adsorption height (3.14 to 3.29 ± 0.08 Å). Specifically, the Co, N and C species adsorb in average up to ∼0.14 Å higher than at low coverage, which can be understood by the *h*-BN corrugation leading to the occupation of *h*-BN areas that are more distant from the copper substrate. Again, XSW measurements conducted on the same sample at 200 K (see Table D.1) indicate that the mean adsorption height decreases for all elements as discussed above.

Focusing on the subtle details of the adsorption geometry, the molecular backbone of Co–P appears significantly more planar than on the Cu(111) surface (see section 5.1.2). Specifically, at 300 K, no difference was observed in the coherent fractions between the N atoms and the C–N carbon atoms in Co–P, whereas on the bare Cu(111) surface a difference of 0.50 ± 0.07 was found (see section 5.1.2). The Co_1 species was found to be completely coplanar with its neighboring N atoms (difference of 0.00 ± 0.06 Å), whereas the Co_2 was displaced below the N plane with a difference in height of 0.12 ± 0.08 Å, similar to that observed on bare Cu(111) (0.08 ± 0.07 Å).[Sch18a]

5.2.3 Discussion

In summary, based on STM observations we propose a Co–P island formation starting on the pore areas of *h*-BN, in line with reports of free-base porphine (2H–P) molecules on *h*-BN/Cu(111).[Jos14] The reason for this site-specific adsorption lies in the geometric and electronic surface potential modulation of the *h*-BN layer.[Bru09] As the moiré sizes of *h*-BN/Cu(111) differ between 1 to 15 nm,[Jos12, Sch17b] an unambiguous determination of whether the nucleation site is perfectly centered or located at the rim of the pores was not

possible, in contrast to a report on Pc/*h*-BN/Rh(111) where an off-centered adsorption site is explained by the lateral gradient of the electrostatic potential along the nanomesh.[Ian14]

In the XPS measurements, a distinctly separated Co signature was observed, and the XSW measurements clearly demonstrate that the presence of two inequivalent Co species is the origin of this separation. A similar inhomogeneous interaction between molecular species and the substrate has recently been reported for Co–TPP on MgO thin films grown on Ag(100).[Fra17] The 0.8 eV shift to lower binding energy in the Co $2p_{3/2}$ XPS, might suggest charge transfer into the Co metal center for the Co_1 species, *via* tunneling through the *h*-BN layer from the underlying copper substrate. It is unlikely that this charge transfer comes from the *h*-BN layer itself, as the latter is a wide band gap insulator, and has no density of states near the Fermi level.[Koi13, Gar16] A transfer of electron density through an *h*-BN layer has previously been reported for graphene sheets grown on *h*-BN.[Kim13, Gao15, Bok11] Specifically, Bokdam *et al.* predicted by means of DFT calculations an intrinsic *n*-type doping of graphene in metal/*h*-BN/graphene stacks even for multiple *h*-BN layers due to interfacial dipole formation.[Bok11] An experimental observation of interfacial charge transfer in the case of vertical *h*-BN/graphene heterostructures on copper has been reported by Gao *et al.* using electrostatic force microscopy.[Gao15] However, STS measurements of Co–P, as well as Co–TPCN, on *h*-BN/Cu(111) show Co-related states only above the Fermi energy (*cf.* Figure 5.12e) on any region of the *h*-BN moiré, refuting the interpretation comprising a charge transfer to the Co–P molecules. This observation is in contrast to Co–Pc/*h*-BN/Ir(111), where a shift of the Co resonance below the Fermi level (*i.e.* a charging of the molecule) has been observed for molecules adsorbed on the pores.[Sch13b, Sch15b] The exact origin of the shift in binding energy between Co_1 and Co_2 remained unclear, with the current working hypothesis being a final state effect, such as polarization screening of the core hole through neighboring atoms or a magnetic interaction, as the possible reason for the observed separation. This question will be further investigated by DFT and through additional experiments in an upcoming beamtime (see Chap. 7).

The system also exhibited a temperature dependence in adsorption height of the Co–P between 50 K and 300 K, indicating an asymmetrical vibrational mode of the Co–P due to it being weakly bound to the *h*-BN layer. If a Co–P molecule were to be moved toward the *h*-BN layer, it would experience a strongly repulsive force, while when moved away from the *h*-BN layer, it would only experience a weakly attractive force as a consequence of the weak van der Waals bonding causing an asymmetrical adsorption potential well. Consequently, although the modal adsorption height may not vary as a function of temperature, the mean adsorption height will. The observed indications are highly remarkable since DFT calculations were usually performed at zero kelvin and compared to measurements performed at higher temperatures. The poor agreements are often rationalized with finite temperature

effects, which have been predicted,[Mer13] but, to the best of our knowledge, never measured experimentally before. The obtained results show that a systematic investigation is required to clarify this effect on the individual components of the system under investigation and might be extended to related systems.

While the *h*-BN layer does significantly decouple the adsorbate electronically from the underlying substrate, this decoupling is not total, and, at least, a significant proportion of the molecules cannot be considered free-standing. This implies that a substrate that perturbs the *h*-BN layer even less is likely required (*e.g.* SiC, Ag, Au) to obtain a more idealized approximation of adsorption on an insulating substrate. Notably, we observed that the Shockley surface state is slightly modified upon adsorption of *h*-BN on Ag(111) (see section 4.2), implying that a small interaction between layer and substrate remains. However, Uihlein *et al.* reported recently that charge transfer to cobalt phthalocyanines on graphene/Ni(111) can be prevented by intercalation of gold.[Uih15] Nonetheless, the reported interaction between the organic semiconductor Co–P and the metallic copper substrate suggest a potential for ultra-thin organic field effect transistors.

5.3 Metal-Organic Coordination Network on *h*-BN/Cu(111)

After the quantitative structure determination of the base-unit Co–P in the two prior sections, this section describes experiments using substituted porphyrins. Through carbonitrile-functionalization, the intermolecular interactions can be modified, in this case leading to the formation of a metal-coordinated nanoarchitecture that has been studied by means of STM.

Contemporarily, the combination of atomically thin sheets of sp^2-hybridized boron nitride (*h*-BN) or graphene with complex molecules has emerged as a powerful strategy to functionalize surfaces and engineer structural, electronic, magnetic, optical, or catalytic properties of such low-dimensional materials.[Sch14a, Qui13, Xu09, Gar13a, Jos12, Xue12] In this context, metal-organic coordination networks presenting organized arrays of metal centers and functional molecular linkers are highly appealing.[Bar07] By contributing their inherent functionality exploited in many natural and artificial systems, versatile tetrapyrrolic macrocycles like porphyrins and their derivatives play an important role in such architectures.[Moh10, Bur01, Auw15] For example, oxidized graphene embedded in a porphyrin-based metal-organic framework shows significant catalytic activity,[Jah12] and graphite surfaces can be patterned by porphyrin-based metal-organic networks stabilized at the solid-liquid interface.[El 14] In an ultra-high vacuum (UHV) scenario, a variety of model systems based on molecules adsorbed on sp^2 overlayers were characterized with sub-molecular resolution, exploiting the real-space

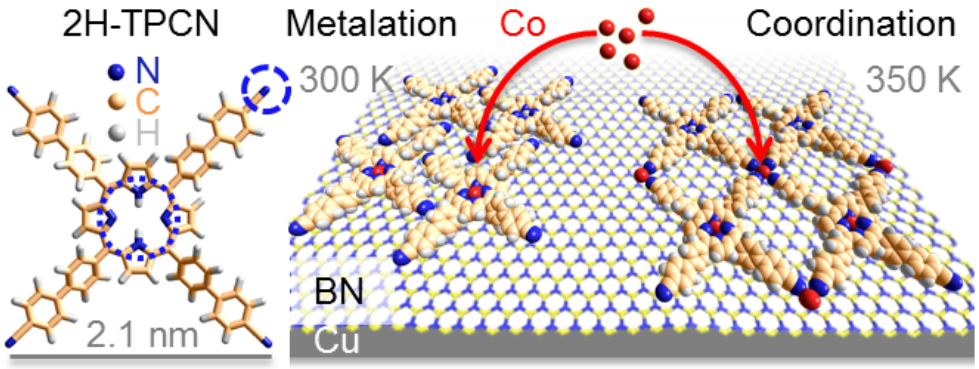

Figure 5.11: *Schematic illustration of two complexation pathways of a CN-functionalized porphyrin derivative (free-base tetra[(4-cyanophenyl)-phen-4-yl]porphyrin, 2H–TPCN) on a h-BN monolayer on Cu(*111*) upon exposure to Co atoms: macrocycle metalation and formation of a metal-organic coordination network. The two competing ligand functionalities of 2H–TPCN, the tetrapyrrole pocket (dotted circle) and the peripheral CN (dashed circle), are highlighted in the left panel.*

imaging capabilities of scanning tunneling microscopy.[Mac14b] Achievements include molecular gating,[Ris14] switches,[Mun05] magnetic order,[Gar13a, Her13] self-assembly of molecular aggregates,[Pol10, Ma10, Mao09, Jos14] or, only very recently, on-surface synthesis of covalent assemblies.[Die14] However, neither coordination networks including functional molecules nor metalation of macrocyclic compounds are reported to date, in striking contrast to the manifold metallo-supramolecular architectures and surface-confined reactions achieved and comprehensively characterized on metal single crystals.[Bar07] This is remarkable, as sp^2-hybridized sheets can be grown with high structural quality *via* scalable chemical vapor deposition (CVD) protocols on diverse supports as large-scale processable Cu foil,[Kim12] offering potential for mass production of molecule/sp^2 hybrid systems. In this respect, the ultimate thinness of a *h*-BN monolayer discriminates *h*-BN/Cu substrates from other insulating films or bulk supports used, *e.g.* for the assembly of porphyrin aggregates[Mai08] or metal-organic sheets[Abe11] and makes them fascinating platforms for 2D metallo-supramolecular nanostructures.[Jos12, Jos14] Specifically, the decoupling of coordination nodes from a metallic substrate creates possibilities to sustain magnetic moments, oxidation states, or catalytic activity otherwise impaired.

In the following sections, we introduce an exemplary surface-confined coordination architecture on an sp^2-hybridized *h*-BN sheet. To this end, we combine carbonitrile-functionalized free-base porphyrins (2H–TPCN) and Co atoms under UHV conditions on a *h*-BN monolayer grown on Cu(111) *via* CVD. Figure 5.11 sketches the two on-surface complexation reactions of 2H–TPCN upon exposure to the atomic beam of Co: the metalation reaction occurring

with the tetrapyrrolic macrocycle and the CN-Co coordination governing the formation of metal-organic networks.

Experimental Methods

The experiments were performed in the LT-STM system operating at 6 K.[Seu11a, Wie15, Urg15a] The *h*-BN spacer layer on Cu(111) was prepared as detailed in section 4.1. The 2H–TPCN molecules were synthesized by D. Stassen and D. Bonifazi [Bon17] at UNamur and deposited using organic molecular beam epitaxy (OMBE) from a quartz container held at 740 K. During deposition, the *h*-BN/Cu(111) substrate was kept at room temperature. Co was evaporated from a water-cooled cell by resistively heating a tungsten filament surrounded by a Co wire (99.995 % purity, Alfa Aesar). All STM images were recorded in constant current mode and the scanning tunneling spectra (STS) were taken using a lock-in amplifier ($f = 969$ Hz, $\Delta V_{rms} = 18$ mV).

5.3.1 Metalation of the 2H–TPCN Network

Figure 5.12a displays a constant-current STM image of an 2H–TPCN array on *h*-BN/Cu(111) self-assembled after room temperature deposition. The dense-packed layer exhibits a square unit cell ($a = 20.7 \pm 1.0$ Å, red square) and is stabilized by lateral non-covalent interactions between the terminal cyano-bi-phenylene groups (see structural models in Figure 5.12b). While the molecular packing resembles the one of 2H–TPCN/Ag(111),[Bis16] the molecular appearance shows a spatial modulation not observed on metallic substrates.

At a bias voltage of 1 V, most 2H–TPCN units appear with a characteristic depression in the center, in accordance with free-base tetrapyrrolic units on inert metal substrates as Ag(111)[Auw10, Auw11] or graphene layers.[Mao09] The bright, four-lobe contrast of specific TPCN molecules reflects tunneling through the lowest unoccupied molecular orbitals (*vide infra*). This spatial dependence of the molecular appearance is induced by the lateral electronic superstructure of the *h*-BN template (see rhombi, Figures 5.12a, 5.14a, and D.7), which governs the energy alignment of molecular orbitals, in full agreement with observations on similar systems.[Jos14, Jär14, Pal15]

Figure 5.12c shows a TPCN array after exposure to Co at room temperature. Clearly, a new species characterized by a bright central protrusion is observed, whose occurrence scales with the Co dose (see Figure 5.13).

Consequently, we assign it to Co–TPCN. Indeed, the prominent appearance of the Co center embedded in the porphyrin macrocycle at this specific bias voltage closely resembles the contrast of Co–Pc on graphene or *h*-BN sheets,[Jär14, Pal15, Sch13b, Jär13] which is assigned to the lowest unoccupied molecular orbital (LUMO) and is reminiscent of individual

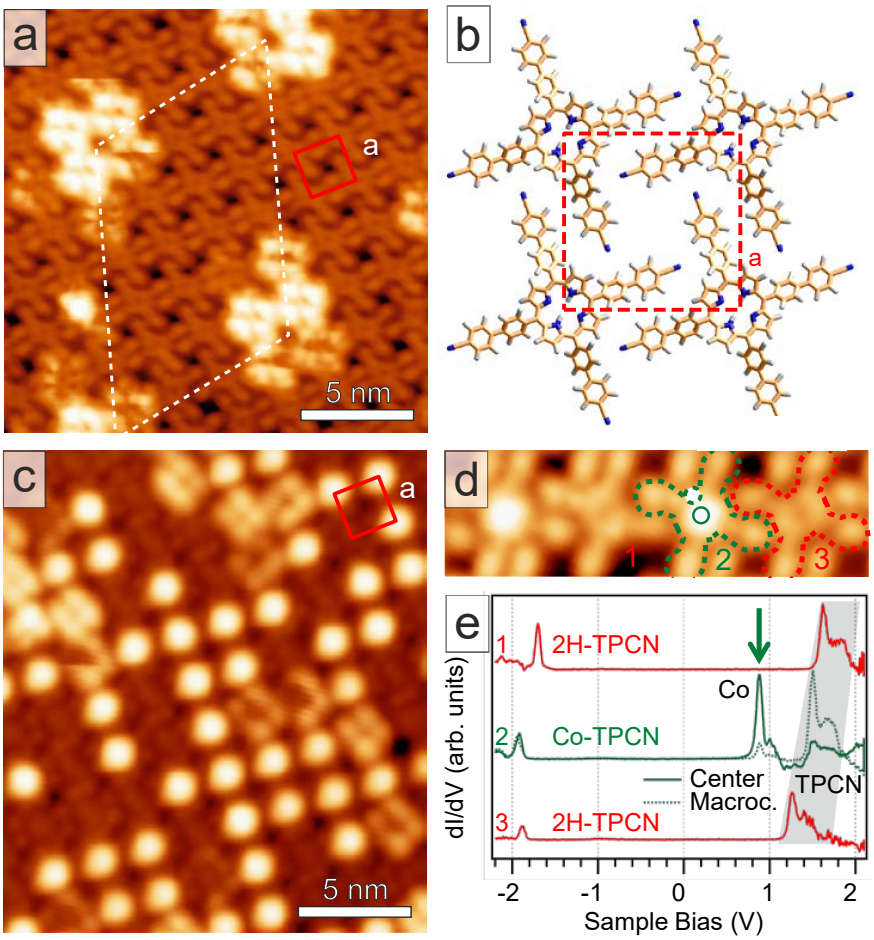

Figure 5.12: *Two-dimensional assembly of 2H–TPCN on h-BN/Cu(111) and macrocycle metalation with Co.* ***(a)*** *STM image of a supra-molecular array prior to Co exposure ($U_b = 1.2\,\mathrm{V}$).* ***(b)*** *Corresponding structural model highlighting the square unit cell.* ***(c)*** *Partially metalated TPCN array ($U_b = 1.2\,\mathrm{V}$).* ***(d)*** *High-resolution image of Co–TPCN (green) and 2H–TPCN (red).* ***(e)*** *Characteristic STS spectra recorded on three molecules as numbered in panel d. Upon TPCN metalation, a pronounced Co related electronic feature (green arrow) appears ≈0.6 eV below the unoccupied signature of the TPCN ligand (shaded in gray). The Co signal is most pronounced at the center (solid line) while the porphyrin contribution dominates on the macrocycle (dashed line).*

Co–Pc on a homomolecular spacer layer.[Ge09] Figure 5.12d shows a high-resolution image of Co–TPCN coexisting with 2H–TPCN. Importantly, the molecular packing is not modified by the metalation. It should be noted that the four-lobe contrast of some TPCN units apparent in Figure 5.12c is based on molecular orbitals located on the macrocycle, which are rather insensitive to the metalation of the porphyrin core. Thus, the choice of the bias voltage is crucial to detect a clear fingerprint of the porphyrin metalation. The successful *in-situ* metalation of 2H–TPCN on *h*-BN is furthermore reflected in STS data summarized in Figure 5.12e. The differential conductance ($\mathrm{d}I/\mathrm{d}V$) spectra show two prominent features,

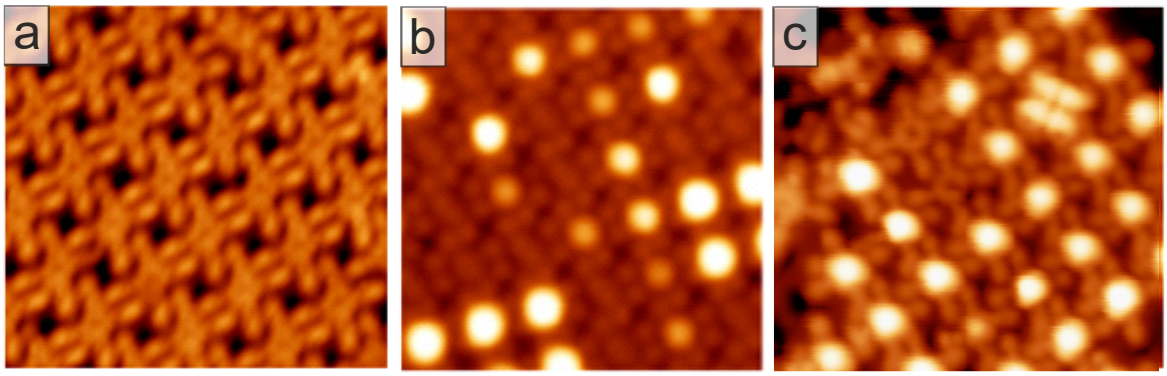

Figure 5.13: *STM images of partially metalated TPCN arrays. Upon increasing the Co dose, the percentage of Co–TPCN increases (**(a)** 0%, **(b)** 60%, **(c)** 90%). Bias voltage from left to right: $U_b = 1.0\,\mathrm{V}$, $1.2\,\mathrm{V}$ and $1.35\,\mathrm{V}$. The appearance of the Co centers in TPCN depends on the bias voltage (compare middle and right panel) and on the lateral position on the superstructure of h-BN/Cu(111) (middle panel). This effect is reflected in the scanning tunneling spectra shown in Figure D.7g. In addition to the key arguments listed in the main text, a successful Co metalation is corroborated by the following findings. The metalated species show a high stability during tunneling spectroscopy where the bias voltage exceeds $2\,\mathrm{V}$. This is expected for Co–Porphyrin units but not for possible reaction intermediates, where hydrogen could still bind to the molecular core. Indeed, gas phase calculations addressing the mechanism of Co metalation reveal small barriers consistent with a fast formation of a Co–Porphyrin at room temperature.[Shu07]*

representing occupied and unoccupied states of the free-base porphyrin ligand, respectively. The gap of about 3 eV separating these sharp resonances evidences an electronic decoupling of the 2H–TPCN units from the underlying Cu support by the *h*-BN monolayer.[Jos14, Cho12] The latter also induces the shift in energy of the molecular states with the lateral position of the molecule that is clearly seen in Figure 5.12e (shaded area) and is responsible for the variable molecular appearance in the STM data (Figures 5.12a and D.7).[Jos14] Importantly, the $\mathrm{d}I/\mathrm{d}V$ spectra recorded on the Co–TPCN units reveal an additional feature localized at the center of the molecule ≈0.6 eV below the intrinsic unoccupied TPCN orbital, which we assign to Co-derived states (green arrow). Indeed the Co–TPCN spectra qualitatively agree with the data reported for Co–Pc on *h*-BN/Ir(111), corroborating the successful on-surface metalation.[Sch13b]

While nowadays metalation and self-metalation processes of tetrapyrrolic compounds are routinely applied on a wide variety of metallic single crystals,[Auw07b, Gol12, Dil12, Mar10b] the results of this experiment provide, to the best of our knowledge, the first experimental evidence of *in-situ* metalation on sp^2-hybridized supports or insulators,[Urg15c] and highlights the potential to exploit metal-ligand interactions or perform chemical transformations even on inert *h*-BN sheets, in line with a recent study addressing dehalogenation processes on a *h*-BN nanomesh.[Die14]

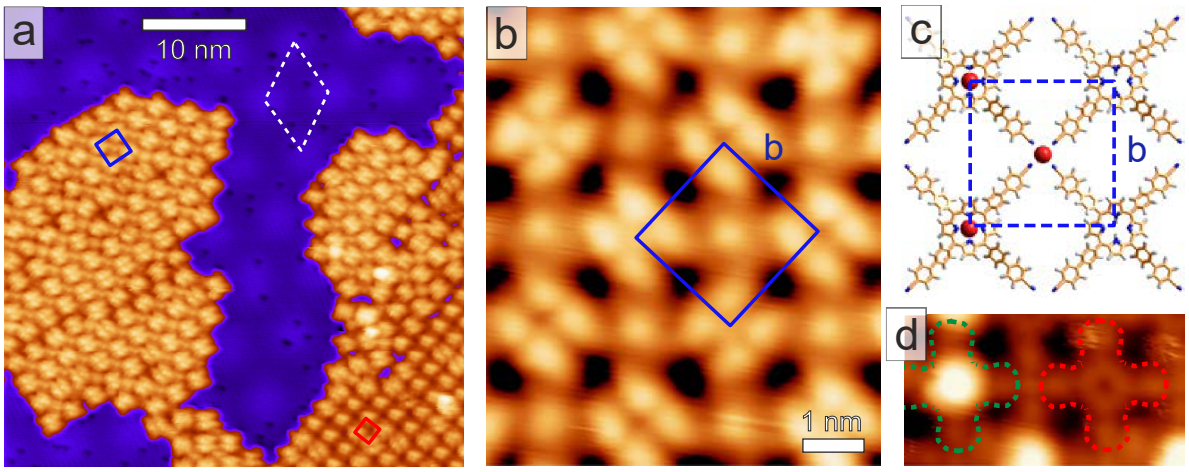

Figure 5.14: *Co-directed assembly of a metal-organic coordination network on h-BN/Cu(111). **(a)** STM image of the network domains coexisting with the dense-packed TPCN phase (U_b = 1.6 V). **(b)** Detailed view on the metallo-supramolecular structure evidencing a 4-fold coordination motif (U_b = 1.6 V). **(c)** Structural model of the coordination node. **(d)** STM image of a Co–TPCN (green) and a 2H–TPCN (red) linked by a Co node (cf. Figure 5.12d; U_b = 1.0 V).*

5.3.2 Co-Directed Coordination Network

For the construction of coordination networks, we exposed TPCN submonolayers to Co at 350 K. Figure 5.14a displays a resulting STM topography, recorded at a bias voltage insensitive to porphyrin metalation. Bare *h*-BN/Cu(111) areas evidence a moiré-like superstructure of electronic origin characteristic for this substrate (see rhombus in Figure 5.14a and section 4.1). Clearly, two different packing schemes of the brick-like protrusion representing TPCN units are discernible. A dense-packed array representing the pure molecular phase discussed above (red square) coexists with network structures exhibiting a larger square unit cell ($b = 24.1 \pm 1.0$ Å, blue squares), including one central protrusion. This new architecture is assigned to a Co-directed assembly of a metal-organic coordination network, featuring coexisting domains with different orientations. The network exhibits a grid-like topology where the nodes correspond to single Co atoms (Figure 5.14b). This assignment relies on an inspection of calibrated STM data and yields a 1:1 stoichiometry between Co nodes and TPCN (see structural model in Figure 5.14c).

Clearly, the network bases on a 4-fold coordination of Co with the nitrile termini of TPCN, where the projected Co–N bond length equals to 2.4 ± 0.8 Å. Importantly, while lateral coordination does not prevail over metalation at room temperature, the latter persists at 350 K, resulting in partially metalated metal-organic networks (Figure 5.14d).

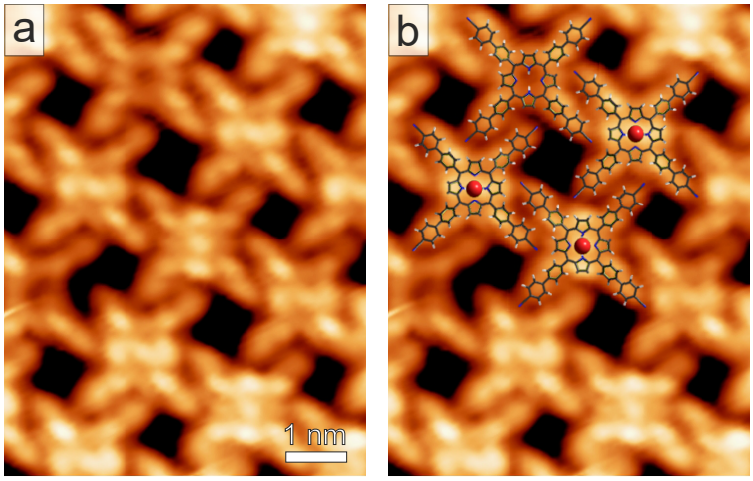

Figure 5.15: *High-resolution STM image of coexisting 2H–TPCN and Co–TPCN visualizing a two-fold symmetry, which is attributed to a saddle-shape deformation of Co–TPCN on h-BN/Cu(111). The structural models in the right panel help to assign the intra-molecular contrast in the STM image ($U_b = -1\,\mathrm{V}$). Clearly, two TPCN orientations differing by 90° are resolved. The same applies for the coordination networks (see Figure D.7h). Importantly, the two coexisting molecular orientations do not disrupt the structural order of the arrays.*

5.3.3 Discussion

Several aspects make this all-Co metallo-supramolecular structure highly interesting, demonstrating the important role of the *h*-BN support. First, 3-fold coordination motifs dominate in Co-carbonitrile complexes on metal substrates.[Küh09, Mar10b, Hen11, Rei13] As exemplified for dicarbonitrile oligophenylenes on Ag(111),[Sch07] the metal support stabilizes a 3-fold motif in two-dimensions in contrast to the 4-fold environment in high-symmetry planes of the octahedral coordination sphere of transition metal-carbonitrile complexes.[Feh93]

Even for TPCN, where the match between the molecular symmetry and a 4-fold coordination would promote a regular packing, a 3-fold motif prevails on Ag(111).[Bis16] Thus, the non-metallic *h*-BN monolayer allows one to create 2D metal-organic networks reflecting coordination motifs observed in symmetry planes of three-dimensional structures and complexes. Second, one can directly identify the Co nodes as round protrusions in STM images of both polarities, at variance with the usual invisibility of 3*d* transition metal centers on metallic supports.[Hen11] Third, the Co–N bond length exceeds the 1.8 to 2 Å typically reported for Co–NC coordination bonds on metals.[Sch07, Mar10b] Though the 4-fold linkage to N is characteristic for both the macrocycle center and the coordination nodes, there are pronounced differences in their coordination spheres and their electronic properties. Notably, the spectral fingerprints of Co in Co–TPCN and in the coordination node (Figure D.7g) reveal an upshift of the lowest unoccupied resonance by ≈0.5 eV in the latter. This points to a higher oxidation state of Co in Co–TPCN, related to an increased electron

affinity,[Wal13] and is consistent with a reduced ionic radius compared to the Co atoms at the nodes. Indeed, in analogy to free Co–TPP an oxidation state of +2 is assumed for isolated Co–TPCN,[Luk07] while the Co coordination nodes might maintain the 0 oxidation state of isolated adatoms,[Hen11] thus yielding a mixed oxidation and valence metallic network.[Li12] Furthermore, correlation effects and geometric considerations influencing the ligand field might contribute to the observed differences as there is evidence for a saddle-type distortion of the central Co–TPCN macrocycle inducing a deviation from a perfect square 4-fold geometry (see Figure 5.15).

5.4 Cobalt Atoms in Different Environments

The porphyrins described in the previous sections comprise Co atoms in the center of their macrocycle. As Co has an unpaired electron in its 3*d* shell, it is expected to act as a magnetic impurity on metallic substrates and potentially on *h*-BN supports. It is known, that surface interactions sensitively affect the coordination spheres of the metal centers in porphyrins, modifying their electronic and magnetic properties.[Auw15] Thus, as a basic prerequisite, it seems natural to study single Co atoms on the particular substrates first, in order to achieve a comprehensive understanding of the complexed Co center embedded in the molecular pocket later on. Therefore, we probed the magnetic moment of Co atoms on Cu(111) and on *h*-BN/Cu(111), which both reveal a prominent Kondo resonance in $\mathrm{d}I/\mathrm{d}V$ spectra as described in this section.

The Kondo effect is a phenomenon that has captured the attention of physicists for decades.[Kou01] It was first observed in 1934 by de Haas,[Haa34] who reported an anomalous resistance increase in a gold sample with magnetic impurities as a function of temperature, and explained theoretically by Kondo in 1964.[Kon64] The Kondo effect describes the spin-flip scattering process caused by the presence of a magnetic impurity in bulk metal samples. Specifically, below a characteristic temperature, the local spin of a magnetic impurity is screened by a cloud of anti-ferromagnetically aligned spins of the conduction electrons of the metal host leading to an increased resistance of the system.

In the last decades, the advancement in STM enabled the measurement of the Kondo resonance at surfaces.[Kou01, Zha05] Utilizing its atomic resolution, STM is a powerful tool to explore magnetism on surfaces.[Kom14] Various experimental and theoretical studies report the observation of the Kondo resonance in single magnetic atoms,[Mad98, Li98, Man00, Kno02, Ren14] and molecules[Ian06b, Ian06a, Jia11, Mug11, Zha13, Gar14c, Dia09] on non-magnetic surfaces. In the following, we briefly discuss the accessibility of Kondo resonances by means of STS.

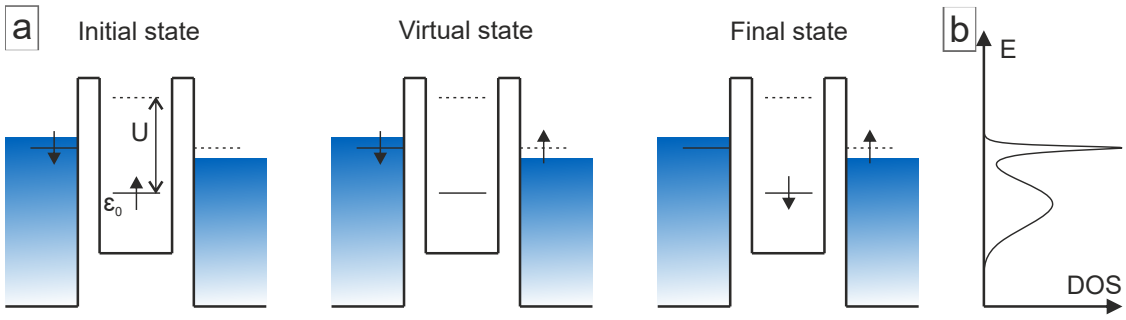

Figure 5.16: *Schematic illustration of the Anderson impurity model that explains the spin-flip in tunneling through magnetic impurities.* ***(a)*** *The magnetic impurity has one electron level with energy ϵ_0 below the Fermi energy of the metal, which is occupied by one spin-up electron. Adding a second electron to the impurity would cost an extra energy equal to the Coulomb repulsion U, while it would cost at least $|\epsilon_0|$ to remove the electron. In a quantum mechanical view, the spin-up electron is allowed to tunnel into the continuum of metal states during a time scale determined by the Heisenberg uncertainty principle ("virtual state"). Subsequently, the electron will be replaced by a spin-down electron from the tip, effectively flipping the spin of the impurity.* ***(b)*** *The combination of various spin-flip events results in a sharp resonance in the DOS at the Fermi energy. Adapted from [Kou01].*

On the basis of the Anderson impurity model,[And61] two different channels can be identified for the tunneling process through a single magnetic adatom on a metal surface.[Kom14, Gar13b] (i) An electron with spin $\downarrow$ in the STM tip can tunnel directly into the empty state of the sample. (ii) The electron can tunnel indirectly *via* a spin-flip process in the localized state of the magnetic impurity, as depicted in Figure 5.16a. Thereby, the unpaired spin $\uparrow$ electron in the singly occupied impurity orbital of the impurity atom with energy $\epsilon_0 < E_F$ tunnels first into an unoccupied sample state for a very short period of time ($\frac{h}{\epsilon_0}$), which is possible due to Heisenbergs uncertainty principle ("virtual state"). Subsequently, the electron with energy E_F from the STM tip can fill the unoccupied state of the impurity balancing the total energy of the system. Importantly, the spin of this electron can be opposite ($\downarrow$), *i.e.* the initial and final state can have different spins. The combination of multiple spin exchange events results in a new state, which manifests as a sharp feature in the DOS at the Fermi energy E_F (Figure 5.16b) that can be visualized in an energy spectrum by means of STS.

The Kondo resonance in $\mathrm{d}I/\mathrm{d}V$ spectra is spatially localized at the impurity and can be described by the Fano equation.[Fan61, Mad98] The tunneling conductance reads

$$\frac{dI}{dV} \propto \frac{(\epsilon + q)^2}{1 + \epsilon^2}, \qquad \epsilon = \frac{eV - \epsilon_0}{\Gamma}. \tag{5.1}$$

Here, Γ denotes the half-width at half-maximum (HWHM) of the resonance, q is the form factor and ϵ_0 the energy shift of the resonance from the Fermi level. The form factor de-

termines the ratio between direct and indirect tunneling processes at the resonance energy. Depending on its value, the resonance can appear as a dip ($q = 0$), as an asymmetric curve (intermediate values, *e.g.* $q = 1$) or as a peak ($q \to \infty$).[Ter09, Gar13b] Physically, large values of q indicate a dominating contribution of indirect tunneling through the impurity, which is usually the case for organic molecules interacting only weakly with the substrate or magnetic adatoms decoupled on insulating layers.[Zha05] In contrast, low values of q suggest a strong coupling between tip and sample leading to enhanced direct tunneling. This behavior is observed for impurities that interact strongly with the substrate.[Ian06a, Per10]

In general, the Kondo temperature T_K is lower for surface impurities compared to those embedded in bulk systems. This is due to the reduced coupling strength between the conduction electrons of the metal substrate and the magnetic impurity when it is located on the surface. In the analysis of STS measurements conducted at finite temperature, the Kondo temperature T_K can be extracted from the FWHM (2Γ) of the fitting curve of the Kondo resonance through[Ter09]

$$2\Gamma = \sqrt{(\alpha k_B T)^2 + (2k_B T_K)^2}, \tag{5.2}$$

and is one of the most important parameters in Kondo physics. The parameter α accounts for the smearing of the Fermi-Dirac distribution.[Ter09]

Experimental Methods

The experiments were carried out in the LT-STM setup. Co atoms were evaporated *in-situ* on bare Cu(111), *h*-BN/Cu(111), and *h*-BN + graphene/Cu(111) samples by means of two different evaporators (see section 3.1). In the case of the e-beam evaporator a filament current $I_{fil} = \sim$1.9 A together with a high voltage of $V = 800$ V typically yielded an emission current $I_{em} = \sim$18 mA resulting in a flux of ~50 nA. Co atoms were deposited for 30 to 60 s with the ion suppressor of the evaporator enabled. The sample was hanging freely in the STM and pulled down after the deposition to allow for cooling. In the case of the resistive evaporator, a power of 10.2 W ($I = 5.5$ A, $V = 1.86$ V) was utilized to heat a 99.95 % W filament surrounded by a thoroughly degassed Co wire (purity 99.996 %). Co atoms were deposited for 15 min. The temperature during all *in-situ* depositions was below 15 K. In order to record high-resolution STS spectra around the Fermi energy an external lock-in amplifier was utilized. The employed settings during the data acquisition for Kondo resonances were: $f = 947$ Hz, time-constant $\tau = 300$ ms, sensitivity: 20 mV, a rms modulation

System	Magnetic moment
Single Co atom ($S = 3/2$)	$3\,\mu_B$
Single Co atom on h-BN/Cu	$2.2\,\mu_B$
Co coordinated to –CN terminal groups, free-standing	$2.4\,\mu_B$
Co coordinated to –CN terminal groups, on h-BN/Cu	$2.4\,\mu_B$
Co–P, gas phase ($S = 1/2$)	$1\,\mu_B$
Co–P/ Cu	0
Co–P/ h-BN/ Cu	$0.2\,\mu_B$ to $0.9\,\mu_B$

Table 5.5: *Magnetic moments predicted by DFT for Co atoms in different chemical environments. The DFT calculations were carried out by the group of Andrés Arnau from Basque Country University,[Arn17] and Alejandro Pérez Paz (see section 5.1).*

amplitude of 0.05 V with the digital signal devider set to 1 : 100 resulting in an actual amplitude $A_{rms} = 0.5\,\mathrm{mV}$. Note that the peak-to-peak amplitude is hence given by

$$A_{pp} = 2\sqrt{2} \cdot A_{rms} \approx 2.8 \cdot 0.5\,\mathrm{mV} = 1.4\,\mathrm{mV}. \tag{5.3}$$

This amplitude is sufficiently small to probe spectral features, which manifest with widths of typically some mV. $\mathrm{d}I/\mathrm{d}V$ spectra were recorded at low temperature (∼6 K), at zero magnetic field ($B = 0\,\mathrm{T}$), in a bias windows of either ±25 mV or ±50 mV around the Fermi energy with usually 200 data points and an acquisition time of typically 70 s. A Mathematica script was employed to fit the STS data to the Fano equation (Eq. (5.1)) amended by an additional linear slope and a constant offset:

$$f = A \cdot eV + B \cdot \frac{(\frac{eV-\epsilon_0}{\Gamma} + q)^2}{1 + (\frac{eV-\epsilon_0}{\Gamma})^2} + C, \tag{5.4}$$

to deal with the inhomogeneous background in STS spectra.

Table 5.5 summarizes the magnetic moments predicted by DFT calculations for Co atoms in different chemical environments, which are model systems that simulate the situation in experimental settings as discussed *e.g.* in sections 5.2 and 5.3. In the following section, we present a concise summary of preliminary results as this project is still on-going. We want to emphasize that the presented values have to be regarded with caution as discussed below.

5.4.1 Experimental Results

In order to calibrate the resistive *in-situ* evaporator and to determine the ideal lock-in parameters to resolve Kondo resonances, we studied Co adatoms on Cu(111), a system well-characterized in literature.[Kno02] Figure 5.17a displays the Co atoms on the copper

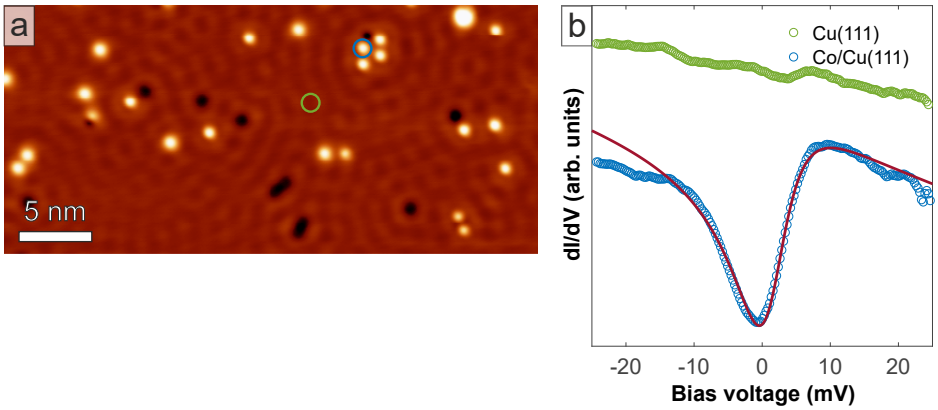

Figure 5.17: *Kondo effect in Co atoms on Cu(*111*). **(a)** STM image showing single Co atoms on the Cu(*111*) surface. **(b)** dI/dV spectra around the Fermi energy taken on the substrate (green) and the indicated Co atom (blue). The fit of the data to Eq.* (5.4) *yields a Kondo temperature* $T_K = 54.7\,\mathrm{K}$.

surface. The majority of atoms appear similar with an apparent height of 0.7 Å (U_b = 25 mV, I_t = 1 nA) and a FWHM of ∼7 Å, consistent with previous studies.[Kno02] The fit of a representative $\mathrm{d}I/\mathrm{d}V$ spectra recorded around the Fermi energy is consistent for all atoms that are identified as single Co atoms and yields a Kondo temperature $T_K = 54 \pm 3\,\mathrm{K}$, which is in good agreement with the reported values of $54 \pm 2\,\mathrm{K}$,[Kno02] and $53 \pm 5\,\mathrm{K}$.[Man00, Wah04] Besides the most prevalent species, some smaller and one bigger protrusion were observed, which are tentatively assigned to impurity atoms or Co atoms trapped on defects and Co clusters, respectively. Both species do not present a Kondo resonance.

Afterwards, Kondo resonances were studied at Co atoms deposited on insulating 2D overlayers such as *h*-BN and graphene. First, Co was deposited on *h*-BN/Cu(111) by means of an e-beam evaporator. Figure 5.18a displays the sample surface after *in-situ* deposition where no preferred adsorption site of Co atoms on the moiré superlattice is observed. At least three different Co species can be identified: The first species (white circle) appears as small bright protrusion with an apparent height of 1.6 ± 0.1 Å and a FWHM of 8.7 ± 1.0 Å and is tentatively assigned to single Co atoms. The second (third) species (black and red circle, respectively) present an apparent height of 2.9 ± 0.2 Å (0.9 ± 0.1 Å) and a FWHM of 10.4 ± 1.2 Å (9.4 ± 0.8 Å) at the tunneling parameters given in the caption of Figure 5.18. Jacobson *et al.* recently reported on CoH_x complexes, observed in the Co on *h*-BN/Rh(111) system.[Jac15] However, in contrast to their study, we did not observe inelastic excitations in our $\mathrm{d}I/\mathrm{d}V$ spectra, which suggests that the assignment to CoH_x complexes can be ruled out for the second and third species.

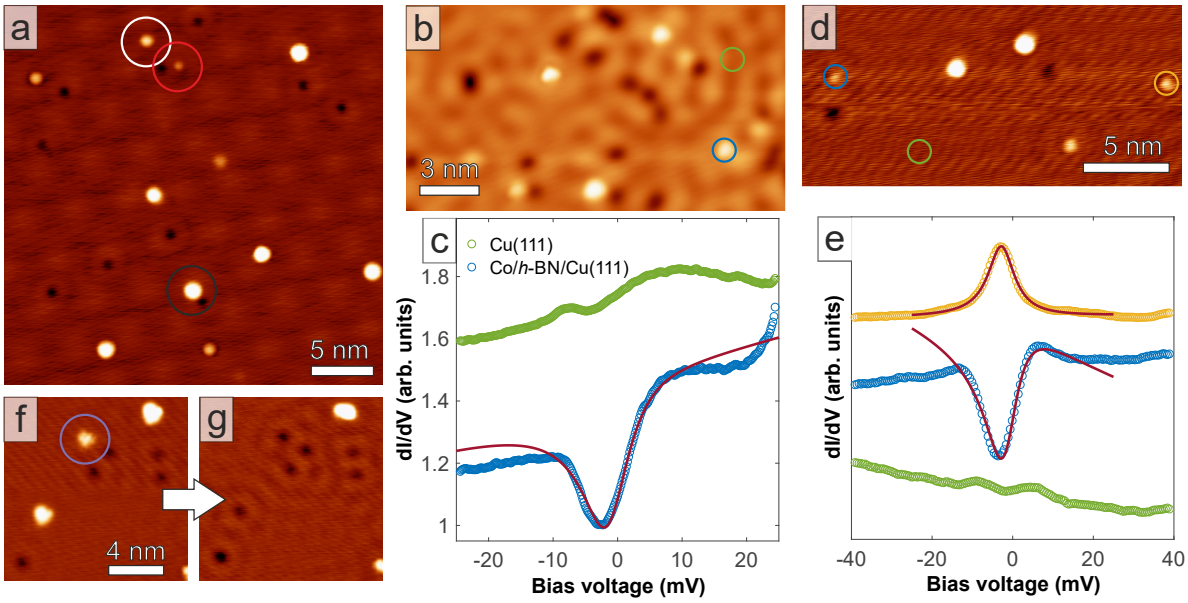

Figure 5.18: *Kondo measurements at Co atoms on h-BN and G on Cu(111). **(a)** Constant-current STM image displaying different atomic Co species on h-BN/Cu(111). $U_b = 0.156\,\mathrm{V}$, $I_t = 0.17\,\mathrm{nA}$. **(b)** Single Co atoms were identified to present a Kondo resonance (blue circle). **(c)** dI/dV spectra around the Fermi energy taken on the substrate (green) and the indicated Co atom (blue) in (b). The fit of the data to Eq. (5.4) yields a Kondo temperature $T_K = 49 \pm 3\,\mathrm{K}$. **(d)** STM image of Co atoms on a Cu(111) surface covered with h-BN and G. **(e)** dI/dV spectra around the Fermi energy taken on the substrate (green) and the two indicated Co atom (blue, yellow) in (d). The fit of the data yields Kondo temperatures $T_K = 46.2 \pm 3.1\,\mathrm{K}$ and $T_K = 55.0 \pm 2.6\,\mathrm{K}$, respectively. **(f),(g)** Co atoms are very mobile and subsequent scans reveal that they are often attached to defects, potentially influencing the magnetic exchange coupling between adsorbate atom and metal substrate.*

Figure 5.18b displays Co atoms deposited on *h*-BN/Cu(111) by means of the resistive evaporator utilized for the Co on Cu(111) experiments described above. Again, different atomic species are present on the surface and the Co atom where a Kondo resonance was observed reproducibly (blue circle) had an apparent height of 0.3 Å ($U_b = 25\,\mathrm{mV}$, $I_t = 0.3\,\mathrm{nA}$) and a FWHM of ∼5 Å. Fitting the corresponding $\mathrm{d}I/\mathrm{d}V$ spectrum shown in Figure 5.18c yields a $T_K = 49 \pm 3\,\mathrm{K}$. However, we want to emphasize that the Co atoms turned out to be highly mobile and either jump to the STM tip or aggregate in clusters on the surface after some scans. Furthermore, not all Co atoms presented a Kondo resonance even if the appearance in STM was very similar. In a recent publication,[Zha17a] the authors claim that Co adsorption in monomers, dimers, and trimers is enhanced on grain boundaries compared to pristine *h*-BN. Although the localized defect states at the grain boundaries strengthen the binding of Co atoms to the *h*-BN, the magnetic properties are predicted to remain unperturbed.

Co atoms deposited on ateral h-BN/graphene heterostructures on Cu(111) (see section 6.1) are displayed in Figure 5.18d. We were not able to clarify whether h-BN or G was present in the displayed area (see section 6.1.2). However, clearly, the two indicated atoms (blue and yellow circle) reproducibly showed pronounced Kondo resonances (Figure 5.18e). While the first Co atom (yellow circle) shows a peak and the fit yields a Kondo temperature $T_K = 46.2 \pm 3.1\,\mathrm{K}$ the second Co atom (blue circle) presents a dip and an increased Kondo temperature $T_K = 55.0 \pm 2.6\,\mathrm{K}$. The characteristic line shapes are due to the different form factors q, which indicate dominating indirect tunneling in the first case as discussed above. The dominating direct tunneling channel in the second case (blue) can be understood by the presence of a defect close to the Co atom. Although AFM measurements suggest that those kinds of defects are situated mostly underneath the h-BN layer they can interact with the Co atom on top of h-BN and influence the magnetic exchange coupling significantly. We want to note, that we observed Co atoms attached to defects quite frequently, as evidenced by Figure 5.18e,f, where the probed atom is removed after a series of measurements, revealing the defect imaged as a dark depression. In this case, a Kondo temperature of $T_K = 73.3 \pm 2.3\,\mathrm{K}$ was determined reproducibly. The increased Kondo temperature, compared to the values described above, suggests that defects can exert a significant influence on the Kondo exchange interaction between the Co atom and the Cu substrate, necessitating further experiments to gather more statistics for an unambiguous quantification. Furthermore, it should be noted that the substrate could have been h-BN or graphene impeding a clear conclusion on this value. Moreover, we tried to measure the Kondo resonance on the Co center of Co–P on h-BN/Cu(111), but did not obtain a reliable conclusion for this system.

5.4.2 Discussion

As predicted by DFT, all studied systems presented characteristic Kondo resonances with different temperatures ranging from $54 \pm 3\,\mathrm{K}$ in the case of Co/Cu(111) up to 73.3 K in the case of Co on h-BN/Cu(111). We find that only Co on Cu(111) is a stable and well-defined system. In the case of Co on h-BN + G/Cu(111) no final conclusion could be reached yet. The obtained results from various atoms of different experiments are consistent and reproducible on the particular atom. However the reason for why only some Co atoms and also Co–P molecules on h-BN/G present a Kondo resonance remained unclear. Moreover, we were not able to identify atoms/molecules in STM that will present a Kondo resonance prior to the actual acquisition of $\mathrm{d}I/\mathrm{d}V$ spectra. The fact that Co atoms on h-BN supports are adsorbed only weakly and are hence prone to hopping during the acquisition of STS spectra further hampers the reliable characterization of this system. Frequently, this leads

to Co atoms covering the STM tip resulting in virtual Kondo resonances in spectra recorded on *h*-BN/Cu(111) regions.

The obtained Kondo temperature ($T_K = 49 \pm 3\,\mathrm{K}$) for Co atoms adsorbed on *h*-BN on Cu(111) is significantly increased compared to *e.g.* Co on epitaxial graphene, where values of 15 to 17 K are reported in a theoretical study on freestanding graphene,[Weh10] and an experimental study on G/Pt(111).[Mat09] The presence of a Kondo peak instead of a dip has also been reported for Co-, Fe- and MnPc on metal surfaces, and can be understood by the decoupling from the substrate.[Zha05, Gao07, Fu07] In a very recent study using first-principle DFT calculations, the structural and magnetic properties of Co adatoms on graphene/Cu were compared to other 3*d* transition metal adsorbates, however, no Kondo temperatures were quoted.[Pét17]

We speculate that three parameters have a direct impact on the magnetic moment of the Co atoms. (i) The configuration as a Co atom or a complex. Single Co atoms need to be identified and selected from a zoo of different species. Moreover, it needs to be clarified whether or not CoH_x complexes are present on the surface, and what the impact of different Co coordination states on the unpaired electron is. It has been shown for example that Co atoms on Ag(111) undergo oxidation reactions with residual hydrogen, which leads to a complete quenching of the Kondo resonance.[Ser14] (ii) The *h*-BN layers possess a significant corrugation (see section 4.1). Therefore, one might expect that the *h*-BN layer could smoothly tune the Kondo exchange interaction between the spin and the underlying metal as reported for the strongly corrugated *h*-BN/Rh(111) system,[Jac15] and organic molecules on nanostructured graphene.[Gar14c, Gar14b] Possibly, the presence of a Kondo resonance is even adsorption site dependent. For example, one could conjecture to observe a Kondo resonance only for Co atoms located in pore regions, where they are closer to the metal substrate and hence the screening would be enhanced. (iii) The role of defects within or underneath the *h*-BN/G layer needs to be investigated as various observations suggest that Co atoms trapped at those defects are more likely to show a Kondo resonance.

5.5 Conclusions

In the first section, we have determined the local adsorption geometry and the lateral registry of Co–P on Cu(111) with atomic precision. Specifically, the molecules adsorb with the central cobalt atom on a bridge site at an average adsorption height of (2.25 ± 0.04) Å (as measured by XSW), and the macrocycle of the molecule adopts a moderate asymmetric saddle-shape conformation. The symmetry of this adsorption site is reflected in three equivalent molecular orientations observed by STM. The adsorption mode of Co–P molecules

is mainly governed by vdW interactions, although some indications of chemical adsorption (short Co–Cu distance and large Bader charge transfer) are present. The Co center exhibits a significant interaction with the Cu(111) substrate, being the closest atom to the surface with a DFT-predicted Co–Cu bond distance of 2.65 Å. The twofold symmetric appearance of the Co–P molecules is rationalized by an asymmetric deformation along the long bridge direction. This distortion, which was previously not recognized for porphines on coinage metals,[Dil13b, Bis13, Hie11, Hou15] is less pronounced than in pyridyl-,[Auw07a] and phenyl-functionalized porphyrins.[Di 11, Web08, Hou15, Seu11b, Buc10] The knowledge of the geometric structure and the adsorption height of Co–P/Cu(111) is of fundamental relevance in order to understand the functionality of Co–P and related metal-organic complexes on surfaces.

In the case of Co–P on *h*-BN/Cu(111), we have observed island nucleation in the pores of the *h*-BN layer and we determined the vertical heights of the individual components: While the *h*-BN layer itself is not altered significantly, the adsorption height of the Co–P molecules above the surface (*i.e.* the *h*-BN layer) increased compared to the bare Cu(111) substrate. Interestingly, we have observed two chemically inequivalent Co species, although the origin of this splitting remained to be investigated. Additionally, we have noted indications of a temperature dependence in the adsorption height of the Co–P molecules.

Further, we have introduced protocols for *in-situ* metalation and lateral coordination of functionalized tetrapyrrolic species on a *h*-BN monolayer, or more generally on insulating supports or sp^2 sheets. Upon Co exposure at 350 K, the formation of a metal-organic porphyrin network was promoted, featuring a distinct 4-fold coordination motif. The insulating character of the *h*-BN support is furthermore reflected in the narrow electronic resonances representing the molecular and atomic states, addressable with submolecular resolution. Thus, our system opens up the opportunity to engineer and probe the electronic properties of coordination networks in a peculiar 2D environment, addressing, for example, bimetallic structures featuring tailored oxidation states. This approach provides access to a new class of complex metallo-supramolecular arrays and hybrid architectures with prospects for functionalities, *e.g.* in spintronics, photonics, or heterogeneous catalysis.

Regarding Co centers, we studied the magnetic properties of Co atoms with a single unpaired electron spin in different environments by means of STM and STS. We provide a first experimental evidence of a Co-related Kondo resonance on *h*-BN sheets on Cu(111), opening paths for a further characterization of the related molecular systems.

Chapter 6

Hybrid *h*-BNC Heterostructures

This chapter includes content that will be published in

M. Schwarz, M. Garnica, F. Fasano, N. Demitri, D. Bonifazi, W. Auwärter, **BN-Patterning of Metallic Substrates through Metal Coordination of Decoupled Borazines**, *Chem. - Eur. J.* **24**, 9565-9571 (2018); Copyright (2018) by Wiley-VCH.

This chapter presents our work on lateral boron-nitrogen-carbon (*h*-BNC) heterostructures. Hybrid *h*-BNC heterostructures hold great prospects in the development of bandgap-engineered applications in novel electronic devices with unprecedented magnetic and optoelectronic properties that are distinct from those of pristine *h*-BN and graphene.[Ci10, Lev12, Gei13, Nov12, Nov16] Two different strategies are currently pursued to achieve these highly appealing hybrid materials.[Wan14a, Lim14, Bon15] First, *h*-BN and graphene (G) can be grown simultaneously or sequentially on a solid substrate, *e.g.* by CVD and atomic C deposition resulting in truly 2D thin films,[Lee14] as will be discussed in the first section of this chapter. Second, deliberately synthesized organic molecules with BN doping units can be used. Specifically, borazine derivatives have emerged as an interesting building block in recent years.[Bon15] The self-assembly of two particular borazine derivatives into a metal-organic coordination network will be described in section 6.2.

6.1 In-Plane *h*-BN–Graphene Interfaces

Research on graphene is pervasive in the scientific community in the last decade and numerous breakthroughs have been achieved.[Nov12] One of the key challenges is the opening of a band gap in graphene.[Pen12] Various approaches have been proposed so far including the use of strain,[Gui08] disruption of the hexagonal lattice,[App10] spatial confinement,[Li08, Son06]

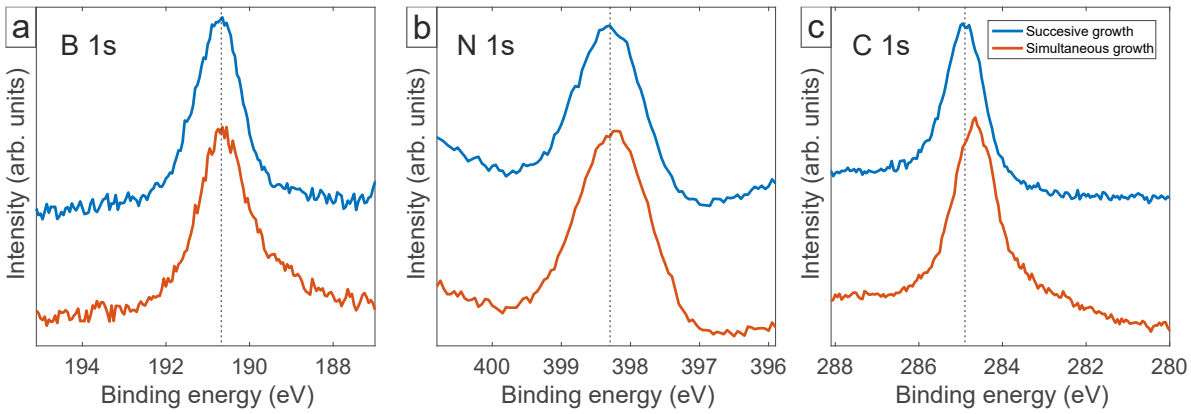

Figure 6.1: *XP spectra of the* ***(a)*** *B 1s,* ***(b)*** *N 1s and* ***(c)*** *C 1s core levels of a h-BN–G heterostructure on Cu(111) following a successive (blue lines, first growth of graphene, followed by h-BN) and a simultaneous (orange lines) growth of the both materials.*

substrate surface chemistry,[She09] and doping.[Fer07, Liu11, Gio08, Wan12a, Wei09, Red10] Recently, the fabrication of lateral heterostructures consisting of *h*-BN and graphene domains has been reported.[Ci10, Son10, Liu13] An atomically precise control of the boundaries where the two materials are stitched together in-plane would yield hybrid atomic layers with interesting electronic properties.[Lev12] First principle calculations predict, *e.g.* a tunable band gap of up to 4.7 eV.[Pen12]

h-BN–G heterostructures have been grown experimentally on various transition metal substrates including Rh(111),[Gao13, Rot16] Ru(0001),[Lu14] Ir(111),[Liu14a] Pt(111),[Sut14] Ni(111),[Dro15] and in particular on the widely used Cu.[Ci10, Liu14b, Lev12, Han13, Liu13, Kim12, Men15] In the following section, we will present a concise summary of the results that we have obtained by means of a combined STM, STS and XPS analysis from *h*-BN–G heterostructures, fabricated on a Cu(111) single crystal.

6.1.1 Growth and Characterization

For the growth of the *h*-BN–G in-plane heterostructures we utilized borazine as a CVD precursor for the *h*-BN growth (see section 4.1) and atomic carbon evaporated from a graphite rod for graphene (see section 3.5 and Ref. [Gar16]). The graphene and *h*-BN coverage are controlled by the carbon deposition time and flux, and the borazine dose, respectively. We studied both a simultaneous and a successive deposition of C and BN material.

In the first case, the sample was heated to 1020 K with its surface plane facing towards the carbon evaporator while the chamber was back-filled with borazine ($p = 7 \times 10^{-6}$ mbar) for 5 min resulting in a total exposure of ∼1600 L. In STM, we observed graphene and *h*-BN islands as well as extended, unordered regions presenting a triangular reconstruction of unknown origin (not shown), similar to a report on BCN domains enclosed by graphene

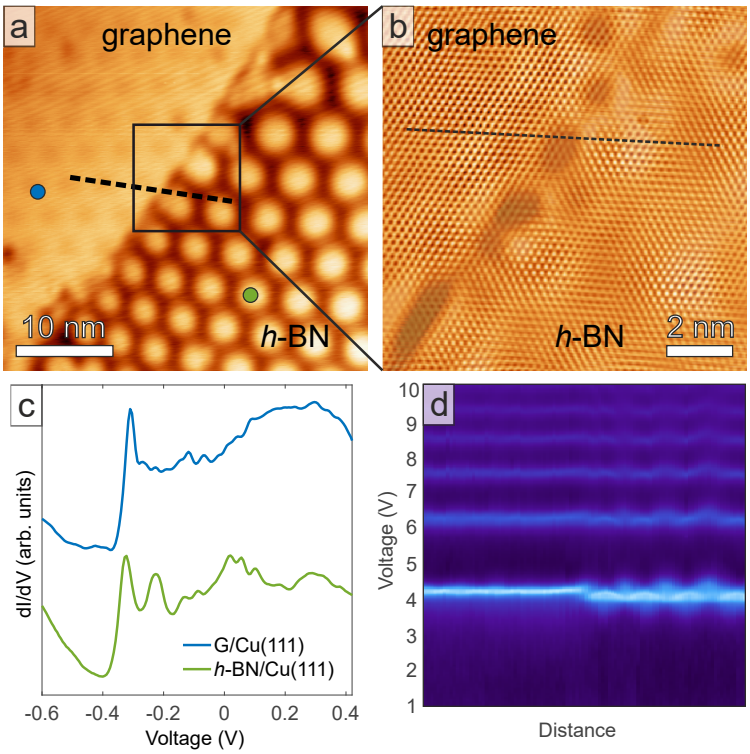

Figure 6.2: ***(a)*** *STM image of the in-plane h-BN–G interface on Cu(111) ($U_b = 4.0\,\mathrm{V}$, $I_t = 110\,\mathrm{pA}$).* ***(b)*** *Atomically resolved, FFT-filtered STM image of the h-BN–G junction (marked by the black square in (a)) indicating a continuous lattice. $U_b = 0.2\,\mathrm{V}$, $I_t = 1.2\,\mathrm{nA}$.* ***(c)*** *dI/dV spectra on G (blue) and h-BN (green), acquired in the positions marked in (a).* ***(d)*** *2D color plot of the FERs acquired along the dashed line in (a).*

nanoribbons on Ru(0001) in the literature.[Lu13] In accordance with this study, we speculate that heterogeneous networks containing B, N and C atoms could have formed in this regions on the surface (as indicated by XPS) in addition to the homogeneous graphene and *h*-BN islands. This is further corroborated by the presence of shoulders in the B 1*s* and C 1*s* core-level spectra (see orange lines in Figure 6.1) indicating significant contributions of C–B and/or C–N bonding configurations,[Liu14b] exceeding the ones expected from the boundary between the BN and the C material. In addition, the C 1*s* main component is shifted by ∼0.3 eV toward lower binding energies compared to the layer obtained from a successive growth (discussed next). Therefore, we infer that this approach hampers the fabrication of well-defined *h*-BN–G heterostructures on a large scale within this set of growth parameters that have been explored.

In a second approach, a sub-monolayer of graphene was grown prior to the growth of *h*-BN, by depositing carbon onto the sample for 1 min, which was kept at 1020 K. A high voltage of 1.5 kV and a filament current of $I_{fil} = 1.95\,\mathrm{A}$ gave rise to an emission current $I_{em} = 110\,\mathrm{mA}$ in the carbon evaporator. Subsequently, *h*-BN was grown following the established CVD

procedure (see section 4.1). The growth of *h*-BN presumably takes place only on bare copper regions, as on graphene covered regions the dehydrogenation and cracking of the borazine precursor are suppressed.

Compared to the previous approach, the obtained *h*-BN and graphene islands are of superior quality, similar to preparations with only one kind of 2D layer present on the Cu(111) crystal. The binding energies of the B 1*s*, N 1*s* and C 1*s* core levels are 190.7 eV, 398.3 eV, and 284.9 eV, respectively. Surprisingly, the interfaces between the two materials mostly coincide with one or several copper step edges, impeding the analysis of the junction. This can be understood by the fact that the sample is kept at elevated temperatures after the graphene layer has been formed, possibly leading to an evaporation of material in uncovered substrate regions. A similar effect has been observed for the growth of *h*-BN on Ag(111) (see section 4.2). The nucleation of *h*-BN layers presumably starts at the edges of the graphene layer, defect sites, and/or adsorbates on the surface. Moreover, we find indications that BN material substitutes graphene on the surface for extended dosing times, in line with the report of Lu *et al.*,[Lu13].

Occasionally, in-plane *h*-BN–G interfaces are observed on the very same Cu terrace. Figure 6.2a shows an STM image of such an *h*-BN–G interface grown by the second approach. The two materials can be distinguished by the appearance of their characteristic moiré patterns. At a bias voltage of 4 V the moiré pattern of *h*-BN is typically imaged as bright protrusions in STM (see section 4.1), whereas in the graphene island, the contrast is inverted and the wires of the superstructure are imaged brighter than the pores. Importantly, Figure C.6b shows that both moiré superstructures can be observed at room temperature. This observation provides the first experimental evidence that the templating effect of the *h*-BN sheet can also be expected at room temperature. The apparent corrugation is larger in case of the *h*-BN (∼90 pm) compared to graphene (∼35 pm), as illustrated in Figure C.6c.

Figure 6.2b shows an atomically resolved, FFT-filtered STM image of an *h*-BN–G interface overlaid with the partly transparent raw image. The atomic lattice is clearly visible in both regions, *h*-BN and graphene, at the same time, and continuous across the junction indicating that both layers are indeed stitched together. In the raw STM image, a significant electronic signal is present at the junction displayed as dark depressions. It should be noted that the orientations of the two atomic lattices differ by some degrees resulting in strain and sheered superstructures as can be seen in the top part of Figure 6.2a and in Figure C.6b.

STS measurements of the *h*-BN–G heterostructure are shown in Figures 6.2c,d. We probed the surface state on *h*-BN and graphene (Figure 6.2c), and found that the onset is located at a similar energy in both materials and that it is in good agreement with previous observations (see section 4.1). The 2D color plot in Figure 6.2d shows the FERs acquired along the line in Figure 6.2a (see section 4.2.2). The resonances are also found at almost the same energy

in both materials. They show the well-known modulation in *h*-BN (see Figure C.2) and are almost unperturbed in the graphene region. Most notably, our STS measurements present no indication of boundary states upon formation of *h*-BN–G heterostructures. This is in contrast to a report of Park *et al.* on *h*-BN–G interfaces on Cu(100), who observed one-dimensional boundary states at about 0.6 eV below or above the Fermi level, depending on the termination (B–C and N–C, respectively) of the *h*-BN sheet, which are localized at a zigzag heterojunction of the two materials.[Par14] The work functions of the *h*-BN- and G-covered Cu regions, derived from the FERs that have been probed through $\mathrm{d}I/\mathrm{d}V$ measurements (see section 4.2.2), are identical within the error bars with a faintly visible variation by ~ 0.3 eV on *h*-BN reflecting the moiré superstructure (see section 4.1, Figure C.2 and Ref. [Sch17b]). As mentioned before, this method does not allow to quote absolute values for the work function. In literature, a work function decrease of $\Delta\Phi = -0.82$ eV has been predicted upon adsorption of graphene on Cu compared to the clean metal substrate.[Gio08] Our DFT calculations (see appendix C.0.2) suggest a work function decrease between $\Delta\Phi = -0.64$ eV and $\Delta\Phi = -0.98$ eV in the *h*-BN/Cu(111) system, depending on the moiré registry.

6.1.2 Discussion

In agreement with earlier studies,[Lu13, Gop16] we find that *h*-BN–G heterostructures form on the metallic Cu(111) surface in coexistence with unordered regions containing an *h*-BNC alloy. It should be mentioned that these earlier studies suggest that continued dosage of borazine over an extended period of time eventually substitutes the C material on the surface leading to extended homogeneous islands on the surface.

The binding energies of the B 1*s* and N 1*s* core-level spectra of the *h*-BN–G heterostructure on Cu(111) are slightly increased compared to the measurements of *h*-BN/Cu(111) conducted at DLS (see section 4.1.3.2), but in line with previous studies;[Gao15] the binding energy of the C 1*s* band is in excellent agreement with values reported in the literature for *h*-BN–G/Cu(111),[Liu14b, Gao15] indicating that the atomic species are present in a sp^2 configuration as expected for laterally stitched heterostructures.

The alignment of the atomic *h*-BN and graphene lattices on Cu in STM is in line with previous reports.[Liu14b] Moreover, Liu *et al.* observe solely zigzag graphene edges due to the hydrogen etching of the graphene layer acting as a template for the *h*-BN nucleation.[Liu14b] Our results based on the atomically resolved STM images suggest the same zigzag edges for the *h*-BN–G heterojunction, even without the hydrogen etching procedure. Nevertheless, a more detailed characterization of the interface of as-grown *h*-BN–G samples remains to be done.

A discrimination of the two materials in STM is not straightforward as the binding energy of the surface state onset of both is very similar. At a bias voltage of 4 V the contrast of the two layers is characteristic. However, scanning at high bias is not always possible, *e.g.* if mobile atomic adsorbates are on the 2D layers (see section 5.4). Another characteristic feature that can be considered is the shape of the island: for graphene typically almost perfectly straight borders are observed, whereas in the case of *h*-BN, the borders appear more irregular.

6.2 Network of Decoupled Borazine Derivatives

Borazine derivatives have recently attracted increasing interest[Bon15, Lor17] as molecular building blocks, due to their high potential for applications in the fields of electronics,[Sha05, Faz95, Wak05, Ker13a, Rie17, Ayh18, Lor16] and non-linear optics.[Kar14, Ote17, Ote16] In particular hybrid *h*-BNC nanostructures, where carbon-carbon bonds are replaced by isoelectronic and isostructural BN couples are emerging as a new route to functionalize polycyclic aromatic hydrocarbons without a significant structural perturbation of the molecular periphery and of its skeleton.[Rie17, Ayh18, Lor16, Cam12, Liu08, Wan15] The presence of BN bonds imparts strong local dipole moments that can tailor both, the optoelectronic properties and the self-assembly behavior of the molecule.[Wan14b, Mar17, Dos17, Ker13b, Kri15, Cic16] For instance, one can conjecture that the polar BN bonds could serve as anchoring point for non-covalent adsorption of polar gases like CO_2 and CO, which can in principle interact with BN bonds through dipolar interactions, thus making BN-doped materials very good candidates for gas adsorption.[Jac11, Rei12] Together with the possibility of tuning the molecular bandgap into the visible range of the solar spectrum, these structures could emerge as unique photoactive materials triggering photo-chemical transformations. Given these premises, we conjectured that two-dimensional structures formed through non-covalent interaction on a surface could act as unique model architectures to study the self-assembly and recognition properties of BN-materials at the molecular level through STM.

In particular, precisely tailored substituents of molecules can be utilized to realize targeted adsorption geometries, as well as to preserve the intrinsic properties of molecules upon adsorption on a metal support.[Ros03, Cir17, Sch11, Pio08] Recently, it has been proposed that the borazine scaffold of a molecule can be protected and electronically decoupled from the conductive substrate by di-methylphenyl terminal groups through steric hindrance without affecting the possibility of the molecule itself to adsorb and self-assemble.[Kal14] Additionally, the selection of the substituent's termination (*e.g.* -carbonitrile (CN), -carboxylate, -pyridyl) steers the supramolecular interactions, driving for example the formation of two

dimensional metal-organic coordination networks (2D-MOCNs) in the presence of metal adatoms. The formation of such a 2D-MOCN combining borazine and metal adatoms has not been reported to date, although those porous architectures are highly appealing as they can act as templates featuring cavities and molecular units on regular and well-defined sites linked by metallic nodes.[Urg15b, Bar09, Ari16, Don16]

Indulging this line of thought, here we describe the synthesis and the self-assembly properties of borazine derivatives on Cu(111), Ag(100) and Ag(111) surfaces that, exposing peripheral pyridyl groups, can undergo metal-coordination in the presence of copper adatoms to yield porous patterns. Specifically, STM studies show that the molecules behave differently on the two metals, with those deposited on Ag undergoing self-assembly through weak interactions (van der Waals (vdW) and H-bonding), whereas on Cu the molecules engage in metal-coordination. Using STS, we also provide evidence that the borazine core is electronically decoupled from the conductive metal substrate. The architectures on Cu(111) substrates were exposed to CO gas and their chemical properties investigated by XPS. Additionally, we explored the thermal stability of the network on Cu(111) at room temperature, and the effect of post-annealing on both metal substrates by STM.

Experimental Methods

STM experiments were performed in the LT-STM setup at low temperature and the XPS-STM setup at room temperature. The Cu(111) and the Ag(100) single crystals were prepared following the procedures described in section 3.5. Ag(111) was prepared by e-beam evaporation of several layers of Ag on a Cu(111) crystal, which was held at 575 K as detailed in.[Gar16] The borazine derivatives **BNPPy** and **BNAPy** were synthesized in the group of D. Bonifazi.[Sch18b] In the UHV chamber, the molecules were dosed from a thoroughly degassed quartz crucible held at 600 K onto the sample held at room temperature. All XP spectra were excited with the Al K_α photon energy of 1486 eV (see section 3.2). A Shirley-type background was subtracted and Voigt profiles were used to fit the data.

Appearance of BNPPy upon Adsorption

High-resolution STM images of individual **BNPPy** molecules on Cu(111) and Ag(100) show sub-molecular features with a very similar appearance (Figure 6.3b and c). The central part of the molecule appears as three bright lobes pointing along the axes defined by the pyridyl-terminated substituents, which are imaged dimmer. The molecular contrast does not change for moderate bias voltages of both polarities, suggesting that it reflects the molecular conformation. We simulated STM images for different adsorption geometries using the extended Heckel method (see Figure E.1). The best agreement between experiment and

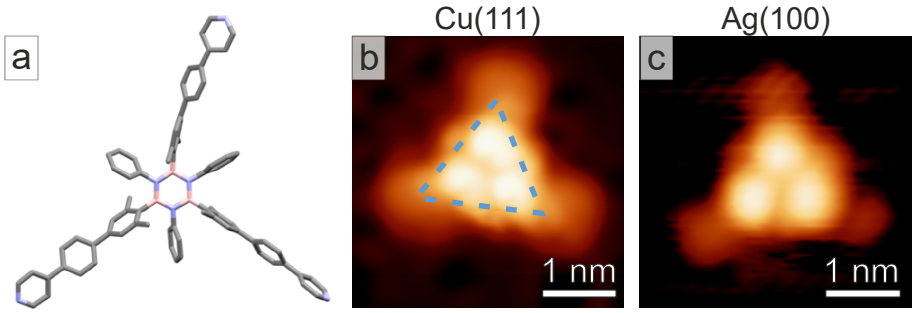

Figure 6.3: ***(a)****Structure of* ***BNPPy*** *determined by X-ray diffraction. STM images of an individual* ***BNPPy*** *molecule on* ***(b)*** *Cu(111) ($U_b = 1.9\,\mathrm{V}$, $I_t = 170\,\mathrm{pA}$) and* ***(c)*** *Ag(100) ($U_b = 0.5\,\mathrm{V}$, $I_t = 81\,\mathrm{pA}$). The superimposed dashed triangle in (b) indicates the orientation of the molecule.*

simulation is obtained for a **BNPPy** geometry where the borazine core and the peripheral pyridyl-groups are aligned (nearly) parallel to the surface plane while all phenyl rings are rotated out of this plane. Specifically, the three prominent lobes observed in STM can be reasonably associated with the bulky di-methyl-bearing aryl rings. This assignment is in line with STM observations and complementary molecular dynamics (MD) modeling reported for dimethyl-bearing aryl borazine derivatives on Au(111) andCu(111).[Kal14] Consistently, we observe a very similar intramolecular contrast featuring three bright protrusions for **BNAPy** on Cu(111) (see Figure E.6).

The molecular structure determined by X-ray diffraction (in collaboration with D. Bonifazi) on **BNPPy** crystals shows that the expected three-fold symmetry of the molecule can be disturbed due to the flexibility of the substituents (Figure 6.3a). Upon adsorption, a similar behavior is observed, as can be seen in Figures 6.3b,c. The pyridyl-terminated substituents appear bent in the surface plane, resulting in angles enclosed by them deviating from 120°.

6.2.1 BNPPy on Ag Surfaces

Extended, highly ordered molecular islands of **BNPPy** were observed on silver samples with different surface terminations, namely a Ag(100) single crystal and a Ag(111) film (see Figures 6.4 and 6.7c, respectively). The molecules, deposited onto the sample held at room temperature, arrange in six-membered rings and form porous honeycomb networks. A similar self-assembly was observed for related molecules on the Au(111) surface. [Kal14] Molecular domains with sizes of several hundreds of nm and arbitrary orientation with respect to the crystal high-symmetry directions were present on the samples.

A high-resolution close-up view (Figure 6.4b) reveals that each molecule in the honeycomb structure is surrounded by three neighbors and three pores. The rhombic unit cell (white

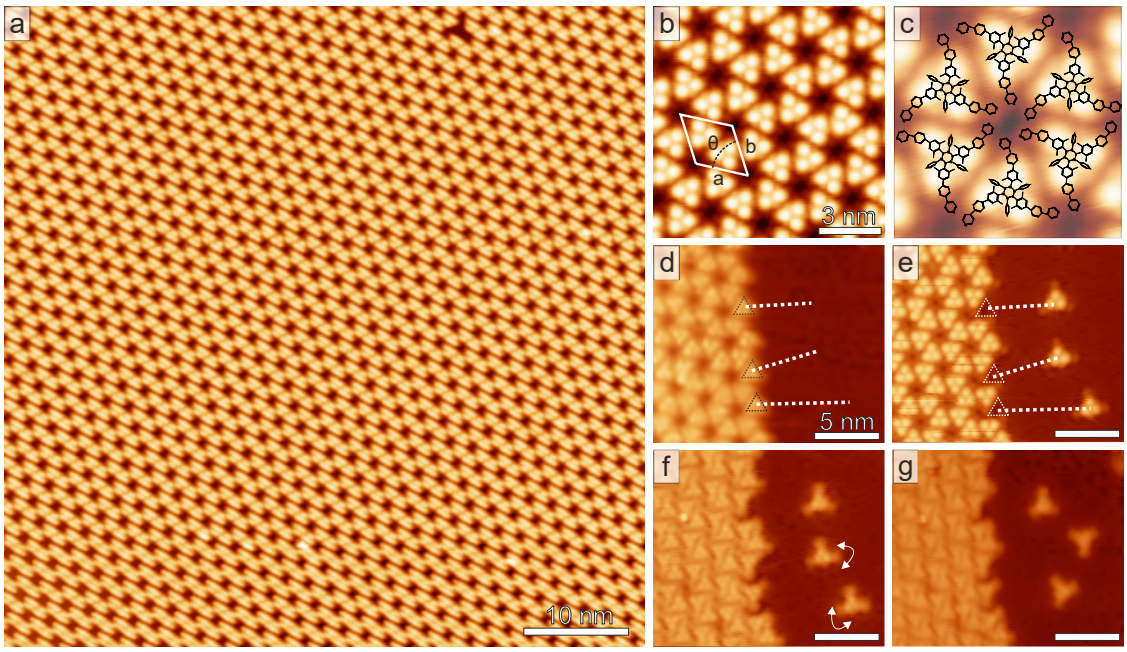

Figure 6.4: *STM images of **BNPPy** on Ag(100). **(a)** Large-scale image of the close-packed hexagonal network of **BNPPy** molecules. Scan parameters: $U_b = 1.0\,\mathrm{V}$, $I_t = 64\,\mathrm{pA}$. **(b)** High-resolution STM image (unit cell highlighted by white rhombus). Scan parameters: $U_b = 0.2\,\mathrm{V}$, $I_t = 40\,\mathrm{pA}$. **(c)** STM image overlaid with a tentative structural model of the molecular assembly. **(d)** Individual molecules can be manipulated by STM in a controlled way (dotted white lines represent the tip path). **(e)** Three individual **BNPPy** molecules were detached from the dense-packed island. (Scan parameters of (d),(e): $U_b = 0.5\,\mathrm{V}$, $I_t = 81\,\mathrm{pA}$ **(d)**, **(f,g)** Additionally, the orientation of the protruding substituents can be changed as indicated by the white arrows in (f). Scan parameters of (d),(e): $U_b = 1.7\,\mathrm{V}$, $I_t = 81\,\mathrm{pA}$.*

lines in Figure 6.4b) has the parameters $a = b = 26.0 \pm 0.5\,\text{Å}$ and $\Theta = 60 \pm 3°$, which results in a packing density of 0.34 molecules/nm^2. The network is stabilized by intermolecular vdW and H-bonding interactions between the aryl moieties decorating the BN core. The small molecule–molecule distance suggests that the flexible substituents are bent to reduce steric hindrance (see Figure 6.4c).

Nevertheless, STM-based manipulation experiments indicate weak intermolecular attraction as individual molecules can be removed from the edges of the islands in a controlled fashion without significantly perturbing the self-assembled network (Figure 6.4d,e). For this purpose, the STM tip is positioned above a rim molecule, which is dragged out to the bare Ag terrace (indicated by the white dashed lines) applying a bias voltage of $U_b = 50\,\mathrm{mV}$ and a tunneling current of $I_t = 20\,\mathrm{nA}$. Furthermore, the molecules can be rotated by STM manipulation, changing the orientation of the pyridyl-terminated substituents with respect to the molecular axes (Figure 6.4f,g). The flexibility of the substituents is clearly revealed in Figure 6.4f where apparent angles between 90° and almost 180° are observed between adjacent aryl substituents.

In addition to the most abundant arrangement in six-membered rings, a second dense-packed phase (packing density 0.41 molecules/nm^2) embedded in the honeycomb network is occasionally observed (see Figure E.2). In this phase, **BNPPy** are assembled in rows consisting of pairs of molecules oriented in opposite directions. This pair of molecules constitutes the base unit observed in both structures on the Ag substrates, suggesting that the molecular packing is governed by the same intramolecular interactions and the concentration of molecules on the surface (see Figures 6.4 and E.2). Large coverage deposition promotes the formation of the second phase, which presents a more compact network.

After annealing the sample to 570 K, the hexagonal arrays still occur, including some dislocation lines. Additionally, disordered regions are observed (see Figure E.4b), where covalent structures, formed through thermal activation of C–H bonds, are presumably present.

6.2.2 BNPPy on Cu(111)

The self-assembly behavior of **BNPPy** molecules on Cu(111) is summarized in Figure 6.5a. A highly ordered porous 2D network with molecules arranged in interconnected chains (Figure 6.5d) is formed after deposition of the molecules onto the sample at room temperature. The trapezoidal unit cell of the network has the parameters $a = 38.4 \pm 2.9$ Å, $b = 26.5 \pm 2.3$ Å and $\Theta = 75 \pm 5°$. The packing density is 0.20 molecules/nm^2 and the short axis of the unit cell is found to be parallel to one of the $\langle 1\bar{1}0 \rangle$ directions of the Cu(111) surface. The growth of the network initiates at step edges. Subsequently, the anisotropic islands expand onto the terraces (Figure E.3a). A similar self-assembled chain-like structure was observed for the borazine derivative **BNAPy** on the same support (see Figure E.6). Due to the reduced length of the aryl substituents, the **BNAPy** network presents a smaller trapezoidal unit cell with the parameters $a = 32.6 \pm 2.6$ Å, $b = 19.2 \pm 2.4$ Å and $\Theta = 75 \pm 4°$.

Along the rows, the molecules are alternately rotated by $180 \pm 6°$ and remarkably close-packed. The center-to-center distance (20.5 ± 0.5 Å for **BNPPy** and 17.9 ± 0.4 Å a for **BNAPy**, respectively) suggests that the substituents are slightly bent (Figure 6.5d). Adjacent rows are connected *via* opposing substituents in **BNPPy** and **BNAPy** networks with a center-to-center distance of 32.2 ± 0.6 Å and 27.2 ± 0.5 Å, respectively. This long distance suggests a pyridyl–Cu–pyridyl coordination motif, where the N atoms of the peripheral pyridyl groups are coordinated to a copper atom. Notably, due to the flexibility of the lateral aryl substituents, the molecules are not necessarily connected in a straight line. This results in the formation of a porous network featuring voids of unequal size.[Sch18b, Éci12]

Deposition of additional copper atoms with the sample kept at 420 K gives rise to a structural transformation of the chain-like network: patches of fully Cu-coordinated hexagonal arrays embedded in the former assembly of **BNPPy** on Cu(111) emerge (Figure 6.5b).

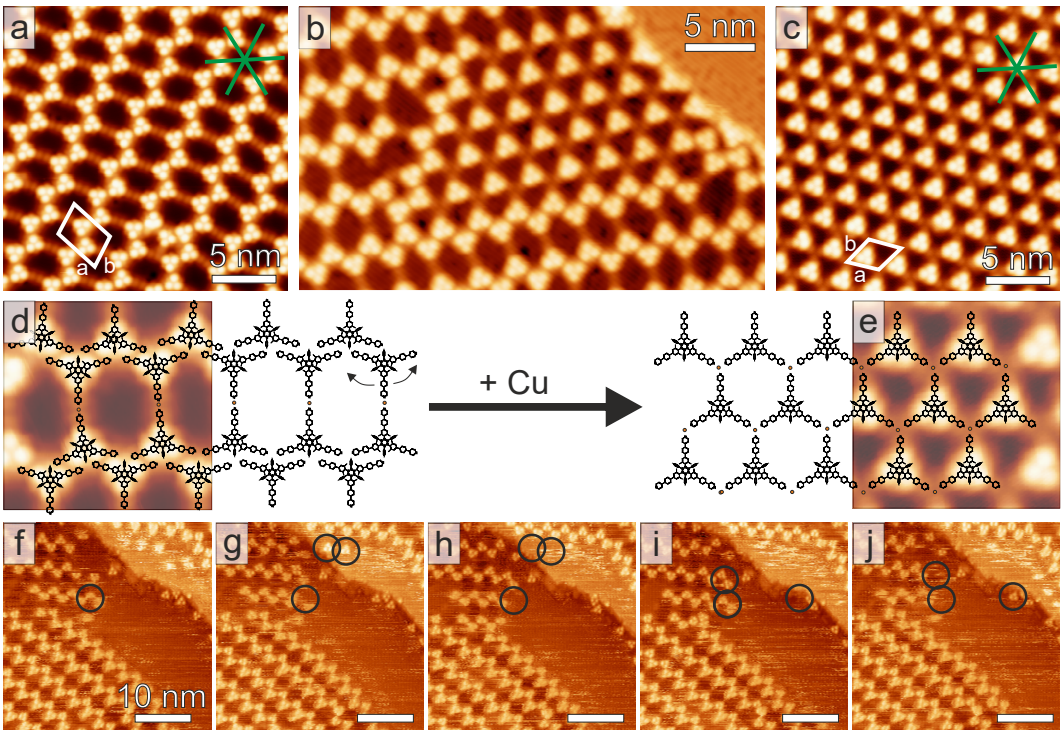

Figure 6.5: *STM images of **BNPPy** on Cu(111). **(a)** Upon room temperature deposition, the **BNPPy** molecules form chains that are interconnected by the protruding substituents coordinated to a Cu adatom. Scan parameters: $U_b = 1.2\,\mathrm{V}$, $I_t = 100\,\mathrm{pA}$ **(b)** Deposition of additional Cu atoms while the sample is held at 420 K, leads to a structural transformation and patches of molecules with all three substituents coordinated to Cu atoms are formed. Scan parameters: $U_b = 1.0\,\mathrm{V}$, $I_t = 64\,\mathrm{pA}$. **(c)** With sufficient Cu adatoms available, extended islands with fully three-fold coordinated **BNPPy** molecules are observed. The models of the molecular network is superimposed on the STM images in (a) and (c). Scan parameters: $U_b = 0.96\,\mathrm{V}$, $I_t = 40\,\mathrm{pA}$. **(d)-(h)** A series of STM images acquired at 300 K shows that the chain-like network is observable at room temperature. Consecutive scans of the same area reveal that individual molecules at the edge of the molecular islands are mobile (highlighted by black circles). Scan parameters: $U_b = 1.0\,\mathrm{V}$, $I_t = 110\,\mathrm{pA}$.*

Annealing to this temperature in the absence of extra copper atoms or deposition of the molecules at 420 K does not trigger the formation of this phase. In this new network structure, three **BNPPy** molecules are coordinated with the N atoms of their terminal pyridyl groups to a node that presumably consists of a single Cu atom (see discussion below). As in the previous chain-like assembly, the individual Cu atoms are not resolved in the STM images. Increasing the dose of additional Cu atoms completely transforms the chain-like architecture into a three-fold coordinated, fully reticulated metal-organic network (Figure 6.5c,e and Figure E.3b). The trapezoidal unit cell has the parameters $a = 25.5 \pm 1.7$ Å, $b = 24.2 \pm 1.6$ Å with an internal angle $\Theta = 60 \pm 2°$, resulting in a packing density of 0.18 molecules/nm^2. Notably, the nanostructure does not align with the high symmetry directions of the crystal. Further annealing of either network to temperatures higher than 470 K results in a poly-

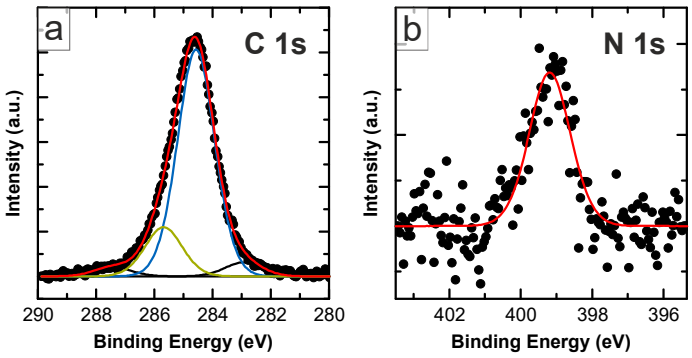

Figure 6.6: *XP spectra of the* ***(a)*** *C*1*s and* ***(b)*** *N*1*s core level of* ***BNPPy*** *on Cu(*111*). Both spectra are background subtracted with a Shirley background. The red line is the fit to the data.*

meric phase. Contrary to a recent study employing bromine-substituted borazine derivatives aiming for highly regular polymeric nanostructures,[Sán15] only disordered structures were observed. Molecules have presumably lost part of their peripheral substituents and are bond covalently (see Figure E.4a). A similar observation was made for the dense-packed structure on Ag, when it was annealed to 570 K (see Figure E.4b).

STM measurements performed at 300 K (Figure 6.5f-j) reveal that the chain-like **BNPPy** network, comprehensively characterized at 5 K (Figure 6.5a), prevails at room temperature. However, consecutive scans indicate that borazine modules at the edge of molecular islands are mobile, while the bulk of the self-assembled architecture remains mostly unperturbed. Likely, this is a consequence of the weak molecule–substrate interaction combined with the high mobility of Cu adatoms at room temperature that, enabling diffusion of the molecules, allow the dynamic formation and rupture of coordination bonds at the periphery of the self-assembled islands.

Finally, we have carried out XPS measurements on the chain-like network on Cu(111) in order to investigate the ability of the **BNPPy** molecule to adsorb CO through its central borazine core, thus exploring the potential binding of polar guest gases alluded to in the introduction. XP core-level spectra of a sub-monolayer of **BNPPy** on Cu(111) before dosing CO are shown in Figure 6.6. The main component of the C 1*s* core level is observed at a binding energy $E_b = 284.8$ eV. The N 1*s* core level is found at a binding energy 399.2 eV. Due to its low cross-section, the B 1*s* core-level could not be resolved for sub-monolayer coverage. In **BNPPy** multilayers on Cu(111), the C 1*s* and N 1*s* core levels (Figure E.5) reveal a slight upshift by 0.4 eV and 0.2 eV, respectively. This is attributed to a suppressed polarization screening by the metallic substrate in the case of the multilayer.

After a CO dosage of 60 L at room temperature and a dose of 6 L at ∼100 K, no changes in either core level have been detected in XPS for sub-monolayer coverages. Also in STM measurements no structural changes were detected after an *in-situ* dose of 10 K of CO at

temperatures below 15 K. Therefore, we infer that the CO is not adsorbed on the self-assembled network. Presumably, this is caused by the presence of the sterically-hindering methyl substituents that, shielding the borazine core, impede the formation of favorable dipolar interactions between the BN bonds and CO gas molecules.

6.2.3 STS Characterization of BNPPy

STS data of **BNPPy** on a Cu(111) single crystal and a Ag(111) film are summarized in Figure 6.7. In the case of Cu(111), the spectra taken in the pore of the chain-like assembly (Figure 6.7b, blue spectrum) show a pronounced feature at ~ -400 meV, which is attributed to the increase of the local density of states due to the surface state of Cu(111). This feature is still detected in the spectra taken at the center (red spectrum) and at the bright lobe (yellow spectrum) of the molecule as indicated in Figure 6.7a. In analogy to reports on other physisorbed adsorbates,[Zir09] the persistence of the surface state feature signals that the borazine core is only weakly interacting with the substrate. Moreover, an additional broad resonance is observed at 2.3 V, reflecting an electronic feature of the **BNPPy** molecule, as no such signature is observed on the bare metal. Spectra taken at the coordinated pyridyl substituent (Figure 6.7b, green spectrum) show a pronounced resonance shifted by ∼350 meV toward lower energy compared to the spectral feature observed on the molecular core. Indeed, the alignment and spatial distribution of molecular orbitals can be affected by the site-specific bonding with metal adatoms as previously reported.[Yan14, Umb14]

In the case of **BNPPy** on the Ag(111) film, the lowest unoccupied molecular resonance is found at ∼2 eV and the related surface state feature at ∼50 meV (Figure 6.7d, black spectrum) is also detected on the core of the molecule (red and yellow spectrum). However, for spectra taken at the center of the pore (Figure 6.7c, blue dot), the surface state feature is not observed. This can be tentatively explained by the presence of the terminal pyridyl rings (Figure 6.4c), which are clearly visualized in STM images only at certain bias voltage. The real pore size is drastically reduced compared to that appearing at low bias voltages. Indeed, this bias dependent contrast is revealed in an STM voltage series of **BNPPy** on Ag(111) displayed in Figures 6.7e-g. At low bias voltages, the contrast of the **BNPPy** molecule is dominated by the three bright protrusions in the center, while the peripheral substituents are only faintly visible (Figure 6.7e, $U_b = 0.6$ V). At higher bias voltages, the terminal pyridyl groups of the substituents are imaged brighter than the molecular core (Figure 6.7g, $U_b = 2.4$ V), indicative of unoccupied molecular resonances located on the terminal moieties.

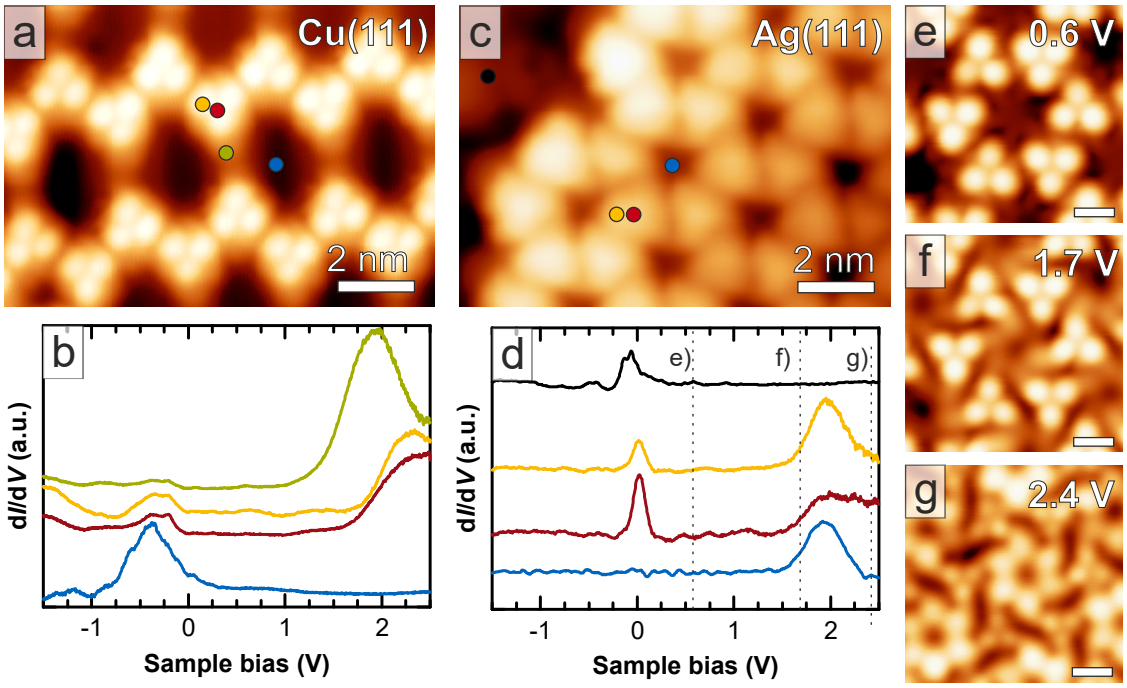

Figure 6.7: *STM images of* ***BNPPy*** *on* ***(a)*** *Cu(111) and* ***(c)*** *a Ag(111) film (Scan parameters in both images:* $U_b = 1.0\,\mathrm{V}$, $I_t = 100\,\mathrm{pA}$. *The corresponding STS spectra recorded on characteristic positions of the respective assembly are shown in* ***(b)*** *and* ***(d)****.* ***(e)-(g)*** *Voltage series of* ***BNPPy*** *on Ag(111). The scale bar is* 1 nm. *Set point:* $I_t = 200\,\mathrm{pA}$.

6.2.4 Discussion

Using high-resolution STM imaging and X-ray diffraction, we show that individual **BNPPy** molecules have a remarkable flexibility, which is expressed by the possibility of their pyridyl-terminated substituents to bend in-plane. The terminal pyridyl groups drive the self-assembly, which can be controlled by the choice of the metal substrate. On Ag(111) and Ag(100) surfaces, the molecule–substrate interaction is weak and no influence of the surface termination on the network architecture was observed. The self-assembly is driven by intermolecular vdW forces and H-bonding leading to a dense-packed network (0.34 molecules/nm^2) and no indication for metal coordination has been observed. Previous studies have been devoted to the coordination chemistry of pyridyl-functionalized molecules in the quest to achieve supramolecular networks.[Kla08, Hei10a, Hei10b, Li11, Lan08, Li12, Tai07, Stu15, Lin13] In particular, utilizing Cu atoms as metallic coordination nodes, two-fold pyridyl–Cu–pyridyl coordination has been reported on Ag(111) and Cu(111).[Umb14, Kla08, Hei10b] However, a coordinated **BNPPy** network could not be achieved on silver surfaces, neither by annealing nor by providing additional Cu atoms within the experimental parameter space that was explored.

Contrary to borazine derivates terminating with phenyl moieties,[Kal14] **BNPPy** forms a highly ordered assembly on Cu(111), in which chain-like structures are formed involving Cu coordination. The resulting porous network features a packing density (0.20 molecules/nm^2) clearly reduced compared to that formed by **BNPPy** on Ag(111) and Ag(100), as well as compared to similar phenyl-terminated borazine derivatives on Cu(111) [Kal14] (0.33 molecules/nm^2). Thus, pyridyl-mediated metal-coordination allows for the fabrication of stable borazine arrays with unprecedented pore sizes. Interestingly, this network does not reflect the three-fold symmetry of **BNPPy**, but bases on interconnected chains where only one of the three pyridyl-substituents seems to engage in Cu coordination. Even if we cannot exclude the presence of some coordinative interactions along the chains, our data suggest the simultaneous expression of metal-organic and organic bonding motifs.[Vij13, Bis16] The measured center-to-center distance between **BNPPy** units along the coordinated substituents, that is, perpendicular to the chain direction, is 32.2 ± 0.6 Å. With a pyridyl-substituent length of 14.4 Å, extracted from the structural model (after geometry optimization with the semi-empirical AM1 method in HyperChem), this results in a projected pyridyl–Cu–pyridyl bond length of 3.4 Å, slightly reduced compared to the 3.6 Å reported in the literature.[Hei10a, Li12, Tai07, Bis16] This can be rationalized by the in-plane bending of the substituents. Accordingly, the projected N–Cu bond length corresponds to 1.7 Å.

A fully reticulated coordination network with a three-fold symmetry was achieved by the deposition of additional Cu atoms. Three-fold Cu coordination has previously been reported for CN end groups,[Pac15, Sir13, Paw08] bipyridyl molecules,[Lan12, Tai08] and pyridyl-terminated tectons.[Hei10a, Vij12, Yan17] However, for the latter case, reports on two-fold pyridyl–Cu–pyridyl coordination clearly prevail.[Kla08, Hei10a, Hei10b, Lin13, Li11, Lan08, Li12, Shi09, Wur16] In the present system, the N–Cu bond distance in the three-fold node ((3.0 ± 0.5) Å) significantly exceeds the theoretically predicted value of 1.6 Å[Li12] and the 1.7 Å characteristic for the two-fold motif, which might reflect steric hindrance between the (nearly) co-planar pyridyl rings. Nevertheless, we cannot exclude a minor rotation of the terminal pyridyl moieties out of the surface plane. For instance, such rotations can enable a four-fold coordination of tetra-pyridyl-porphyrins to mononuclear centers.[Wur16] We assign the coordination center to a single Cu atom (see Figure 6.5e), as no protrusion is apparent at the three-fold node. Protrusions were previously observed in three-fold motifs featuring Cu dimers coordinated to pyridyl termini.[Hei10a]

Our STS data on **BNPPy** and **BNAPy** molecules (Figures 6.7 and Ref.[Sch18b]) reveal that the surface state feature is still detected on the molecular core on both the Cu(111) and the Ag substrates. This observation shows that the borazine core is decoupled from the metallic substrates by means of the dimethyl substituents, a fact which has been anticipated for similar borazine derivatives in a previous report.[Kal14] Additionally, the XPS binding

energy of the N 1*s* line is at 399.2 eV, comparable to the value reported for other borazine derivatives on noble metal supports,[Cic16] and exceeding the value for *h*-BN/Cu(111) by about 1 eV.[Pre05] The different contributions of the N atoms located in the borazine core and in the pyridyl moieties could not be resolved with our lab-based XPS setup.

6.3 Conclusions

In this chapter, we presented our results on in-plane *h*-BNC heterostructures. First, we have demonstrated the successful CVD synthesis of *h*-BN–G junctions on Cu(111) and presented a concise characterization of the interface by means of XPS, STM, and STS. A successive growth of the two materials seems to be favorable and yields in-plane junctions with the lattices of *h*-BN and G aligned along the same direction. A different growth sequence, *i.e.* growing graphene on a sub-monolayer *h*-BN-covered sample could be pursued in the future.

In a second set of experiments, we combined pyridyl-functionalized borazine derivatives with selected substrates to achieve distinct network architectures, exploiting the remarkable flexibility of the substituents. While the **BNPPy** molecules form a dense-packed hexagonal network on Ag substrates, a porous network evolves for **BNPPy** and **BNAPy** on Cu(111) with stability up to room temperature. The deposition of additional Cu atoms yields a structural transformation of the metal-organic architecture on Cu(111), which leads to a fully reticulated network with a three-fold pyridyl–Cu coordination motif. Following this approach, the molecular density could be varied from 0.20 mol/nm^2 to 0.18 mol/nm^2, expanding the corresponding pore size from 0.7 nm^2 to 6.0 nm^2. These findings thus provide unprecedented metal-organic coordination architectures on surfaces based on BNC-containing molecules. Our experiments likely suggest that the presence of the sterically shielding methyl groups on the aryl B-bearing substituents prevents the adsorption of CO on the BN core, notwithstanding, they electronically decouple the BN core from the conducting substrate. This findings provide valuable insight for the design of borazine derivatives targeting the anchoring of CO in functional nanostructures comprising for example functionalized hybrid *h*-BNC polyphenylenes and graphene-like structures.[Bon15, Lor17]

Chapter 7

Conclusions and Perspectives

This thesis describes the characterization of interfacial interactions between atoms, molecules, 2D materials and noble metal surfaces. To this end, we have employed several complementary surface science techniques, such as STM, AFM, LEED, XPS and XSW and have learned that it is the combination of these powerful techniques that has provided a fully grounded understanding of the system under investigation. Studying the fundamental structural, electronic and magnetic properties of those systems constitutes a valuable source of knowledge for potential technological applications in future nanoscale devices.

In Chap. 4, epitaxial *h*-BN layers on the noble metal substrates Cu(111) and Ag(111) were introduced. In the case of Cu(111) the adsorption height of the atomically thin *h*-BN layer was determined unambiguously by combining XPS and XSW. The structural parameters of XSW suggested a significant corrugation in the system, which was verified by complementary AFM measurements in the course of which a novel experimental method was developed. The described AFM technique — presumably even applicable to similar STM measurements — enables to determine relative height differences in two-dimensional layers, as well as potentially in large polycyclic molecules. Its combination with XSW thus provides exciting opportunities for a detailed structure determination at the nanoscale. We showed that also the relatively inert Ag(111) substrate allows to grow epitaxial *h*-BN layers utilizing ion-gun assisted CVD. The weak interaction between the *h*-BN layer and the metal substrate is reflected by the conservation of the Shockley surface state, which is still detectable in STS measurements upon adsorption of *h*-BN. However, as the direct growth of *h*-BN on Ag(111) results only in *h*-BN domains of minor structural quality, intercalation of silver in *h*-BN/Cu(111) was explored. Our promising results suggest that this approach yields large-scale *h*-BN domains on a silver substrate and that the electronic properties of the interface (*e.g.* the work function and the electronic corrugation) can be tuned smoothly between the ones achieved on Cu(111) and on Ag(111) supports through the employed thickness of silver, providing a tailored platform for molecular adsorbates.

Future experiments in this field could tackle the systematic investigation of the *h*-BN corrugation on Cu(111) as a function of the moiré size. This question could even be studied by DFT once the exchange-correlation functionals are further refined, confidence in its predictive power is attained, and enough computing power is available to perform efficient calculations on full *h*-BN moiré cells. In order to get a comprehensive understanding of the interfacial interactions between *h*-BN and Ag/Cu(111), the geometric structure of the system needs to be studied in more detail, *e.g.* by high-resolution nc-AFM. *h*-BN on Ir(111) represents a potential test system for the applicability of the AFM method to highly corrugated systems, with a quantitative structure determination by means of XSW having been reported in the literature.[Zum16]

Chap. 5 presented experiments with porphyrin molecules as well as single cobalt atoms on solid surfaces and *h*-BN supports. We determined the conformation of Co–P on Cu(111) and obtained the exact lateral registry, a surface bridge site, unambiguously by a combined STM and XSW analysis. Furthermore, we provided evidence that photoemission-based techniques are capable of exploring the wide range of organic molecular adsorbates on epitaxial 2D overlayers as evidenced by our adsorption geometry determination of Co–P on *h*-BN/Cu(111) as a prototypic system. The adsorption height of Co–P on the *h*-BN layer as well as the molecule–substrate interaction was discussed. Utilizing carbonitrile-functionalized porphyrin molecules, we demonstrated the formation of 2D metal-organic coordination networks on an insulating *h*-BN layer promoted by cobalt adatoms. Moreover, we showed for the first time an *in-situ* metalation of a porphyrin macrocycle with metal atoms directly on an insulating sp^2 sheet. The resulting nanoporous network features Co centers in distinct environments, hence constituting a mixed oxidation and valence network with prospects for applications in hybrid nanoarchitectures. Surface magnetism was studied on cobalt atoms in different structural and chemical environments through characterization of the Kondo exchange interaction between the single unpaired electron spin of Co and the underlying metal.

Based on the gained insights, we propose to study the metallo-supramolecular coordination network, Co–TPCN on *h*-BN/Cu(111) in more detail, where interesting Kondo physics and spin excitations can be expected. Moreover, the fundamental studies on the adsorption geometry of porphyrin molecules on *h*-BN have opened paths to further investigate several topics: first, the effect that molecular adsorbates exert on an atomically thin layer has yet to be studied experimentally. Second, the presented measurements have indicated an intriguing temperature dependence in the adsorption height of Co–P on a Cu(111)-supported monolayer of *h*-BN. This effect has been anticipated in the literature[Mer13] to explain the discrepancies between DFT calculations representing a kelvin environment and measurements performed at finite or ambient temperatures, but to date not measured experimentally. However these experiments have been performed on two different preparations of the boron nitride layer,

thus a more reliable measurement of this effect is required and will be performed in an upcoming synchrotron beamtime. The data analysis could yield corrections to the DFT calculations to model this finite temperature effect, shedding significant insight into the interaction of molecular semiconductors on *h*-BN, and more generally into the underlying physics of molecular adsorption. Ultimately, the measurements have revealed that, although the *h*-BN layer does significantly decouple the Co–P molecules, this decoupling is not total, and a measurable interaction remains between molecular adsorbates and the underlying substrate. This illustrates the need for an even more inert substrate for the *h*-BN layer (such as *e.g.* SiC, Ag or Au) or to employ multiple *h*-BN layers to obtain a more idealized approximation of adsorption on an insulating substrate.

Chap. 6 summarized the experimental findings on *h*-BNC heterostructures, which can be realized *via* two systematically different approaches. First *h*-BN and G domains were stitched together in-plane through simultaneous as well as sequential growth of *h*-BN and G *via* CVD and atomic carbon evaporation, respectively. The electronic properties such as the work function and the modification of the surface state were found to be very similar in both materials. Second, as an alternative strategy to obtain well-defined B/N–C bonds, tailored molecules comprising doping BN-hexagons within a poly-aromatic hydrocarbon scaffold were employed. The self-assembly of two custom-designed borazine derivatives was studied on the noble metal substrates Cu(111) and Ag(111). We observed that the substrate plays an important role leading to a metal-organic coordination network in the case of Cu(111) and resulting in densely-packed islands in the case of Ag(111).

For future work, advanced borazine derivatives with a slightly modified structure or carefully chosen, cleavable protection groups could be employed, possibly resulting in the formation of truly in-plane covalent networks. Moreover, the exploration of in-plane *h*-BN–G heterostructures holds great prospects, *e.g.* as a method to tune the graphene band gap,[Ci10, Wan13] and to pave the way toward the construction of atomically thin graphene-based integrated circuits.[Lev12, Liu13] A detailed understanding of the *h*-BN–G junction on the atomic level could be pursued by means of high-resolution nc-AFM, which might lead to the development of protocols for large-scale synthesis of well-defined heterostructures. Moreover, it could be beneficial to explore another growth sequence: having sub-monolayer *h*-BN on the sample before the evaporation of carbon. In this context, also the defined edges of graphene nanoribbons[Cai10, Ruf16] could also be exploited. Another possible approach could be to functionalize *h*-BN domains with tailored molecular building blocks, similar to what has been achieved recently by fusing porphine molecules to graphene edges.[He17a, He17b] Moreover, vertical heterostructures consisting of *h*-BN and various other 2D materials are conceivable and of great interest.[Bri12, Gei13, Nov16] Especially the combination of *h*-BN and transition metal dichalcogenides (TMD) such as WS_2, MoS_2 or $MoSe_2$ seems very promising, owing to

the decoupling characteristic of boron nitride, and the demonstrations that monolayer TMDs form atomically thin direct band gap semiconductors,[Mak10, Spl10, Ton13] providing new opportunities for technological innovations in the field of optoelectronics[Che18b] as well as for the exploration of new physical phenomena.[Wan12b] Eventually, the direct, on-surface synthesis of graphene nanoribbons or other molecular complexes on *h*-BN sheets might be interesting to obtain a better understanding of physics at the nanoscale.

On a broader perspective, quantum materials are more and more in the focus of research lately. In this class of materials that include *e.g.* graphene, superconductors, and topological insulators, electrons are strongly correlated and quantum effects manifest over large ranges of energy and length scales.[Kei17] Since many of these phenomena occur at surfaces or interfaces, they are predestined for experiments utilizing the broad toolbox of surface science, opening new avenues of research on a vast variety of materials with fascinating properties.

Appendix A

List of Devices

A.1 LT-STM

Analysis chamber	
STM	CreaTec LT-STM (Besocke Beetle type)
In-situ evaporator	Home-built 3-cell evaporator
Pressure gauge	PfeifferVacuum IKR 270 Active Piezo Transmitter
Ion pump	Varian VacIon Plus 300 Starcell
Preparation chamber	
Sample manipulator	VAb UHV Präzisions-Manipulator PM-25-500
	VAb UHV Präzisions-Durchführung DDF 63 P
	VAb He-Verdampfer-Kryostat HVK-STM-500
Ion source	SPECS IQE 11/35
Resistive evaporator	Home-built evaporator for copper
E-beam evaporator	Focus EFM 3s
OMBE source	Dodecon Molecular Beam 4-cell evaporator
LEED	MDC Vacuum Products HTBRM-133-SP
Pressure gauge	PfeifferVacuum IKR 270 Active Kaltkathode Transmitter
Ion pump	Varian VacIon Plus 300 Diode
Titanium sublimation pump	Varian Titan Sublimations Cryopanel
Turbo pumps	OerlikonLeybold TVP TURBOVAC 340 M
	Alcatel ATS 100
Diaphragm pump	Vacuubrand Membranpumpe MD 4 NT
Electronics	
STM DSP board	CreaTec LT-STM Electronic Type DSP-10-CB-02
STM HV amplifier	CreaTec HV-Amplifier
Current to voltage amplifier	Femto DLPCA-200 Current Amplifier

Lock-in amplifier	Stanford Research System SRS850
Oscilloscope	Tektronix TBS 1052B-EDU
Ion source controller	SPECS PU-IQE 11/35
Pressure gauge display	PfeifferVacuum TPG 256 A MaxiGauge
LEED controller	Omicron SPECTALEED CONTROL UNIT
E-beam evaporator controller	Focus EVC 300
Voltage sources	Laboratory Power Supply EA-PS-3016-10 B

A.2 XPS-STM

STM chamber	
STM	CreaTec STM with PAN-Slider
Pressure gauge	Vacom BARION-BASIC (Bayard-Alpert)
Ion pump	GammaVacuum 600TV
XPS / Preparation chamber	
Sample manipulator	VAb UHV Präzisions-Manipulator PM-25-600
	VAb UHV Präzisions-Durchführung DDF 63 P
	VAb He-Verdampfer-Kryostat HVK-STM-600
Ion source	SPECS IQE11/35
Resistive evaporator	Home-built evaporator for copper
E-beam evaporator	Focus EFM 3s
OMBE source	Home-built Knudsen-cell evaporator (3 cells)
X-Ray gun	SPECS XR 50
Electron analyzer	SPECS PHOIBOS 100 with MCD detector
Residual gas analyzer	Stanford Research Systems RGA100/12
Pressure gauge (UHV)	Vacom BARION-BASIC (Bayard-Alpert)
Pressure gauge (FV)	Vacom LH-230035 (Pirani)
Titanium sublimation pump	GammaVacuum TSP 3 FILAMENT
Turbo pumps	Oerlikon Leybold MAG W 400 iP
	Oerlikon Leybold TURBOVAC SL 80
Diaphragm pump	KNF N920AP.29.18
Electronics	
STM DSP board	CreaTec DSP-10-CB-03-STM
STM HV amplifier	CreaTec HV Verstärker
Current to voltage amplifier	Femto DLPCA-200 Current Amplifier
Oscilloscope	VOLTCRAFT DSO-1062D

Sputter gun controller	Home-built ion source controller
Pressure gauge display	Vacom MVC3-B0
	Vacom MVC3-BM
Ion pump controller	GammaVacuum MPC-1-P-S-1-EC230-232-H-ITSP
Electron analyzer controller	SPECS HSA 3500 plus
X-Ray gun controller	SPECS XRC 1000
X-Ray gun water cooling controller	SPECS CCX 60/R2
Cooling unit	Van der Heijden KÜHLMOBIL
	002-B400-SON-SPECS-16
E-beam evaporator controller	Focus EVC 300
Voltage sources	Laboratory Power Supply EA-PS-3016-10 B

A.3 Diamond Light Source - i09 Beamline

UHV chamber	
X-Ray energy ranges	Hard X-Rays: 2.1 - 18 keV
	Soft X-Rays: 230 - 2000 eV
Electron Analyzer	VG Scienta EW4000 HAXPES
	with a 70 frame/sec CCD camera
	Analyzer-incdent beam angle = 60° or 90°
Sample manipulator	5 axes: X, Y, Z, polar (0 - 360°) and azimuth (0 - 360°)
	Omicron type sample plates
E-beam evaporator	Focus EFM 3s
OMBE source	Home-built Knudsen-cell evaporator (3 cells)

Appendix B

Vacuum Distillation of Borazine

In the course of this thesis, borazine was used as a precursor for the growth of *h*-BN via CVD (see section 4). Borazine is liquid at room temperature and, importantly, decomposes rapidly to boric acid, ammonia and H_2 in the presence of ambient humidity,[Bon15] and ultra-violet light.[Kön15] It is very reactive due to its electrophilic boron atoms, which favor the opening of the aromatic ring leading to the degradation of the borazine molecule. To circumvent this issue and enable its use as a precursor that is stable over reasonable timescales, a special approach is necessary to handle borazine.

In the following, the vacuum distillation transfer of borazine, from the delivered stainless steel container into smaller quantities that are used for sample preparation in the UHV chamber, is explained in detail. The method has two major advantages: First, it prevents borazine from contamination (by air and hence in particular water) and thus decomposition during the transfer. Second, the glass tube is filled with pure borazine, as gaseous decomposition products of borazine do not condense at the applied temperature. The borazine with a purity of 99% was purchased from KatChem, Prague, Czech Republic.[Kat17] The glass tube in which the borazine is stored when attached to the UHV chamber is basically a glass tube equipped with a vacuum tight, low leakage PRODURAN valve,[DUR17] and a glass-metal transition in order to mount it to the CF flange of a leak valve. The glass tube allows for visual inspection of the borazine quality.

Figure B.1a shows the employed setup for transferring borazine by condensation from the stainless steel container into the glass tube. The borazine container is mounted with either of its two valves to a KF/CF vacuum (Schlenk) line connecting it to the glass tube. Additionally, two valves are required. One connects the vacuum line to a pumping station, while the other valve connects a He bottle. In our case, a combined rough/turbo pumping station is used, but in general, also a scroll pump or only a rough pump can be used. The He gas is utilized to flush the vacuum line and acts as transport gas. Note that Ar gas should not be employed since the boiling point of Ar is 87.3 K,[Twu80] and therefore, Ar condenses when it is introduced into the liquid nitrogen cooled borazine container. For the transfer,

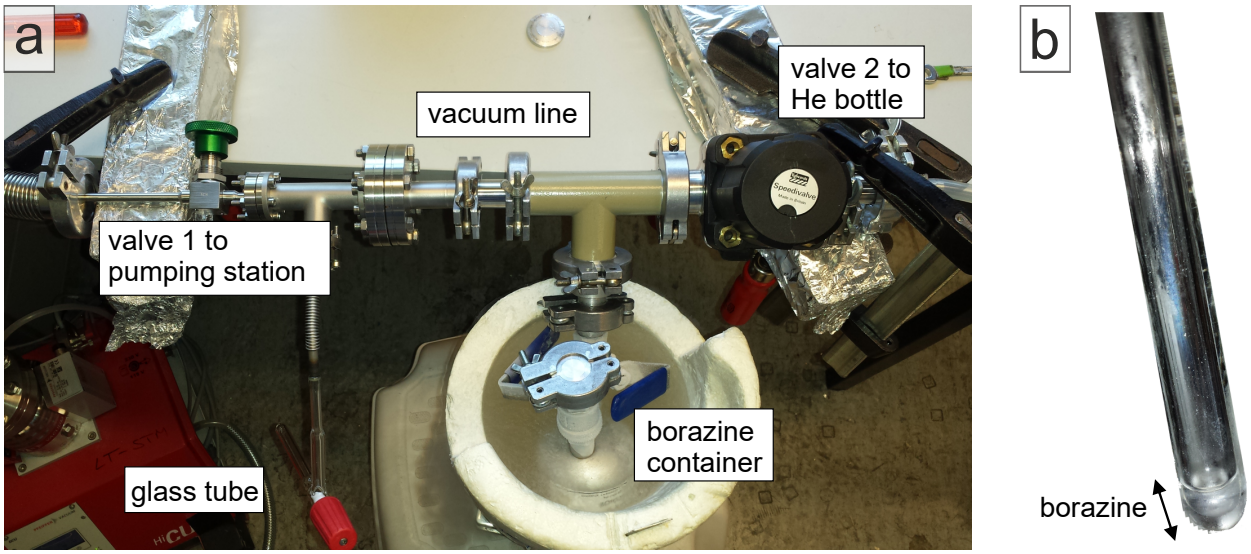

Figure B.1: ***a)*** *Photo of the vacuum distillation setup. The stainless steel container with the borazine and the glass tube are connected to a KF/CF vacuum (Schlenk) line. Two valves separate a pumping station and a He bottle from the vacuum line.* ***b)*** *Photo of* $\sim$2 ml *liquid borazine in the glass tube. Already very small quantities of borazine are sufficient for sample preparations over a period of several months.*

the vacuum line is evacuated, the borazine in the container is cleaned by two freeze-thaw cycles and subsequently condensed into the glass tube. The exact procedure is as follows:

- Open the valve to the glass tube. Then, adjust the pressure of the He bottle to have a slight overpressure and connect the tube to valve 2 of the transfer line. Next, close valve 2 (between the vacuum line and He bottle).
- Freeze the borazine container (its both valves are still closed) with liquid nitrogen.
- Open valve 1 (to the pumping station) and pump the vacuum line for some minutes.
- Close valve 1 and open valve 2 to introduce He into the vacuum line.
- Close valve 2.
- Slowly open valve 1 to pump the vacuum line for some minutes. The vacuum line should now be clean and under vacuum.
- Close valve 1 and then open the valve of the borazine container.
- Slowly open valve 1 and pump the transfer line for some minutes.
- Close valve 1 and open valve 2 to introduce He into the transfer line. The borazine container is still cooled by nitrogen and the connecting valve is open.

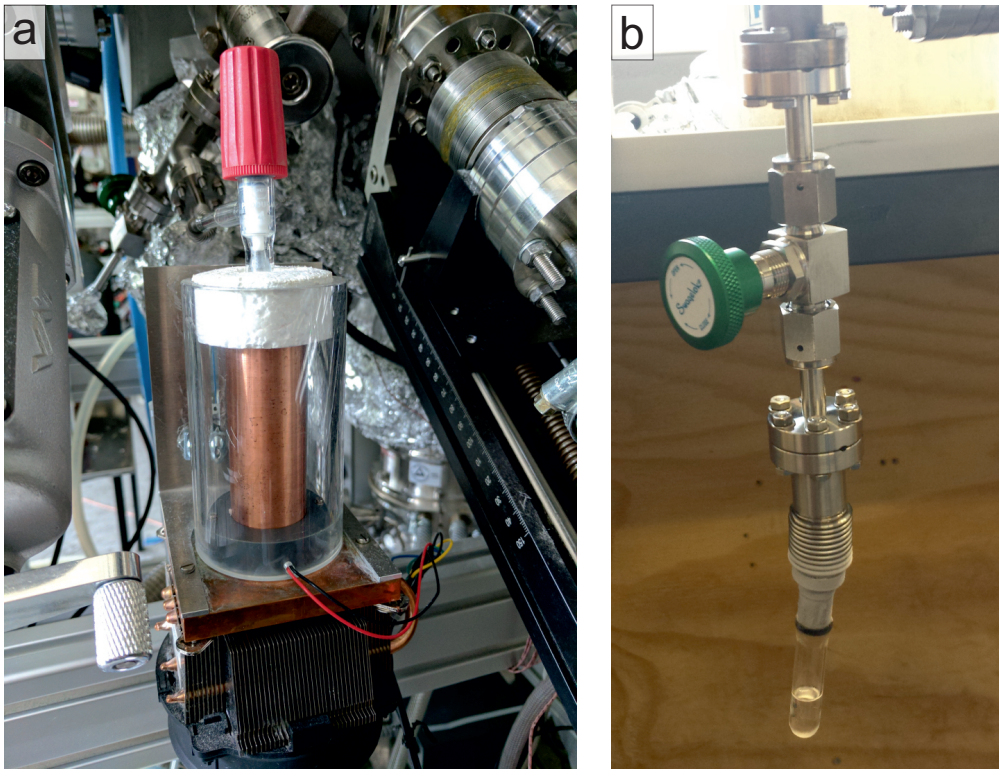

Figure B.2: ***a)*** *Photo of the Peltier Cooler in which the borazine glass tube is stored when attached to the UHV chamber.* ***b)*** *Photo of a new glass tube equipped with a Swagelok valve instead of the PRODURAN teflon stamp.*

- Close valve 2 and slowly open valve 1 to pump the transfer line and the borazine container for several minutes. (The last two steps may be repeated twice.)
- Close valve 1.
- Remove the liquid nitrogen dewar from the borazine container allowing it to warm up. This step may take 15 to 20 min.
- The glass tube should now be placed in liquid nitrogen. Take care that the nitrogen does not get too close to the glass T-piece with the Teflon stamp to avoid leakage.
- As soon as the borazine in the container melts and becomes liquid, a vapor pressure of 300 mbar will be established in the vacuum line. Due to the temperature gradient toward the glass tube that is cooled with liquid nitrogen (acting as a cold trap), the borazine will condense into the glass tube.
- Remove the nitrogen dewar from time to time to allow the borazine, which freezes to the inner walls of the glass tube, to melt and rinse down into the glass tube.
- The filling procedure may take 1 to 2 h

Once ∼1 to 3 ml of borazine are filled into the glass tube (Figure B.1b), the transfer can be stopped. The borazine in the glass tube is frozen with liquid nitrogen and mounted to the leak valve of the UHV chamber. There, the metal T-piece (connecting the leak valve, the borazine glass tube and a Swagelok valve that allows to clean the borazine prior to every sample preparation) should be pumped and heated with a heat gun in order to get rid of water adsorbed on the inner tube walls. To protect the borazine from decomposition during storage, the glass tube is placed in a Peltier cooler (Figure B.2a) maintaining a temperature of $\sim -15\,^{\circ}\mathrm{C}$ and protected against ultraviolet light by wrapping it into aluminum foil. The stainless steel container should be stored in a fridge to reduce the decomposition of the borazine. Figure B.2b shows a new version of the glass tube equipped with a Swagelok valve, which may be used in the future to circumvent the flaws of the PRODURAN teflon-stamp valves.

Appendix C

Experimental Details for Chapter 4

C.0 Experimental and Computational Details

C.0.1 Data Acquisition and Analysis

Nc-AFM measurements were performed with a qPlus tuning fork sensor (resonance frequency ∼30 kHz, oscillation amplitude 80 pm, Q value ∼46 000) operated in the frequency modulation mode.[Gie98] The tip was prepared by indentation into bare Cu(111) and used without deliberate (CO-)functionalization. The actual corrugation of the *h*-BN layer was obtained with an experimental method in which we correlate the atomic contrast observed in the AFM frequency shift Δf to a height. First, the local atomically resolved *h*-BN lattice was measured in a series of constant height scans with different tip heights (Figure 4.2f–i and Figure C.3). Here, small-size images of 1 nm × 1 nm were acquired on pore and wire regions. A Gaussian high-pass filter (σ of 0.15 nm) and a low-pass filter (σ of 0.05 nm) were applied for background correction and noise reduction, respectively. For each pixel in the small-size images, the Δf amplitude $A_{\Delta f}$ is determined as the difference between the brightest and darkest regions in a surrounding square box with side lengths of 0.28 nm, 10 % bigger than the *h*-BN unit cell. By averaging over all pixels in each image, the average Δf amplitudes on wire ($A_{\Delta f,W}$) and pore regions ($A_{\Delta f,P}$) were determined and plotted as a function of the relative tip height (see Figure 4.2b,e). The tip height is defined with respect to a reference point that corresponds to the lowest tip height that was probed within the experiment. No noticeable influence of piezo creep and thermal drift was found as verified by repeated calibration scans in both directions, *i.e.* increasing and decreasing relative tip heights. An averaged linear calibration curve $A_{\Delta f}$ (solid lines in Figure 4.2b,e) is obtained from the linear fits to $A_{\Delta f,W}$ and $A_{\Delta f,P}$. The local Δf amplitude $A_{\Delta f}$ is proportional to the tip-sample distance $\Delta d_{tip-sample}$, *i.e.* $A_{\Delta f} \propto \Delta d_{tip-sample}$. Utilizing this relationship, the large-area AFM constant-height image of the *h*-BN layer (Figure 4.2a) can be translated into a calculated

height map $z_{calc}(A_{\Delta f})$ (Figure 4.2c) by converting the local Δf amplitude of each pixel of the constant-height image into a height difference.

The XPS and XSW experiments were carried out at the I09 end station of DLS as described in section 3.7. The XSW scans were acquired from the (111) Bragg reflection of Cu and were repeated over 20 unique spots, resulting in 10 individual B 1s and N 1s XSW data sets, which were then averaged to improve the signal to noise ratio. The uncertainty of the given structural parameters reflects the spread of results obtained by analyzing each measurement individually. The B 1s and N 1s peaks were fitted with two Voigt profiles, each given by a convolution of independent Gaussian $G(E_b, \sigma)$ and Lorentzian $L(E_b, \Gamma)$ contributions:[Hes07]

$$Voigt(A, E_b, E_{b0}, \Gamma, A) = A \cdot \delta(E_b - E_{b,0}) \times G(E_b, \sigma) \times L(E_b, \Gamma), \tag{C.1}$$

where A is the amplitude, E_b is the photoelectron binding energy scale, $E_{b,0}$ is the central binding energy of the Voigt profile, σ is the FWHM of the Gaussian, and Γ the HWHM (half-width at half-maximum) of the Lorentzian. The chosen widths of the Lorentzian components are in good agreement with reported core-hole lifetimes of B 1s and N 1s, respectively.[Nic12] The Gaussian and Lorentzian line shapes are both normalized, prior to convolution, to have an integrated area of 1. The Cu 3p peak, used to define the binding energy of the XP spectra, was fitted with a convolution of a Doniach-Šunjić function with a Gaussian line shape.[Sch17b] The integrated intensities of B 1s and N 1s photoemission peaks were used to obtain the relative X-ray absorption of the B and N atoms, respectively. Nondipolar effects in the angular dependence of the photoemission were accounted for with the asymmetry parameter Q which was calculated theoretically using the angle that corresponded to the average angle weighted by emission intensity at an off Bragg energy ($\Phi = 18°$ where Φ is as defined in reference [Fis98]).

To simulate the effect of the various height distributions (either extracted from the nc-AFM measurement or given by a Gaussian/rectangular function) on the geometric factor, and thus the coherent fraction, the structural parameters f^{111} and p^{111} were expressed as the amplitude and phase (respectively) of a Fourier component of the adsorption site, projected along the (111) direction of the Cu crystal. This component can then be expressed by an integral, between $p^{111} = 0$ and $p^{111} = 1$, and an associated probability assigned to each position, as described in Eq. (C.2) and Eq. (17) of Ref. [Woo05]. The length of the vector represents the coherent fraction and the angle is defined by the coherent position. Each individual component within the respective distribution was assumed to have a coherent fraction of 0.88 (taking into account the vibrational amplitudes discussed above) and weighted by a factor dependent on the distribution. An exemplary profile is shown in Figure 4.6a together

with its structural fit parameter. Simulated XSW absorption profiles for a Gaussian and a uniform height distribution are displayed in Figure C.5.

C.0.2 DFT Calculations of *h*-BN/Cu(111) in a (1×1) Unit Cell

DFT calculations using the Quantum ESPRESSO code[Gia09] were carried out by Ari Seitsonen. We employed several approximations (vdW-DF2-rB86,[Ham14, Lee10] vdW-DF-optB86,[Kli11] vdW-DF,[Dio04, Dio05] and revPBE+D2,[Zha98, Per96, Gri06]) in the exchange-correlation term, and compare to previous results to clarify the apparent discrepancies between those calculations. For simplicity we used the experimental lattice constant of 3.61 Å, four substrate layer-slabs with two bottom layers fixed, projector augmented wave (PAW) data sets for the pseudisation of the core electrons, and cut-off energy of 40 Ry for the wavefunctions and 400 Ry for the electron density and augmentation terms in the plane wave expansion. We first investigated the *h*-BN layer laterally positioned at the six high-symmetry registries,[Gom13] where the B and N atoms are located either at fcc, hcp or on-top position above the Cu(111) substrate. For example, the notation $B_f N_o$ corresponds to a B atom at lateral fcc site and N at on-top site. 24×24 grid of k points was employed in the integral over the first Brillouin zone. We checked that in ten-layer slabs with vdW-DF2-rB86 the results are only marginally changed (up to 0.01 Å in layer distances, 1 meV in energies and 0.01 eV in work functions). We further performed two calculations in a $(4\sqrt{3} \times 4\sqrt{3})R30°$ super-structure, where the *h*-BN layer was rotated by 30° relative to the substrate, yielding 49 BN pairs on 48 substrate atoms. Two additional calculations with a commensurate structure, with 48 BN pairs in the same cell as before, were performed with $B_o N_f$ and $B_f N_o$ registries in order to allow a comparison of the results with minimal qualitative differences in the system. A 2×2 grid of k points was employed.

$E_{N\,1s}$ core-level binding energies with the vdW-DF-rB86,[Ham14, Dio04, Dio05] as the exchange-correlation term were evaluated with the VASP code,[Kre96] in lateral 4×4 commensurate lateral cell with ten layers of substrate and 2×2 grid of k points in the commensurate cells and four layers with Γ-point only in the $(4\sqrt{3} \times 4\sqrt{3})R30°$ *h*-BN-rotated cells. We note that in the smaller 2×2 cell even the sign of the binding energy difference between the two N-on-top and the four other configurations was the opposite, thus requiring such a larger cell to better isolate the atoms with a core hole. In Table C.1 we collect the results for the vertical height of the B and N from the top-most Cu layer (Δz_{B-Cu}, Δz_{N-Cu}, in Å), the corresponding height from the coordinate of bulk-truncated Cu slab extrapolated to the outermost layer (Δz^{ext}_{B-Cu}, Δz^{ext}_{N-Cu}, in Å), the relative total energy from the minimum $B_f N_o$ configuration (ΔE, in meV), and the work function (Φ, in eV). Additional calculations are published in Ref. [Sch17b].

		B_fN_o	B_hN_o	B_oN_h	B_fN_h	B_oN_f	B_hN_f	
vdW-DF2-rB86	Δz_{B-Cu}	3.12	3.13	3.36	3.37	3.34	3.36	Present work
	Δz_{N-Cu}	3.13	3.14	3.36	3.38	3.35	3.37	
	Δz^{ext}_{B-Cu}	3.03	3.04	3.27	3.29	3.26	3.28	
	Δz^{ext}_{N-Cu}	3.06	3.05	3.28	3.29	3.26	3.28	
	ΔE	Ref	1	22	22	21	22	
	Φ	4.11	4.12	4.45	4.43	4.45	4.42	$\Phi_{Cu(111)} = 5.09$
vdW-DF-optB86	Δz_{B-Cu}	3.04	3.06	3.31	3.32	3.29	3.32	Present work
	Δz_{N-Cu}	3.06	3.07	3.32	3.33	3.30	3.32	
	Δz^{ext}_{B-Cu}	2.94	2.96	3.21	3.22	3.19	3.22	
	Δz^{ext}_{N-Cu}	2.95	2.97	3.22	3.23	3.20	3.22	
	ΔE	Ref	1	25	26	24	25	
	Φ	3.96	3.99	4.34	4.33	4.35	4.33	$\Phi_{Cu(111)} = 5.05$
vdW-DF-rB86	Δz_{B-Cu}	3.03	3.04	3.27	3.28	3.26	3.28	Present work
	Δz_{N-Cu}	3.04	3.05	3.28	3.29	3.27	3.29	
	Δz^{ext}_{B-Cu}	2.95	2.96	3.19	3.20	3.18	3.20	
	Δz^{ext}_{N-Cu}	2.96	2.97	3.20	3.21	3.19	3.20	
	ΔE	Ref	0	25	26	24	26	
	Φ	3.98	3.97	4.31	4.32	4.31	4.32	$\Phi_{Cu(111)} = 5.03$

Table C.1: *Adsorption properties of h-BN/Cu(111) from DFT calculations in a* (1×1) *cell*

The results show a large variation in the layer heights, relative energies between the registries and the work function. The same observation has recently been made on *h*-BN/Ir(111). The present results with revPBE+D2 approach are close to those in Refs [Gom13, Koi13] with revPBE+D3. Results from vdW-DF2-rB86 and vdW-DF-optB86 are close to each other, and we do trust in those most.

We cannot directly compare the layer distances extracted from the XSW measurements and our commensurate 1×1 systems, as our calculations are in the commensurate cell with the B and N atoms placed at high-symmetry sites. Assuming that the N-on-top configurations yield extremal layer distances in a moiré-like structure the adsorption height from the DFT calculations averaged over regions where N is close to the on-top positions would result in a value smaller than the ≈ 0.2 Å obtained at B_fN_o and B_hN_o. Extended calculations in larger cells would be required to further investigate the issue.

In a separate approach, we compared the mean adsorption height of a 30° rotated *h*-BN sheet on Cu(111) modeled by a $(4\sqrt{3} \times 4\sqrt{3})R30°$ super-structure with the non-rotated one (1×1) following the vdW-DF2-rB86 scheme. The heights are listed below:
Rotated structure with one B on-top: 3.32 Å Non-rotated B_oN_f: 3.36 Å
Rotated structure with one N on-top: 3.31 Å Non-rotated B_fN_o: 3.15 Å

The rotated structure features a very small corrugation as compared to the non-rotated one, most likely due to adjacent N on-top positions in the latter, leading to regions, or "pores", where the *h*-BN layer is closer to the substrate. In the rotated structure this is not the case, and the whole layer is located at the large distance from the surface.

The calculated XPS $E_{N\,1s}$ core-level binding energies in the commensurate cells are larger by about 0.3 eV in the $B_f N_o$ registry than when the N atoms are located on hollow sites. In the rotated $(4\sqrt{3} \times 4\sqrt{3})R30°$ cell the difference in $E_{N\,1s}$ between the two configurations are very small, reflecting the very similar vertical corrugation. This also implies that the $E_{N\,1s}$ is different in the $B_f N_o$ configuration not because of the on-top position of the N atom, but because of the difference in the layer height.

C.1 Moiré Calculations of *h*-BN Domains on Cu(111)

The right *h*-BN island in Figure C.1a clearly shows a moiré pattern with a periodicity of 6.9 nm. In the left *h*-BN island the moiré pattern is not discernible at the given scan parameters: $U_b = 2.0\,\mathrm{V}, I_t = 80\,\mathrm{pA}$. Figure C.1b displays an STM image with atomically resolved *h*-BN lattice and the moiré super structure of a zoom into the left island evidences the existence of a moiré with only 1.03 nm periodicity. The *h*-BN lattice is rotated around 12° with respect to the substrate lattice. Inequivalent contrast of the moiré beatings might indicate, that multiple beatings are present within the moiré unit cell. Figure C.1d,e display calculations of the moiré lattice constant a_m *versus* angle between *h*-BN and Cu(111) lattice according to the procedure devised by Artaud *et al.* [Art16] ($a_{Cu} = 2.556$ Å[Str69] and $a_{BN} = 2.504\,68$ Å[Pas02] used for calculations) assuming commensurability between the two lattices. Each point corresponds to a commensurate super lattice with lattice constant a_m and rotation Φ between substrate and *h*-BN lattice. The color indicates the strain level of the *h*-BN layer. If one considers multiple beatings per moiré unit cell, moiré super structures with angles between 0° and 30° can be explained.

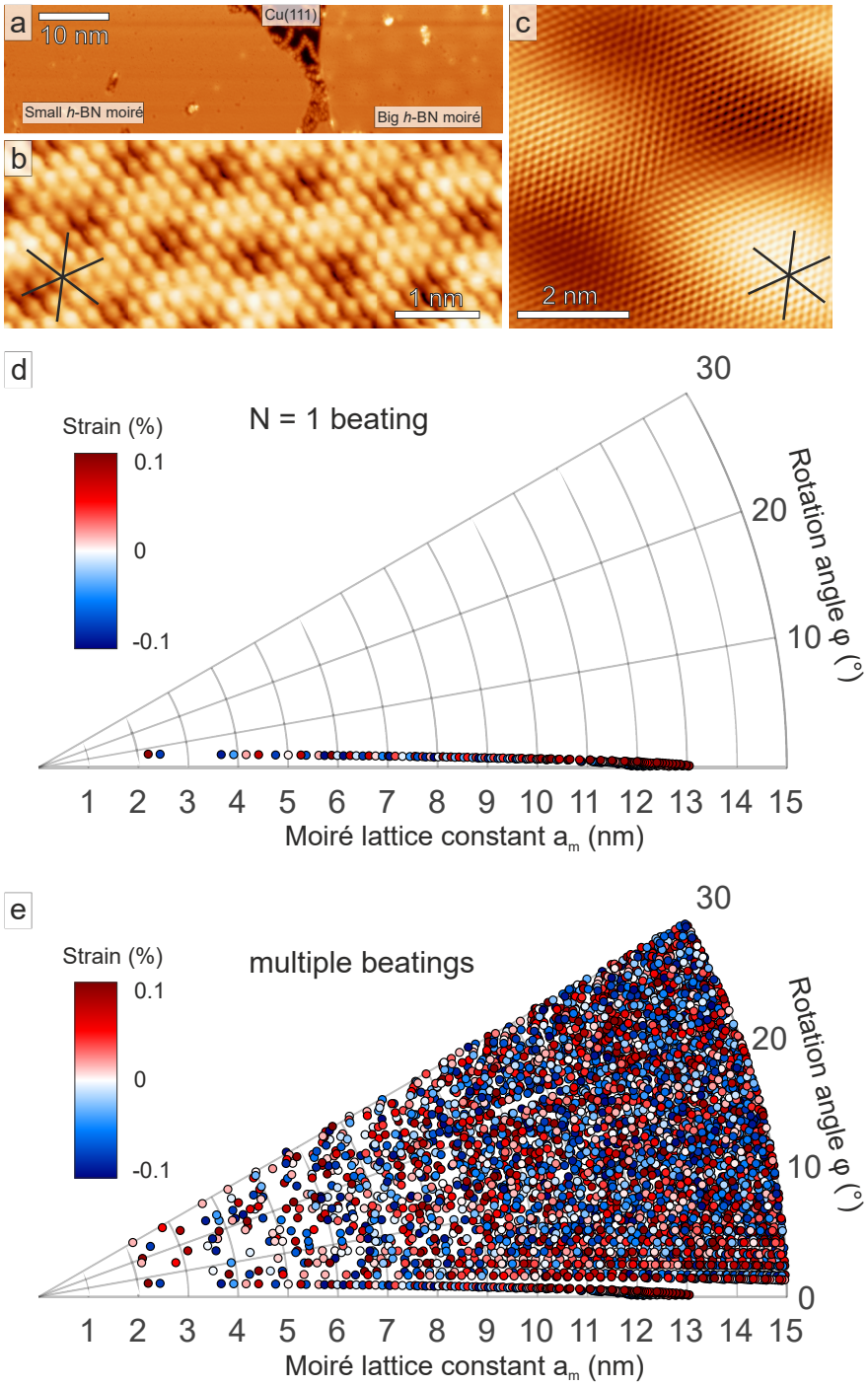

Figure C.1: ***(a)*** *STM topography image showing two different h-BN islands on Cu(111). STM image of the h-BN lattice of* ***(b)*** *the left island ($U_b = 0.28\,\mathrm{V}, I_t = 2.8\,\mathrm{nA}$), and* ***(c)*** *the right island in (a). $U_b = 0.28\,\mathrm{V}, I_t = 1.7\,\mathrm{nA}$.* ***(d,e)*** *Moiré calculations based on the works of Artaud et al. [Art16] predict possible moiré periodicities for considering* ***(d)*** *only one, or* ***(e)*** *multiple beatings per unit cell.*

C.2 Local Work Function Differences of *h*-BN/Cu(111)

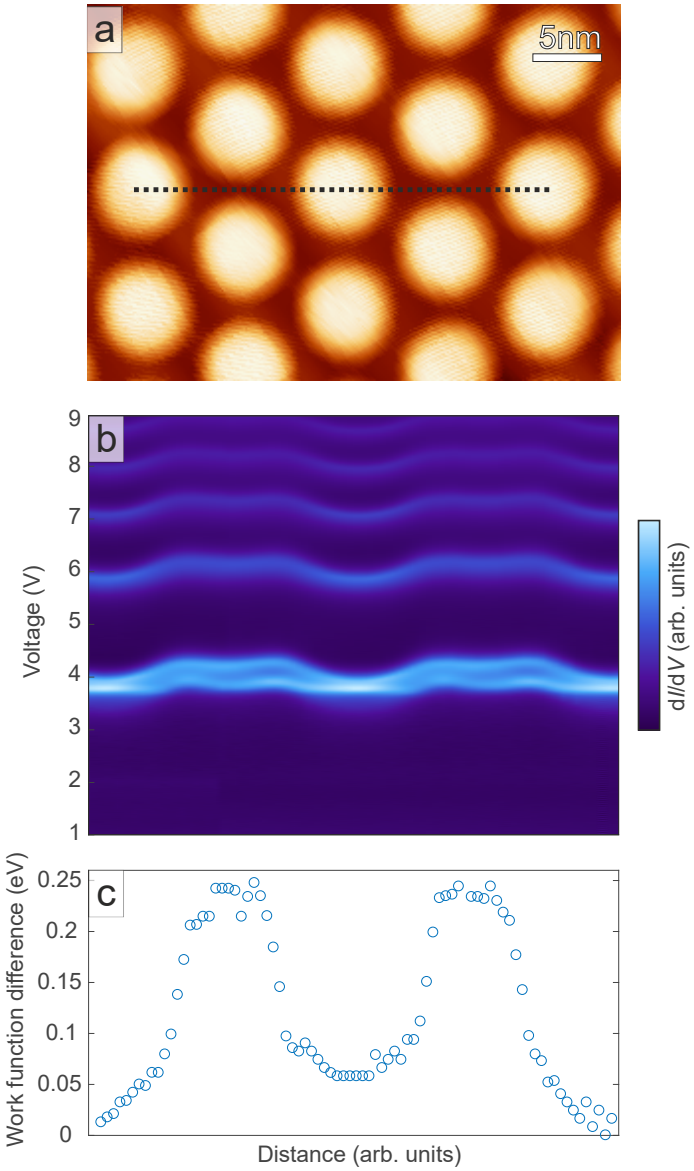

Figure C.2: *Work function variation along h-BN/Cu*(111) *moiré.* ***(a)*** *STM image showing the h-BN moiré with a periodicity of* 8.4 nm. *Scan parameter:* $U_b = 4.0\,\mathrm{V}$, $I_t = 40\,\mathrm{pA}$. ***(b)*** *Field emission resonances acquired along the black dotted line in a) revealing a variation of the peak positions.* ***(c)*** *Work function differences between bright ("hill"/pore) and dark ("valley"/wire) regions obtained from the dI/dV curves of the field emission resonances displayed in b).*

C.3 Atomic Contrast Series for Different Tip Heights

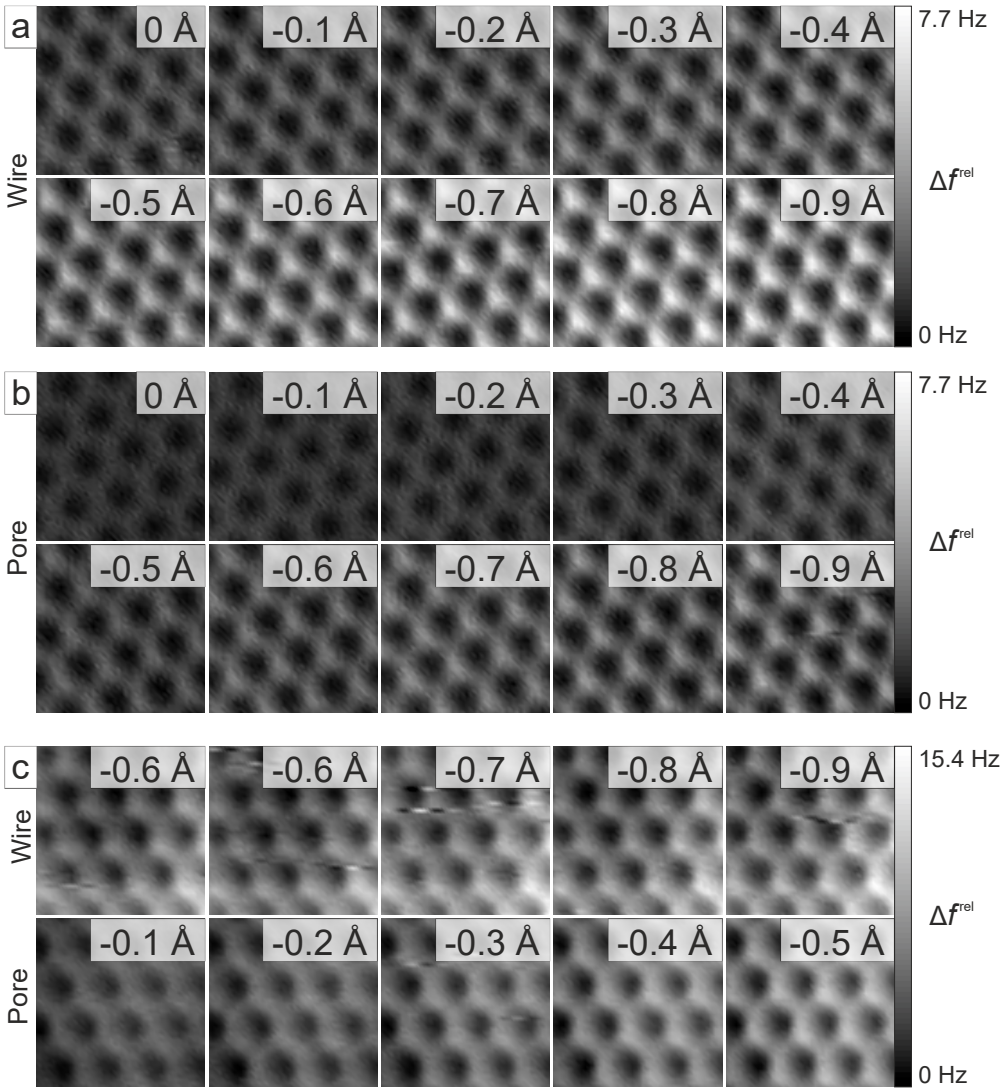

Figure C.3: *Constant-height AFM series showing the increase of atomic contrast of the h-BN lattice with reduced tip-sample distances. The z-dependence of the atomic contrast in the images shows a similar behavior for both,* ***(a)*** *wire and* ***(b)*** *pore regions of the h-BN/Cu(*111*) moiré. All images are* $1\,\mathrm{nm} \times 1\,\mathrm{nm}$ *and are offset to have the same color scales as indicated for each series. The images (Size:* $1\,\mathrm{nm} \times 1\,\mathrm{nm}$*) in* ***(c)*** *compare directly the wire (upper panel) and pore (lower panel, offset by* $0.4\,\text{Å}$*) regions to highlight the different tip heights required for similar atomic contrast. The images were acquired in the region shown in Figure 4.2 in the section 4.1.3.1. For better comparability across images we use relative* Δf^{rel} *scales, where the lowest* Δf^{rel} *value in each image amounts to* $0\,\mathrm{Hz}$*.*

C.4 Dissipation

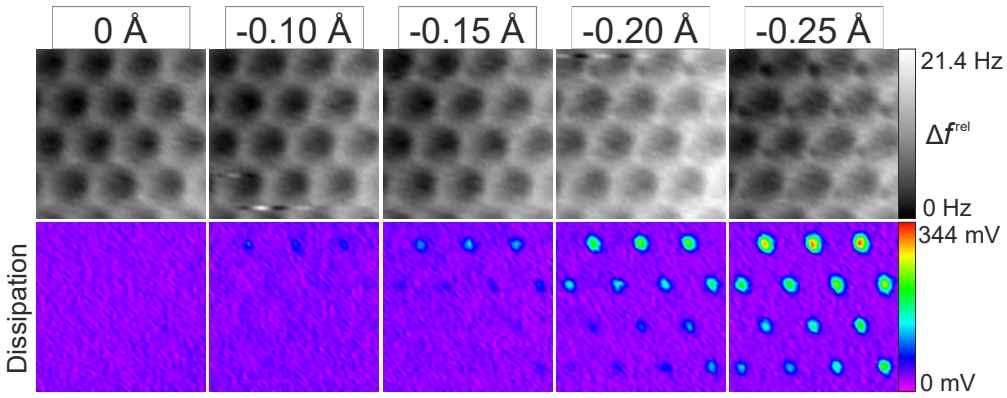

Figure C.4: *Constant-height AFM series for very close tip-sample distances shows pronounced features in the atomic h-BN lattice accompanied by enhanced dissipation. Dissipation reflects the energy lost by direct tip-substrate interactions.*

C.5 Simulation of XSW Absorption Profiles

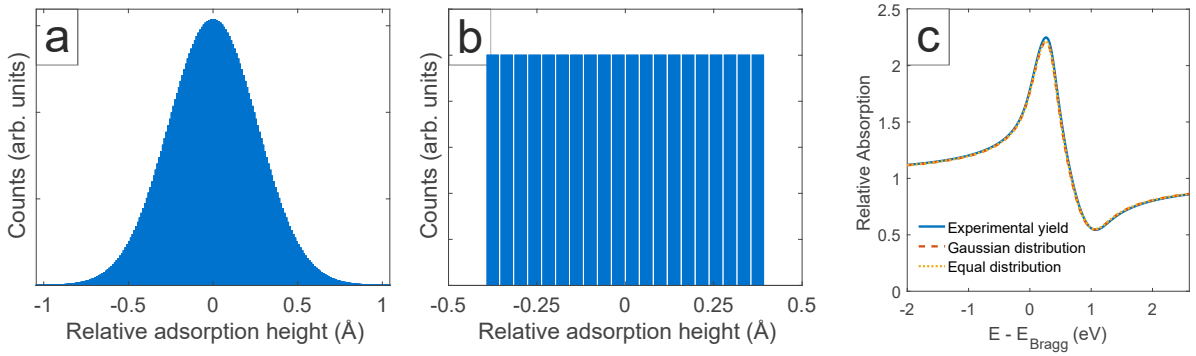

Figure C.5: *Calculated XSW absorption profiles for theoretical height distributions. The height distribution in* ***(a)*** *is given by a Gaussian distribution with a* σ *spread of* 0.45 Å *and in* ***(b)*** *by an uniform height distribution with width* $w = 0.75$ Å*.* ***(c)*** *The obtained XSW profiles both exhibit a coherent fraction of* 0.71 *similar to the one experimentally observed.*

To simulate the effects of the height distributions displayed in Figure C.5, the coherent fraction and position were expressed as a Fourier component projected along the (111) direction for the Fourier series that describes the distribution of adsorption sites. The component can itself then be expressed as an integral along the (111) direction (z) over a period defined by the (111) layer spacing (d_{111}):

$$f^{111} \exp\left(-2\pi i p^{111}\right) = \int_0^{d_{111}} f(z) \exp\left(2\pi i z / d_{111}\right) \delta z, \tag{C.2}$$

where $f(z)$ is in turn, as by Eq. (4.1) in the main text:

$$f(z) = C \cdot a_z \cdot D_{111}, \tag{C.3}$$

where a_z is the probability of finding an atom at position z (as defined by the functions shown in Figure C.5). Thus, assuming the ordered fraction is unity, the resulting geometric factor becomes:

$$a_{111} = \frac{f^{111}}{D_{111}}. \tag{C.4}$$

C.6 Moiré Superstructures at Room Temperature

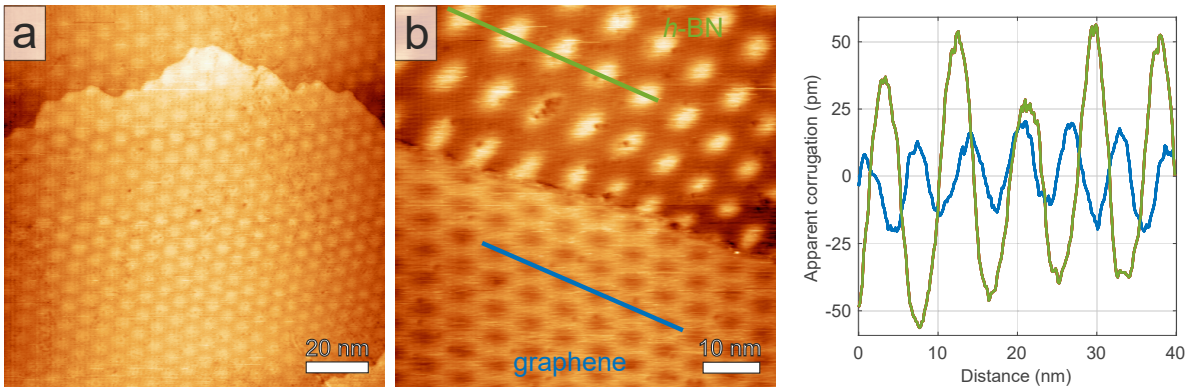

Figure C.6: *STM images of the moiré superstructure of* ***(a)*** *h-BN/Cu(111) ($U_b = -0.75\,\mathrm{V}$, $I_t = 74\,\mathrm{pA}$) and* ***(b)*** *an h-BN–graphene interface on Cu(111) ($U_b = -1.16\,\mathrm{V}$, $I_t = 2.3\,\mathrm{nA}$), recorded at room temperature.* ***(c)*** *The apparent corrugation in the STM image displayed in (c) is clearly larger in the case of h-BN (∼90 pm) compared to graphene (∼35 pm). For a smaller bias voltage of $U_b = -0.11\,\mathrm{V}$ and in a different region, apparent corrugations of ∼40 pm (h-BN) and ∼20 pm (graphene) were measured, respectively.*

C.7 Geometric Corrugation Measurements on a Larger Moiré Unit Cell

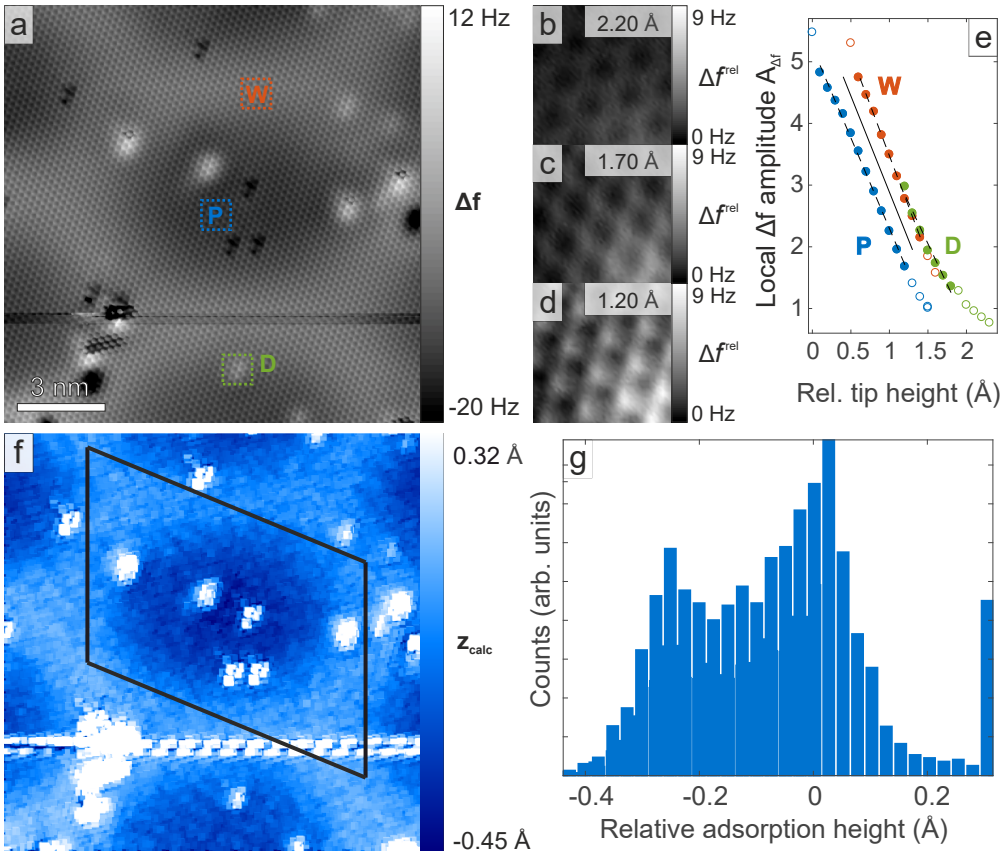

Figure C.7: ***(a)*** *Constant-height AFM image of h-BN/Cu(111) showing the atomic h-BN lattice together with the moiré unit cell. Orange and blue squares indicate spots on the wire and pore region of the moiré pattern. Green square indicates an area with a defect underneath the h-BN layer.* ***(b)-(d)*** *Series of constant height AFM scans showing the atomic contrast of the h-BN lattice acquired on the indicated defect in (a) for decreasing tip heights. All boxes are* $1\,\mathrm{nm} \times 1\,\mathrm{nm}$ *and have the same color scale.* ***(e)*** *Mean local* Δf *amplitude* $A_{\Delta f}$ *(solid line) of the atomic h-BN contrast for such boxes recorded at various tip heights in the indicated wire and pore region and for the defect. Dashed lines represent linear fits of filled data points.* ***(f)*** *Calculated* z_{calc} (Δf) *map of the constant height AFM scan in (a). The moiré unit cell is indicated with black lines.* ***(g)*** *Extracted height distribution histogram of indicated moiré unit cell (black parallelogram) in the* z_{calc} (Δf) *map in* ***(f)****. Values exceeding* $\pm 2\sigma$ *were replaced by* $\pm 2\sigma$*. AFM data analysis was done in Python using NumPy,[van11] SciPy,[Jon1] Matplotlib[Hun07] and scikit-image.[van14]*

C.8 Silver Deposition on Cu(111)

Silver was deposited by e-beam evaporation while the Cu sample was kept at 573 K. After depositing silver on Cu(111) we observed the well-known reconstruction resulting from the lattice parameter difference between Ag and Cu ($a_{Ag} = 2.89$ Å, and $a_{Ag} = 2.56$ Å), see Figure C.8a. The 9×9 superstructure has a periodicity of 2.4 nm.

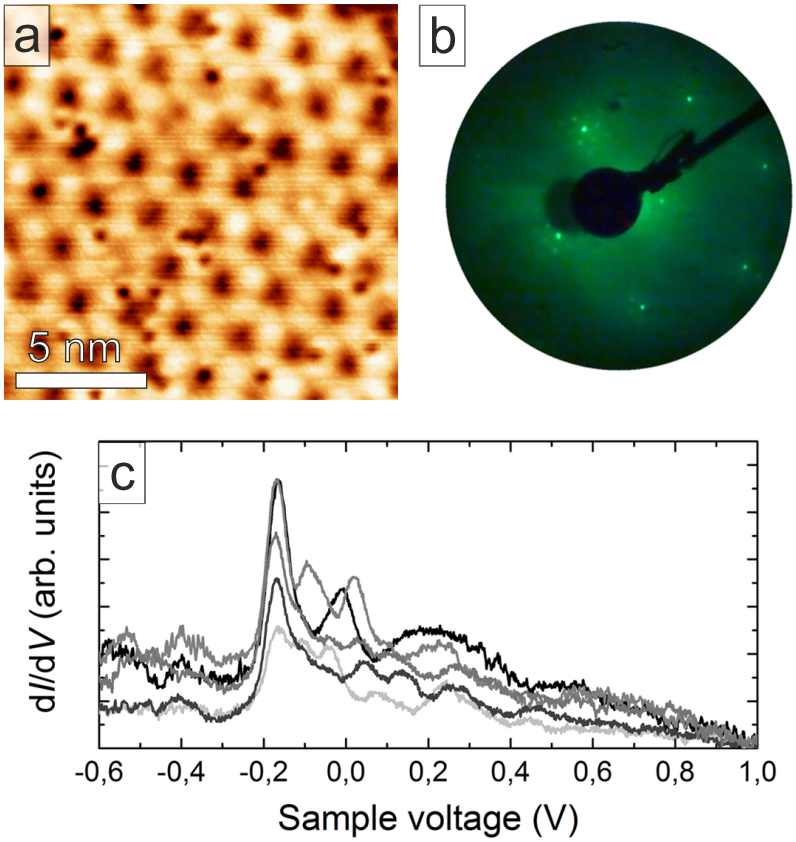

Figure C.8: *Silver overlayer on a Cu(111) crystal.* ***(a)*** $15 \times 15\,\mathrm{nm}^2$ *STM image of 2 ML of Ag on Cu(111) ($U_b = 2$ V, $I_t = 0.1$ nA).* ***(b)*** *Corresponding LEED pattern at 70 eV. The pattern presents an offset from (0,0) due to technical issues.* ***(c)*** *dI/dV spectra measured on different areas of the 9×9 superstructure.*

The LEED pattern in Figure C.8b shows the six main spots of the Cu(111) substrate surrounded by Ag satellite spots. The Ag/Cu(111) surface has also been studied by means of scanning tunneling spectroscopy. Figure C.8c shows individual $\mathrm{d}I/\mathrm{d}V$ curves measured on different areas of the Ag/Cu(111) superstructure. All spectra show an increase in the local density of states around −235 eV that correspond to the surface state onset of Ag/Cu(111). Previous studies have shown, that the surface state binding energy depends on the Ag thickness.[Wes04] Comparing our $\mathrm{d}I/\mathrm{d}V$ spectra with this previous work, we conclude that the Cu(111) crystal is covered by about 3 ML of Ag.

C.9 Evolution of the Surface State of *h*-BN on Ag(111) and Ag/Cu(111)

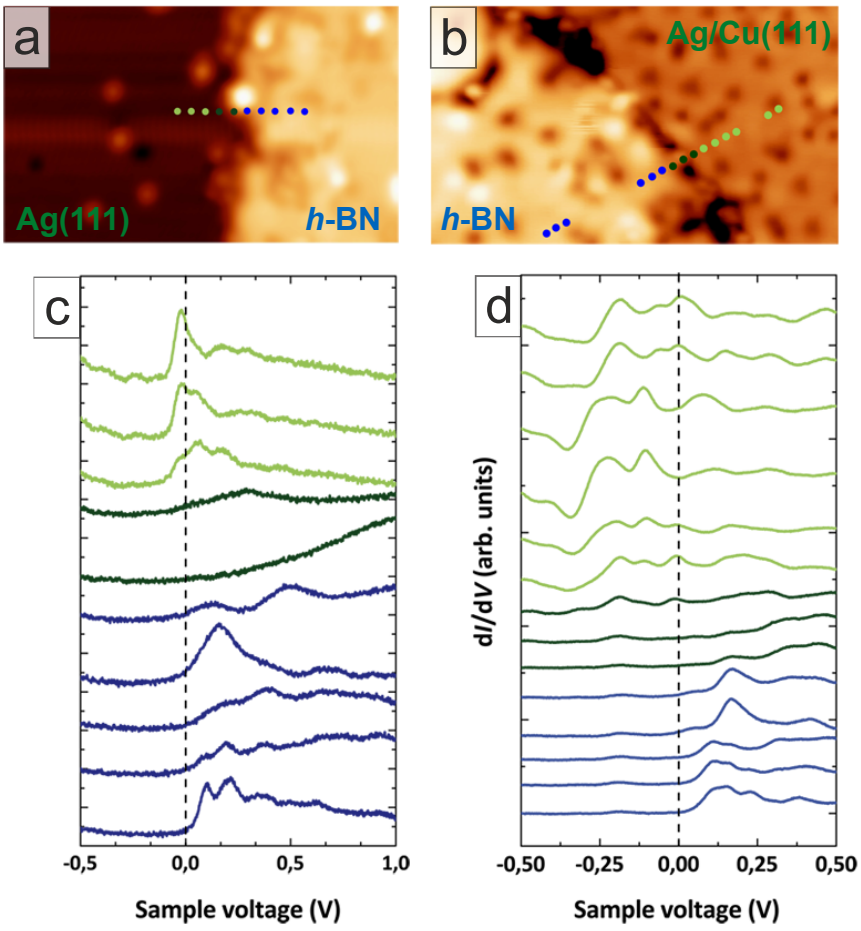

Figure C.9: *Evolution of the surface state. STM images of* ***(a)*** *h-BN/Ag(*111*) and* ***(b)*** *h-BN/Ag/Cu(*111*). (**c**) and (**d**) display the corresponding dI/dV spectra around the Fermi energy measured along a line going from the metallic surface to the 2D layer.*

Appendix D

Experimental Details for Chapter 5

D.0 Geometric Factor in XSW

The coherent fraction f^{111} can be expressed as a product of the ordered fraction (C), a geometric factor (a_{111}) and the Debye-Waller factor (D_{111}) such that:

$$f^{111} = C \cdot a_{111} \cdot D_{111}, \tag{D.1}$$

which model, respectively, the level of order, the static geometric distribution, and the dynamic geometric distribution of the atomic species under investigation.[Woo05] Taken that the molecular coverage was low (∼20 %) during our experiments and the STM images suggest well-ordered Co–P molecules, the ordered fraction C is assumed to be ∼0.9, the coherent fraction of the Co $2p_{3/2}$ core level. The Debye-Waller factor DWF ≤ 1 takes into account thermal vibrations. In the harmonic approximation, it is defined as

$$D_{111} = \exp\left[-\left(q^2 \left\langle u^2 \right\rangle\right)/3\right] \tag{D.2}$$

where q is the scattering vector:

$$q = 2\pi/d_{111}. \tag{D.3}$$

Here, $\langle u^2 \rangle$ is the mean-square vibrational amplitude of the considered atom and d_{111} denotes the spacing of the used diffraction planes.[Zeg09]

D.1 XSW Triangulation Measurement

XSW allows to determine the lateral atomic registry via real-space triangulation.[Woo05] In case of an fcc (111) surface, a set of two experiments at both the (111) and the $(1\bar{1}1)$ Bragg reflections are needed in order to distinguish the high-symmetry adsorption sites of

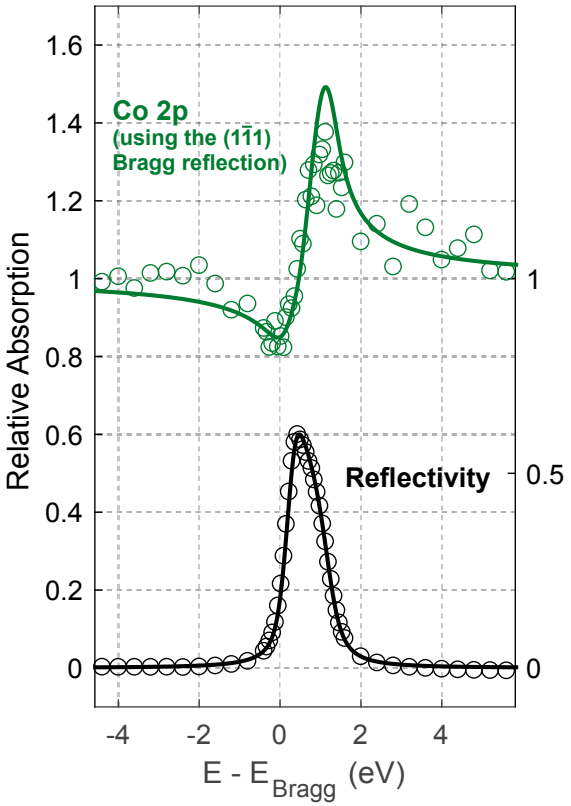

Figure D.1: *Normal-incidence XSW absorption profile for Co $2p_{3/2}$ of a sub-monolayer of Co–P on Cu(111) using the (1$\bar{1}$1) Bragg reflection. A Debye-Waller factor of* 0.95 *is included in the XSW fit to account for the thermal vibrations of the substrate at room temperature. The solid green line denotes the fit to the data. Black data points represent the reflectivity curve.*

the surface. The obtained layer spacings p^{111} and $p^{1\bar{1}1}$ can then be used to determine the lateral atomic position. In case the adsorber atom occupies the bridge site, the relationship between the two layer spacings is given by:[Woo05]

$$p^{1\bar{1}1} = (p^{111})/3 + 1/2 \tag{D.4}$$

taking into account the three distinct bridge sites. The same layer spacing relationship is obtained for an adsorber atom equally populating fcc and hcp hollow sites.[Woo05]

D.2 Co–P Molecules Imaged with Different Tips

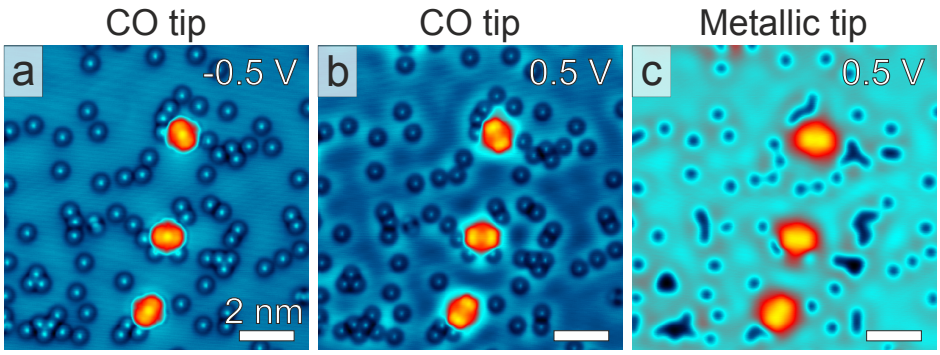

Figure D.2: *STM images of Co–P molecules with three different orientations on Cu(111) imaged with* ***(a)*** *a CO terminated tip at negative bias,* ***(b)*** *a CO terminated tip with positive bias, and* ***(c)*** *a metallic tip at positive bias. Set point of all images:* $I_t = 800\,\mathrm{pA}$.

D.3 XSW Absorption Profiles of Co–P on *h*-BN/Cu(111) – Low Coverage, 50 K

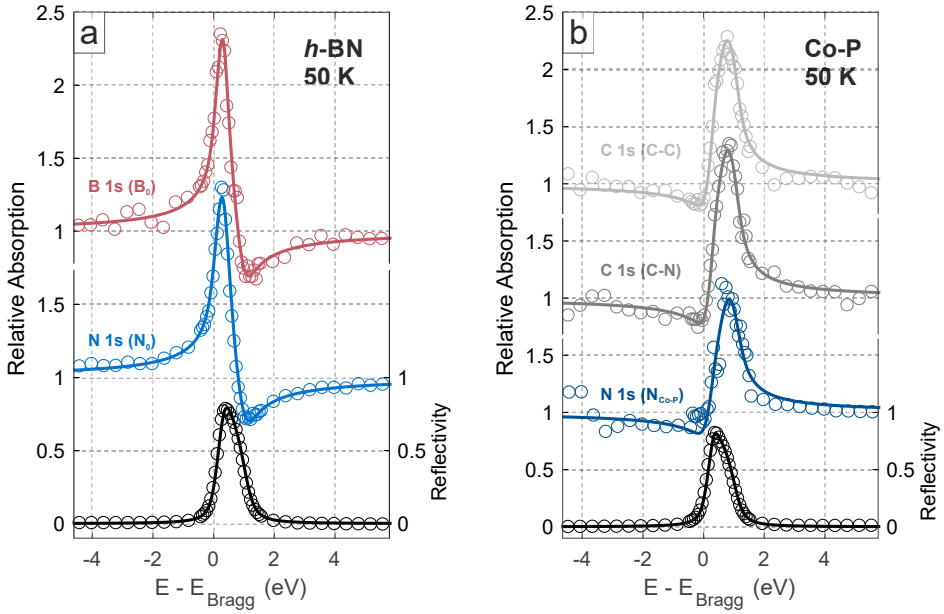

Figure D.3: *XSW absorption profiles of the atomic species in* ***(a)*** *the h-BN layer, and* ***(b)*** *the Co–P molecules on h-BN/Cu(111) at the (111) Bragg reflection at* 50 K *and in the low coverage regime (*∼0.15 ML*). Solid lines are fits to the data. Black data points represent the reflectivity.*

D.4 XPS Data of the Co 2*p* Core Level for High Coverage on *h*-BN/Cu(111)

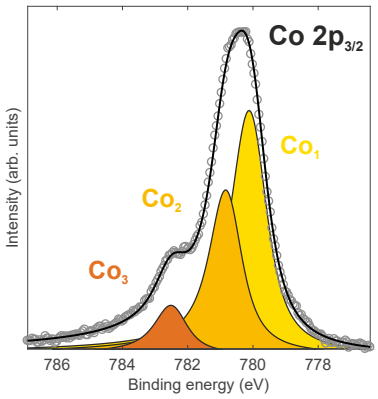

Figure D.4: *XP spectrum of the Co* $2p_{3/2}$ *core level for a high Co–P coverage on h-BN/Cu*(111) *(*$\sim$0.95 ML*) acquired at* 300 K*. The ratio of* Co_1 *to* Co_2 *is* $\sim 1.55 : 1$*.*

D.5 XSW Absorption Profiles of Co–P on *h*-BN/Cu(111) – Low Coverage, 300 K

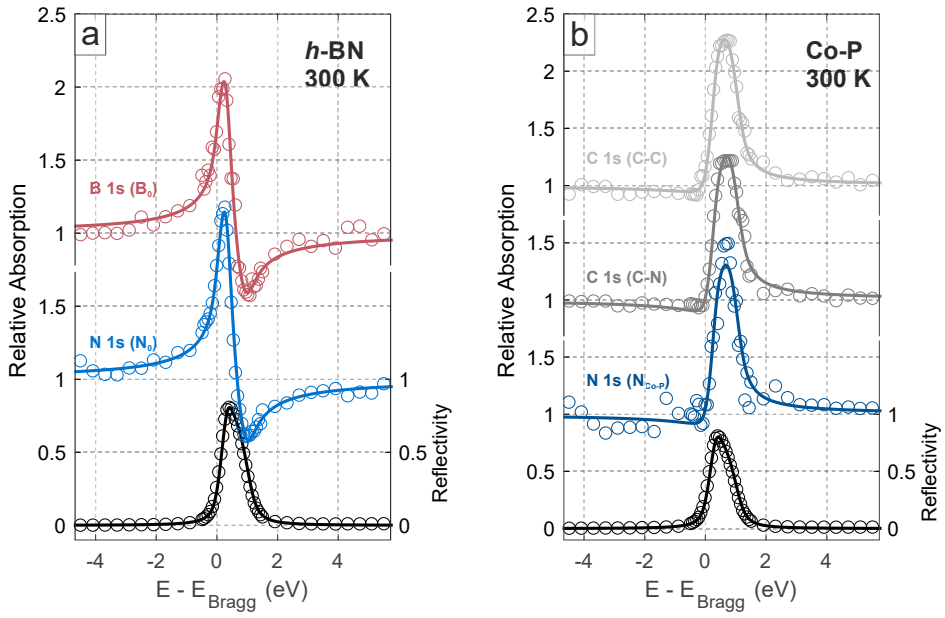

Figure D.5: *XSW absorption profiles of the atomic species in* ***(a)*** *the h-BN layer, and* ***(b)*** *the Co–P molecules on h-BN/Cu*(111) *at the* (111) *Bragg reflection at* 300 K *and in the low coverage regime (*$\sim$0.15 ML*). Solid lines are fits to the data. Black data points represent the reflectivity curve.*

D.6 XSW Absorption Profiles of Co–P on *h*-BN/Cu(111) – High Coverage, 300 K

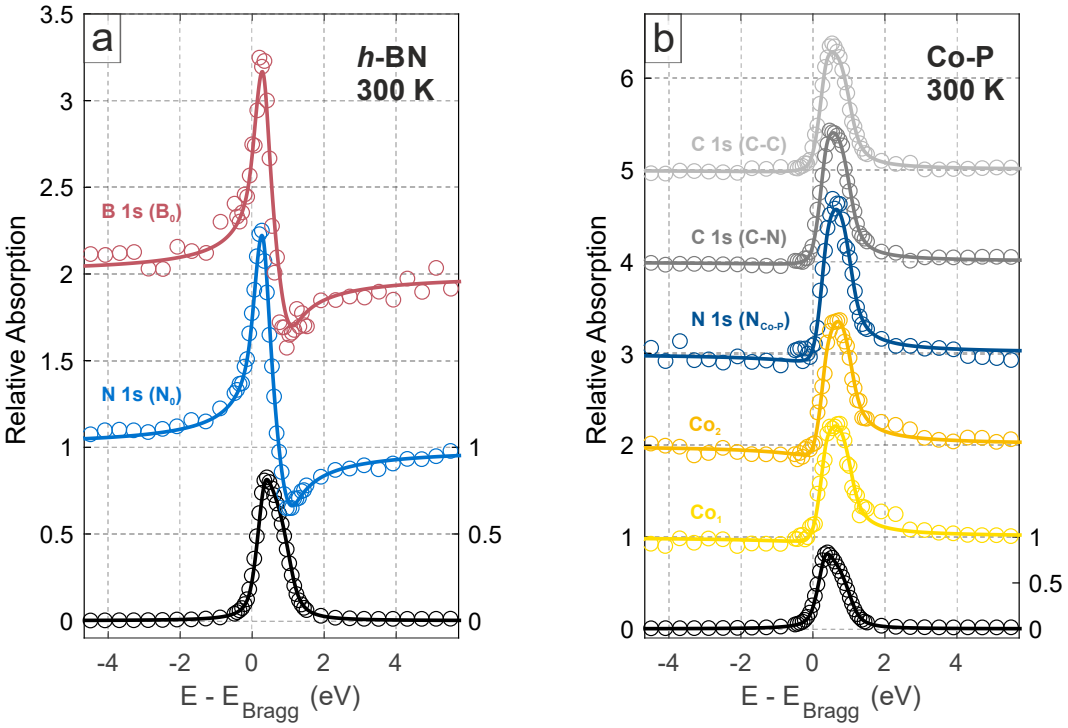

Figure D.6: *XSW absorption profiles of the atomic species in* ***(a)*** *the h-BN layer, and* ***(b)*** *the Co–P molecules on h-BN/Cu*(111) *at the* (111) *Bragg reflection at* 300 K *and in the high coverage regime (*∼0.95 ML*). Solid lines are fits to the data. Black data points are the reflectivity curve.*

		High coverage, 200 K			**High coverage,** 300 K		
	Core level	f^{111}	p^{111}	Adsorption height $\overline{h}_0$ (Å)	f^{111}	p^{111}	Adsorption height $\overline{h}_0$ (Å)
Co–P	C 1*s* (C–C)	0.30 ± 0.02	0.16 ± 0.02	6.59 ± 0.04	0.24 ± 0.02	0.18 ± 0.02	6.64 ± 0.04
	C 1*s* (C–N)	0.32 ± 0.03	0.16 ± 0.02	6.59 ± 0.04	0.31 ± 0.02	0.19 ± 0.02	6.66 ± 0.04
	N 1*s* (N_{CoP})	0.37 ± 0.06	0.13 ± 0.04	6.53 ± 0.08	0.47 ± 0.05	0.16 ± 0.03	6.60 ± 0.06
	Co 2*p* (Co_1)	0.33 ± 0.06	0.09 ± 0.04	6.45 ± 0.08	0.27 ± 0.04	0.12 ± 0.03	6.51 ± 0.06
	Co 2*p* (Co_2)	0.40 ± 0.08	0.07 ± 0.05	6.41 ± 0.10	0.40 ± 0.03	0.11 ± 0.02	6.49 ± 0.04
	Co 2*p* (Co_3)	0.34 ± 0.14	0.02 ± 0.13	6.30 ± 0.26	0.39 ± 0.10	0.03 ± 0.06	6.32 ± 0.12
h-BN	B 1*s* (B_0)	0.53 ± 0.04	0.60 ± 0.02	3.34 ± 0.04	0.58 ± 0.06	0.61 ± 0.03	3.36 ± 0.06
	N 1*s* (N_0)	0.62 ± 0.02	0.60 ± 0.01	3.34 ± 0.02	0.61 ± 0.02	0.60 ± 0.01	3.34 ± 0.03

Table D.1: *Comparison of the structural parameters of the XSW analysis of Co–P/h-BN/Cu*(111) *at* 200 K *and at* 300 K*. The table summarizes the coherent fraction* f^{111}*, the coherent position* p^{111} *and the mean adsorption height* $\overline{h}$ *for all atomic species in the Co–P molecule and the h-BN layer.*

D.7 Voltage-Dependent Contrast of the TPCN Network

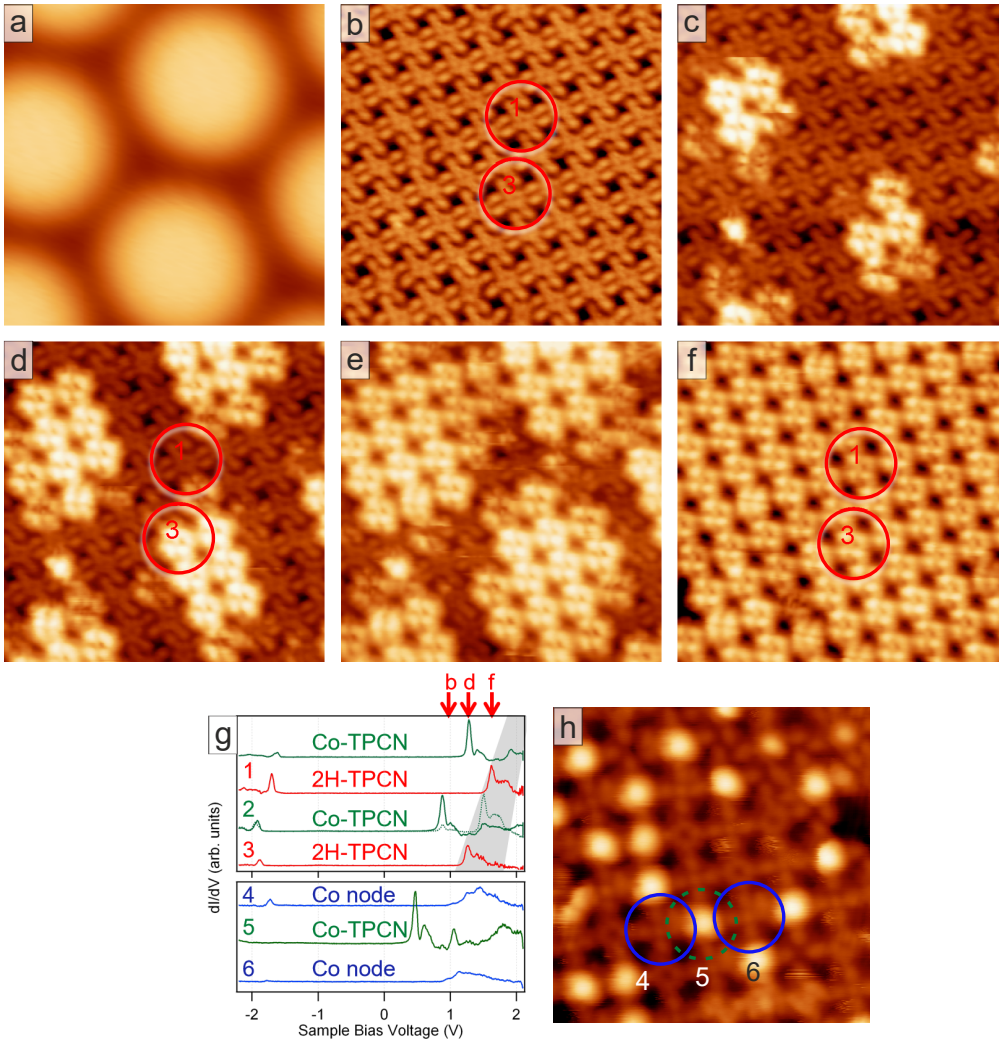

Figure D.7: *Voltage dependent contrast due to the electronic superstructure of h-BN/Cu(111) and STS signature of coordination nodes in comparison to Co–TPCN and 2H–TPCN.* ***(a)*** *Lateral electronic superstructure of the bare h-BN/Cu(111) template ($U_b = 4\,\mathrm{V}$).* ***(b-f)*** *Continuous variation of the appearance of the TPCN layer with increasing bias voltage ($U_b = 1 - 1.5\,\mathrm{V}$), reflecting the onset of the LUMO energy, which varies with position on the h-BN/Cu(111) superstructure. (a-f: Image size $16\,\mathrm{nm} \times 16\,\mathrm{nm}$).* ***(g)*** *STS data of 2H–TPCN molecules (red, 1, 3) evidencing the shift of the LUMO energy (compare Figure 5.12). Exemplary positions of molecules 1 and 3 are highlighted in (b), (d) and (f). At the bias voltage corresponding to image (d), tunneling proceeds via the LUMO only for the molecules on the moiron (3), i.e. they show a four-lobe contrast. At the bias voltage corresponding to image (f), tunneling proceeds via the LUMO for all molecules. The bottom panel compares the STS signature of coordination nodes (blue, 4, 6) with Co centers in Co–TPCN (green, 5), evidencing an upshift of the lowest unoccupied resonance in the former.* ***(h)*** *STM image of the mixed-valence coordination network, where the positions of nodes 4 and 6 are marked.*

Appendix E

Experimental Details for Chapter 6

E.1 STM Simulations of Individual BNPPy Molecules

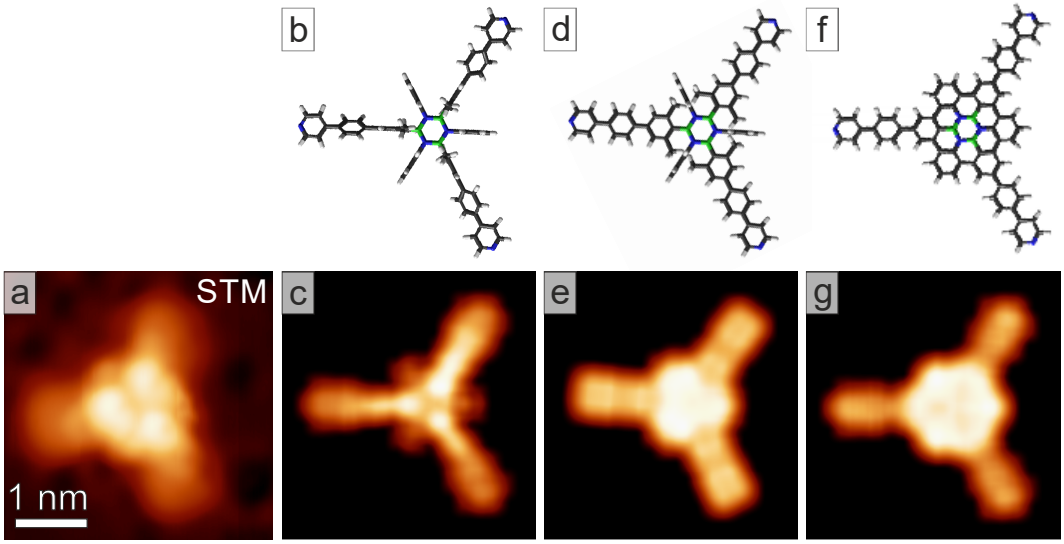

Figure E.1: *Comparison between the experimental and simulated STM images of an individual BNPPy molecule for different molecular conformations.* ***(a)*** *Experimental STM image of a BNPPy molecule on Cu(111). Scan parameters:* $U_b = 1.9\,\mathrm{V}$, $I_t = 170\,\mathrm{pA}$. ***(b)*** *Wireframe model of BNPPy where the phenyl rings attached to the borazine core are standing upright and the terminal pyridine rings in the legs are lying flat.* ***(c)*** *The corresponding STM simulation of the occupied states is in good agreement with the experimental STM image.* ***(d)*** *Wireframe model of BNPPy where the phenyl rings are upright while the three legs are completely planar.* ***(e)*** *The STM simulated image of the occupied states reveals that in this adsorption geometry, the contrast is dominated by the upstanding phenyl rings and does not match the experiment.* ***(f)*** *Wireframe model of the cyclodehydrogenated, planar BNPPy molecule.* ***(g)*** *The appearance in the corresponding simulated STM image of the occupied states is dominated by a hexagonal shaped bright core unit. STM images were simulated under the Tersoff-Hamann approximation. The occupied states are described best by the HOMO, HOMO-1 and HOMO-2 orbitals. A Gaussian filter was applied to smooth the simulated images.*

E.2 Molecular Phases on the Ag Substrate

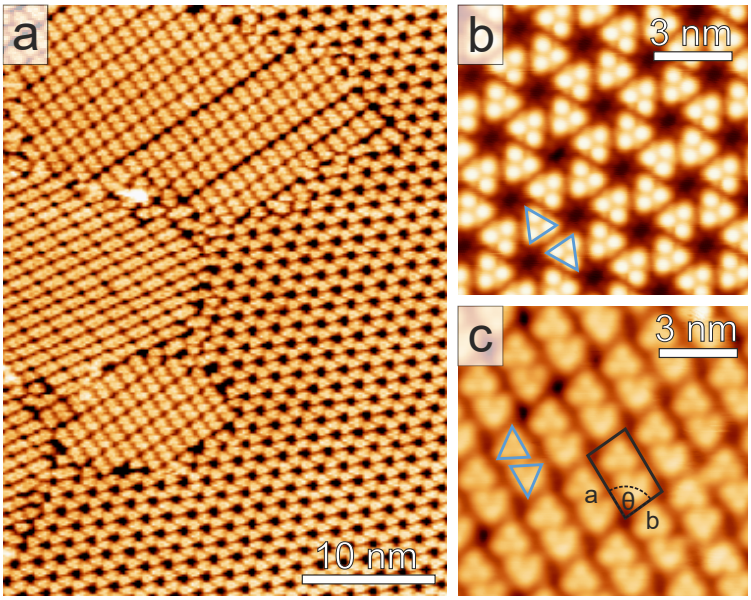

Figure E.2: *Self-assembled molecular phases of BNPPy on the Ag surface.* ***(a)*** *The large-scale STM image reveals that within the well-ordered hexagonal network, several domains of a different phase occur. Scan parameters:* $U_b = 1.0\,\mathrm{V}$, $I_t = 910\,\mathrm{pA}$. ***(b)*** *In the most abundant phase the molecules arrange in six-membered rings with hexagonal symmetry. Scan parameters:* $U_b = 0.2\,\mathrm{V}$, $I_t = 40\,\mathrm{pA}$. ***(c)*** *In the second phase, the BNPPy assemble in rows consisting of two molecules rotated by* $60°$ *relative to each other. Scan parameters:* $U_b = 1.4\,\mathrm{V}$, $I_t = 100\,\mathrm{pA}$.

E.3 Large-Scale STM Images on Cu(111)

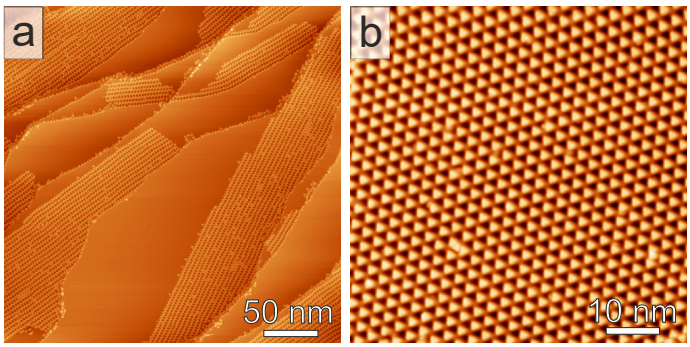

Figure E.3: ***(a)*** *Large-scale STM image of BNPPy on Cu(*111*). For sub-monolayer coverages, the growth initiates at step edges. Scan parameters:* $U_b = 1.0\,\mathrm{V}$, $I_t = 91\,\mathrm{pA}$. ***(b)*** *Deposition of additional Cu atoms, leads to a structural transformation of the self-assembly. The large-scale molecular network consists of three-fold coordinated BNNPy molecules. Scan parameters:* $U_b = 1.5\,\mathrm{V}$, $I_t = 58\,\mathrm{pA}$.

E.4 High Temperature Post-Annealing

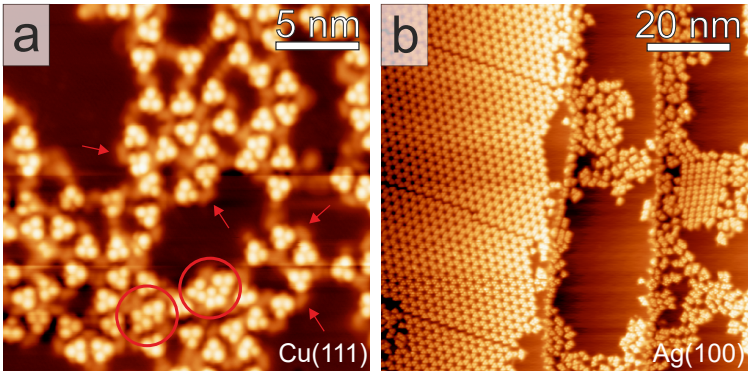

Figure E.4: ***(a)*** *STM image of the BNPPy network on Cu(111) after annealing to 470 K. Only disordered structures are observed on the surface. Presumably, covalent bonds are formed between some molecules (indicated by red arrows), while other molecules might have lost at least parts of their legs (indicated by red circles) leading to very densely packed structures. Scan parameters:* $U_b = 1.0\,\mathrm{V}$, $I_t = 80\,\mathrm{pA}$. ***(b)*** *STM image of the BNPPy network on Ag(100) after annealing to 570 K. The highly ordered hexagonal network is still mostly intact, although some defect lines begin to appear. In addition, regions with disordered structures are observed on the sample. Scan parameters:* $U_b = 1.0\,\mathrm{V}$, $I_t = 100\,\mathrm{pA}$.

E.5 XPS Data of a Multilayer on Cu(111)

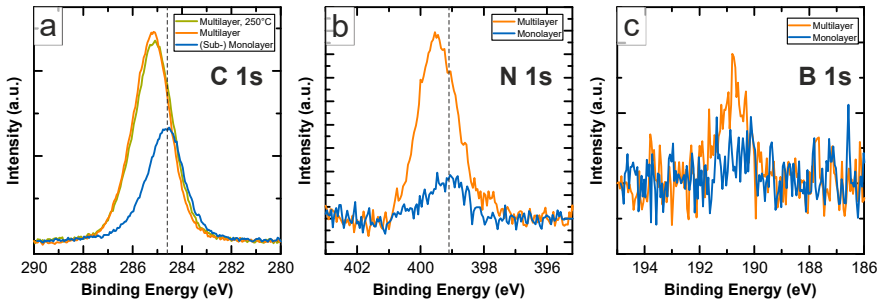

Figure E.5: *Coverage dependent XP spectra of BNPPy on Cu(111).* ***(a)*** *The peak of the C1s core level of a (sub-) monolayer BNPPy coverage (blue line) is observed at* $E_b = 284.8\,\mathrm{eV}$. *Increasing the molecular coverage to ∼5 layers (orange line) leads to an upshift of the core-level binding energy to* $E_b = 285.2\,\mathrm{eV}$, *due to suppressed polarization screening by the metallic substrate in the multilayer. Annealing the multilayer sample to 520 K for 5 min (green line) does not change the C1s core-level spectra. It is inferred that the molecular coverage on the sample does not substantially decrease upon annealing.* ***(b)*** *N1s core-level spectra of a BNPPy monolayer (blue line) and ∼5 layer coverages (orange line). In the case of the monolayer, the peak is observed at* $E_b = 399.2\,\mathrm{eV}$, *while it is upshifted by* $\sim 0.2\,\mathrm{eV}$ *in the case of the BNPPy multilayer sample.* ***(c)*** *Due to the small cross-section, the B1s core level is only resolved for multilayer coverages. The determined binding energy is* $E_b = 190.8\,\mathrm{eV}$.

E.6 Modified Borazine Derivative BNAPy

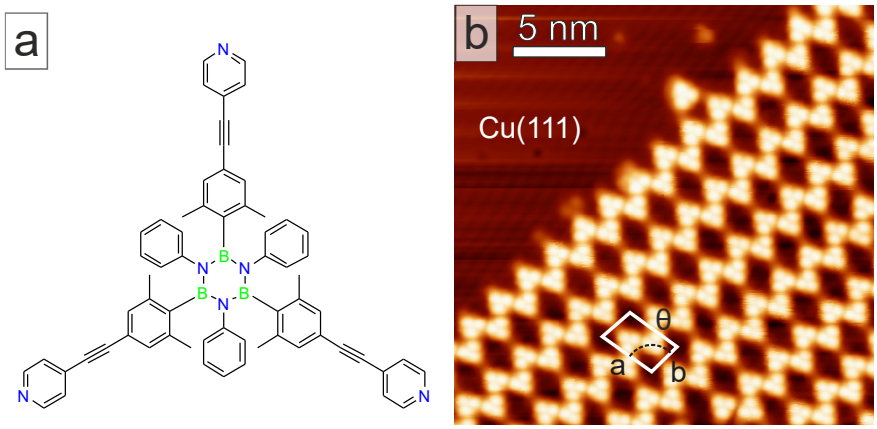

Figure E.6: ***(a)*** *Structural model of N,N',N"-triphenyl-B,B',B"-tri(2,6-dimethyl-4-(4-(pyridyl)phenyl)pnehyl)borazine (BNAPy).* ***(b)*** *The STM image of BNAPy on Cu(*111*) shows the same self-assembly in molecular chains with one coordinated leg. The trapezoidal unit cell of the network has the parameters* $a = 32.6 \pm 2.6\,\text{Å}$, $b = 19.2 \pm 2.4\,\text{Å}$ *and* $\Theta = 75 \pm 4°$. *Scan parameters:* $U_b = 1.0\,\text{V}$, $I_t = 100\,\text{pA}$.

Bibliography

[Abe11] M. Abel, S. Clair, O. Ourdjini, M. Mossoyan, and L. Porte, Single layer of polymeric Fe-phthalocyanine: An organometallic sheet on metal and thin insulating film, *J. Am. Chem. Soc.*, **133**, 1203–1205 (2011). (Cited on page 108.)

[Al-15] Y. S. Al-Hamdani, M. Ma, D. Alfè, O. A. von Lilienfeld, and A. Michaelides, Communication: Water on hexagonal boron nitride from diffusion Monte Carlo, *J. Chem. Phys.*, **142**, 181101 (2015). (Cited on page 99.)

[Al 16] Z. Y. Al Balushi, K. Wang, R. K. Ghosh, R. A. Vilá, S. M. Eichfeld, J. D. Caldwell, X. Qin, Y.-C. Lin, P. A. DeSario, G. Stone, S. Subramanian, D. F. Paul, R. M. Wallace, S. Datta, J. M. Redwing, and J. A. Robinson, Two-dimensional gallium nitride realized via graphene encapsulation, *Nat. Mater.*, **15**, 1166–1171 (2016). (Cited on page 2.)

[Alb94] O. Albrektsen, H. Salemink, K. A. Morch, and A. R. Thölen, Reliable tip preparation for high-resolution scanning tunneling microscopy, *J. Vac. Sci. Technol. B*, **12**, 3187 (1994). (Cited on page 48.)

[Alb16] F. Albrecht, F. Bischoff, W. Auwärter, J. V. Barth, and J. Repp, Direct Identification and Determination of Conformational Response in Adsorbed Individual Nonplanar Molecular Species Using Noncontact Atomic Force Microscopy, *Nano Lett.*, **16**, 7703–7709 (2016). (Cited on pages 87 and 99.)

[Alf07] T. L. Alford, L. C. Feldman, and J. W. Mayer, *Fundamentals of nanoscale film analysis*. Springer, New York, N.Y. and London, (2007). (Cited on pages 16, 17, and 18.)

[Ame16] American Institute of Physics, Studying structure to understand function within 'material families' (2016), `https://www.sciencedaily.com/releases/2016/11/161108123852.htm`, (Accessed: 2017-09-03). (Cited on page 2.)

[And61] P. W. Anderson, Localized Magnetic States in Metals, *Phys. Rev.*, **124**, 41–53 (1961). (Cited on page 115.)

[Ann11] E. Annese, J. Fujii, I. Vobornik, and G. Rossi, Structure and Electron States of Co-Phthalocyanine Interacting With the Cu(111) Surface, *J. Phys. Chem. C*, **115**, 17409–17416 (2011). (Cited on page 98.)

[App10] D. J. Appelhans, Z. Lin, and M. T. Lusk, Two-dimensional carbon semiconductor: Density functional theory calculations, *Phys. Rev. B*, **82**, 73410 (2010). (Cited on page 123.)

[Ari16] K. Ariga, V. Malgras, Q. Ji, M. B. Zakaria, and Y. Yamauchi, Coordination nanoarchitectonics at interfaces between supramolecular and materials chemistry, *Coord. Chem. Rev.*, **320-321**, 139–152 (2016). (Cited on page 129.)

[Arn17] A. Arnau, Centro de Fisica de Materiales, University of the Basque Country (2017), http://cfm.ehu.es/team/andres-arnau-pino/, (Accessed: 2017-08-25). (Cited on page 117.)

[Aro65] A. B. Arons and M. B. Peppard, Einstein's Proposal of the Photon Concept—a Translation of the Annalen der Physik Paper of 1905, *Am. J. Phys.*, **33**, 367–374 (1965). (Cited on page 16.)

[Art16] A. Artaud, L. Magaud, T. Le Quang, V. Guisset, P. David, C. Chapelier, and J. Coraux, Universal Classification of Twisted, Strained and Sheared Graphene Moire Superlattices, *Sci. Rep.*, **6**, 25670 (2016). (Cited on pages 58, 155, and 156.)

[Art17] K. Artyushkova, Art or black magic of curvefitting XPS spectra (2017), http://www.unm.edu/~kartyush/research_xps.xhtml, (Accessed: 2017-05-13). (Cited on page 22.)

[Auw99] W. Auwärter, T. J. Kreutz, T. Greber, and J. Osterwalder, XPD and STM investigation of hexagonal boron nitride on Ni(111), *Surf. Sci.*, **429**, 229–236 (1999). (Cited on pages 56 and 71.)

[Auw02] W. Auwärter, M. Muntwiler, T. Greber, and J. Osterwalder, Co on h-BN/Ni(111): From island to island-chain formation and Co intercalation, *Surf. Sci.*, **511**, 379–386 (2002). (Cited on page 78.)

[Auw07a] W. Auwärter, F. Klappenberger, A. Weber-Bargioni, A. Schiffrin, T. Strunskus, C. Wöll, Y. Pennec, A. Riemann, and J. V. Barth, Conformational Adaptation and Selective Adatom Capturing of Tetrapyridyl-Porphyrin Molecules on a Copper (111) Surface, *J. Am. Chem. Soc.*, **129**, 11279–11285 (2007). (Cited on pages 87, 94, 98, 99, and 122.)

[Auw07b] W. Auwärter, A. Weber-Bargioni, S. Brink, A. Riemann, A. Schiffrin, M. Ruben, and J. V. Barth, Controlled Metalation of Self-Assembled Porphyrin Nanoarrays in Two Dimensions, *ChemPhysChem*, **8**, 250–254 (2007). (Cited on pages 86, 87, and 111.)

[Auw10] W. Auwärter, K. Seufert, F. Klappenberger, J. Reichert, A. Weber-Bargioni, A. Verdini, D. Cvetko, M. Dell'Angela, L. Floreano, A. Cossaro, G. Bavdek, A. Morgante, A. P. Seitsonen, and J. V. Barth, Site-Specific Electronic and Geometric Interface Structure of Co-Tetraphenyl-Porphyrin Layers on Ag(111), *Phys. Rev. B*, **81**, 245403 (2010). (Cited on pages 96, 101, and 109.)

[Auw11] W. Auwärter, K. Seufert, F. Bischoff, D. Écija, S. Vijayaraghavan, S. Joshi, F. Klappenberger, N. Samudrala, and J. V. Barth, A surface-anchored molecular four-level conductance switch based on single proton transfer, *Nat. Nanotechnol.*, **7**, 41–46 (2011). (Cited on page 109.)

[Auw15] W. Auwärter, D. Écija, F. Klappenberger, and J. V. Barth, Porphyrins at Interfaces, *Nat. Chem.*, **7**, 105–120 (2015). (Cited on pages 1, 2, 86, 107, and 114.)

[Avo17] P. Avouris, T. F. Heinz, and T. Low, editors, *2D materials: Properties and devices*. Cambridge University Press, Cambridge United Kingdom and New York NY, (2017). (Cited on page 2.)

[Ayh18] O. Ayhan, N. A. Riensch, C. Glasmacher, and H. Helten, Cyclolinear Oligo- and Poly(iminoborane)s: The Missing Link in Inorganic Main-Group Macromolecular Chemistry, *Chem. - Eur. J.*, **24**, 5883–5894 (2018). (Cited on page 128.)

[Bab17] A. Baby, M. Gruenewald, C. Zwick, F. Otto, R. Forker, G. van Straaten, M. Franke, B. Stadtmüller, C. Kumpf, G. P. Brivio, G. Fratesi, T. Fritz, and E. Zojer, Fully Atomistic Understanding of the Electronic and Optical Properties of a Prototypical Doped Charge-Transfer Interface, *ACS Nano*, **11**, 10495–10508 (2017). (Cited on page 87.)

[Bai00] C. Bai, *Scanning tunneling microscopy and its application*, volume 32 of *Springer series in surface sciences, 0931-5195*. Springer, Berlin and London, 2nd rev. ed. edition, (2000). (Cited on page 12.)

[Bar61] J. Bardeen, Tunnelling from a Many-Particle Point of View, *Phys. Rev. Lett.*, **6**, 57–59 (1961). (Cited on page 9.)

[Bar98] L. Bartels, G. Meyer, K.-H. Rieder, D. Velic, E. Knoesel, A. Hotzel, M. Wolf, and G. Ertl, Dynamics of Electron-Induced Manipulation of Individual CO Molecules on Cu(111), *Phys. Rev. Lett.*, **80**, 2004–2007 (1998). (Cited on page 94.)

[Bar05] J. V. Barth, G. Costantini, and K. Kern, Engineering atomic and molecular nanostructures at surfaces, *Nature*, **437**, 671–679 (2005). (Cited on page 1.)

[Bar07] J. V. Barth, Molecular Architectonic on Metal Surfaces, *Annu. Rev. Phys. Chem.*, **58**, 375–407 (2007). (Cited on pages 1, 86, 107, and 108.)

[Bar09] J. V. Barth, Fresh perspectives for surface coordination chemistry, *Surf. Sci.*, **603**, 1533–1541 (2009). (Cited on page 129.)

[Bat64a] B. W. Batterman, Effect of Dynamical Diffraction in X-Ray Fluorescence Scattering, *Phys. Rev.*, **133**, A759–A764 (1964). (Cited on page 24.)

[Bat64b] B. W. Batterman and H. Cole, Dynamical Diffraction of X Rays by Perfect Crystals, *Rev. Mod. Phys.*, **36**, 681–717 (1964). (Cited on page 24.)

[Bat69] B. W. Batterman, Detection of Foreign Atom Sites by Their X-Ray Fluorescence Scattering, *Phys. Rev. Lett.*, **22**, 703–705 (1969). (Cited on page 24.)

[Bat00] A. R. Battersby, Tetrapyrroles: The Pigments of Life, *Nat. Prod. Rep.*, **17**, 507–526 (2000). (Cited on pages 2 and 86.)

[Bea67] J. A. Bearden, X-Ray Wavelengths, *Rev. Mod. Phys.*, **39**, 78–124 (1967). (Cited on page 40.)

[Ben02] A. Bendounan, Y. Fagot Revurat, B. Kierren, F. Bertran, V. Yurov, and D. Malterre, Surface state in epitaxial Ag ultrathin films on Cu(111), *Surf. Sci.*, **496**, L43–L49 (2002). (Cited on page 78.)

[Ber92] A. Berkó and F. Solymosi, Adsorption of Nitrogen Atoms on Cu(111), Rh(111) and Pt(110) Surfaces, *Appl. Surf. Sci.*, **55**, 193–202 (1992). (Cited on page 66.)

[Bes87] K. Besocke, An easily operable scanning tunneling microscope, *Surf. Sci.*, **181**, 145–153 (1987). (Cited on page 35.)

[Bie96] Biedermann, Genser, Hebenstreit, Schmid, Redinger, Podloucky, and Varga, Scanning tunneling spectroscopy of one-dimensional surface states on a metal surface, *Phys. Rev. Lett.*, **76**, 4179–4182 (1996). (Cited on page 11.)

[Bin82a] G. Binnig, H. Rohrer, C. Gerber, and E. Weibel, Surface Studies by Scanning Tunneling Microscopy, *Phys. Rev. Lett.*, **49**, 57–61 (1982). (Cited on pages 5 and 11.)

[Bin82b] G. Binnig, H. Rohrer, C. Gerber, and E. Weibel, Tunneling through a controllable vacuum gap, *Appl. Phys. Lett.*, **40**, 178–180 (1982). (Cited on pages 1, 5, and 11.)

[Bin83] G. Binnig, H. Rohrer, C. Gerber, and E. Weibel, 7 x 7 Reconstruction on Si(111) Resolved in Real Space, *Phys. Rev. Lett.*, **50**, 120–123 (1983). (Cited on page 5.)

[Bin85] G. Binnig, K. H. Frank, H. Fuchs, N. Garcia, B. Reihl, H. Rohrer, F. Salvan, and A. R. Williams, Tunneling Spectroscopy and Inverse Photoemission: Image and Field States, *Phys. Rev. Lett.*, **55**, 991–994 (1985). (Cited on pages 11, 12, and 71.)

[Bin86] G. Binnig, C. F. Quate, and C. Gerber, Atomic Force Microscope, *Phys. Rev. Lett.*, **56**, 930–933 (1986). (Cited on pages 1 and 6.)

[Bin87] G. Binnig and H. Rohrer, Scanning tunneling microscopy—from birth to adolescence, *Rev. Mod. Phys.*, **59**, 615–625 (1987). (Cited on page 6.)

[Bis13] F. Bischoff, K. Seufert, W. Auwärter, S. Joshi, S. Vijayaraghavan, D. Écija, K. Diller, A. C. Papageorgiou, S. Fischer, F. Allegretti, D. A. Duncan, F. Klappenberger, F. Blobner, R. Han, and J. V. Barth, How Surface Bonding and Repulsive Interactions Cause Phase Transformations: Ordering of a Prototype Macrocyclic Compound on Ag(111), *ACS Nano*, **7**, 3139–3149 (2013). (Cited on pages 87, 88, 97, and 122.)

[Bis16] F. Bischoff, Y. He, K. Seufert, D. Stassen, D. Bonifazi, J. V. Barth, and W. Auwärter, Tailoring Large Pores of Porphyrin Networks on Ag(111) by Metal-Organic Coordination, *Chem. - Eur. J.*, **22**, 15298–15306 (2016). (Cited on pages 109, 113, and 137.)

[Bis17] F. Bischoff, *Scanning probe microscopy studies of surface confined molecules and (metal-organic) nanostructures*, PhD thesis, Technische Universität München (2017). (Cited on pages 13 and 35.)

[Blo17] P. J. Blowey, L. A. Rochford, D. A. Duncan, D. A. Warr, T.-L. Lee, D. P. Woodruff, and G. Costantini, Probing the Interplay Between Geometric and Electronic Structure in a Two-Dimensional K-TCNQ Charge Transfer Network, *Faraday Discuss.*, **204**, 97–110 (2017). (Cited on pages 92 and 97.)

[Bob11] S. C. Bobaru, E. Salomon, J.-M. Layet, and T. Angot, Structural Properties of Iron Phtalocyanines on Ag(111): From the Submonolayer to Monolayer Range, *J. Phys. Chem. C*, **115**, 5875–5879 (2011). (Cited on page 24.)

[Bod01] M. Bode, O. Pietzsch, A. Kubetzka, S. Heinze, and R. Wiesendanger, Experimental evidence for intra-atomic noncollinear magnetism at thin film probe tips, *Phys. Rev. Lett.*, **86**, 2142–2145 (2001). (Cited on page 11.)

[Boe94] H. P. Boehm, Some aspects of the surface chemistry of carbon blacks and other carbons, *Carbon*, **32**, 759–769 (1994). (Cited on page 1.)

[Bok11] M. Bokdam, P. A. Khomyakov, G. Brocks, Z. Zhong, and P. J. Kelly, Electrostatic doping of graphene through ultrathin hexagonal boron nitride films, *Nano Lett.*, **11**, 4631–4635 (2011). (Cited on page 106.)

[Bon15] D. Bonifazi, F. Fasano, M. M. Lorenzo-Garcia, D. Marinelli, H. Oubaha, and J. Tasseroul, Boron-nitrogen doped carbon scaffolding: Organic chemistry, self-assembly and materials applications of borazine and its derivatives, *Chem. Commun.*, **51**, 15222–15236 (2015). (Cited on pages 46, 123, 128, 138, and 147.)

[Bon17] D. Bonifazi, Department of Chemistry and Namur Research College (NARC), University of Namur (UNamur), Namur, Belgium (2017), `https://www.unamur.be/en/research/narc/davide-bonifazi`, (Accessed: 2017-02-05). (Cited on pages 47 and 109.)

[Bor10] B. Borca, S. Barja, M. Garnica, D. Sánchez-Portal, V. M. Silkin, E. V. Chulkov, C. F. Hermanns, J. J. Hinarejos, A. L. Vázquez de Parga, A. Arnau, P. M. Echenique, and R. Miranda, Potential energy landscape for hot electrons in periodically nanostructured graphene, *Phys. Rev. Lett.*, **105**, 036804 (2010). (Cited on pages 71 and 76.)

[Bri99] G. A. D. Briggs and A. J. Fisher, STM experiment and atomistic modelling hand in hand: Individual molecules on semiconductor surfaces, *Surf. Sci. Rep.*, **33**, 1–81 (1999). (Cited on page 9.)

[Bri03] D. Briggs and J. T. Grant, *Surface Analysis by Auger and X-ray Photoelectron Spectroscopy*. IM Publications, Chichester, (2003). (Cited on pages 18, 20, and 21.)

[Bri12] L. Britnell, R. V. Gorbachev, R. Jalil, B. D. Belle, F. Schedin, A. Mishchenko, T. Georgiou, M. I. Katsnelson, L. Eaves, S. V. Morozov, N. M. R. Peres, J. Leist, A. K. Geim, K. S. Novoselov, and L. A. Ponomarenko, Field-effect tunneling transistor based on vertical graphene heterostructures, *Science*, **335**, 947–950 (2012). (Cited on page 141.)

[Brö10] B. Bröker, *Electronic and structural properties of interfaces between electron donor & acceptor molecules and conductive electrodes*, PhD thesis, Humbold-Universität Berlin (2010). (Cited on page 83.)

[Bru76] C. R. Brundle, T. J. Chuang, and D. W. Rice, X- ray photoemission study of the interaction of oxygen and air with clean cobalt surfaces, *Surf. Sci.*, **60**, 286–300 (1976). (Cited on page 20.)

[Bru09] T. Brugger, S. Günther, B. Wang, J. H. Dil, M.-L. Bocquet, J. Osterwalder, J. Wintterlin, and T. Greber, Comparison of electronic structure and template function of single-layer graphene and a hexagonal boron nitride nanomesh on Ru(0001), *Phys. Rev. B*, **79**, 045407 (2009). (Cited on page 105.)

[Brü17] C. Brülke, T. Heepenstrick, N. Humberg, I. Krieger, M. Sokolowski, S. Weiß, F. S. Tautz, and S. Soubatch, Long Vertical Distance Bonding of the Hexagonal Boron Nitride Monolayer on the Cu(111) Surface, *J. Phys. Chem. C*, **121**, 23964–23973 (2017). (Cited on page 70.)

[Buc10] F. Buchner, I. Kellner, W. Hieringer, A. Gorling, H.-P. Steinrück, and H. Marbach, Ordering Aspects and Intramolecular Conformation of Tetraphenylporphyrins on Ag(111), *Phys. Chem. Chem. Phys.*, **12**, 13082–13090 (2010). (Cited on page 122.)

[Bur01] A. K. Burrell, D. L. Officer, P. G. Plieger, and D. C. W. Reid, Synthetic Routes to Multiporphyrin Arrays, *Chem. Rev.*, **101**, 2751–2796 (2001). (Cited on page 107.)

[Bür13] C. Bürker, N. Ferri, A. Tkatchenko, A. Gerlach, J. Niederhausen, T. Hosokai, S. Duhm, J. Zegenhagen, N. Koch, and F. Schreiber, Exploring the Bonding of Large Hydrocarbons on Noble Metals: Diindoperylene on Cu(111), Ag(111), and Au(111), *Phys. Rev. B*, **87**, 165443 (2013). (Cited on pages 87, 88, and 99.)

[Bür14] C. Bürker, A. Franco-Cañellas, K. Broch, T.-L. Lee, A. Gerlach, and F. Schreiber, Self-Metalation of 2H-Tetraphenylporphyrin on Cu(111) Studied with XSW: Influence of the Central Metal Atom on the Adsorption Distance, *J. Phys. Chem. C*, **118**, 13659–13666 (2014). (Cited on pages 24, 87, and 88.)

[But88] M. Buttiker, Coherent and sequential tunneling in series barriers, *IBM J. Res. & Dev.*, **32**, 63–75 (1988). (Cited on page 8.)

[Cac12] V. Caciuc, N. Atodiresei, M. Callsen, P. Lazić, and S. Blügel, Ab initio and semi-empirical van der Waals study of graphene-boron nitride interaction from a molecular point of view, *J. Phys. Cond. Matter*, **24**, 424214 (2012). (Cited on pages 99 and 104.)

[Cai10] J. Cai, P. Ruffieux, R. Jaafar, M. Bieri, T. Braun, S. Blankenburg, M. Muoth, A. P. Seitsonen, M. Saleh, X. Feng, K. Müllen, and R. Fasel, Atomically Precise Bottom-up Fabrication of Graphene Nanoribbons, *Nature*, **466**, 470–473 (2010). (Cited on page 141.)

[Cai15] B. Cai, S. Zhang, Z. Yan, and H. Zeng, Noncovalent Molecular Doping of Two-Dimensional Materials, *ChemNanoMat*, **1**, 542–557 (2015). (Cited on page 99.)

[Cam12] P. G. Campbell, A. J. V. Marwitz, and S.-Y. Liu, Recent advances in azaborine chemistry, *Angew. Chem., Int. Ed. Engl.*, **51**, 6074–6092 (2012). (Cited on page 128.)

[Cam14] L. Camilli, E. Sutter, and P. Sutter, Growth of two-dimensional materials on non-catalytic substrates: h-BN/Au(111), *2D Mater.*, **1**, 025003 (2014). (Cited on page 71.)

[Cas16] CasaXPS, Neal Fairley, Registrant Street 26 Burford Crescent, Wilmslow, Cheshire, SK9 6BN, UK (2016), `http://www.casaxps.com/`, (Accessed: 2017-02-27). (Cited on page 39.)

[Che88] C. J. Chen, Theory of scanning tunneling spectroscopy, *J. Vac. Sci. Technol. A*, **6**, 319–322 (1988). (Cited on page 9.)

[Che90] C. J. Chen, Origin of atomic resolution on metal surfaces in scanning tunneling microscopy, *Phys. Rev. Lett.*, **65**, 448–451 (1990). (Cited on page 5.)

[Che07] W. Chen, S. Chen, D. C. Qi, X. Y. Gao, and A. T. S. Wee, Surface transfer p-type doping of epitaxial graphene, *J. Am. Chem. Soc.*, **129**, 10418–10422 (2007). (Cited on page 99.)

[Che08] H. Chen, M. Ikeda-Saito, and S. Shaik, Nature of the Fe-O2 Bonding in Oxy-Myoglobin: Effect of the Protein, *J. Am. Chem. Soc.*, **130**, 14778–14790 (2008). (Cited on pages 5, 8, 9, and 10.)

[Che10a] C.-M. Che and F.-M. Siu, Metal Complexes in Medicine with a Focus on Enzyme Inhibition, *Curr. Opin. Chem. Biol.*, **14**, 255–261 (2010). (Cited on page 85.)

[Che10b] X. Chen and M. Alouani, Effect of Metallic Surfaces on the Electronic Structure, Magnetism, and Transport Properties of Co-Phthalocyanine Molecules, *Phys. Rev. B*, **82**, 094443 (2010). (Cited on page 98.)

[Che16] X. Chen, S. Jia, N. Ding, J. Shi, and Z. Wang, Capture of aromatic organic pollutants by hexagonal boron nitride nanosheets: Density functional theoretical and molecular dynamic investigation, *Environ. Sci.: Nano*, **3**, 1493–1503 (2016). (Cited on page 99.)

[Che18a] ChemSpider, Borazine | $H_6B_3N_3$ | ChemSpider (2018), `http://www.chemspider.com/Chemical-Structure.122374.html`, (Accessed: 2018-03-07). (Cited on page 38.)

[Che18b] Y. Chen, S. Huang, X. Ji, K. Adepalli, K. Yin, X. Ling, X. Wang, J. Xue, M. Dresselhaus, J. Kong, and B. Yildiz, Tuning Electronic Structure of Single Layer MoS_2 through Defect and Interface Engineering, *ACS Nano*, **12**, 2569–2579 (2018). (Cited on page 142.)

[Cho12] J. Cho, J. Smerdon, L. Gao, O. Süzer, J. R. Guest, and N. P. Guisinger, Structural and electronic decoupling of C_{60} from epitaxial graphene on SiC, *Nano Lett.*, **12**, 3018–3024 (2012). (Cited on pages 99 and 111.)

[Ci10] L. Ci, L. Song, C. Jin, D. Jariwala, D. Wu, Y. Li, A. Srivastava, Z. F. Wang, K. Storr, L. Balicas, F. Liu, and P. M. Ajayan, Atomic Layers of Hybridized Boron Nitride and Graphene Domains, *Nat. Mater.*, **9**, 430–435 (2010). (Cited on pages 55, 123, 124, and 141.)

[Cic16] F. Ciccullo, A. Calzolari, I. P, S.-A. Savu, M. Krieg, H. F. Bettinger, E. Magnano, T. Chassé, and M. B. Casu, A Quasi-Free-Standing Single Layer of a B_3N_3 -Doped Nanographene Molecule Deposited on Au(111) Single Crystals, *J. Phys. Chem. C*, **120**, 17645–17651 (2016). (Cited on pages 128 and 138.)

[Cir17] B. Cirera, J. Matarrubia, T. Kaposi, N. Giménez-Agulló, M. Paszkiewicz, F. Klappenberger, R. Otero, J. M. Gallego, P. Ballester, J. V. Barth, R. Miranda, J. R. Galán-Mascarós, W. Auwärter, and D. Écija, Preservation of electronic properties of double-decker complexes on metallic supports, *Phys. Chem. Chem. Phys.*, **19**, 8282–8287 (2017). (Cited on page 128.)

[Col10] C. Coletti, C. Riedl, D. S. Lee, B. Krauss, L. Patthey, K. von Klitzing, J. H. Smet, and U. Starke, Charge neutrality and band-gap tuning of epitaxial graphene on SiC by molecular doping, *Phys. Rev. B*, **81**, 505 (2010). (Cited on page 99.)

[Col15] J. A. Colon Santana, *Quantitative core level photoelectron spectroscopy: A primer*, IOP concise physics. Morgan & Claypool, San Rafael, (2015). (Cited on page 40.)

[Coo69] J. W. Cooper and S. T. Manson, Photo-Ionization in the Soft X-Ray Range: Angular Distributions of Photoelectrons and Interpretation in Terms of Subshell Structure, *Phys. Rev.*, **177**, 157–163 (1969). (Cited on page 30.)

[Coo88] J. H. Coombs and J. K. Gimzewski, Fine structure in field emission resonances at surfaces, *J. Microsc.*, **152**, 841–851 (1988). (Cited on pages 73 and 74.)

[Coo93] J. W. Cooper, Photoelectron-angular-distribution parameters for rare-gas subshells, *Phys. Rev. A*, **47**, 1841–1851 (1993). (Cited on page 30.)

[Cor04] M. Corso, W. Auwärter, M. Muntwiler, A. Tamai, T. Greber, and J. Osterwalder, Boron Nitride Nanomesh, *Science*, **303**, 217–220 (2004). (Cited on pages 56 and 58.)

[Cre02] CreaTec Fischer & Co. GmbH, Manual: How to assemble a metal sample holder (2002). (Cited on page 45.)

[Cre13] CreaTec Fischer & Co. GmbH, Manual: How to install the LT-STM head (2013). (Cited on page 43.)

[Cre15] CreaTec Fischer & Co. GmbH, Manual: Hardware 2.0 Installation (2015). (Cited on pages 44 and 45.)

[Cre17] CreaTec Fischer & Co. GmbH, Industriestr. 9, 74391 Erligheim, Germany (2017), `http://createc.de`, (Accessed: 2017-04-02). (Cited on pages 36 and 42.)

[Cri02] X. Crispin, V. Geskin, A. Crispin, J. Cornil, R. Lazzaroni, W. R. Salaneck, and J.-L. Brédas, Characterization of the Interface Dipole at Organic/ Metal Interfaces, *J. Am. Chem. Soc.*, **124**, 8131–8141 (2002). (Cited on page 83.)

[Cro93a] M. F. Crommie, C. P. Lutz, and D. M. Eigler, Confinement of electrons to quantum corrals on a metal surface, *Science*, **262**, 218–220 (1993). (Cited on pages 11 and 13.)

[Cro93b] M. F. Crommie, C. P. Lutz, and D. M. Eigler, Imaging standing waves in a two-dimensional electron gas, *Nature*, **363**, 524–527 (1993). (Cited on page 11.)

[Cua10] R. Cuadrado, J. I. Cerda, Y. Wang, G. Xin, R. Berndt, and H. Tang, CoPc Adsorption on Cu(111): Origin of the C_4 to C_2 Symmetry Reduction, *J. Chem. Phys.*, **133**, 154701–1–154701–7 (2010). (Cited on pages 95, 97, and 98.)

[Das08] B. Das, R. Voggu, C. S. Rout, and C. N. R. Rao, Changes in the electronic structure and properties of graphene induced by molecular charge-transfer, *Chem. Commun.*, **0**, 5155–5157 (2008). (Cited on page 99.)

[Dav27a] C. Davisson and L. H. Germer, Diffraction of Electrons by a Crystal of Nickel, *Phys. Rev.*, **30**, 705–740 (1927). (Cited on page 33.)

[Dav27b] C. Davisson and L. H. Germer, The Scattering of Electrons by a Single Crystal of Nickel, *Nature*, **119**, 558–560 (1927). (Cited on page 33.)

[Dea10] C. R. Dean, A. F. Young, I. Meric, C. Lee, L. Wang, S. Sorgenfrei, K. Watanabe, T. Taniguchi, P. Kim, K. L. Shepard, and J. Hone, Boron Nitride Substrates for High-Quality Graphene Electronics, *Nat. Nanotechnol.*, **5**, 722–726 (2010). (Cited on page 70.)

[Dec11] R. Decker, Y. Wang, V. W. Brar, W. Regan, H.-Z. Tsai, Q. Wu, W. Gannett, A. Zettl, and M. F. Crommie, Local Electronic Properties of Graphene on a BN Substrate via Scanning Tunneling Microscopy, *Nano Lett.*, **11**, 2291–2295 (2011). (Cited on page 55.)

[Dei16] P. S. Deimel, R. M. Bababrik, B. Wang, P. J. Blowey, L. A. Rochford, P. K. Thakur, T.-L. Lee, M.-L. Bocquet, J. V. Barth, D. P. Woodruff, D. A. Duncan, and F. Allegretti, Direct Quantitative Identification of the "Surface Trans-Effect", *Chem. Sci.*, **7**, 5647–5656 (2016). (Cited on pages 90 and 98.)

[Des11] Des McMorrow and J. Als-Nielsen, *Elements of modern X-ray physics*. Wiley-Blackwell, Oxford, 2nd ed. edition, (2011). (Cited on page 40.)

[Di 11] G. Di Santo, C. Castellarin-Cudia, M. Fanetti, B. Taleatu, P. Borghetti, L. Sangaletti, L. Floreano, E. Magnano, F. Bondino, and A. Goldoni, Conformational Adaptation and Electronic Structure of 2H-Tetraphenylporphyrin on Ag(111) during Fe Metalation, *J. Phys. Chem. C*, **115**, 4155–4162 (2011). (Cited on pages 90 and 122.)

[Dia09] L. G. G. V. Dias da Silva, M. L. Tiago, S. E. Ulloa, F. A. Reboredo, and E. Dagotto, Many-body electronic structure and Kondo properties of cobalt-porphyrin molecules, *Phys. Rev. B*, **80**, 155443 (2009). (Cited on page 114.)

[Die14] T. Dienel, J. Gomez Diaz, A. P. Seitsonen, R. Widmer, M. Iannuzzi, K. Radican, H. Sachdev, K. Müllen, J. Hutter, and O. Gröning, Dehalogenation and Coupling of a Polycyclic Hydrocarbon on an Atomically Thin Insulator, *ACS Nano*, **8**, 6571–6579 (2014). (Cited on pages 99, 108, and 111.)

[Dil12] K. Diller, F. Klappenberger, M. Marschall, K. Hermann, A. Nefedov, C. Woll, and J. V. Barth, Self-Metalation of 2H-Tetraphenylporphyrin on Cu(111): an X-ray Spectroscopy Study, *J. Chem. Phys.*, **136**, 014705 (2012). (Cited on pages 87, 97, and 111.)

[Dil13a] K. Diller, F. Klappenberger, F. Allegretti, A. C. Papageorgiou, S. Fischer, A. Wiengarten, S. Joshi, K. Seufert, D. Écija, W. Auwärter, and J. V. Barth, Investigating the Molecule-Substrate Interaction of Prototypic Tetrapyrrole Compounds: Adsorption and Self-Metalation of Porphine on Cu(111), *J. Chem. Phys.*, **138**, 154710–1–154710–9 (2013). (Cited on page 21.)

[Dil13b] K. Diller, *Free-Base and Metalated Porphyrins on Metal Surfaces - a Systematic X-ray Spectroscopy and Density Functional Theory Investigation*, PhD thesis, Technische Universität München (2013). (Cited on pages 87, 90, 95, 97, 98, and 122.)

[Dil16] K. Diller, A. C. Papageorgiou, F. Klappenberger, F. Allegretti, J. V. Barth, and W. Auwärter, In Vacuo Interfacial Tetrapyrrole Metallation, *Chem. Soc. Rev.*, **45**, 1629–1656 (2016). (Cited on pages 86 and 87.)

[Dio04] M. Dion, H. Rydberg, E. Schroder, D. C. Langreth, and B. I. Lundqvist, van der Waals Density Functional for General Geometries, *Phys. Rev. Lett.*, **92**, 246401 (2004). (Cited on page 153.)

[Dio05] M. Dion, H. Rydberg, E. Schröder, D. C. Langreth, and B. I. Lundqvist, Erratum: Van der Waals Density Functional for General Geometries [Phys. Rev. Lett. 92 , 246401 (2004)], *Phys. Rev. Lett.*, **95**, 109902 (2005). (Cited on page 153.)

[Dod17] Dodecon Nanotechnology GmbH, Leipzigerstr. 13, 71111 Waldenbuch, Germany (2017), `http://www.dodecon.de`, (Accessed: 2017-02-18). (Cited on page 38.)

[Don70] S. Doniach and M. Sunjic, Many-electron singularity in X-ray photoemission and X-ray line spectra from metals, *J. Phys. C: Solid State Phys.*, **3**, 285–291 (1970). (Cited on page 22.)

[Don10] P. Donovan, A. Robin, M. S. Dyer, M. Persson, and R. Raval, Unexpected Deformations Induced by Surface Interaction and Chiral Self-Assembly of Co(II)-

Tetraphenylporphyrin (Co-TPP) Adsorbed on Cu(110): A Combined STM and Periodic DFT Study, *Chem. - Eur. J.*, **16**, 11641–11652 (2010). (Cited on page 97.)

[Don16] L. Dong, Z. Gao, and N. Lin, Self-assembly of metal–organic coordination structures on surfaces, *Prog. Surf. Sci.*, **91**, 101–135 (2016). (Cited on page 129.)

[Dos17] J. Dosso, J. Tasseroul, F. Fasano, D. Marinelli, N. Biot, A. Fermi, and D. Bonifazi, Synthesis and Optoelectronic Properties of Hexa-peri-hexabenzoborazinocoronene, *Angew. Chem., Int. Ed. Engl.*, **56**, 4483–4487 (2017). (Cited on page 128.)

[Dra01] D. Drakova, Theoretical modelling of scanning tunnelling microscopy, scanning tunnelling spectroscopy and atomic force microscopy, *Rep. Prog. Phys.*, **64**, 205–290 (2001). (Cited on page 11.)

[Dre86] K. E. Drexler, *Engines of Creation - The Coming Era of Nanotechnology*, The Anchor library of science. Anchor Press/Doubleday, Garden City, N.Y., (1986). (Cited on page 1.)

[Dro15] R. Drost, S. Kezilebieke, M. M Ervasti, S. K. Hämäläinen, F. Schulz, A. Harju, and P. Liljeroth, Synthesis of Extended Atomically Perfect Zigzag Graphene - Boron Nitride Interfaces, *Sci. Rep.*, **5**, 16741 (2015). (Cited on page 124.)

[Duc18] J. Ducke, A. Riss, A. Pérez Paz, K. Seufert, M. Schwarz, M. Garnica, A. Rubio, and W. Auwärter, Layered Insulator/Molecule/Metal Heterostructures with Molecular Functionality through Porphyrin Intercalation, *ACS Nano*, **12**, 2677–2684 (2018). (Cited on page 2.)

[Dun15] D. A. Duncan, P. S. Deimel, A. Wiengarten, R. Han, R. G. Acres, W. Auwärter, P. Feulner, A. C. Papageorgiou, F. Allegretti, and J. V. Barth, Immobilised molecular catalysts and the role of the supporting metal substrate, *Chem. Commun.*, **51**, 9483–9486 (2015). (Cited on page 24.)

[DUR17] DURAN Group GmbH, Otto-Schott-Straße 21, 97877 Wertheim/Main, Deutschland (2017), `http://www.duran-group.com/en/products-solutions/glassware-for-manipulators/products/stopcocks-valves/produran-valves.html`. (Cited on page 147.)

[Dye11] M. S. Dyer, A. Robin, S. Haq, R. Raval, M. Persson, and J. Klimes, Understanding the Interaction of the Porphyrin Macrocycle to Reactive Metal Substrates: Structure, Bonding, and Adatom Capture, *ACS Nano*, **5**, 1831–1838 (2011). (Cited on page 87.)

[Éci12] D. Écija, S. Vijayaraghavan, W. Auwärter, S. Joshi, K. Seufert, C. Aurisicchio, D. Bonifazi, and J. V. Barth, Two-dimensional short-range disordered crystalline networks from flexible molecular modules, *ACS Nano*, **6**, 4258–4265 (2012). (Cited on page 132.)

[Eck12] M. Eckert, Max von Laue and the discovery of X-ray diffraction in 1912, *Ann. Phys.*, **524**, A83–A85 (2012). (Cited on page 23.)

[Eig90] D. M. Eigler and E. K. Schweizer, Positioning single atoms with a scanning tunnelling microscope, *Nature*, **344**, 524–526 (1990). (Cited on pages 1 and 13.)

[Ein05] A. Einstein, Über einen die Erzeugung und Verwandlung des Lichtes betreffenden heuristischen Gesichtspunkt, *Ann. Phys.*, **322**, 132–148 (1905). (Cited on page 16.)

[El 14] M. El Garah, A. Ciesielski, N. Marets, V. Bulach, M. W. Hosseini, and P. Samorì, Molecular tectonics based nanopatterning of interfaces with 2D metal-organic frameworks (MOFs), *Chem. Commun.*, **50**, 12250–12253 (2014). (Cited on page 107.)

[End09] A. Endo, M. Ogasawara, A. Takahashi, D. Yokoyama, Y. Kato, and C. Adachi, Thermally Activated Delayed Fluorescence from Sn($^{4+}$)-Porphyrin Complexes and their Application to Organic Light Emitting Diodes-a Novel Mechanism for Electroluminescence, *Adv. Mater.*, **21**, 4802–4806 (2009). (Cited on page 1.)

[Ert08] G. Ertl, Reactions at surfaces: From atoms to complexity (Nobel Lecture), *Angew. Chem., Int. Ed. Engl.*, **47**, 3524–3535 (2008). (Cited on page 1.)

[Fan61] U. Fano, Effects of Configuration Interaction on Intensities and Phase Shifts, *Phys. Rev.*, **124**, 1866–1878 (1961). (Cited on page 115.)

[Faz95] P. J. Fazen, E. E. Remsen, J. S. Beck, P. J. Carroll, A. R. McGhie, and L. G. Sneddon, Synthesis, Properties, and Ceramic Conversion Reactions of Polyborazylene. A High-Yield Polymeric Precursor to Boron Nitride, *Chem. Mater.*, **7**, 1942–1956 (1995). (Cited on page 128.)

[Fed15] A. Fedorov, C. S. Praveen, N. I. Verbitskiy, D. Haberer, D. Usachov, D. V. Vyalikh, A. Nefedov, C. Wöll, L. Petaccia, S. Piccinin, H. Sachdev, M. Knupfer, B. Büchner, S. Fabris, and A. Grüneis, Efficient gating of epitaxial boron nitride monolayers by substrate functionalization, *Phys. Rev. B*, **92**, 125440 (2015). (Cited on page 2.)

[Feh93] W. P. Fehlhammer and M. Fritz, Emergence of a CNH and cyano complex based organometallic chemistry, *Chem. Rev.*, **93**, 1243–1280 (1993). (Cited on page 113.)

[Fei89] R. Feidenhans'l, Surface structure determination by X-ray diffraction, *Surf. Sci. Rep.*, **10**, 105–188 (1989). (Cited on page 23.)

[Fei15] B. N. Feigelson, V. M. Bermudez, J. K. Hite, Z. R. Robinson, V. D. Wheeler, K. Sridhara, and S. C. Hernandez, Growth and Spectroscopic Characterization of Monolayer and Few-Layer Hexagonal Boron Nitride on Metal Substrates, *Nanoscale*, **7**, 3694–3702 (2015). (Cited on page 56.)

[Fel86] L. C. Feldman and J. W. Mayer, *Fundamentals of surface and thin film analysis.* North Holland, New York and London, (1986). (Cited on page 40.)

[Fer07] A. C. Ferrari, Raman spectroscopy of graphene and graphite: Disorder, electron–phonon coupling, doping and nonadiabatic effects, *Solid State Commun.*, **143**, 47–57 (2007). (Cited on page 124.)

[Feu16] P. Feulner, Anleitung: Reinigen von Metal Oberflächen (2016). (Cited on page 46.)

[Fey60] R. P. Feynman, There's plenty of room at the bottom, *Eng. Sci.*, **23**, 22–36 (1960). (Cited on pages 1 and 13.)

[Fis98] C. J. Fisher, R. Ithin, R. G. Jones, G. J. Jackson, D. P. Woodruff, and B. C. C. Cowie, Non-Dipole Photoemission Effects in X-ray Standing Wavefield Determination of Surface Structure, *J. Phys. Cond. Matter*, **10**, L623–L629 (1998). (Cited on page 152.)

[Fle07] K. Flechtner, A. Kretschmann, H.-P. Steinrück, and J. M. Gottfried, NO-Induced Reversible Switching of the Electronic Interaction Between a Porphyrin-Coordinated Cobalt Ion and a Silver Surface, *J. Am. Chem. Soc.*, **129**, 12110–12111 (2007). (Cited on page 90.)

[Fli61] P. A. Flinn, G. M. McManus, and J. A. Rayne, Effective X-Ray and Calorimetric Debye Temperature for Copper, *Phys. Rev.*, **123**, 809–812 (1961). (Cited on page 68.)

[FOC17] FOCUS GmbH, Geräte zur Elektronenspektroskopie und Oberflächenanalytik, Neukirchner Str. 2, 65510 Huenstetten, Germany (2017), `http://www.focus-gmbh.com`, (Accessed: 2017-02-05). (Cited on pages 36 and 38.)

[For03] F. Forster, G. Nicolay, F. Reinert, D. Ehm, S. Schmidt, and S. Hüfner, Surface and interface states on adsorbate covered noble metal surfaces, *Surf. Sci.*, **532-535**, 160–165 (2003). (Cited on page 71.)

[Fra17] M. Franke, D. Wechsler, Q. Tariq, M. Röckert, L. Zhang, P. Kumar Thakur, N. Tsud, S. Bercha, K. Prince, T.-L. Lee, H.-P. Steinrück, and O. Lytken, Interfacial interactions between CoTPP molecules and MgO(100) thin films, *Phys. Chem. Chem. Phys.*, **19**, 11549–11553 (2017). (Cited on page 106.)

[Fri13] W. Friedrich, P. Knipping, and M. Laue, Interferenzerscheinungen bei Röntgenstrahlen, *Ann. Phys.*, **346**, 971–988 (1913). (Cited on page 23.)

[Fro89] J. Frohn, J. F. Wolf, K. Besocke, and M. Teske, Coarse tip distance adjustment and positioner for a scanning tunneling microscope, *Rev. Sci. Instrum.*, **60**, 1200–1201 (1989). (Cited on page 35.)

[Fro17] Frontier Scientific, P.O. Box 31, Logan, UT 84323-0031 (2017), `http://www.frontiersci.com/`, (Accessed: 2017-08-12). (Cited on page 47.)

[Fu07] Y.-S. Fu, S.-H. Ji, X. Chen, X.-C. Ma, R. Wu, C.-C. Wang, W.-H. Duan, X.-H. Qiu, B. Sun, P. Zhang, J.-F. Jia, and Q.-K. Xue, Manipulating the Kondo resonance through quantum size effects, *Phys. Rev. Lett.*, **99**, 256601 (2007). (Cited on page 121.)

[Gam97] Y. Gamo, A. Nagashima, M. Wakabayashi, M. Terai, and C. Oshima, Atomic structure of monolayer graphite formed on Ni(111), *Surf. Sci.*, **374**, 61–64 (1997). (Cited on page 71.)

[Gam17] Gamma Vacuum, 2915 133rd Street West, Shakopee, MN 55379, United States (2017), `http://gammavacuum.com/`, (Accessed: 2017-02-05). (Cited on page 36.)

[Gao07] L. Gao, W. Ji, Y. B. Hu, Z. H. Cheng, Z. T. Deng, Q. Liu, N. Jiang, X. Lin, W. Guo, S. X. Du, W. A. Hofer, X. C. Xie, and H.-J. Gao, Site-Specific Kondo Effect at Ambient Temperatures in Iron-Based Molecules, *Phys. Rev. Lett.*, **99**, 106402–1–106402–4 (2007). (Cited on page 121.)

[Gao13] Y. Gao, Y. Zhang, P. Chen, Y. Li, M. Liu, T. Gao, D. Ma, Y. Chen, Z. Cheng, X. Qiu, W. Duan, and Z. Liu, Toward single-layer uniform hexagonal boron nitride-graphene patchworks with zigzag linking edges, *Nano Lett.*, **13**, 3439–3443 (2013). (Cited on page 124.)

[Gao15] T. Gao, X. Song, H. Du, Y. Nie, Y. Chen, Q. Ji, J. Sun, Y. Yang, Y. Zhang, and Z. Liu, Temperature-triggered chemical switching growth of in-plane and vertically stacked graphene-boron nitride heterostructures, *Nat. Commun.*, **6**, 6835 (2015). (Cited on pages 106 and 127.)

[Gao16] X. Gao, S. Wang, and S. Lin, Defective Hexagonal Boron Nitride Nanosheet on Ni(111) and Cu(111): Stability, Electronic Structures, and Potential Applications, *ACS Appl. Mater. Interfaces*, **8**, 24238–24247 (2016). (Cited on page 67.)

[Gar13a] M. Garnica, *Electron acceptor molecules deposited on epitaxial graphene studied by means of low temperature scanning tunneling microscopy/spectroscopy*, PhD thesis, Instituto Madrileño de Estudios Avanzados (2013). (Cited on pages 11, 107, and 108.)

[Gar13b] M. Garnica, D. Stradi, S. Barja, F. Calleja, C. Díaz, M. Alcamí, N. Martín, Vázquez de Parga, Amadeo L., F. Martín, and R. Miranda, Long-range magnetic order in a purely organic 2D layer adsorbed on epitaxial graphene, *Nat. Phys.*, **9**, 368–374 (2013). (Cited on pages 115 and 116.)

[Gar14a] A. Garcia-Lekue, T. Balashov, M. Olle, G. Ceballos, A. Arnau, P. Gambardella, D. Sanchez-Portal, and A. Mugarza, Spin-dependent electron scattering at graphene edges on Ni(111), *Phys. Rev. Lett.*, **112**, 066802 (2014). (Cited on page 76.)

[Gar14b] M. Garnica, F. Calleja, Vázquez de Parga, Amadeo L., and R. Miranda, Mapping spin distributions in electron acceptor molecules adsorbed on nanostructured graphene by the Kondo effect, *Surf. Sci.*, **630**, 356–360 (2014). (Cited on page 121.)

[Gar14c] M. Garnica, D. Stradi, F. Calleja, S. Barja, C. Díaz, M. Alcamí, A. Arnau, Vázquez de Parga, Amadeo L., F. Martín, and R. Miranda, Probing the site-dependent Kondo response of nanostructured graphene with organic molecules, *Nano Lett.*, **14**, 4560–4567 (2014). (Cited on pages 11, 114, and 121.)

[Gar16] M. Garnica, M. Schwarz, J. Ducke, Y. He, F. Bischoff, J. V. Barth, W. Auwärter, and D. Stradi, Comparative Study of the Interfaces of Graphene and Hexagonal Boron Nitride with Silver, *Phys. Rev. B*, **94**, 155431 (2016). (Cited on pages 11, 48, 56, 76, 82, 106, 124, and 129.)

[Ge09] X. Ge, C. Manzano, R. Berndt, L. T. Anger, F. Köhler, and R. Herges, Controlled Formation of an Axially Bonded Co-Phthalocyanine Dimer, *J. Am. Chem. Soc.*, **131**, 6096–6098 (2009). (Cited on page 110.)

[Gei07] A. K. Geim and K. S. Novoselov, The rise of graphene, *Nat. Mater.*, **6**, 183–191 (2007). (Cited on page 2.)

[Gei13] A. K. Geim and I. V. Grigorieva, Van der Waals heterostructures, *Nature*, **499**, 419–425 (2013). (Cited on pages 2, 55, 71, 123, and 141.)

[Gia60] I. Giaever, Electron Tunneling Between Two Superconductors, *Phys. Rev. Lett.*, **5**, 464–466 (1960). (Cited on page 6.)

[Gia09] P. Giannozzi, S. Baroni, N. Bonini, M. Calandra, R. Car, C. Cavazzoni, D. Ceresoli, G. L. Chiarotti, M. Cococcioni, I. Dabo, A. Dal Corso, S. de Gironcoli, S. Fabris, G. Fratesi, R. Gebauer, U. Gerstmann, C. Gougoussis, A. Kokalj, M. Lazzeri,

L. Martin-Samos, N. Marzari, F. Mauri, R. Mazzarello, S. Paolini, A. Pasquarello, L. Paulatto, C. Sbraccia, S. Scandolo, G. Sclauzero, A. P. Seitsonen, A. Smogunov, P. Umari, and R. M. Wentzcovitch, QUANTUM ESPRESSO: A Modular and Open-Source Software Project for Quantum Simulations of Materials, *J. Phys. Cond. Matter*, **21**, 395502 (2009). (Cited on page 153.)

[Gie97] F. J. Giessibl, Forces and frequency shifts in atomic-resolution dynamic-force microscopy, *Phys. Rev. B*, **56**, 16010–16015 (1997). (Cited on pages 14 and 15.)

[Gie98] F. J. Giessibl, High-speed force sensor for force microscopy and profilometry utilizing a quartz tuning fork, *Appl. Phys. Lett.*, **73**, 3956–3958 (1998). (Cited on pages 13 and 151.)

[Gie03] F. J. Giessibl, Advances in atomic force microscopy, *Rev. Mod. Phys.*, **75**, 949–983 (2003). (Cited on pages 13 and 14.)

[Gie16] D. Gielen, F. Boshell, and D. Saygin, Climate and energy challenges for materials science, *Nat. Mater.*, **15**, 117–120 (2016). (Cited on page 1.)

[Gio08] G. Giovannetti, P. A. Khomyakov, G. Brocks, V. M. Karpan, J. van den Brink, and P. J. Kelly, Doping graphene with metal contacts, *Phys. Rev. Lett.*, **101**, 026803 (2008). (Cited on pages 124 and 127.)

[Gol82] J. A. Golovchenko, J. R. Patel, D. R. Kaplan, P. L. Cowan, and M. J. Bedzyk, Solution to the Surface Registration Problem Using X-ray Standing Waves, *Phys. Rev. Lett.*, **49**, 560–563 (1982). (Cited on pages 32 and 91.)

[Gol12] A. Goldoni, C. A. Pignedoli, G. Di Santo, C. Castellarin-Cudia, E. Magnano, F. Bondino, A. Verdini, and D. Passerone, Room temperature metalation of 2H-TPP monolayer on iron and nickel surfaces by picking up substrate metal atoms, *ACS Nano*, **6**, 10800–10807 (2012). (Cited on page 111.)

[Gom13] J. Gomez Diaz, Y. Ding, R. Koitz, A. P. Seitsonen, M. Iannuzzi, and J. Hutter, Hexagonal boron nitride on transition metal surfaces, *Theor. Chem. Acc.*, **132**, 1–17 (2013). (Cited on pages 56, 153, and 154.)

[Gop16] D. P. Gopalan, P. C. Mende, S. C. de La Barrera, S. Dhingra, J. Li, K. Zhang, N. A. Simonson, J. A. Robinson, N. Lu, Q. Wang, M. J. Kim, B. D'Urso, and R. M. Feenstra, Formation of hexagonal boron nitride on graphene-covered copper surfaces, *J. Mater. Res.*, **31**, 945–958 (2016). (Cited on page 127.)

[Got06] J. M. Gottfried, K. Flechtner, A. Kretschmann, T. Lukasczyk, and H.-P. Steinrück, Direct Synthesis of a Metalloporphyrin Complex on a Surface, *J. Am. Chem. Soc.*, **128**, 5644–5645 (2006). (Cited on page 90.)

[Got15] J. M. Gottfried, Surface Chemistry of Porphyrins and Phthalocyanines, *Surf. Sci. Rep.*, **70**, 259–379 (2015). (Cited on pages 1, 2, and 86.)

[Gri06] S. Grimme, Semiempirical GGA-Type Density Functional Constructed with a Long-Range Dispersion Correction, *J. Comput. Chem.*, **27**, 1787–1799 (2006). (Cited on page 153.)

[Gro05] F. d. Groot, Multiplet effects in X-ray spectroscopy, *Coord. Chem. Rev.*, **249**, 31–63 (2005). (Cited on page 21.)

[Gro11] L. Gross, N. Moll, F. Mohn, A. Curioni, G. Meyer, F. Hanke, and M. Persson, High-Resolution Molecular Orbital Imaging Using a *p*-Wave STM Tip, *Phys. Rev. Lett.*, **107**, 086101 (2011). (Cited on page 95.)

[Gui08] G. Gui, J. Li, and J. Zhong, Band structure engineering of graphene by strain: First-principles calculations, *Phys. Rev. B*, **78**, 075435 (2008). (Cited on page 123.)

[Gun66] K. H. Gundlach, Zur Berechnung des Tunnelstroms durch eine Trapezförmige Potentialstufe, *Solid-State Electron.*, **9**, 949–957 (1966). (Cited on page 73.)

[Haa34] W. J. de Haas, J. de Boer, and G. J. van dën Berg, The electrical resistance of gold, copper and lead at low temperatures, *Physica*, **1**, 1115–1124 (1934). (Cited on page 114.)

[Ham37] H. C. Hamaker, The London-Van der Waals attraction between spherical particles, *Physica*, **4**, 1058–1072 (1937). (Cited on page 14.)

[Ham89] R. J. Hamers, Atomic-Resolution Surface Spectroscopy with the Scanning Tunneling Microscope, *Annu. Rev. Phys. Chem.*, **40**, 531–559 (1989). (Cited on page 12.)

[Ham01] R. J. Hamers and D. F. Padowitz, *Scanning Probe Microscopy and Spectroscopy*. Wiley-VCH, (2001). (Cited on page 12.)

[Ham14] I. Hamada, van der Waals Density Functional Made Accurate, *Phys. Rev. B*, **89**, 121103 (2014). (Cited on pages 59 and 153.)

[Han13] G. H. Han, J. A. Rodríguez-Manzo, C.-W. Lee, N. J. Kybert, M. B. Lerner, Z. J. Qi, E. N. Dattoli, A. M. Rappe, M. Drndic, and A. T. C. Johnson, Continuous growth of hexagonal graphene and boron nitride in-plane heterostructures by atmospheric pressure chemical vapor deposition, *ACS Nano*, **7**, 10129–10138 (2013). (Cited on page 124.)

[Har85] F. R. Hartley, *Supported Metal Complexes: A New Generation of Catalysts*, volume 6 of *Catalysis by Metal Complexes, 0920-4652*. Springer Netherlands, Dordrecht, (1985). (Cited on page 85.)

[Hau05] A. Hauschild, K. Karki, B. C. C. Cowie, M. Rohlfing, F. S. Tautz, and M. Sokolowski, Molecular Distortions and Chemical Bonding of a Large π-Conjugated Molecule on a Metal Surface, *Phys. Rev. Lett.*, **94**, 036106 (2005). (Cited on page 88.)

[He17a] Y. He, *Bottom-Up Construction and Direct Characterization of Porphyrin- and Graphene-Based Nanostructures*, PhD thesis, Technische Universität München (2017). (Cited on pages 35 and 141.)

[He17b] Y. He, M. Garnica, F. Bischoff, J. Ducke, M.-L. Bocquet, M. Batzill, W. Auwärter, and J. V. Barth, Fusing Tetrapyrroles to Graphene Edges by Surface-Assisted Covalent Coupling, *Nat. Chem.*, **9**, 33–38 (2017). (Cited on pages 2 and 141.)

[Hei04] A. J. Heinrich, J. A. Gupta, C. P. Lutz, and D. M. Eigler, Single-atom spin-flip spectroscopy, *Science*, **306**, 466–469 (2004). (Cited on page 8.)

[Hei10a] D. Heim, D. Écija, K. Seufert, W. Auwärter, C. Aurisicchio, C. Fabbro, D. Bonifazi, and J. V. Barth, Self-assembly of flexible one-dimensional coordination polymers on metal surfaces, *J. Am. Chem. Soc.*, **132**, 6783–6790 (2010). (Cited on pages 136 and 137.)

[Hei10b] D. Heim, K. Seufert, W. Auwärter, C. Aurisicchio, C. Fabbro, D. Bonifazi, and J. V. Barth, Surface-assisted assembly of discrete porphyrin-based cyclic supramolecules, *Nano Lett.*, **10**, 122–128 (2010). (Cited on pages 136 and 137.)

[Hei10c] B. W. Heinrich, C. Iacovita, T. Brumme, D.-J. Choi, L. Limot, M. V. Rastei, W. A. Hofer, J. Kortus, and J.-P. Bucher, Direct Observation of the Tunneling Channels of a Chemisorbed Molecule, *J. Phys. Chem. Lett.*, **1**, 1517–1523 (2010). (Cited on page 95.)

[Hen94] M. Henzler and W. Göpel, *Oberflächenphysik des Festkörpers*. Vieweg+Teubner Verlag, Wiesbaden, (1994). (Cited on page 33.)

[Hen11] N. Henningsen, R. Rurali, C. Limbach, R. Drost, J. I. Pascual, and K. J. Franke, Site-Dependent Coordination Bonding in Self-Assembled Metal-Organic Networks, *J. Phys. Chem. Lett.*, **2**, 55–61 (2011). (Cited on pages 113 and 114.)

[Her87] H. Hertz, Über einen Einfluss des ultravioletten Lichtes auf die electrische Entladung, *Ann. Phys.*, **267**, 983–1000 (1887). (Cited on page 16.)

[Her13] C. F. Hermanns, K. Tarafder, M. Bernien, A. Krüger, Y.-M. Chang, P. M. Oppeneer, and W. Kuch, Magnetic coupling of porphyrin molecules through graphene, *Adv. Mater.*, **25**, 3473–3477 (2013). (Cited on page 108.)

[Her14] T. Herden, M. Ternes, and K. Kern, Lateral and Vertical Stiffness of the Epitaxial h-BN Monolayer on Rh(111), *Nano Lett.*, **14**, 3623–3627 (2014). (Cited on page 68.)

[Hes07] R. Hesse, P. Streubel, and R. Szargan, Product or sum: Comparative tests of Voigt, and product or sum of Gaussian and Lorentzian functions in the fitting of synthetic Voigt-based X-ray photoelectron spectra, *Surf. Interface Anal.*, **39**, 381–391 (2007). (Cited on pages 22 and 152.)

[Hie11] W. Hieringer, K. Flechtner, A. Kretschmann, K. Seufert, W. Auwärter, J. V. Barth, A. Görling, H.-P. Steinrück, and J. M. Gottfried, The Surface Trans Effect: Influence of Axial Ligands on the Surface Chemical Bonds of Adsorbed Metalloporphyrins, *J. Am. Chem. Soc.*, **133**, 6206–6222 (2011). (Cited on pages 98 and 122.)

[Hir06] C. F. Hirjibehedin, C. P. Lutz, and A. J. Heinrich, Spin coupling in engineered atomic structures, *Science*, **312**, 1021–1024 (2006). (Cited on page 99.)

[Hof03] W. A. Hofer, A. S. Foster, and A. L. Shluger, Theories of scanning probe microscopes at the atomic scale, *Rev. Mod. Phys.*, **75**, 1287–1331 (2003). (Cited on page 9.)

[Hol15] S. M. Hollen, G. A. Gambrel, S. J. Tjung, N. M. Santagata, E. Johnston-Halperin, and J. A. Gupta, Modification of electronic surface states by graphene islands on Cu(111), *Phys. Rev. B*, **91**, 195425 (2015). (Cited on page 71.)

[Hou15] T. Houwaart, T. Le Bahers, P. Sautet, W. Auwärter, K. Seufert, J. V. Barth, and M.-L. Bocquet, Scrutinizing Individual CoTPP Molecule Adsorbed on Coinage Metal Surfaces from the Interplay of STM Experiment and Theory, *Surf. Sci.*, **635**, 108–114 (2015). (Cited on page 122.)

[Höv01] H. Hövel, B. Grimm, and B. Reihl, Modification of the Shockley-type surface state on Ag(111) by an adsorbed xenon layer, *Surf. Sci.*, **477**, 43–49 (2001). (Cited on page 71.)

[Hüf10] S. Hüfner, *Photoelectron spectroscopy: Principles and applications*, Advanced Texts in Physics. Springer, Berlin and New York, 3rd ed. edition, (2010). (Cited on pages 16, 17, 19, and 42.)

[Hun07] J. D. Hunter, Matplotlib: A 2D Graphics Environment, *Comput. Sci. Eng.*, **9**, 90–95 (2007). (Cited on page 161.)

[Hwa16] B. Hwang, J. Hwang, J. K. Yoon, S. Lim, S. Kim, M. Lee, J. H. Kwon, H. Baek, D. Sung, G. Kim, S. Hong, J. Ihm, J. A. Stroscio, and Y. Kuk, Energy Bandgap and Edge States in an Epitaxially Grown Graphene/h-BN Heterostructure, *Sci. Rep.*, **6**, 31160 (2016). (Cited on page 55.)

[I0917] I09 Beamline, Diamond Light Source, Didcot, Oxfordshire, OX11 0DE, United Kingdom (2017), `http://www.diamond.ac.uk/Beamlines/Surfaces-and-Interfaces/I09.html`, (Accessed: 2017-02-12). (Cited on pages 49 and 51.)

[Ian06a] V. Iancu, A. Deshpande, and S.-W. Hla, Manipulating Kondo temperature via single molecule switching, *Nano Lett.*, **6**, 820–823 (2006). (Cited on pages 114 and 116.)

[Ian06b] V. Iancu, A. Deshpande, and S.-W. Hla, Manipulation of the Kondo effect via two-dimensional molecular assembly, *Phys. Rev. Lett.*, **97**, 266603 (2006). (Cited on page 114.)

[Ian14] M. Iannuzzi, F. Tran, R. Widmer, T. Dienel, K. Radican, Y. Ding, J. Hutter, and O. Gröning, Site-selective adsorption of phthalocyanine on h-BN/Rh(111) nanomesh, *Phys. Chem. Chem. Phys.*, **16**, 12374–12384 (2014). (Cited on pages 104 and 106.)

[Iij91] S. Iijima, Helical microtubules of graphitic carbon, *Nature*, **354**, 56–58 (1991). (Cited on page 1.)

[Isr11] J. N. Israelachvili, *Intermolecular and surface forces*. Academic Press, Burlington MA, 3rd ed. edition, (2011). (Cited on page 14.)

[ite17] item Industrietechnik GmbH, Friedenstrasse 107-109, 42699 Solingen, Germany (2017), `http://www.item24.de`, (Accessed: 2017-02-17). (Cited on page 36.)

[Jac11] K. T. Jackson, M. G. Rabbani, T. E. Reich, and H. M. El-Kaderi, Synthesis of highly porous borazine-linked polymers and their application to H_2, CO_2, and CH_4 storage, *Polym. Chem.*, **2**, 2775 (2011). (Cited on page 128.)

[Jac15] P. Jacobson, T. Herden, M. Muenks, G. Laskin, O. Brovko, V. Stepanyuk, M. Ternes, and K. Kern, Quantum Engineering of Spin and Anisotropy in Magnetic Molecular Junctions, *Nat. Commun.*, **6**, 8536 (2015). (Cited on pages 56, 118, and 121.)

[Jah12] M. Jahan, Q. Bao, and K. P. Loh, Electrocatalytically active graphene-porphyrin MOF composite for oxygen reduction reaction, *J. Am. Chem. Soc.*, **134**, 6707–6713 (2012). (Cited on page 107.)

[Jam62] R. W. James and W. L. Bragg, *The optical principles of the diffraction of x-rays*. G. Bell & Sons, London, (1962). (Cited on page 24.)

[Jär13] P. Järvinen, S. K. Hämäläinen, K. Banerjee, P. Häkkinen, M. Ijäs, A. Harju, and P. Liljeroth, Molecular self-assembly on graphene on SiO_2 and h-BN substrates, *Nano Lett.*, **13**, 3199–3204 (2013). (Cited on page 109.)

[Jär14] P. Järvinen, S. K. Hämäläinen, M. Ijäs, A. Harju, and P. Liljeroth, Self-Assembly and Orbital Imaging of Metal Phthalocyanines on a Graphene Model Surface, *J. Phys. Chem. C*, **118**, 13320–13325 (2014). (Cited on page 109.)

[Jel17] P. Jelínek, High Resolution SPM Imaging of Organic Molecules with Functionalized Tips, *J. Phys. Cond. Matter*, **29**, 343002 (2017). (Cited on page 94.)

[Jia11] Y. Jiang, Y. N. Zhang, J. X. Cao, R. Q. Wu, and W. Ho, Real-space imaging of Kondo screening in a two-dimensional O_2 lattice, *Science*, **333**, 324–328 (2011). (Cited on page 114.)

[Jol15] W. Jolie, F. Craes, and C. Busse, Graphene on weakly interacting metals: Dirac states versus surface states, *Phys. Rev. B*, **91**, 115419 (2015). (Cited on pages 71 and 78.)

[Jon1] E. Jones, E. Oliphant, and P. Peterson, SciPy: Open Source Scientific Tools for Python (2001-). (Cited on page 161.)

[Jos12] S. Joshi, D. Écija, R. Koitz, M. Iannuzzi, A. P. Seitsonen, J. Hutter, H. Sachdev, S. Vijayaraghavan, F. Bischoff, K. Seufert, J. V. Barth, and W. Auwärter, Boron nitride on Cu(111): an electronically corrugated monolayer, *Nano Lett.*, **12**, 5821–5828 (2012). (Cited on pages 48, 56, 57, 58, 59, 70, 71, 73, 82, 101, 105, 107, and 108.)

[Jos14] S. Joshi, F. Bischoff, R. Koitz, D. Écija, K. Seufert, A. P. Seitsonen, J. Hutter, K. Diller, J. I. Urgel, H. Sachdev, J. V. Barth, and W. Auwärter, Control of molecular organization and energy level alignment by an electronically nanopatterned boron nitride template, *ACS Nano*, **8**, 430–442 (2014). (Cited on pages 8, 11, 56, 58, 99, 105, 108, 109, and 111.)

[Jos17] S. Joshi, *Hexagonal Boron Nitride Monolayers as Templates for Molecular Nanostructures*, PhD thesis, Technische Universität München (2017). (Cited on pages 57, 58, and 70.)

[Kad03] K. M. Kadish, K. M. Smith, and R. Guilard, *The Porphyrin Handbook*. Academic Press, San Diego (Calif.) and London and Sydney, (2003). (Cited on page 86.)

[Kal98] K. Kalyanasundaram, Applications of Functionalized Transition Metal Complexes in Photonic and Optoelectronic Devices, *Coord. Chem. Rev.*, **177**, 347–414 (1998). (Cited on page 85.)

[Kal14] N. Kalashnyk, P. Ganesh Nagaswaran, S. Kervyn, M. Riello, B. Moreton, T. S. Jones, A. de Vita, D. Bonifazi, and G. Costantini, Self-assembly of decoupled borazines on metal surfaces: the role of the peripheral groups, *Chem. - Eur. J.*, **20**, 11856–11862 (2014). (Cited on pages 128, 130, and 137.)

[Kan04] L. N. Kantorovich and T. Trevethan, General Theory of Microscopic Dynamical Response in Surface Probe Microscopy: From Imaging to Dissipation, *Phys. Rev. Lett.*, **93**, 236102 (2004). (Cited on pages 14 and 68.)

[Kan15] K. Kanazawa, M. Nakamura, H. Huang, A. Taninaka, and H. Shigekawa, Variation in Anisotropic Dispersion Relations of Self-Assembled Monolayer on Cu(001) Induced by Modulation of Molecular Structures, *Surf. Sci.*, **632**, L1–L4 (2015). (Cited on page 71.)

[Kar14] P. Karamanis, N. Otero, and C. Pouchan, Unleashing the Quadratic Nonlinear Optical Responses of Graphene by Confining White-Graphene (h-BN) Sections in its Framework, *J. Am. Chem. Soc.*, **136**, 7464–7473 (2014). (Cited on page 128.)

[Kat17] KatChem, E. Krasnohorske 6, 110 00 Praha 1, Czech Republic (2017), `http://www.katchem.cz/en/`, (Accessed: 2017-02-28). (Cited on pages 46 and 147.)

[Kei17] B. Keimer and J. E. Moore, The Physics of Quantum Materials, *Nat. Phys.*, **13**, 1045–1055 (2017). (Cited on page 142.)

[Ker92a] Kerkar, Fisher, Woodruff, Jones, Diehl, and Cowie, Structural study of alkali/simple metal adsorption: Rb and Na on Al(111), *Phys. Rev. Lett.*, **68**, 3204–3207 (1992). (Cited on page 32.)

[Ker92b] M. Kerkar, D. Fisher, D. P. Woodruff, and B. Cowie, Adsorption site determination for oxygen on Al(111) using normal incidence standing X-ray wavefield absorption, *Surf. Sci.*, **271**, 45–56 (1992). (Cited on page 32.)

[Ker92c] M. Kerkar, A. B. Hayden, D. P. Woodruff, M. Kadodwala, and R. G. Jones, An unusual adsorption site for methoxy on Al(111) surfaces, *J. Phys. Cond. Matter*, **4**, 5043–5052 (1992). (Cited on page 32.)

[Ker92d] M. Kerkar, D. P. Woodruff, J. Avila, M. C. Asensio, M. Fernandez-Garcia, and J. C. Conesa, Structure determination for PF_3 absorption on Ni(111), *J. Phys. Cond. Matter*, **4**, 6509–6522 (1992). (Cited on page 32.)

[Ker13a] S. Kervyn, O. Fenwick, F. Di Stasio, Y. S. Shin, J. Wouters, G. Accorsi, S. Osella, D. Beljonne, F. Cacialli, and D. Bonifazi, Polymorphism, fluorescence, and optoelectronic properties of a borazine derivative, *Chem. - Eur. J.*, **19**, 7771–7779 (2013). (Cited on page 128.)

[Ker13b] S. Kervyn, N. Kalashnyk, M. Riello, B. Moreton, J. Tasseroul, J. Wouters, T. S. Jones, A. de Vita, G. Costantini, and D. Bonifazi, Magic surface clustering of borazines driven by repulsive intermolecular forces, *Angew. Chem., Int. Ed. Engl.*, **52**, 7410–7414 (2013). (Cited on page 128.)

[Kev87] S. D. Kevan and R. H. Gaylord, High-resolution photoemission study of the electronic structure of the noble-metal (111) surfaces, *Phys. Rev. B*, **36**, 5809–5818 (1987). (Cited on page 48.)

[Kil13] K. J. Kilpin and P. J. Dyson, Enzyme Inhibition by Metal Complexes: Concepts, Strategies and Applications, *Chem. Sci.*, **4**, 1410 (2013). (Cited on page 85.)

[Kim12] K. K. Kim, A. Hsu, X. Jia, S. M. Kim, Y. Shi, M. Hofmann, D. Nezich, J. F. Rodriguez-Nieva, M. Dresselhaus, T. Palacios, and J. Kong, Synthesis of monolayer hexagonal boron nitride on Cu foil using chemical vapor deposition, *Nano Lett.*, **12**, 161–166 (2012). (Cited on pages 55, 56, 108, and 124.)

[Kim13] S. M. Kim, A. Hsu, P. T. Araujo, Y.-H. Lee, T. Palacios, M. Dresselhaus, J.-C. Idrobo, K. K. Kim, and J. Kong, Synthesis of patched or stacked graphene and

hBN flakes: A route to hybrid structure discovery, *Nano Lett.*, **13**, 933–941 (2013). (Cited on page 106.)

[Kim14] J. Kim, C. Bayram, H. Park, C.-W. Cheng, C. Dimitrakopoulos, J. A. Ott, K. B. Reuter, S. W. Bedell, and D. K. Sadana, Principle of direct van der Waals epitaxy of single-crystalline films on epitaxial graphene, *Nat. Commun.*, **5**, 4836 (2014). (Cited on page 2.)

[Kla08] F. Klappenberger, A. Weber-Bargioni, W. Auwärter, M. Marschall, A. Schiffrin, and J. V. Barth, Temperature dependence of conformation, chemical state, and metal-directed assembly of tetrapyridyl-porphyrin on Cu(111), *J. Chem. Phys.*, **129**, 214702 (2008). (Cited on pages 136 and 137.)

[Kli00] J. Kliewer, Dimensionality Effects in the Lifetime of Surface States, *Science*, **288**, 1399–1402 (2000). (Cited on page 73.)

[Kli11] J. Klimeš, D. R. Bowler, and A. Michaelides, Van der Waals Density Functionals Applied to Solids, *Phys. Rev. B*, **83**, 195131 (2011). (Cited on pages 59 and 153.)

[Kno02] N. Knorr, M. A. Schneider, L. Diekhöner, P. Wahl, and K. Kern, Kondo effect of single Co adatoms on Cu surfaces, *Phys. Rev. Lett.*, **88**, 096804 (2002). (Cited on pages 114, 117, and 118.)

[Koc07] N. Koch, Organic Electronic Devices and their Functional Interfaces, *ChemPhysChem*, **8**, 1438–1455 (2007). (Cited on page 86.)

[Koe16] J. C. Koepke, J. D. Wood, Y. Chen, S. W. Schmucker, X. Liu, N. N. Chang, L. Nienhaus, J. W. Do, E. A. Carrion, J. Hewaparakrama, A. Rangarajan, I. Datye, R. Mehta, R. T. Haasch, M. Gruebele, G. S. Girolami, E. Pop, and J. W. Lyding, Role of Pressure in the Growth of Hexagonal Boron Nitride Thin Films from Ammonia-Borane, *Chem. Mater.*, **28**, 4169–4179 (2016). (Cited on pages 63, 66, and 67.)

[Koi13] R. Koitz, A. P. Seitsonen, M. Iannuzzi, and J. Hutter, Structural and Electronic Properties of a Large-Scale Moire Pattern of Hexagonal Boron Nitride on Cu(111) Studied with Density Functional Theory, *Nanoscale*, **5**, 5589–5595 (2013). (Cited on pages 56, 106, and 154.)

[Kol00] O. Kolesnychenko, Y. Kolesnichenko, O. I. Shklyarevskii, and H. van Kempen, Field-emission resonance measurements with mechanically controlled break junctions, *Phys. B*, **291**, 246–255 (2000). (Cited on page 74.)

[Kom14] T. Komeda, Spins of adsorbed molecules investigated by the detection of Kondo resonance, *Surf. Sci.*, **630**, 343–355 (2014). (Cited on pages 98, 114, and 115.)

[Kon64] J. Kondo, Resistance Minimum in Dilute Magnetic Alloys, *Prog. Theor. Phys.*, **32**, 37–49 (1964). (Cited on page 114.)

[Kön15] M. König, *Scanning Probe Microscopy of size-selected, supported clusters: The cluster-support interaction*, PhD thesis, Technische Universität München (2015). (Cited on page 147.)

[Kor15] V. V. Korolkov, S. A. Svatek, A. Summerfield, J. Kerfoot, L. Yang, T. Taniguchi, K. Watanabe, N. R. Champness, N. A. Besley, and P. H. Beton, van der Waals-Induced Chromatic Shifts in Hydrogen-Bonded Two-Dimensional Porphyrin Ar-

rays on Boron Nitride, *ACS Nano*, **9**, 10347–10355 (2015). (Cited on pages 99 and 104.)

[Kou01] L. Kouwenhoven and L. Glazman, Revival of the Kondo effect, *Phys. World*, **14**, 33–38 (2001). (Cited on pages 114 and 115.)

[Kra79] M. O. Krause and J. H. Oliver, Natural widths of atomic K and L levels, K_α X–ray lines and several KLL Auger lines, *J. Phys. Chem. Ref. Data*, **8**, 329–338 (1979). (Cited on page 40.)

[Kre96] G. Kresse and J. Furthmüller, Efficient Iterative Schemes for Ab Initio Total-Energy Calculations Using a Plane-Wave Basis Set, *Phys. Rev. B*, **54**, 11169–11186 (1996). (Cited on page 153.)

[Kri15] M. Krieg, F. Reicherter, P. Haiss, M. Ströbele, K. Eichele, M.-J. Treanor, R. Schaub, and H. F. Bettinger, Construction of an Internally B_3N_3-Doped Nanographene Molecule, *Angew. Chem., Int. Ed. Engl.*, **54**, 8284–8286 (2015). (Cited on page 128.)

[Kro85] H. W. Kroto, J. R. Heath, S. C. O'Brien, R. F. Curl, and R. E. Smalley, C_{60}: Buckminsterfullerene, *Nature*, **318**, 162–163 (1985). (Cited on page 1.)

[Krö11] I. Kröger, B. Stadtmüller, C. Kleimann, P. Rajput, and C. Kumpf, Normal-Incidence X-ray Standing-Wave Study of Copper Phthalocyanine Submonolayers on Cu(111) and Au(111), *Phys. Rev. B*, **83**, 195414 (2011). (Cited on pages 24 and 88.)

[Krö16] I. Kröger, B. Stadtmüller, and C. Kumpf, Submonolayer and Multilayer Growth of Titaniumoxide-Phthalocyanine on Ag(111), *New J. Phys.*, **18**, 113022 (2016). (Cited on page 88.)

[Küh09] D. Kühne, F. Klappenberger, R. Decker, U. Schlickum, H. Brune, S. Klyatskaya, M. Ruben, and J. V. Barth, High-quality 2D metal-organic coordination network providing giant cavities within mesoscale domains, *J. Am. Chem. Soc.*, **131**, 3881–3883 (2009). (Cited on page 113.)

[Kum17] A. Kumar, K. Banerjee, and P. Liljeroth, Molecular Assembly on Two-Dimensional Materials, *Nanotechnology*, **28**, 082001 (2017). (Cited on pages 1, 2, 56, and 99.)

[La 16] B. de La Torre, M. Ellner, P. Pou, N. Nicoara, R. Perez, and J. M. Gómez-Rodríguez, Atomic-Scale Variations of the Mechanical Response of 2D Materials Detected by Noncontact Atomic Force Microscopy, *Phys. Rev. Lett.*, **116**, 245502 (2016). (Cited on pages 14 and 68.)

[Lan08] A. Langner, S. L. Tait, N. Lin, R. Chandrasekar, M. Ruben, and K. Kern, Ordering and stabilization of metal-organic coordination chains by hierarchical assembly through hydrogen bonding at a surface, *Angew. Chem., Int. Ed. Engl.*, **47**, 8835–8838 (2008). (Cited on pages 136 and 137.)

[Lan12] A. Langner, S. L. Tait, N. Lin, R. Chandrasekar, V. Meded, K. Fink, M. Ruben, and K. Kern, Selective coordination bonding in metallo-supramolecular systems on surfaces, *Angew. Chem., Int. Ed. Engl.*, **51**, 4327–4331 (2012). (Cited on page 137.)

[Las08] R. Laskowski, P. Blaha, and K. Schwarz, Bonding of hexagonal BN to transition metal surfaces: An ab initio density-functional theory study, *Phys. Rev. B*, **78**, 45409 (2008). (Cited on pages 56 and 76.)

[Lee01] J. J. Lee, C. J. Fisher, D. P. Woodruff, M. G. Roper, R. G. Jones, and B. Cowie, Non-dipole effects in photoelectron-monitored X-ray standing wave experiments: Characterisation and calibration, *Surf. Sci.*, **494**, 166–182 (2001). (Cited on page 31.)

[Lee10] K. Lee, É. D. Murray, L. Kong, B. I. Lundqvist, and D. C. Langreth, Higher-Accuracy van der Waals Density Functional, *Phys. Rev. B*, **82**, 081101 (2010). (Cited on pages 59 and 153.)

[Lee13] J.-H. Lee, Y.-K. Choi, H.-J. Kim, R. H. Scheicher, and J.-H. Cho, Physisorption of DNA Nucleobases on h-BN and Graphene: VdW-Corrected DFT Calculations, *J. Phys. Chem. C*, **117**, 13435–13441 (2013). (Cited on page 99.)

[Lee14] C.-H. Lee, G.-H. Lee, A. M. van der Zande, W. Chen, Y. Li, M. Han, X. Cui, G. Arefe, C. Nuckolls, T. F. Heinz, J. Guo, J. Hone, and P. Kim, Atomically thin p-n junctions with van der Waals heterointerfaces, *Nat. Nanotechnol.*, **9**, 676–681 (2014). (Cited on page 123.)

[Lee17a] T. H. Lee, K. Kim, G. Kim, H. J. Park, D. Scullion, L. Shaw, M.-G. Kim, X. Gu, W.-G. Bae, E. J. G. Santos, Z. Lee, H. S. Shin, Y. Nishi, and Z. Bao, Chemical Vapor-Deposited Hexagonal Boron Nitride as a Scalable Template for High-Performance Organic Field-Effect Transistors, *Chem. Mater.*, **29**, 2341–2347 (2017). (Cited on page 53.)

[Lee17b] T.-L. Lee and F. Yuan, I09 Technical Documentation: Basic Analyzer Scans (2017), `http://confluence.diamond.ac.uk/display/I09Tesc/Basic+Analyzer+Scans`, (Accessed: 2017-06-19). (Cited on page 56.)

[Lei14] P. Leicht, L. Zielke, S. Bouvron, R. Moroni, E. Voloshina, L. Hammerschmidt, Y. S. Dedkov, and M. Fonin, In situ fabrication of quasi-free-standing epitaxial graphene nanoflakes on gold, *ACS Nano*, **8**, 3735–3742 (2014). (Cited on page 71.)

[Leo17] P. Leone, *Characterization of Cu, Ag and h-BN interfaces by scanning probe microscopy*, Bachelor thesis, Technische Universität München (2017). (Cited on pages 81 and 83.)

[Lep17] M. Lepper, J. Köbl, T. Schmitt, M. Gurrath, A. de Siervo, M. A. Schneider, H.-P. Steinrück, B. Meyer, H. Marbach, and W. Hieringer, Inverted Porphyrins: A Distorted Adsorption Geometry of Free-Base Porphyrins on Cu(111), *Chem. Commun.*, **53**, 8207–8210 (2017). (Cited on page 87.)

[Leu06] K. Leung, S. B. Rempe, P. A. Schultz, E. M. Sproviero, V. S. Batista, M. E. Chandross, and C. J. Medforth, Density Functional Theory and DFT+U Study of Transition Metal Porphines Adsorbed on Au(111) Surfaces and Effects of Applied Electric Fields, *J. Am. Chem. Soc.*, **128**, 3659–3668 (2006). (Cited on page 87.)

[Lev12] M. P. Levendorf, C.-J. Kim, L. Brown, P. Y. Huang, R. W. Havener, D. A. Muller, and J. Park, Graphene and boron nitride lateral heterostructures for atomically thin circuitry, *Nature*, **488**, 627–632 (2012). (Cited on pages 123, 124, and 141.)

[Ley17] Leybold GmbH, Bonner Str. 498, 50968 Köln, Germany (2017), `https://www.leybold.com/de/`, (Accessed: 2017-02-05). (Cited on page 36.)

[Li98] J. Li, W.-D. Schneider, R. Berndt, and B. Delley, Kondo Scattering Observed at a Single Magnetic Impurity, *Phys. Rev. Lett.*, **80**, 2893–2896 (1998). (Cited on pages 73 and 114.)

[Li04] B. Li, J. Li, Y. Fu, and Z. Bo, Porphyrins with Four Monodisperse Oligofluorene Arms as Efficient Red Light-Emitting Materials, *J. Am. Chem. Soc.*, **126**, 3430–3431 (2004). (Cited on page 1.)

[Li08] X. Li, X. Wang, L. Zhang, S. Lee, and H. Dai, Chemically derived, ultrasmooth graphene nanoribbon semiconductors, *Science*, **319**, 1229–1232 (2008). (Cited on page 123.)

[Li09] H. I. Li, K. Pussi, K. J. Hanna, L.-L. Wang, D. D. Johnson, H.-P. Cheng, H. Shin, S. Curtarolo, W. Moritz, J. A. Smerdon, R. McGrath, and R. D. Diehl, Surface geometry of C_{60} on Ag(111), *Phys. Rev. Lett.*, **103**, 056101 (2009). (Cited on page 81.)

[Li11] Y. Li and N. Lin, Combined scanning tunneling microscopy and kinetic Monte Carlo study on kinetics of Cu-coordinated pyridyl-porphyrin supramolecular self-assembly on a Au(111) surface, *Phys. Rev. B*, **84**, 125418 (2011). (Cited on pages 136 and 137.)

[Li12] Y. Li, J. Xiao, T. E. Shubina, M. Chen, Z. Shi, M. Schmid, H.-P. Steinrück, J. M. Gottfried, and N. Lin, Coordination and metalation bifunctionality of Cu with 5,10,15,20-tetra(4-pyridyl)porphyrin: toward a mixed-valence two-dimensional coordination network, *J. Am. Chem. Soc.*, **134**, 6401–6408 (2012). (Cited on pages 114, 136, and 137.)

[Li15] Q. Li, X. Zou, M. Liu, J. Sun, Y. Gao, Y. Qi, X. Zhou, B. I. Yakobson, Y. Zhang, and Z. Liu, Grain Boundary Structures and Electronic Properties of Hexagonal Boron Nitride on Cu(111), *Nano Lett.*, **15**, 5804–5810 (2015). (Cited on page 58.)

[Lim14] H. Lim, S. I. Yoon, G. Kim, A.-R. Jang, and H. S. Shin, Stacking of Two-Dimensional Materials in Lateral and Vertical Directions, *Chem. Mater.*, **26**, 4891–4903 (2014). (Cited on page 123.)

[Lin13] X. Lin, Y. Xu, A. A. Hakro, T. Hasan, R. Hao, B. Zhang, and H. Chen, Ab Initio Optical Study of Graphene on Hexagonal Boron Nitride and Fluorographene Substrates, *J. Mater. Chem. C*, **1**, 1618 (2013). (Cited on pages 70, 136, and 137.)

[Lin15] S. Lin, J. Huang, and X. Gao, A Cu(111) Supported h-BN Nanosheet: A Potential Low-Cost and High-Performance Catalyst for CO Oxidation, *Phys. Chem. Chem. Phys.*, **17**, 22097–22105 (2015). (Cited on page 56.)

[Liu03] L. Liu, Y. P. Feng, and Z. X. Shen, Structural and electronic properties of h-BN, *Phys. Rev. B*, **68**, 104102 (2003). (Cited on page 1.)

[Liu08] Z. Liu and T. B. Marder, B-N versus C-C: How similar are they?, *Angew. Chem., Int. Ed. Engl.*, **47**, 242–244 (2008). (Cited on page 128.)

[Liu11] H. Liu, Y. Liu, and D. Zhu, Chemical doping of graphene, *J. Mater. Chem.*, **21**, 3335–3345 (2011). (Cited on page 124.)

[Liu13] Z. Liu, L. Ma, G. Shi, W. Zhou, Y. Gong, S. Lei, X. Yang, J. Zhang, J. Yu, K. P. Hackenberg, A. Babakhani, J.-C. Idrobo, R. Vajtai, J. Lou, and P. M. Ajayan,

In-plane heterostructures of graphene and hexagonal boron nitride with controlled domain sizes, *Nat. Nanotechnol.*, **8**, 119–124 (2013). (Cited on pages 124 and 141.)

[Liu14a] L. Liu, J. Park, D. A. Siegel, K. F. McCarty, K. W. Clark, W. Deng, L. Basile, J. C. Idrobo, A.-P. Li, and G. Gu, Heteroepitaxial growth of two-dimensional hexagonal boron nitride templated by graphene edges, *Science*, **343**, 163–167 (2014). (Cited on page 124.)

[Liu14b] M. Liu, Y. Li, P. Chen, J. Sun, D. Ma, Q. Li, T. Gao, Y. Gao, Z. Cheng, X. Qiu, Y. Fang, Y. Zhang, and Z. Liu, Quasi-freestanding monolayer heterostructure of graphene and hexagonal boron nitride on Ir(111) with a zigzag boundary, *Nano Lett.*, **14**, 6342–6347 (2014). (Cited on pages 124, 125, and 127.)

[Lor16] T. Lorenz, A. Lik, F. A. Plamper, and H. Helten, Dehydrocoupling and Silazane Cleavage Routes to Organic-Inorganic Hybrid Polymers with NBN Units in the Main Chain, *Angew. Chem., Int. Ed. Engl.*, **55**, 7236–7241 (2016). (Cited on page 128.)

[Lor17] M. M. Lorenzo-García and D. Bonifazi, Renaissance of an Old Topic: From Borazines to BN-doped Nanographenes, *Chimia*, **71**, 550–557 (2017). (Cited on pages 128 and 138.)

[Lu13] J. Lu, K. Zhang, X. F. Liu, H. Zhang, T. C. Sum, A. H. Castro Neto, and K. P. Loh, Order-disorder transition in a two-dimensional boron-carbon-nitride alloy, *Nat. Commun.*, **4**, 2681 (2013). (Cited on pages 125, 126, and 127.)

[Lu14] J. Lu, L. C. Gomes, R. W. Nunes, A. H. Castro Neto, and K. P. Loh, Lattice relaxation at the interface of two-dimensional crystals: Graphene and hexagonal boron-nitride, *Nano Lett.*, **14**, 5133–5139 (2014). (Cited on page 124.)

[Luk07] T. Lukasczyk, K. Flechtner, L. R. Merte, N. Jux, F. Maier, J. M. Gottfried, and H.-P. Steinrück, Interaction of Cobalt(II) Tetraarylporphyrins with a Ag(111) Surface Studied with Photoelectron Spectroscopy, *J. Phys. Chem. C*, **111**, 3090–3098 (2007). (Cited on pages 90, 98, 101, and 114.)

[Lya14] A. Lyalin, A. Nakayama, K. Uosaki, and T. Taketsugu, Adsorption and Catalytic Activation of the Molecular Oxygen on the Metal Supported h-BN, *Top. Catal.*, **57**, 1032–1041 (2014). (Cited on page 56.)

[Ma10] H. Ma, T. Brugger, S. Berner, Y. Ding, M. Iannuzzi, J. Hutter, J. Osterwalder, and T. Greber, Nano-ice on boron nitride nanomesh: Accessing proton disorder, *Chem. Phys. Chem.*, **11**, 399–403 (2010). (Cited on page 108.)

[Mac14a] D. Maccariello, M. Garnica, M. A. Niño, C. Navío, P. Perna, S. Barja, Vázquez de Parga, Amadeo L., and R. Miranda, Spatially Resolved, Site-Dependent Charge Transfer and Induced Magnetic Moment in TCNQ Adsorbed on Graphene, *Chem. Mater.*, **26**, 2883–2890 (2014). (Cited on page 99.)

[Mac14b] J. M. MacLeod and F. Rosei, Molecular self-assembly on graphene, *Small*, **10**, 1038–1049 (2014). (Cited on page 108.)

[Mad98] V. Madhavan, W. Chen, T. Jamneala, M. F. Crommie, and N. S. Wingreen, Tunneling into a Single Magnetic Atom: Spectroscopic Evidence of the Kondo Resonance, *Science*, **280**, 567–569 (1998). (Cited on pages 114 and 115.)

[Mah15] F. Mahvash, E. Paradis, D. Drouin, T. Szkopek, and M. Siaj, Space-Charge Limited Transport in Large-Area Monolayer Hexagonal Boron Nitride, *Nano Lett.*, **15**, 2263–2268 (2015). (Cited on page 56.)

[Mah17] F. Mahvash, S. Eissa, T. Bordjiba, A. C. Tavares, T. Szkopek, and M. Siaj, Corrosion Resistance of Monolayer Hexagonal Boron Nitride on Copper, *Sci. Rep.*, **7**, 42139 (2017). (Cited on page 56.)

[Mai08] S. Maier, L.-A. Fendt, L. Zimmerli, T. Glatzel, O. Pfeiffer, F. Diederich, and E. Meyer, Nanoscale engineering of molecular porphyrin wires on insulating surfaces, *Small*, **4**, 1115–1118 (2008). (Cited on page 108.)

[Mak10] K. F. Mak, C. Lee, J. Hone, J. Shan, and T. F. Heinz, Atomically thin MoS_2: A new direct-gap semiconductor, *Phys. Rev. Lett.*, **105**, 136805 (2010). (Cited on page 142.)

[Man00] H. C. Manoharan, C. P. Lutz, and D. M. Eigler, Quantum mirages formed by coherent projection of electronic structure, *Nature*, **403**, 512–515 (2000). (Cited on pages 114 and 118.)

[Man17] A. J. Mannix, B. Kiraly, M. C. Hersam, and N. P. Guisinger, Synthesis and chemistry of elemental 2D materials, *Nat. Rev. Chem.*, **1**, 0014 (2017). (Cited on page 2.)

[Mao09] J. Mao, H. Zhang, Y. Jiang, Y. Pan, M. Gao, W. Xiao, and H.-J. Gao, Tunability of supramolecular Kagome lattices of magnetic phthalocyanines using graphene-based moire patterns as templates, *J. Am. Chem. Soc.*, **131**, 14136–14137 (2009). (Cited on pages 108 and 109.)

[Mar10a] N. Marom, J. Bernstein, J. Garel, A. Tkatchenko, E. Joselevich, L. Kronik, and O. Hod, Stacking and Registry Effects in Layered Materials: The Case of Hexagonal Boron Nitride, *Phys. Rev. Lett.*, **105**, 046801 (2010). (Cited on page 70.)

[Mar10b] M. Marschall, J. Reichert, A. Weber-Bargioni, K. Seufert, W. Auwärter, S. Klyatskaya, G. Zoppellaro, M. Ruben, and J. V. Barth, Random two-dimensional string networks based on divergent coordination assembly, *Nat. Chem.*, **2**, 131–137 (2010). (Cited on pages 111 and 113.)

[Mar10c] D. Martoccia, M. Björck, C. M. Schlepütz, T. Brugger, S. A. Pauli, B. D. Patterson, T. Greber, and P. R. Willmott, Graphene on Ru(0001): A Corrugated and Chiral Structure, *New J. Phys.*, **12**, 043028 (2010). (Cited on page 57.)

[Mar11] A. J. Martínez-Galera, I. Brihuega, and J. M. Gómez-Rodríguez, Ethylene irradiation: A new route to grow graphene on low reactivity metals, *Nano Lett.*, **11**, 3576–3580 (2011). (Cited on page 72.)

[Mar17] D. Marinelli, F. Fasano, B. Najjari, N. Demitri, and D. Bonifazi, Borazino-Doped Polyphenylenes, *J. Am. Chem. Soc.*, **139**, 5503–5519 (2017). (Cited on page 128.)

[Mas14] L. Massimi, M. Angelucci, P. Gargiani, M. G. Betti, S. Montoro, and C. Mariani, Metal-phthalocyanine ordered layers on Au(110): Metal-dependent adsorption energy, *J. Chem. Phys.*, **140**, 244704 (2014). (Cited on page 101.)

[Mat09] L. S. d. Mattos, *Correlated electrons probed by scanning tunneling microscopy*, PhD thesis, Stanford University (2009). (Cited on page 121.)

[Mat14] S. Mathew, A. Yella, P. Gao, R. Humphry-Baker, B. F. E. Curchod, N. Ashari-Astani, I. Tavernelli, U. Rothlisberger, M. K. Nazeeruddin, and M. Grätzel, Dye-Sensitized Solar Cells with 13% Efficiency Achieved through the Molecular Engineering of Porphyrin Sensitizers, *Nat. Chem.*, **6**, 242–247 (2014). (Cited on page 1.)

[Mat16] A. Matković, J. Genser, D. Lüftner, M. Kratzer, R. Gajić, P. Puschnig, and C. Teichert, Epitaxy of highly ordered organic semiconductor crystallite networks supported by hexagonal boron nitride, *Sci. Rep.*, **6**, 38519 (2016). (Cited on page 99.)

[Mau16] R. J. Maurer, V. G. Ruiz, J. Camarillo-Cisneros, W. Liu, N. Ferri, K. Reuter, and A. Tkatchenko, Adsorption Structures and Energetics of Molecules on Metal Surfaces: Bridging Experiment and Theory, *Prog. Surf. Sci.*, **91**, 72–100 (2016). (Cited on page 87.)

[May10] J. Mayer, K. Khairy, and J. Howard, Drawing an elephant with four complex parameters, *Am. J. Phys.*, **78**, 648–649 (2010). (Cited on page 22.)

[McI02] N. S. McIntyre and M. G. Cook, X-ray photoelectron studies on some oxides and hydroxides of cobalt, nickel, and copper, *Anal. Chem.*, **47**, 2208–2213 (2002). (Cited on page 101.)

[McM92] W. E. McMahon, E. S. Hirschorn, and T.-C. Chiang, Scanning tunneling microscopy study of a Ag monolayer on Cu(111), *Surf. Sci. Lett.*, **279**, L231–L235 (1992). (Cited on page 78.)

[Men15] J. H. Meng, X. W. Zhang, H. L. Wang, X. B. Ren, C. H. Jin, Z. G. Yin, X. Liu, and H. Liu, Synthesis of in-plane and stacked graphene/hexagonal boron nitride heterostructures by combining with ion beam sputtering deposition and chemical vapor deposition, *Nanoscale*, **7**, 16046–16053 (2015). (Cited on page 124.)

[Mer13] G. Mercurio, R. J. Maurer, W. Liu, S. Hagen, F. Leyssner, P. Tegeder, J. Meyer, A. Tkatchenko, S. Soubatch, K. Reuter, and F. S. Tautz, Quantification of Finite-Temperature Effects on Adsorption Geometries of π-Conjugated Molecules: Azobenzene/Ag(111), *Phys. Rev. B*, **88**, 035421 (2013). (Cited on pages 97, 99, 107, and 140.)

[Met16] G. Mette, D. Sutter, Y. Gurdal, S. Schnidrig, B. Probst, M. Iannuzzi, J. Hutter, R. Alberto, and J. Osterwalder, From porphyrins to pyrphyrins: Adsorption study and metalation of a molecular catalyst on Au(111), *Nanoscale*, **8**, 7958–7968 (2016). (Cited on page 101.)

[Meu92] B. Meunier, Metalloporphyrins as versatile catalysts for oxidation reactions and oxidative DNA cleavage, *Chem. Rev.*, **92**, 1411–1456 (1992). (Cited on page 1.)

[Mey96a] G. Meyer, A simple low-temperature ultrahigh-vacuum scanning tunneling microscope capable of atomic manipulation, *Rev. Sci. Instrum.*, **67**, 2960–2965 (1996). (Cited on page 35.)

[Mey96b] G. Meyer, S. Zöphel, and K.-H. Rieder, Scanning Tunneling Microscopy Manipulation of Native Substrate Atoms: A New Way to Obtain Registry Information on Foreign Adsorbates, *Phys. Rev. Lett.*, **77**, 2113–2116 (1996). (Cited on page 42.)

[Mob15] S. Mobilio, F. Boscherini, and C. Meneghini, *Synchrotron radiation: Basics, methods and applications*. Springer, Heidelberg, (2015). (Cited on pages 50 and 51.)

[Moh10] S. Mohnani and D. Bonifazi, Supramolecular architectures of porphyrins on surfaces: The structural evolution from 1D to 2D to 3D to devices, *Coord. Chem. Rev.*, **254**, 2342–2362 (2010). (Cited on page 107.)

[Moh11] F. Mohn, L. Gross, and G. Meyer, Measuring the Short-Range Force Field Above a Single Molecule with Atomic Resolution, *Appl. Phys. Lett.*, **99**, 053106 (2011). (Cited on page 60.)

[Moh12] F. Mohn, *Probing electronic and structural properties of single molecules on the atomic scale*, PhD thesis, University of Regensburg (2012). (Cited on page 14.)

[Mon15] E. Monazami, L. Bignardi, P. Rudolf, and P. Reinke, Strain Lattice Imprinting in Graphene by C_{60} Intercalation at the Graphene/Cu Interface, *Nano Lett.*, **15**, 7421–7430 (2015). (Cited on page 2.)

[Moo65] G. E. Moore, Cramming more components onto integrated circuits, *Electronics*, **38**, 114–117 (1965). (Cited on page 1.)

[Moo75] G. E. Moore, *Progress in digital integrated electronics*. Vol. 21, (1975). (Cited on page 1.)

[Mor10] W. Moritz, B. Wang, M.-L. Bocquet, T. Brugger, T. Greber, J. Wintterlin, and S. Günther, Structure Determination of the Coincidence Phase of Graphene on Ru(0001), *Phys. Rev. Lett.*, **104**, 136102 (2010). (Cited on page 57.)

[Mor15] S. Morita, F. J. Giessibl, E. Meyer, and R. Wiesendanger, *Noncontact Atomic Force Microscopy*. Springer International Publishing, Cham, (2015). (Cited on pages 13 and 14.)

[Mug11] A. Mugarza, C. Krull, R. Robles, S. Stepanow, G. Ceballos, and P. Gambardella, Spin coupling and relaxation inside molecule-metal contacts, *Nat. Commun.*, **2**, 490 (2011). (Cited on page 114.)

[Mül10] F. Müller, S. Hüfner, H. Sachdev, R. Laskowski, P. Blaha, and K. Schwarz, Epitaxial growth of hexagonal boron nitride on Ag(111), *Phys. Rev. B*, **82**, 113406 (2010). (Cited on pages 58, 65, 71, 73, 76, and 77.)

[Mül13] F. Müller and S. Grandthyll, Monolayer formation of hexagonal boron nitride on Ag(001), *Surf. Sci.*, **617**, 207–210 (2013). (Cited on page 77.)

[Mül16] M. Müller, K. Diller, R. J. Maurer, and K. Reuter, Interfacial Charge Rearrangement and Intermolecular Interactions: Density-Functional Theory Study of Free-Base Porphine Adsorbed on Ag(111) and Cu(111), *J. Chem. Phys.*, **144**, 024701 (2016). (Cited on pages 87, 88, and 98.)

[Mun05] M. Muntwiler, W. Auwärter, A. P. Seitsonen, J. Osterwalder, and T. Greber, Rocking-motion-induced charging of C_{60} on h-BN/Ni(111), *Phys. Rev. B*, **71**, 101 (2005). (Cited on page 108.)

[Mun17] M. Muntwiler, J. Zhang, R. Stania, F. Matsui, P. Oberta, U. Flechsig, L. Patthey, C. Quitmann, T. Glatzel, R. Widmer, E. Meyer, T. A. Jung, P. Aebi, R. Fasel, and T. Greber, Surface Science at the PEARL Beamline of the Swiss Light Source, *J. Synchrotron Rad.*, **24**, 354–366 (2017). (Cited on pages 56 and 57.)

[Mur10] Y. Murata, E. Starodub, B. B. Kappes, C. V. Ciobanu, N. C. Bartelt, K. F. McCarty, and S. Kodambaka, Orientation-dependent work function of graphene on Pd(111), *Appl. Phys. Lett.*, **97**, 143114 (2010). (Cited on page 71.)

[Nee13] M. Neek-Amal, J. Beheshtian, A. Sadeghi, K. H. Michel, and F. M. Peeters, Boron Nitride Monolayer: A Strain-Tunable Nanosensor, *J. Phys. Chem. C*, **117**, 13261–13267 (2013). (Cited on page 66.)

[Nes95] H. Ness and F. Gautier, The electronic structure and stability of transition metal nanotips. I, *J. Phys. Cond. Matter*, **7**, 6625–6640 (1995). (Cited on page 47.)

[Nic12] C. Nicolas and C. Miron, Lifetime Broadening of Core-Excited and -Ionized States, *J. Electron Spectrosc. Relat. Phenom.*, **185**, 267–272 (2012). (Cited on page 152.)

[Niw74] Y. Niwa, H. Kobayashi, and T. Tsuchiya, X–ray Photoelectron Spectroscopy of Tetraphenylporphin and Phthalocyanine, *J. Chem. Phys.*, **60**, 799–807 (1974). (Cited on page 90.)

[Nob14] Nobelprize.org, The Nobel Prize in Physics 1914 (1914), `http://www.nobelprize.org/nobel_prizes/physics/laureates/1914/`, (Accessed: 2017-05-14). (Cited on page 23.)

[Nob15] Nobelprize.org, The Nobel Prize in Physics 1915 (1915), `http://www.nobelprize.org/nobel_prizes/physics/laureates/1915/`, (Accessed: 2017-05-14). (Cited on page 24.)

[Nob21] Nobelprize.org, The Nobel Prize in Physics 1921 (1921), `http://www.nobelprize.org/nobel_prizes/physics/laureates/1921/`, (Accessed: 2017-05-07). (Cited on page 16.)

[Nob37] Nobelprize.org, The Nobel Prize in Physics 1937 (1937), `http://www.nobelprize.org/nobel_prizes/physics/laureates/1937/`, (Accessed: 2017-03-11). (Cited on page 33.)

[Nob81] Nobelprize.org, The Nobel Prize in Physics 1981 (1981), `http://www.nobelprize.org/nobel_prizes/physics/laureates/1981/`, (Accessed: 2017-05-07). (Cited on page 16.)

[Nob86] Nobelprize.org, The Nobel Prize in Physics 1986 (1986), `http://www.nobelprize.org/nobel_prizes/physics/laureates/1986/`, (Accessed: 2017-04-16). (Cited on page 5.)

[Non91] M. Nonnenmacher, M. P. O'Boyle, and H. K. Wickramasinghe, Kelvin probe force microscopy, *Appl. Phys. Lett.*, **58**, 2921–2923 (1991). (Cited on page 14.)

[Nor57] C. Nordling, E. Sokolowski, and K. Siegbahn, Precision Method for Obtaining Absolute Values of Atomic Binding Energies, *Phys. Rev.*, **105**, 1676–1677 (1957). (Cited on page 16.)

[Nor72] C. Nordling, ESCA: Electron Spectroscopy for Chemical Analysis, *Angew. Chem., Int. Ed. Engl.*, **11**, 83–92 (1972). (Cited on page 16.)

[Nov04] K. S. Novoselov, A. K. Geim, S. V. Morozov, D. Jiang, Y. Zhang, S. V. Dubonos, I. V. Grigorieva, and A. A. Firsov, Electric field effect in atomically thin carbon films, *Science*, **306**, 666–669 (2004). (Cited on page 2.)

[Nov05] K. S. Novoselov, D. Jiang, F. Schedin, T. J. Booth, V. V. Khotkevich, S. V. Morozov, and A. K. Geim, Two-dimensional atomic crystals, *Proc. Natl. Acad. Sci. U. S. A.*, **102**, 10451–10453 (2005). (Cited on page 2.)

[Nov07] K. S. Novoselov, Z. Jiang, Y. Zhang, S. V. Morozov, H. L. Stormer, U. Zeitler, J. C. Maan, G. S. Boebinger, P. Kim, and A. K. Geim, Room-temperature quantum Hall effect in graphene, *Science*, **315**, 1379 (2007). (Cited on page 2.)

[Nov12] K. S. Novoselov, V. I. Fal'ko, L. Colombo, P. R. Gellert, M. G. Schwab, and K. Kim, A roadmap for graphene, *Nature*, **490**, 192–200 (2012). (Cited on pages 2 and 123.)

[Nov16] K. S. Novoselov, A. Mishchenko, A. Carvalho, and A. H. Castro Neto, 2D materials and van der Waals heterostructures, *Science*, **353**, aac9439 (2016). (Cited on pages 2, 123, and 141.)

[O'B17] E. S. O'Brien, M. T. Trinh, R. L. Kann, J. Chen, G. A. Elbaz, A. Masurkar, T. L. Atallah, M. V. Paley, N. Patel, D. W. Paley, I. Kymissis, A. C. Crowther, A. J. Millis, D. R. Reichman, X.-Y. Zhu, and X. Roy, Single-crystal-to-single-crystal intercalation of a low-bandgap superatomic crystal, *Nat. Chem.*, **9**, 1170–1174 (2017). (Cited on page 78.)

[Oer07] Oerlikon Leybold, Grundlagen der Vakuumtechnik (2007). (Cited on page 36.)

[Oht17] M. Ohtomo, Y. Yamauchi, X. Sun, A. A. Kuzubov, N. S. Mikhaleva, P. V. Avramov, S. Entani, Y. Matsumoto, H. Naramoto, and S. Sakai, Direct observation of site-selective hydrogenation and spin-polarization in hydrogenated hexagonal boron nitride on Ni(111), *Nanoscale*, **9**, 2369–2375 (2017). (Cited on page 99.)

[Ols13] T. Olsen and K. S. Thygesen, Random phase approximation applied to solids, molecules, and graphene-metal interfaces: From van der Waals to covalent bonding, *Phys. Rev. B*, **87**, 920 (2013). (Cited on page 76.)

[Ono17] J. Onoda, M. Ondracek, P. Jelinek, and Y. Sugimoto, Electronegativity Determination of Individual Surface Atoms by Atomic Force Microscopy, *Nat. Commun.*, **8**, 15155 (2017). (Cited on page 60.)

[Orl14] F. Orlando, P. Lacovig, L. Omiciuolo, N. G. Apostol, R. Larciprete, A. Baraldi, and S. Lizzit, Epitaxial growth of a single-domain hexagonal boron nitride monolayer, *ACS Nano*, **8**, 12063–12070 (2014). (Cited on page 63.)

[Osh97] C. Oshima and A. Nagashima, Ultra-Thin Epitaxial Films of Graphite and Hexagonal Boron Nitride on Solid Surfaces, *J. Phys. Cond. Matter*, **9**, 1–20 (1997). (Cited on page 55.)

[Ote16] N. Otero, P. Karamanis, K. E. El-Kelany, M. Rérat, L. Maschio, B. Civalleri, and B. Kirtman, Exploring the Linear Optical Properties of Borazine (B_3N_3) Doped Graphenes. 0D Flakes vs 2D Sheets, *J. Phys. Chem. C*, **121**, 709–722 (2016). (Cited on page 128.)

[Ote17] N. Otero, C. Pouchan, and P. Karamanis, Quadratic nonlinear optical (NLO) properties of borazino (B_3N_3)-doped nanographenes, *J. Mater. Chem. C*, **5**, 8273–8287 (2017). (Cited on page 128.)

[Our03] K. Oura, M. Katayama, A. V. Zotov, V. G. Lifshits, and A. A. Saranin, *Surface Science*. Springer Berlin Heidelberg, Berlin, Heidelberg, (2003). (Cited on page 33.)

[Oya06] N. Oyabu, P. Pou, Y. Sugimoto, P. Jelinek, M. Abe, S. Morita, R. Perez, and O. Custance, Single Atomic Contact Adhesion and Dissipation in Dynamic Force Microscopy, *Phys. Rev. Lett.*, **96**, 106101 (2006). (Cited on pages 14 and 68.)

[Pac15] G. E. Pacchioni, M. Pivetta, and H. Brune, Competing Interactions in the Self-Assembly of NC-Ph_3-CN Molecules on Cu(111), *J. Phys. Chem. C*, **119**, 25442–25448 (2015). (Cited on page 137.)

[Pal15] C.-A. Palma, S. Joshi, T. Hoh, D. Écija, J. V. Barth, and W. Auwärter, Two-level spatial modulation of vibronic conductance in conjugated oligophenylenes on boron nitride, *Nano Lett.*, **15**, 2242–2248 (2015). (Cited on page 109.)

[Pan93] S. H. Pan, Piezo-electric Motor (1993), World Intellectual Property Organization WO 93/19494. (Cited on page 43.)

[Par00] J.-Y. Park, U. D. Ham, S.-J. Kahng, Y. Kuk, K. Miyake, K. Hata, and H. Shigekawa, Modification of surface-state dispersion upon Xe adsorption: A scanning tunneling microscope study, *Phys. Rev. B*, **62**, R16341–R16344 (2000). (Cited on page 71.)

[Par14] J. Park, J. Lee, L. Liu, K. W. Clark, C. Durand, C. Park, B. G. Sumpter, A. P. Baddorf, A. Mohsin, M. Yoon, G. Gu, and A.-P. Li, Spatially resolved one-dimensional boundary states in graphene-hexagonal boron nitride planar heterostructures, *Nat. Commun.*, **5**, 5403 (2014). (Cited on page 127.)

[Pas02] W. Paszkowicz, J. B. Pelka, M. Knapp, T. Szyszko, and S. Podsiadlo, Lattice Parameters and Anisotropic Thermal Expansion of Hexagonal Boron Nitride in the 10-297.5 K Temperature Range, *Appl. Phys. A*, **75**, 431–435 (2002). (Cited on pages 55, 58, and 155.)

[Pat89] J. R. Patel, D. W. Berreman, F. Sette, P. H. Citrin, J. E. Rowe, P. L. Cowan, T. Jach, and B. Karlin, Substrate Surface Relaxation for Cl and S on Cu(001), *Phys. Rev. B*, **40**, 1330–1333 (1989). (Cited on page 65.)

[Pat17] L. L. Patera, X. Liu, N. Mosso, S. Decurtins, S.-X. Liu, and J. Repp, Crystallization of a Two-Dimensional Hydrogen-Bonded Molecular Assembly: Evolution of the Local Structure Resolved by Atomic Force Microscopy, *Angew. Chem., Int. Ed. Engl.*, **56**, 10786–10790 (2017). (Cited on page 60.)

[Pau10] C. Pauly, M. Grob, M. Pezzotta, M. Pratzer, and M. Morgenstern, Gundlach oscillations and Coulomb blockade of Co nanoislands on MgO/Mo(100) investigated by scanning tunneling spectroscopy at 300 K, *Phys. Rev. B*, **81**, 125446 (2010). (Cited on page 74.)

[Paw08] G. Pawin, K. L. Wong, D. Kim, D. Sun, L. Bartels, S. Hong, T. S. Rahman, R. Carp, and M. Marsella, A surface coordination network based on substrate-derived metal adatoms with local charge excess, *Angew. Chem., Int. Ed. Engl.*, **47**, 8442–8445 (2008). (Cited on page 137.)

[Pea52] R. S. Pease, An X-Ray Study of Boron Nitride, *Acta Cryst.*, **5**, 356–361 (1952). (Cited on page 68.)

[Pen90] J. B. Pendry, Low-Energy Electron Diffraction, In V. Bortolani, N. H. March, and M. P. Tosi, editors, *Interaction of Atoms and Molecules with Solid Surfaces*, pages 201–211. Springer US, Boston, MA, (1990). (Cited on pages 33 and 34.)

[Pen07] Y. Pennec, W. Auwärter, A. Schiffrin, A. Weber-Bargioni, A. Riemann, and J. V. Barth, Supramolecular gratings for tuneable confinement of electrons on metal surfaces, *Nat. Nanotechnol.*, **2**, 99–103 (2007). (Cited on page 71.)

[Pen12] Q. Peng and S. De, Tunable band gaps of mono-layer hexagonal BNC heterostructures, *Phys. E*, **44**, 1662–1666 (2012). (Cited on pages 123 and 124.)

[Per96] J. P. Perdew, K. Burke, and M. Ernzerhof, Generalized Gradient Approximation Made Simple, *Phys. Rev. Lett.*, **77**, 3865–3868 (1996). (Cited on page 153.)

[Per10] U. G. E. Perera, H. J. Kulik, V. Iancu, L. G. G. V. Dias da Silva, S. E. Ulloa, N. Marzari, and S.-W. Hla, Spatially extended Kondo state in magnetic molecules induced by interfacial charge transfer, *Phys. Rev. Lett.*, **105**, 106601 (2010). (Cited on page 116.)

[Pét17] R. Pétuya and A. Arnau, Magnetic coupling between 3*d* transition metal adatoms on graphene supported by metallic substrates, *Carbon*, **116**, 599–605 (2017). (Cited on page 121.)

[Pie01] O. Pietzsch, A. Kubetzka, M. Bode, and R. Wiesendanger, Observation of magnetic hysteresis at the nanometer scale by spin-polarized scanning tunneling spectroscopy, *Science*, **292**, 2053–2056 (2001). (Cited on page 11.)

[Pio08] L. Piot, C. Marie, X. Feng, K. Müllen, and D. Fichou, Hierarchical Self-Assembly of Edge-On Nanocolumnar Superstructures of Large Disc-Like Molecules, *Adv. Mater.*, **20**, 3854–3858 (2008). (Cited on page 128.)

[Pis15] H. N. Pishkenari, Atomic Interactions Between Metallic Tips and Surfaces in NC-AFM, *J. Phys. D: Appl. Phys.*, **48**, 125301 (2015). (Cited on page 68.)

[Poe92] M. Poensgen, J. F. Wolf, J. Frohn, M. Giesen, and H. Ibach, Step dynamics on Ag(111) and Cu(100) surfaces, *Surf. Sci.*, **274**, 430–440 (1992). (Cited on page 46.)

[Pol10] A. J. Pollard, E. W. Perkins, N. A. Smith, A. Saywell, G. Goretzki, A. G. Phillips, S. P. Argent, H. Sachdev, F. Müller, S. Hüfner, S. Gsell, M. Fischer, M. Schreck, J. Osterwalder, T. Greber, S. Berner, N. R. Champness, and P. H. Beton, Supramolecular assemblies formed on an epitaxial graphene superstructure, *Angew. Chem., Int. Ed. Engl.*, **49**, 1794–1799 (2010). (Cited on page 108.)

[Pre05] A. B. Preobrajenski, A. S. Vinogradov, and N. Mårtensson, Monolayer of h-BN chemisorbed on Cu(111) and Ni(111): The role of the transition metal 3*d* states, *Surf. Sci.*, **582**, 21–30 (2005). (Cited on pages 63, 65, 66, 67, and 138.)

[Pre07a] A. B. Preobrajenski, M. A. Nesterov, M. L. Ng, A. S. Vinogradov, and N. Mårtensson, Monolayer h-BN on lattice-mismatched metal surfaces: On the formation of the nanomesh, *Chem. Phys. Lett.*, **446**, 119–123 (2007). (Cited on page 56.)

[Pre07b] A. B. Preobrajenski, A. S. Vinogradov, M. L. Ng, E. Ćavar, R. Westerström, A. Mikkelsen, E. Lundgren, and N. Mårtensson, Influence of Chemical Interaction at the Lattice-Mismatched h-BN/Rh(111) and h-BN/Pt(111) Interfaces on the Overlayer Morphology, *Phys. Rev. B*, **75**, 245412 (2007). (Cited on page 63.)

[Pre08] A. B. Preobrajenski, M. L. Ng, A. S. Vinogradov, and N. Mårtensson, Controlling graphene corrugation on lattice-mismatched substrates, *Phys. Rev. B*, **78**, 073401 (2008). (Cited on pages 71 and 83.)

[Pre09] A. B. Preobrajenski, M. L. Ng, N. A. Vinogradov, A. S. Vinogradov, E. Lundgren, A. Mikkelsen, and N. Mårtensson, Impact of oxygen coadsorption on intercalation of cobalt under the h-BN nanomesh, *Nano Lett.*, **9**, 2780–2787 (2009). (Cited on page 78.)

[Pur99] R. Purrello, S. Gurrieri, and R. Lauceri, Porphyrin assemblies as chemical sensors, *Coord. Chem. Rev.*, **190-192**, 683–706 (1999). (Cited on page 1.)

[Qiu04] X. H. Qiu, G. V. Nazin, and W. Ho, Vibronic states in single molecule electron transport, *Phys. Rev. Lett.*, **92**, 206102 (2004). (Cited on pages 8 and 11.)

[Qui13] M. Quintana, A. M. López, S. Rapino, F. M. Toma, M. Iurlo, M. Carraro, A. Sartorel, C. Maccato, X. Ke, C. Bittencourt, T. Da Ros, G. van Tendeloo, M. Marcaccio, F. Paolucci, M. Prato, and M. Bonchio, Knitting the catalytic pattern of artificial photosynthesis to a hybrid graphene nanotexture, *ACS Nano*, **7**, 811–817 (2013). (Cited on page 107.)

[Rai02] B. K. Rai, S. M. Durbin, E. W. Prohofsky, J. T. Sage, G. R. Wyllie, W. R. Scheidt, W. Sturhahn, and E. E. Alp, Iron Normal Mode Dynamics in (Nitrosyl)iron(II)tetraphenylporphyrin from X-ray Nuclear Resonance Data, *Biophys. J.*, **82**, 2951–2963 (2002). (Cited on page 95.)

[Red10] A. L. M. Reddy, A. Srivastava, S. R. Gowda, H. Gullapalli, M. Dubey, and P. M. Ajayan, Synthesis of nitrogen-doped graphene films for lithium battery application, *ACS Nano*, **4**, 6337–6342 (2010). (Cited on page 124.)

[Rei12] T. E. Reich, S. Behera, K. T. Jackson, P. Jena, and H. M. El-Kaderi, Highly selective CO_2/CH_4 gas uptake by a halogen-decorated borazine-linked polymer, *J. Mater. Chem.*, **22**, 13524 (2012). (Cited on page 128.)

[Rei13] J. Reichert, M. Marschall, K. Seufert, D. Écija, W. Auwärter, E. Arras, S. Klyatskaya, M. Ruben, and J. V. Barth, Competing Interactions in Surface Reticulation with a Prochiral Dicarbonitrile Linker, *J. Phys. Chem. C*, **117**, 12858–12863 (2013). (Cited on page 113.)

[Ren14] J. Ren, H. Guo, J. Pan, Y. Y. Zhang, X. Wu, H.-G. Luo, S. Du, S. T. Pantelides, and H.-J. Gao, Kondo effect of cobalt adatoms on a graphene monolayer controlled by substrate-induced ripples, *Nano Lett.*, **14**, 4011–4015 (2014). (Cited on page 114.)

[Rep04a] J. Repp, G. Meyer, F. E. Olsson, and M. Persson, Controlling the charge state of individual gold adatoms, *Science*, **305**, 493–495 (2004). (Cited on page 99.)

[Rep04b] J. Repp, G. Meyer, and K.-H. Rieder, Snell's law for surface electrons: Refraction of an electron gas imaged in real space, *Phys. Rev. Lett.*, **92**, 036803 (2004). (Cited on pages 8 and 71.)

[Rep05a] J. Repp, G. Meyer, S. Paavilainen, F. E. Olsson, and M. Persson, Scanning tunneling spectroscopy of Cl vacancies in NaCl films: Strong electron-phonon coupling in double-barrier tunneling junctions, *Phys. Rev. Lett.*, **95**, 225503 (2005). (Cited on page 8.)

[Rep05b] J. Repp, G. Meyer, S. M. Stojkovic, A. Gourdon, and C. Joachim, Molecules on Insulating Films: Scanning-Tunneling Microscopy Imaging of Individual Molecular Orbitals, *Phys. Rev. Lett.*, **94**, 026803–1–026803–4 (2005). (Cited on pages 8, 11, and 99.)

[Rie17] N. A. Riensch, A. Deniz, S. Kühl, L. Müller, A. Adams, A. Pich, and H. Helten, Borazine-based inorganic–organic hybrid cyclomatrix microspheres by silicon/boron exchange precipitation polycondensation, *Polym. Chem.*, **8**, 5264–5268 (2017). (Cited on page 128.)

[Ris14] A. Riss, S. Wickenburg, L. Z. Tan, H.-Z. Tsai, Y. Kim, J. Lu, A. J. Bradley, M. M. Ugeda, K. L. Meaker, K. Watanabe, T. Taniguchi, A. Zettl, F. R. Fischer, S. G. Louie, and M. F. Crommie, Imaging and tuning molecular levels at the surface of a gated graphene device, *ACS Nano*, **8**, 5395–5401 (2014). (Cited on page 108.)

[Rob92] I. K. Robinson and D. J. Tweet, Surface X-ray diffraction, *Rep. Prog. Phys.*, **55**, 599–651 (1992). (Cited on page 23.)

[Rog17] S. M. J. Rogge, A. Bavykina, J. Hajek, H. Garcia, A. I. Olivos-Suarez, A. Sepúlveda-Escribano, A. Vimont, G. Clet, P. Bazin, F. Kapteijn, M. Daturi, E. V. Ramos-Fernandez, F. X. Llabrés I Xamena, V. van Speybroeck, and J. Gascon, Metal-Organic and Covalent Organic Frameworks as Single-Site Catalysts, *Chem. Soc. Rev.*, **46**, 3134–3184 (2017). (Cited on page 85.)

[Roj12] G. Rojas, S. Simpson, X. Chen, D. A. Kunkel, J. Nitz, J. Xiao, P. A. Dowben, E. Zurek, and A. Enders, Surface state engineering of molecule-molecule interactions, *Phys. Chem. Chem. Phys.*, **14**, 4971–4976 (2012). (Cited on page 71.)

[Ros03] F. Rosei, M. Schunack, Y. Naitoh, P. Jiang, A. Gourdon, E. Laegsgaard, I. Stensgaard, C. Joachim, and F. Besenbacher, Properties of Large Organic Molecules on Metal Surfaces, *Prog. Surf. Sci.*, **71**, 95–146 (2003). (Cited on pages 86 and 128.)

[Rot13] S. Roth, F. Matsui, T. Greber, and J. Osterwalder, Chemical vapor deposition and characterization of aligned and incommensurate graphene/hexagonal boron nitride heterostack on Cu(111), *Nano Lett.*, **13**, 2668–2675 (2013). (Cited on page 58.)

[Rot16] S. Roth, T. Greber, and J. Osterwalder, Some Like It Flat: Decoupled h-BN Monolayer Substrates for Aligned Graphene Growth, *ACS Nano*, **10**, 11187–11195 (2016). (Cited on page 124.)

[Ruf16] P. Ruffieux, S. Wang, B. Yang, C. Sánchez-Sánchez, J. Liu, T. Dienel, L. Talirz, P. Shinde, C. A. Pignedoli, D. Passerone, T. Dumslaff, X. Feng, K. Müllen, and R. Fasel, On-Surface Synthesis of Graphene Nanoribbons with Zigzag Edge Topology, *Nature*, **531**, 489–492 (2016). (Cited on pages 1 and 141.)

[Sac11] B. Sachs, T. O. Wehling, M. I. Katsnelson, and A. I. Lichtenstein, Adhesion and Electronic Structure of Graphene on Hexagonal Boron Nitride Substrates, *Phys. Rev. B*, **84**, 195414 (2011). (Cited on page 70.)

[Sán15] C. Sánchez-Sánchez, S. Brüller, H. Sachdev, K. Mullen, M. Krieg, H. F. Bettinger, A. Nicolai, V. Meunier, L. Talirz, R. Fasel, and P. Ruffieux, On-Surface Synthesis of BN-Substituted Heteroaromatic Networks, *ACS Nano*, **9**, 9228–9235 (2015). (Cited on page 134.)

[Sch93] C. Schönenberger, H. van Houten, J. M. Kerkhof, and H. C. Donkersloot, Single-electron tunneling in double-barrier junctions by scanning tunneling microscopy, *Appl. Surf. Sci.*, **67**, 222–227 (1993). (Cited on page 8.)

[Sch07] U. Schlickum, R. Decker, F. Klappenberger, G. Zoppellaro, S. Klyatskaya, M. Ruben, I. Silanes, A. Arnau, K. Kern, H. Brune, and J. V. Barth, Metal-organic honeycomb nanomeshes with tunable cavity size, *Nano Lett.*, **7**, 3813–3817 (2007). (Cited on page 113.)

[Sch11] S. Schlögl, T. Sirtl, J. Eichhorn, W. M. Heckl, and M. Lackinger, Synthesis of two-dimensional phenylene-boroxine networks through in vacuo condensation and on-surface radical addition, *Chem. Commun.*, **47**, 12355–12357 (2011). (Cited on page 128.)

[Sch13a] B. Schuler, W. Liu, A. Tkatchenko, N. Moll, G. Meyer, A. Mistry, D. Fox, and L. Gross, Adsorption Geometry Determination of Single Molecules by Atomic Force Microscopy, *Phys. Rev. Lett.*, **111**, 106103 (2013). (Cited on pages 60, 87, and 99.)

[Sch13b] F. Schulz, R. Drost, S. K. Hämäläinen, and P. Liljeroth, Templated self-assembly and local doping of molecules on epitaxial hexagonal boron nitride, *ACS Nano*, **7**, 11121–11128 (2013). (Cited on pages 106, 109, and 111.)

[Sch14a] A. Schlierf, P. Samorì, and V. Palermo, Graphene–organic composites for electronics: Optical and electronic interactions in vacuum, liquids and thin solid films, *J. Mater. Chem. C*, **2**, 3129 (2014). (Cited on page 107.)

[Sch14b] F. Schulz, R. Drost, S. K. Hämäläinen, T. Demonchaux, A. P. Seitsonen, and P. Liljeroth, Epitaxial hexagonal boron nitride on Ir(111): A work function template, *Phys. Rev. B*, **89**, 235429 (2014). (Cited on pages 56, 71, and 73.)

[Sch15a] B. Schuler, *Characterizing and Identifying single Molecules by Scanning Probe Microscopy using Functionalized Tips*, PhD thesis, Universität Regensburg (2015). (Cited on page 14.)

[Sch15b] F. Schulz, M. Ijäs, R. Drost, S. K. Hämäläinen, A. Harju, A. P. Seitsonen, and P. Liljeroth, Many-body transitions in a single molecule visualized by scanning tunnelling microscopy, *Nat. Phys.*, **11**, 229–234 (2015). (Cited on pages 56 and 106.)

[Sch17a] U. A. Schröder, M. Petrović, T. Gerber, A. J. Martínez-Galera, E. Grånäs, M. A. Arman, C. Herbig, J. Schnadt, M. Kralj, J. Knudsen, and T. Michely, Core level shifts of intercalated graphene, *2D Mater.*, **4**, 015013 (2017). (Cited on page 2.)

[Sch17b] M. Schwarz, A. Riss, M. Garnica, J. Ducke, P. S. Deimel, D. A. Duncan, P. K. Thakur, T.-L. Lee, A. P. Seitsonen, J. V. Barth, F. Allegretti, and W. Auwärter, Corrugation in the Weakly Interacting Hexagonal-BN/Cu(111) System: Structure Determination by Combining Noncontact Atomic Force Microscopy and X-ray Standing Waves, *ACS Nano*, **11**, 9151–9161 (2017). (Cited on pages 24, 60, 66, 82, 96, 100, 101, 105, 127, 152, and 153.)

[Sch18a] M. Schwarz, M. Garnica, D. A. Duncan, A. Pérez Paz, J. Ducke, P. S. Deimel, P. K. Thakur, T.-L. Lee, A. Rubio, J. V. Barth, F. Allegretti, and W. Auwärter, Adsorption Conformation and Lateral Registry of Cobalt Porphine on Cu(111), *J. Phys. Chem. C*, **122**, 5452–5461 (2018). (Cited on pages 89, 92, 95, 100, 101, 102, and 105.)

[Sch18b] M. Schwarz, M. Garnica, F. Fasano, N. Demitri, D. Bonifazi, and W. Auwärter, BN-Patterning of Metallic Substrates through Metal Coordination of Decoupled Borazines, *Chem. - Eur. J.*, **24**, 9565–9571 (2018). (Cited on pages 129, 132, and 137.)

[Scr94] G. Scragg, B. C. C. Cowies, M. Kerkar, D. P. Woodruff, A. Daimellah, S. Turton, and R. G. Jones, A structural study of the Al(111)(square root 3* square root 3)R30degree-Rb phase at different temperatures, *J. Phys. Cond. Matter*, **6**, 1869–1880 (1994). (Cited on page 32.)

[Scu00] L. Scudiero, D. E. Barlow, and K. W. Hipps, Physical Properties and Metal Ion Specific Scanning Tunneling Microscopy Images of Metal(II) Tetraphenylporphyrins Deposited from Vapor onto Gold (111), *J. Phys. Chem. B*, **104**, 11899–11905 (2000). (Cited on page 90.)

[Sea90] M. P. Seah, G. C. Smith, and M. T. Anthony, AES: Energy Calibration of Electron Spectrometers. I - An Absolute, Traceable Energy Calibration and the Provision of Atomic Reference Line Energies, *Surf. Interface Anal.*, **15**, 293–308 (1990). (Cited on pages 22 and 88.)

[Sea98] M. P. Seah, I. S. Gilmore, and G. Beamson, XPS: Binding Energy Calibration of Electron Spectrometers 5 - Evaluation of the Reference Energies, *Surf. Interface Anal.*, **26**, 642–649 (1998). (Cited on pages 22, 76, and 80.)

[Sel85] A. Selloni, P. Carnevali, E. Tosatti, and C. D. Chen, Voltage-dependent scanning-tunneling microscopy of a crystal surface: Graphite, *Phys. Rev. B*, **31**, 2602–2605 (1985). (Cited on page 11.)

[Sen07] M. O. Senge, M. Fazekas, E. G. A. Notaras, W. J. Blau, M. Zawadzka, O. B. Locos, and E. M. Ni Mhuircheartaigh, Nonlinear Optical Properties of Porphyrins, *Adv. Mater.*, **19**, 2737–2774 (2007). (Cited on page 87.)

[Ser14] D. Serrate, M. Moro-Lagares, M. Piantek, J. I. Pascual, and M. R. Ibarra, Enhanced Hydrogen Dissociation by Individual Co Atoms Supported on Ag(111), *J. Phys. Chem. C*, **118**, 5827–5832 (2014). (Cited on page 121.)

[Seu11a] K. Seufert, *Nanochemistry with porphyrins - a 2D perspective*, PhD thesis, Technische Universität München (2011). (Cited on pages 35 and 109.)

[Seu11b] K. Seufert, M.-L. Bocquet, W. Auwärter, A. Weber-Bargioni, J. Reichert, N. Lorente, and J. V. Barth, Cis-Dicarbonyl Binding at Cobalt and Iron Porphyrins with Saddle-Shape Conformation, *Nat. Chem.*, **3**, 114–119 (2011). (Cited on page 122.)

[Sha05] I. H. T. Sham, C.-C. Kwok, C.-M. Che, and N. Zhu, Borazine materials for organic optoelectronic applications, *Chem. Commun.*, **1**, 3547–3549 (2005). (Cited on page 128.)

[She09] P. Shemella and S. K. Nayak, Electronic structure and band-gap modulation of graphene via substrate surface chemistry, *Appl. Phys. Lett.*, **94**, 032101 (2009). (Cited on page 124.)

[Shi72] D. A. Shirley, High-Resolution X-Ray Photoemission Spectrum of the Valence Bands of Gold, *Phys. Rev. B*, **5**, 4709–4714 (1972). (Cited on page 22.)

[Shi09] Z. Shi and N. Lin, Porphyrin-based two-dimensional coordination Kagome lattice self-assembled on a Au(111) surface, *J. Am. Chem. Soc.*, **131**, 5376–5377 (2009). (Cited on page 137.)

[Shi10] Y. Shi, C. Hamsen, X. Jia, K. K. Kim, A. Reina, M. Hofmann, A. L. Hsu, K. Zhang, H. Li, Z.-Y. Juang, M. S. Dresselhaus, L.-J. Li, and J. Kong, Synthesis of Few-Layer Hexagonal Boron Nitride Thin Film by Chemical Vapor Deposition, *Nano Lett.*, **10**, 4134–4139 (2010). (Cited on page 55.)

[Shu07] T. E. Shubina, H. Marbach, K. Flechtner, A. Kretschmann, N. Jux, F. Buchner, H.-P. Steinrück, T. Clark, and J. M. Gottfried, Principle and mechanism of direct porphyrin metalation: Joint experimental and theoretical investigation, *J. Am. Chem. Soc.*, **129**, 9476–9483 (2007). (Cited on page 111.)

[Sie56] K. Siegbahn and K. Edvarson, β-Ray spectroscopy in the precision range of 1: 105, *Nucl. Phys.*, **1**, 137–159 (1956). (Cited on page 16.)

[Sie67] K. Siegbahn, C. Nordling, A. Fahlman, R. Nordberg, K. Hamrin, J. Hedman, G. Johansson, T. Bergmark, S.-E. Karlsson, I. Lindgren, and B. Lindberg, ESCA: atomic, molecular and solid state structure studied by means of electron spectroscopy, *Nova Acta Regiae Soc. Sci. Upsaliensis*, **20**, 5–282 (1967). (Cited on pages 16 and 19.)

[Sie17] G. Siegel, C. V. Ciobanu, B. Narayanan, M. Snure, and S. C. Badescu, Heterogeneous Pyrolysis: A Route for Epitaxial Growth of hBN Atomic Layers on Copper Using Separate Boron and Nitrogen Precursors, *Nano Lett.*, **17**, 2404–2413 (2017). (Cited on pages 60 and 63.)

[Sir13] T. Sirtl, S. Schlogl, A. Rastgoo-Lahrood, J. Jelic, S. Neogi, M. Schmittel, W. M. Heckl, K. Reuter, and M. Lackinger, Control of intermolecular bonds by deposition rates at room temperature: hydrogen bonds versus metal coordination in trinitrile monolayers, *J. Am. Chem. Soc.*, **135**, 691–695 (2013). (Cited on page 137.)

[Sne15] O. Snezhkova, J. Lüder, A. Wiengarten, S. R. Burema, F. Bischoff, Y. He, J. Rusz, J. Knudsen, M.-L. Bocquet, K. Seufert, J. V. Barth, W. Auwärter, B. Brena, and J. Schnadt, Nature of the Bias-Dependent Symmetry Reduction of Iron Phthalocyanine on Cu(111), *Phys. Rev. B*, **92**, 075428 (2015). (Cited on pages 87 and 97.)

[Son06] Y.-W. Son, M. L. Cohen, and S. G. Louie, Half-metallic graphene nanoribbons, *Nature*, **444**, 347–349 (2006). (Cited on page 123.)

[Son10] L. Song, L. Ci, H. Lu, P. B. Sorokin, C. Jin, J. Ni, A. G. Kvashnin, D. G. Kvashnin, J. Lou, B. I. Yakobson, and P. M. Ajayan, Large scale growth and characterization of atomic hexagonal boron nitride layers, *Nano Lett.*, **10**, 3209–3215 (2010). (Cited on page 124.)

[SPE12] SPECS GmbH, SPECS User Manual PHOIBOS 100/150 - Hemispherical Energy Analyzer, Version 4.0 (2012). (Cited on pages 41 and 42.)

[SPE13] SPECS GmbH, SPECS User Manual XR 50, X-Ray Source, Version 2.6 (2013). (Cited on page 40.)

[SPE17] SPECS GmbH, Voltastrasse 5, 13355 Berlin, Germany (2017), `http://www.specs.de`, (Accessed: 2017-04-02). (Cited on pages 36 and 39.)

[Spl10] A. Splendiani, L. Sun, Y. Zhang, T. Li, J. Kim, C.-Y. Chim, G. Galli, and F. Wang, Emerging photoluminescence in monolayer MoS_2, *Nano Lett.*, **10**, 1271–1275 (2010). (Cited on page 142.)

[Sta06] C. Stadler, S. Hansen, F. Pollinger, C. Kumpf, E. Umbach, T.-L. Lee, and J. Zegenhagen, Structural investigation of the adsorption of SnPc on Ag(111) using normal-incidence x-ray standing waves, *Phys. Rev. B*, **74**, 035404 (2006). (Cited on pages 24 and 99.)

[Sta17] Stanford Research Systems Inc., 1290-D Reamwood Avenue, Sunnyvale, CA 94089, United States (2017), `http://thinksrs.com/`, (Accessed: 2017-02-05). (Cited on page 38.)

[Sti98] B. C. Stipe, Single-Molecule Vibrational Spectroscopy and Microscopy, *Science*, **280**, 1732–1735 (1998). (Cited on page 11.)

[Str69] M. E. Straumanis and L. S. Yu, Lattice Parameters, Densities, Expansion Coefficients and Perfection of Structure of Cu and of Cu–In α Phase, *Acta Cryst. A*, **25**, 676–682 (1969). (Cited on pages 58 and 155.)

[Str91] J. A. Stroscio and D. M. Eigler, Atomic and molecular manipulation with the scanning tunneling microscope, *Science*, **254**, 1319–1326 (1991). (Cited on page 13.)

[Stu94] A. Stuck, M. Nowicki, S. Mroz, D. Naumovic, and J. Osterwalder, High-energy electron diffraction on Cu(111) measured with low-energy Auger electrons: Theory and experiment, *Surf. Sci.*, **306**, 21–28 (1994). (Cited on page 46.)

[Stu15] F. Studener, K. Müller, N. Marets, V. Bulach, M. W. Hosseini, and M. Stohr, From hydrogen bonding to metal coordination and back: Porphyrin-based networks on Ag(111), *J. Chem. Phys.*, **142**, 101926 (2015). (Cited on page 136.)

[Sur17] Surface Preparation Laboratory, Penningweg 69-F, 1507 DE Zaandam, The Netherlands (2017), `https://www.spl.eu/`, (Accessed: 2017-02-05). (Cited on page 45.)

[Sut14] P. Sutter, Y. Huang, and E. Sutter, Nanoscale integration of two-dimensional materials by lateral heteroepitaxy, *Nano Lett.*, **14**, 4846–4851 (2014). (Cited on page 124.)

[Tai07] S. L. Tait, A. Langner, N. Lin, S. Stepanow, C. Rajadurai, M. Ruben, and K. Kern, One-Dimensional Self-Assembled Molecular Chains on Cu(100): Interplay between Surface-Assisted Coordination Chemistry and Substrate Commensurability, *J. Phys. Chem. C*, **111**, 10982–10987 (2007). (Cited on pages 136 and 137.)

[Tai08] S. L. Tait, A. Langner, N. Lin, R. Chandrasekar, O. Fuhr, M. Ruben, and K. Kern, Assembling isostructural metal-organic coordination architectures on Cu(100), Ag(100) and Ag(111) substrates, *ChemPhysChem*, **9**, 2495–2499 (2008). (Cited on page 137.)

[Tan74] N. Taniguchi, *On the Basic Concept of 'Nano-Technology'*. Proceedings of the International Conference on Production Engineering, Tokyo, (1974), Part II. Japan Society of Precision Engineering. (Cited on page 1.)

[Tan11] Q. Tang, Z. Zhou, and Z. Chen, Molecular Charge Transfer: A Simple and Effective Route To Engineer the Band Structures of BN Nanosheets and Nanoribbons, *J. Phys. Chem. C*, **115**, 18531–18537 (2011). (Cited on pages 99 and 104.)

[Tao15] L. Tao, E. Cinquanta, D. Chiappe, C. Grazianetti, M. Fanciulli, M. Dubey, A. Molle, and D. Akinwande, Silicene field-effect transistors operating at room temperature, *Nat. Nanotechnol.*, **10**, 227–231 (2015). (Cited on page 71.)

[Tau07] F. S. Tautz, Structure and bonding of large aromatic molecules on noble metal surfaces: The example of PTCDA, *Prog. Surf. Sci.*, **82**, 479–520 (2007). (Cited on page 99.)

[Tem06] R. Temirov, S. Soubatch, A. Luican, and F. S. Tautz, Free-electron-like dispersion in an organic monolayer film on a metal substrate, *Nature*, **444**, 350–353 (2006). (Cited on page 71.)

[Ter83] J. Tersoff and D. R. Hamann, Theory and Application for the Scanning Tunneling Microscope, *Phys. Rev. Lett.*, **50**, 1998–2001 (1983). (Cited on pages 9 and 10.)

[Ter85] J. Tersoff and D. R. Hamann, Theory of the Scanning Tunneling Microscope, *Phys. Rev. B*, **31**, 805–813 (1985). (Cited on pages 9 and 10.)

[Ter09] M. Ternes, A. J. Heinrich, and W.-D. Schneider, Spectroscopic manifestations of the Kondo effect on single adatoms, *J. Phys. Cond. Matter*, **21**, 053001 (2009). (Cited on page 116.)

[Tft17] Tftpd64, The Industry Standard TFTP Server (2017), `http://tftpd32.jounin.net/`, (Accessed: 2017-02-05). (Cited on page 45.)

[Tho27] G. P. Thomson and A. Reid, Diffraction of Cathode Rays by a Thin Film, *Nature*, **119**, 890 (1927). (Cited on page 33.)

[Tho05] J. M. Thomas, R. Raja, and D. W. Lewis, Single-Site Heterogeneous Catalysts, *Angew. Chem., Int. Ed. Engl.*, **44**, 6456–6482 (2005). (Cited on page 85.)

[Ton13] P. Tonndorf, R. Schmidt, P. Böttger, X. Zhang, J. Börner, A. Liebig, M. Albrecht, C. Kloc, O. Gordan, D. R. T. Zahn, S. Michaelis de Vasconcellos, and R. Bratschitsch, Photoluminescence emission and Raman response of monolayer MoS_2, $MoSe_2$, and WSe_2, *Opt. Express*, **21**, 4908–4916 (2013). (Cited on page 142.)

[Tou09] C. Toumey, Plenty of room, plenty of history, *Nat. Nanotechnol.*, **4**, 783–784 (2009). (Cited on page 1.)

[Tou10] C. Toumey, 35 atoms that changed the nanoworld, *Nat. Nanotechnol.*, **5**, 239–241 (2010). (Cited on page 13.)

[Tre07] T. Trevethan, L. Kantorovich, J. Polesel-Maris, and S. Gauthier, Is Atomic-Scale Dissipation in NC-AFM Real? Investigation Using Virtual Atomic Force Microscopy, *Nanotechnology*, **18**, 084017 (2007). (Cited on page 68.)

[Trz01] M. B. Trzhaskovskaya, V. I. Nefedov, and V. G. Yarzhemsky, Photoelectron angular distribution parameters for elements Z=1 to Z=54 in the photoelectron energy range 100–5000 eV, *At. Data Nucl. Data Tables*, **77**, 97–159 (2001). (Cited on page 31.)

[Trz02] M. B. Trzhaskovskaya, V. I. Nefedov, and V. G. Yarzhemsky, Photoelectron angular distribution parameters for elements Z=55 to Z=100 in the photoelectron energy range 100-5000 eV, *At. Data Nucl. Data Tables*, **82**, 257–311 (2002). (Cited on page 31.)

[Twu80] C. H. Twu, L. L. Lee, and K. E. Starling, Improved analytical representation of argon thermodynamic behavior, *Fluid Phase Equilib.*, **4**, 35–44 (1980). (Cited on page 147.)

[Uch17] Y. Uchida, T. Iwaizako, S. Mizuno, M. Tsuji, and H. Ago, Epitaxial Chemical Vapour Deposition Growth of Monolayer Hexagonal Boron Nitride on a Cu(111)/Sapphire Substrate, *Phys. Chem. Chem. Phys.*, **19**, 8230–8235 (2017). (Cited on page 58.)

[Uih15] J. Uihlein, M. Polek, M. Glaser, H. Adler, R. Ovsyannikov, M. Bauer, M. Ivanovic, A. B. Preobrajenski, A. V. Generalov, T. Chassé, and H. Peisert, Influence of Graphene on Charge Transfer between CoPc and Metals: The Role of Graphene–Substrate Coupling, *J. Phys. Chem. C*, **119**, 15240–15247 (2015). (Cited on pages 2, 99, and 107.)

[Umb14] T. R. Umbach, M. Bernien, C. F. Hermanns, L. L. Sun, H. Mohrmann, K. E. Hermann, A. Krüger, N. Krane, Z. Yang, F. Nickel, Y.-M. Chang, K. J. Franke, J. I. Pascual, and W. Kuch, Site-specific bonding of copper adatoms to pyridine end groups mediating the formation of two-dimensional coordination networks on metal surfaces, *Phys. Rev. B*, **89**, 235409 (2014). (Cited on pages 135 and 136.)

[Uos14] K. Uosaki, G. Elumalai, H. Noguchi, T. Masuda, A. Lyalin, A. Nakayama, and T. Taketsugu, Boron Nitride Nanosheet on Gold as an Electrocatalyst for Oxygen Reduction Reaction: Theoretical Suggestion and Experimental Proof, *J. Am. Chem. Soc.*, **136**, 6542–6545 (2014). (Cited on page 56.)

[Urg15a] J. I. Urgel, *Two-dimensional lanthanide-directed metal-organic networks at surfaces*, PhD thesis, Technische Universität München (2015). (Cited on pages 35, 56, and 109.)

[Urg15b] J. I. Urgel, D. Écija, W. Auwärter, D. Stassen, D. Bonifazi, and J. V. Barth, Orthogonal Insertion of Lanthanide and Transition-Metal Atoms in Metal-Organic Networks on Surfaces, *Angew. Chem., Int. Ed. Engl.*, **54**, 6163–6167 (2015). (Cited on page 129.)

[Urg15c] J. I. Urgel, M. Schwarz, M. Garnica, D. Stassen, D. Bonifazi, D. Écija, J. V. Barth, and W. Auwärter, Controlling Coordination Reactions and Assembly on a Cu(111) Supported Boron Nitride Monolayer, *J. Am. Chem. Soc.*, **137**, 2420–2423 (2015). (Cited on pages 87 and 111.)

[Usa10] D. Usachov, V. K. Adamchuk, D. Haberer, A. Grüneis, H. Sachdev, A. B. Preobrajenski, C. Laubschat, and D. V. Vyalikh, Quasifreestanding Single-Layer Hexagonal Boron Nitride as a Substrate for Graphene Synthesis, *Phys. Rev. B*, **82**, 075415 (2010). (Cited on page 65.)

[VAb17] VAb Vakuum-Anlagenbau GmbH, Marie-Curie-Str. 11, 25337 Elmshorn, Germany (2017), `http://www.vab-vakuum.com/`, (Accessed: 2017-02-05). (Cited on page 38.)

[VAC17] VACOM Vakuum Komponenten & Messtechnik GmbH, In den Brückenäckern 3, 07751 Großlöbichau. Germany (2017), `https://www.vacom.de`, (Accessed: 2017-02-05). (Cited on pages 36, 38, and 39.)

[van80] C. J. van Oss, D. R. Absolom, and A. W. Neumann, Applications of net repulsive van der Waals forces between different particles, macromolecules, or biological cells in liquids, *Colloids Surf.*, **1**, 45–56 (1980). (Cited on page 14.)

[van86] M. A. van Hove, *Low-energy electron diffraction: Experiment, Theory and Surface Structure Determination*. Springer Berlin Heidelberg, Berlin, Heidelberg, (1986). (Cited on pages 33 and 34.)

[van11] S. van der Walt, S. C. Colbert, and G. Varoquaux, The NumPy Array: A Structure for Efficient Numerical Computation, *Comput. Sci. Eng.*, **13**, 22–30 (2011). (Cited on page 161.)

[van12] P. van der Heide, *X-ray photoelectron spectroscopy: An introduction to principles and practices*. Wiley-Blackwell, Hoboken, NJ, (2012). (Cited on pages 18, 19, 20, 21, 22, 40, and 42.)

[van14] S. van der Walt, J. L. Schonberger, J. Nunez-Iglesias, F. Boulogne, J. D. Warner, N. Yager, E. Gouillart, and T. Yu, Scikit-Image: Image Processing in Python, *PeerJ*, **2**, e453 (2014). (Cited on page 161.)

[van16] N. J. van der Heijden, P. Hapala, J. A. Rombouts, J. van der Lit, D. Smith, P. Mutombo, M. Svec, P. Jelinek, and I. Swart, Characteristic Contrast in Δfmin Maps of Organic Molecules Using Atomic Force Microscopy, *ACS Nano*, **10**, 8517–8525 (2016). (Cited on page 60.)

[Van17] Van der Heijden, Labortechnik GmbH Tramsmeiers Berg 2, 32694 Dörentrup, Deutschland (2017), `http://www.van-der-heijden.de/`, (Accessed: 2017-02-27). (Cited on page 39.)

[Var99] I. A. Vartanyants and J. Zegenhagen, Photoelectric scattering from an X-ray interference field, *Solid State Commun.*, **113**, 299–320 (1999). (Cited on page 31.)

[Var09] A. Varykhalov and O. Rader, Graphene grown on Co(0001) films and islands: Electronic structure and its precise magnetization dependence, *Phys. Rev. B*, **80**, 1224 (2009). (Cited on page 71.)

[Var10] A. Varykhalov, W. Gudat, and O. Rader, Imaging buried molecules: Fullerenes under graphene, *Adv. Mater.*, **22**, 3307–3310 (2010). (Cited on page 2.)

[VAT17] VAT Germany GmbH, Zur Wetterwarte 50, Haus 337/G 01109 Dresden, Germany (2017), `http://www.vatvalve.com`, (Accessed: 2017-02-17). (Cited on pages 36 and 38.)

[Vég06] J. Végh, The Shirley background revised, *J. Electron Spectrosc. Relat. Phenom.*, **151**, 159–164 (2006). (Cited on page 22.)

[Vic09] J. C. Vickerman, Introduction, In J. C. Vickerman and I. S. Gilmore, editors, *Surface Analysis - The Principal Techniques*, pages 1–8. John Wiley & Sons, Ltd, Chichester, UK, (2009). (Cited on pages 16, 19, 20, and 21.)

[Vij12] S. Vijayaraghavan, D. Écija, W. Auwärter, S. Joshi, K. Seufert, A. P. Seitsonen, K. Tashiro, and J. V. Barth, Selective Supramolecular Fullerene-Porphyrin Interactions and Switching in Surface-Confined C_60−Ce(TPP)$_2$ Dyads, *Nano Lett.*, **12**, 4077–4083 (2012). (Cited on page 137.)

[Vij13] S. Vijayaraghavan, D. Écija, W. Auwärter, S. Joshi, K. Seufert, M. Drach, D. Nieckarz, P. Szabelski, C. Aurisicchio, D. Bonifazi, and J. V. Barth, Supramolecular assembly of interfacial nanoporous networks with simultaneous expression of metal-organic and organic-bonding motifs, *Chem. - Eur. J.*, **19**, 14143–14150 (2013). (Cited on page 137.)

[Vog08] R. Voggu, B. Das, C. S. Rout, and C. N. R. Rao, Effects of charge transfer interaction of graphene with electron donor and acceptor molecules examined using Raman spectroscopy and cognate techniques, *J. Phys. Cond. Matter*, **20**, 472204 (2008). (Cited on page 99.)

[Vog12] P. Vogt, P. de Padova, C. Quaresima, J. Avila, E. Frantzeskakis, M. C. Asensio, A. Resta, B. Ealet, and G. Le Lay, Silicene: Compelling experimental evidence for graphenelike two-dimensional silicon, *Phys. Rev. Lett.*, **108**, 155501 (2012). (Cited on page 71.)

[Vol13] E. N. Voloshina, E. Fertitta, A. Garhofer, F. Mittendorfer, M. Fonin, A. Thissen, and Y. S. Dedkov, Electronic Structure and Imaging Contrast of Graphene Moire on Metals, *Sci. Rep.*, **3**, 1072 (2013). (Cited on page 68.)

[Wäc10] C. Wäckerlin, D. Chylarecka, A. Kleibert, K. Müller, C. Iacovita, F. Nolting, T. A. Jung, and N. Ballav, Controlling Spins in Adsorbed Molecules by a Chemical Switch, *Nat. Commun.*, **1**, 61 (2010). (Cited on pages 1, 87, and 90.)

[Wag79] C. D. Wagner, W. M. Riggs, L. E. Davis, J. F. Moulder, and G. E. Muilenberg, *Handbook of X-ray Photoelectron Spectroscopy: A Reference Book of Standard Data for Use in X-ray Photoelectron Spectroscopy*. Perkin-Elmer Corp., Physical Electronics Division, Eden Prairie, MN, (1979). (Cited on page 98.)

[Wah04] P. Wahl, L. Diekhöner, M. A. Schneider, L. Vitali, G. Wittich, and K. Kern, Kondo temperature of magnetic impurities at surfaces, *Phys. Rev. Lett.*, **93**, 176603 (2004). (Cited on page 118.)

[Wak05] A. Wakamiya, T. Ide, and S. Yamaguchi, Toward pi-conjugated molecule bundles: Synthesis of a series of B,B',B"-trianthryl-N,N',N"-triarylborazines and the bundle effects on their properties, *J. Am. Chem. Soc.*, **127**, 14859–14866 (2005). (Cited on page 128.)

[Wal13] S. E. Waller, M. Ray, B. L. Yoder, and C. C. Jarrold, Simple relationship between oxidation state and electron affinity in gas-phase metal-oxo complexes, *J. Phys. Chem. A*, **117**, 13919–13925 (2013). (Cited on page 114.)

[Wan12a] H. Wang, T. Maiyalagan, and X. Wang, Review on Recent Progress in Nitrogen-Doped Graphene: Synthesis, Characterization, and Its Potential Applications, *ACS Catal.*, **2**, 781–794 (2012). (Cited on page 124.)

[Wan12b] Q. H. Wang, K. Kalantar-Zadeh, A. Kis, J. N. Coleman, and M. S. Strano, Electronics and optoelectronics of two-dimensional transition metal dichalcogenides, *Nat. Nanotechnol.*, **7**, 699–712 (2012). (Cited on page 142.)

[Wan13] J. Wang, R. Zhao, Z. Liu, and Z. Liu, Widely tunable carrier mobility of boron nitride-embedded graphene, *Small*, **9**, 1373–1378 (2013). (Cited on page 141.)

[Wan14a] H. Wang, F. Liu, W. Fu, Z. Fang, W. Zhou, and Z. Liu, Two-dimensional heterostructures: Fabrication, characterization, and application, *Nanoscale*, **6**, 12250–12272 (2014). (Cited on page 123.)

[Wan14b] X. Wang, G. Sun, P. Routh, D.-H. Kim, W. Huang, and P. Chen, Heteroatom-doped graphene materials: Syntheses, properties and applications, *Chem. Soc. Rev.*, **43**, 7067–7098 (2014). (Cited on page 128.)

[Wan15] X.-Y. Wang, J.-Y. Wang, and J. Pei, BN heterosuperbenzenes: Synthesis and properties, *Chem. - Eur. J.*, **21**, 3528–3539 (2015). (Cited on page 128.)

[Was92] M. R. Wasielewski, Photoinduced electron transfer in supramolecular systems for artificial photosynthesis, *Chem. Rev.*, **92**, 435–461 (1992). (Cited on page 1.)

[Wat03] J. F. Watts and J. Wolstenholme, *An introduction to surface analysis by XPS and AES*. J. Wiley, New York and Chichester, (2003). (Cited on pages 16 and 18.)

[Wat04] K. Watanabe, T. Taniguchi, and H. Kanda, Direct-Bandgap Properties and Evidence for Ultraviolet Lasing of Hexagonal Boron Nitride Single Crystal, *Nat. Mater.*, **3**, 404–409 (2004). (Cited on page 55.)

[WB07] A. Weber-Bargioni, *Supramolecular organisation, conformation and electronic properties of porphyrin molecules on metal substrates*, PhD thesis, University of British Columbia (2007). (Cited on page 48.)

[Web08] A. Weber-Bargioni, W. Auwärter, F. Klappenberger, J. Reichert, S. Lefrançois, T. Strunskus, C. Wöll, A. Schiffrin, Y. Pennec, and J. V. Barth, Visualizing the Frontier Orbitals of a Conformationally Adapted Metalloporphyrin, *Chem. Phys. Chem.*, **9**, 89–94 (2008). (Cited on pages 96 and 122.)

[Wec17] D. Wechsler, M. Franke, Q. Tariq, L. Zhang, T.-L. Lee, P. K. Thakur, N. Tsud, S. Bercha, K. C. Prince, H.-P. Steinrück, and O. Lytken, Adsorption Structure of Cobalt Tetraphenylporphyrin on Ag(100), *J. Phys. Chem. C*, **121**, 5667–5674 (2017). (Cited on page 90.)

[Weh08] T. O. Wehling, K. S. Novoselov, S. V. Morozov, E. E. Vdovin, M. I. Katsnelson, A. K. Geim, and A. I. Lichtenstein, Molecular doping of graphene, *Nano Lett.*, **8**, 173–177 (2008). (Cited on page 2.)

[Weh10] T. O. Wehling, A. V. Balatsky, M. I. Katsnelson, A. I. Lichtenstein, and A. Rosch, Orbitally controlled Kondo effect of Co adatoms on graphene, *Phys. Rev. B*, **81**, 115427 (2010). (Cited on page 121.)

[Wei09] D. Wei, Y. Liu, Y. Wang, H. Zhang, L. Huang, and G. Yu, Synthesis of N-doped graphene by chemical vapor deposition and its electrical properties, *Nano Lett.*, **9**, 1752–1758 (2009). (Cited on page 124.)

[Wei17] S. Weiß, I. Krieger, T. Heepenstrick, S. Soubatch, M. Sokolowski, and F. S. Tautz, Determination of the Adsorption Geometry of PTCDA on the Cu(100) Surface, *Phys. Rev. B*, **96**, 075414 (2017). (Cited on page 87.)

[Wes04] M. Wessendorf, C. Wiemann, M. Bauer, M. Aeschlimann, M. A. Schneider, H. Brune, and K. Kern, Electronic surface structure of n -ML Ag/Cu(111) and Cs/n -ML Ag/Cu(111) as investigated by 2PPE and STS, *Appl. Phys. A*, **78**, 183–188 (2004). (Cited on pages 79, 82, and 162.)

[Wey11] A. J. Weymouth, T. Wutscher, J. Welker, T. Hofmann, and F. J. Giessibl, Phantom Force Induced by Tunneling Current: A Characterization on Si(111), *Phys. Rev. Lett.*, **106**, 226801 (2011). (Cited on page 60.)

[Wie01] R. Wiesendanger and M. Bode, Nano- and atomic-scale magnetism studied by spin-polarized scanning tunneling microscopy and spectroscopy, *Solid State Commun.*, **119**, 341–355 (2001). (Cited on page 11.)

[Wie14] A. Wiengarten, K. Seufert, W. Auwärter, D. Écija, K. Diller, F. Allegretti, F. Bischoff, S. Fischer, D. A. Duncan, A. C. Papageorgiou, F. Klappenberger, R. G. Acres, T. H. Ngo, and J. V. Barth, Surface-Assisted Dehydrogenative Homocoupling of Porphine Molecules, *J. Am. Chem. Soc.*, **136**, 9346–9354 (2014). (Cited on page 98.)

[Wie15] A. Wiengarten, *Scanning tunneling microscopy investigation of structure and electronic properties of surface-confined tetrapyrrolic species*, PhD thesis, Technische Universität München (2015). (Cited on pages 35 and 109.)

[Wil11] P. Willmott, *An introduction to synchrotron radiation: Techniques and applications*. Wiley, Chichester, (2011). (Cited on pages 19, 26, 27, 42, 49, and 50.)

[Woo94a] D. P. Woodruff, B. C. C. Cowie, and A. R. H. F. Ettema, Surface Structure Determination Using X-ray Standing Waves: A Simple View, *J. Phys. Cond. Matter*, **6**, 10633–10645 (1994). (Cited on pages 23, 28, and 32.)

[Woo94b] D. P. Woodruff and T. A. Delchar, *Modern techniques of surface science*, Cambridge solid state science series. Cambridge University Press, Cambridge and New York, 2nd ed. edition, (1994). (Cited on page 33.)

[Woo98] D. P. Woodruff, Normal Incidence X-ray Standing Wave Determination of Adsorbate Structures, *Prog. Surf. Sci.*, **57**, 1–60 (1998). (Cited on pages 24, 27, and 91.)

[Woo05] D. P. Woodruff, Surface Structure Determination Using X-ray Standing Waves, *Rep. Prog. Phys.*, **68**, 743–798 (2005). (Cited on pages 23, 24, 25, 27, 28, 29, 30, 31, 32, 52, 92, 96, 97, 152, 165, and 166.)

[Wu04] S. W. Wu, G. V. Nazin, X. Chen, X. H. Qiu, and W. Ho, Control of relative tunneling rates in single molecule bipolar electron transport, *Phys. Rev. Lett.*, **93**, 236802 (2004). (Cited on page 8.)

[Wur16] B. Wurster, D. Grumelli, D. Hötger, R. Gutzler, and K. Kern, Driving the Oxygen Evolution Reaction by Nonlinear Cooperativity in Bimetallic Coordination Catalysts, *J. Am. Chem. Soc.*, **138**, 3623–3626 (2016). (Cited on page 137.)

[Xu09] Y. Xu, Z. Liu, X. Zhang, Y. Wang, J. Tian, Y. Huang, Y. Ma, X. Zhang, and Y. Chen, A Graphene Hybrid Material Covalently Functionalized with Porphyrin: Synthesis and Optical Limiting Property, *Adv. Mater.*, **21**, 1275–1279 (2009). (Cited on page 107.)

[Xue12] T. Xue, S. Jiang, Y. Qu, Q. Su, R. Cheng, S. Dubin, C.-Y. Chiu, R. Kaner, Y. Huang, and X. Duan, Graphene-Supported Hemin as a Highly Active Biomimetic Oxidation Catalyst, *Angew. Chem.*, **124**, 3888–3891 (2012). (Cited on page 107.)

[Yan14] Z. Yang, M. Corso, R. Robles, C. Lotze, R. Fitzner, E. Mena-Osteritz, P. Bäuerle, K. J. Franke, and J. I. Pascual, Orbital redistribution in molecular nanostructures mediated by metal-organic bonds, *ACS Nano*, **8**, 10715–10722 (2014). (Cited on page 135.)

[Yan17] L. Yan, G. Kuang, Q. Zhang, X. Shang, P. N. Liu, and N. Lin, Self-assembly of a binodal metal-organic framework exhibiting a demi-regular lattice, *Faraday Discuss.*, **204**, 111–121 (2017). (Cited on page 137.)

[Yok01] T. Yokoyama, S. Yokoyama, T. Kamikado, and S. Mashiko, Nonplanar Adsorption and Orientational Ordering of Porphyrin Molecules on Au(111), *J. Chem. Phys.*, **115**, 3814–3818 (2001). (Cited on page 87.)

[Yos03] S. Yoshimoto, A. Tada, K. Suto, R. Narita, and K. Itaya, Adlayer Structure and Electrochemical Reduction of O_2 on Self-Organized Arrays of Cobalt and Copper Tetraphenyl Porphines on a Au(111) Surface, *Langmuir*, **19**, 672–677 (2003). (Cited on page 1.)

[Yu14] Y.-X. Yu, A dispersion-corrected DFT study on adsorption of battery active materials anthraquinone and its derivatives on monolayer graphene and h-BN, *J. Mater. Chem. A*, **2**, 8910–8917 (2014). (Cited on page 99.)

[Zeg93] J. Zegenhagen, Surface structure determination with X-ray standing waves, *Surf. Sci. Rep.*, **18**, 202–271 (1993). (Cited on page 24.)

[Zeg09] J. Zegenhagen and A. Kazimirov, *The X-ray standing wave technique: Principles and applications*, volume 7 of *Series on synchrotron radiation techniques & applications*. World Scientific, Singapore and Haackensack N.J., (2009). (Cited on pages 23, 24, and 165.)

[Zel14] P. Zeller and S. Günther, What are the Possible Moiré Patterns of Graphene on Hexagonally Packed Surfaces? Universal Solution for Hexagonal Coincidence Lattices, Derived by a Geometric Construction, *New J. Phys.*, **16**, 083028 (2014). (Cited on page 58.)

[Zha98] Y. Zhang and W. Yang, Comment on "Generalized Gradient Approximation Made Simple", *Phys. Rev. Lett.*, **80**, 890 (1998). (Cited on page 153.)

[Zha03] C. X. Zhang and S. J. Lippard, New Metal Complexes as Potential Therapeutics, *Curr. Opin. Chem. Biol.*, **7**, 481–489 (2003). (Cited on page 85.)

[Zha05] A. Zhao, Q. Li, L. Chen, H. Xiang, W. Wang, S. Pan, B. Wang, X. Xiao, J. Yang, J. G. Hou, and Q. Zhu, Controlling the Kondo effect of an adsorbed magnetic ion through its chemical bonding, *Science*, **309**, 1542–1544 (2005). (Cited on pages 114, 116, and 121.)

[Zha13] Y.-h. Zhang, S. Kahle, T. Herden, C. Stroh, M. Mayor, U. Schlickum, M. Ternes, P. Wahl, and K. Kern, Temperature and magnetic field dependence of a Kondo system in the weak coupling regime, *Nat. Commun.*, **4**, 2110 (2013). (Cited on page 114.)

[Zha15] Q. Zhang, G. Kuang, R. Pang, X. Shi, and N. Lin, Switching Molecular Kondo Effect via Supramolecular Interaction, *ACS Nano*, **9**, 12521–12528 (2015). (Cited on page 98.)

[Zha16] Y. Zhang, J. Qiao, S. Gao, F. Hu, D. He, B. Wu, Z. Yang, B. Xu, Y. Li, Y. Shi, W. Ji, P. Wang, X. Wang, M. Xiao, H. Xu, J.-B. Xu, and X. Wang, Probing Carrier Transport and Structure-Property Relationship of Highly Ordered Organic Semiconductors at the Two-Dimensional Limit, *Phys. Rev. Lett.*, **116**, 016602 (2016). (Cited on page 99.)

[Zha17a] L. Zhang, M. Lepper, M. Stark, T. Menzel, D. Lungerich, N. Jux, W. Hieringer, H.-P. Steinrück, and H. Marbach, On the Critical Role of the Substrate: The Adsorption Behaviour of Tetrabenzoporphyrins on Different Metal Surfaces, *Phys. Chem. Chem. Phys.*, **19**, 20281–20289 (2017). (Cited on page 119.)

[Zha17b] T. Zhang, G. Chen, and L. Zhu, Enhanced Adsorption of Co Atoms on Grain Boundary of Boron Nitride, *J. Nanopart. Res.*, **19**, 17953 (2017). (Cited on page 87.)

[Zir09] J. Ziroff, P. Gold, A. Bendounan, F. Forster, and F. Reinert, Adsorption energy and geometry of physisorbed organic molecules on Au(111) probed by surface-state photoemission, *Surf. Sci.*, **603**, 354–358 (2009). (Cited on pages 71, 82, and 135.)

[Zöp00] S. Zöphel, *Der Aufbau eines Tieftemperatur-Rastertunnelmikroskops und Strukturuntersuchungen auf vicinalen Kupferoberflächen*, PhD thesis, Freie Universität Berlin (2000). (Cited on page 35.)

[Zum16] F. H. Zum Farwick Hagen, D. M. Zimmermann, C. C. Silva, C. Schlueter, N. Atodiresei, W. Jolie, A. J. Martínez-Galera, D. Dombrowski, U. A. Schröder, M. Will, P. Lazić, V. Caciuc, S. Blügel, T.-L. Lee, T. Michely, and C. Busse, Structure and Growth of Hexagonal Boron Nitride on Ir(111), *ACS Nano*, **10**, 11012–11026 (2016). (Cited on pages 24, 56, 57, 58, 66, and 140.)

Publications

- **Controlling Coordination Reactions and Assembly on a Cu(111) Supported Boron Nitride Monolayer**
  J. I. Urgel, M. Schwarz, M. Garnica, D. Stassen, D. Bonifazi, D. Ecija, J. V. Barth, W. Auwärter
  J. Am. Chem. Soc., **137**, 2420-2423, (2015)

- **Comparative study of the interfaces of graphene and hexagonal boron nitride with silver**
  M. Garnica, M. Schwarz, J. Ducke, Y. He, F. Bischoff, J. V. Barth, D. Stradi, W. Auwärter
  Phys. Rev. B, **94**, 155431, (2016)

- **Corrugation in the Weakly Interacting Hexagonal-BN/Cu(111) System: Structure Determination by Combining Noncontact Atomic Force Microscopy and X-ray Standing Waves**
  M. Schwarz, A. Riss, M. Garnica, J. Ducke, P. S. Deimel, D. A. Duncan, P. K. Thakur, T.-L. Lee, A. P. Seitsonen , J. V. Barth, F. Allegretti, W. Auwärter
  ACS Nano, **11**, 9151-9161, (2017)

- **Adsorption Conformation and Lateral Registry of Cobalt Porphine on Cu(111)**
  M. Schwarz, M. Garnica, D. A. Duncan, A. Pérez Paz, J. Ducke, P. S. Deimel, P. K. Thakur, T.-L. Lee, J. V. Barth, F. Allegretti, W. Auwärter
  J. Phys. Chem. C, **122**, 5452-5461, (2018)

- **Layered Insulator/Molecule/Metal Heterostructures with Molecular Functionality through Porphyrin Intercalation**
  J. Ducke, A. Riss, A. Pérez Paz, K. Seufert, M. Schwarz, M. Garnica, A. Rubio, W. Auwärter
  ACS Nano, **12**, 2677-2684, (2018)

- **BN-Patterning of Metallic Substrates through Metal Coordination of Decoupled Borazines**
  M. Schwarz, M. Garnica, F. Fasano, N. Demitri, D. Bonifazi, W. Auwärter
  Chem. - Eur. J. **24**, 9565-9571 (2018)

- **Adsorption Geometry of Cobalt Porphine on Two-Dimensional Hexagonal Boron Nitride**
  M. Schwarz, D. A. Duncan, M. Garnica, J. Ducke, P. S. Deimel, P. K. Thakur, T.-L. Lee, J. V. Barth, F. Allegretti, W. Auwärter
  in preparation

- **Charge state control of F_{16}CoPc on *h*-BN/Cu(111)**
  M. Pörtner, Y. Wei, A. Riss, K. Seufert, M. Schwarz, M. Garnica, J. V. Barth, L. Diekhöner, W. Auwärter
  in preparation

- **Structure Determination of 4×4 Silicene on Ag(111) by means of XSW**
  J. T. Küchle, D. A. Duncan, M. Schwarz, T.-L. Lee, A. P. Seitsonen, W. Auwärter, J. V. Barth, F. Allegretti
  in preparation

Acknowledgments

I had the pleasure to work with a lot of brilliant people during the course of this PhD project, which I want to thank for their contributions to the success of my thesis. Especially mentioned should be:

- First and foremost I want to thank Willi Auwärter for being an excellent supervisor! You have a large share in the success of this work. I am very grateful for your support and guidance in the lab, the relaxed scientific and personal discussions, and that you fostered an environment and an atmosphere in our group where it was always a pleasure to come to work! Thank you for inspiring me with physics at the nanoscale!

- Next, I want to thank Manuela Garnica who was an awesome mentor. You taught me a lot, you pushed me when I needed to be pushed, and you encouraged me when I was desperate. You were not just a colleague with whom I really enjoyed working with, but you have also become a true friend in the course of the last four years! Muchas, muchas gracias!

- Additionally, I want to express gratitude to David Duncan and Francesco Allegretti for their help during our Diamond beamtimes and the outstanding support during data analysis and paper writing afterwards. Thank you for your patience and your answers to all of my questions! I learned a lot from both of you!

- Thank you, Alex Riss! I really appreciated the short AFM project together with you and the countless discussions about science and life. I also want to thank Knud Seufert for his support and advice in the lab.

- Moreover, I want to thank Alex Weber-Bargioni for giving me the opportunity to work in his group at the Lawrence Berkeley National Laboratory. It was a marvelous time and an awesome experience to work in this environment, especially together with Bruno Schuler. Thanks to all the other people of the *groupo sportivo* and the Imaging Facility I met there. I had a blast!

- I further want to thank Ari Seitsonen, Alejandro Pérez Paz and Daniele Stradi for their theoretical support and insightful discussions on the different projects, as well as Davide Bonifazi and his group for the synthesis of the molecules we used.

- Next, I want to thank the group of senior PhD students who introduced me to the experimental setup and helped me a lot during my starting time: Alissa Wiengarten, Nacho Urgel, Tobias Kaposi and Felix Bischoff.

- I also thank my colleagues Aleksandr Baklanov, Peter Deimel, Jacob Ducke, Yuanqin He, Domenik Zimmermann, Martin Uphoff, Andi Walz, Matthias Pörtner, Sabine Synkule, Tobias Paintner, Karo Stoiber and Johannes Küchle for the help in the lab, the scientific discussions, and the time we spent together, which made this period a memorable time.

- Next, I'd like to thank the *Mensa group* for many relaxed discussions besides science in a good atmosphere: Anthoula Papageorgiou, Flo Klappenberger, Carlos Palma, Yiqi Zhang, Tao Lin, Raphael Hellwig, Mateusz Paszkiewicz, Liding Zhang, Wei Ran, and Maryam Ebrahimi.

- Additionally, I want to acknowledge the staff scientists at Diamond Light Source, Pardeep Kumar Thakur and Tien-Lin Lee as well as beamline technician Dave McCue.

- Last but not least, I want to acknowledge the staff of E20: Victoria Blaschek for her support in all administrative manners; Karl Eberle, Reinhold Schneider and Peter Feulner for their help and comprehensive expertise in all technical matters; and Max Glanz for the computer and network support. Also, I like to thank Johannes Barth for providing the excellent infrastructure of the chair E20, and for his assistance with our papers.

- And finally, I want to express my heartfelt gratitude to my family for their unquestioning support during my whole time at the TUM. It was a long journey and a fantastic time!